Università degli studi di Udine

DIPARTIMENTO DI SCIENZE MATEMATICHE, INFORMATICHE E FISICHE
Corso di dottorato di ricerca in Informatica e Scienze Matematiche e Fisiche
33° ciclo

TESI DI DOTTORATO

Multi-wavelength afterglow numerical code and data analysis of MAGIC very high energy emission from gamma-ray bursts

Dottorando:
Davide Miceli
Matricola 131721

Supervisore:
Prof. ssa Barbara De Lotto

Co-supervisori:
Prof. Francesco Longo
Dr.ssa Lara Nava

Anno 2021

Abstract

This PhD thesis is focused on the study of very high energy (E > 100 GeV, VHE) emission from a class of extragalactic transient sources called Gamma-Ray Bursts (GRBs). In particular, I have i) performed data analysis of GRB observations by the MAGIC telescopes; ii) developed a numerical code to exploit such observations and investigate the properties of such astrophysical sources.

Despite been discovered more than 50 years ago, GRBs are still a hot topic in Astrophysics. They are extremely energetic phenomena characterized by two emission phases. The first one, called prompt phase, is a rapid and irregular emission in the X and γ energy range which lasts from milliseconds to thousands of seconds. The second one, called afterglow emission, consists in a long-lasting (days to months) emission covering the entire electromagnetic spectrum, from radio up to γ-rays and interpreted as the synchrotron radiation produced in the external forward shock scenario. The possible extension of the GRB emission in the high energy (0.5 MeV < E < 100 GeV, HE) and to the very high energy domain has always been one of the most debated open questions in GRB physics. The HE observations have revealed an emission component delayed and lasting longer with respect to the prompt one. Moreover, the highest energy photons observed by Fermi-LAT gave the first evidence that a different radiation mechanism with respect to the synchrotron radiation may be needed to explain such energetic emission and point towards the possibility that a VHE component in GRBs is present. A firm conclusion could not be reached until 2019, when an unprecedented discovery was performed: the ground-based imaging Cherenkov telescopes MAGIC and H.E.S.S. revealed for the first time ever the presence of a VHE emission component in GRB afterglows up to TeV energies. Such detections gave birth to unique studies concerning the radiation processes involved in GRBs. For one of these events, namely GRB 190114C, the VHE emission was interpreted as produced via the Synchrotron Self Compton (SSC) mechanism.

First, in this thesis I will present `MUSE-GRB`, a numerical code which I developed to simulate the multi-wavelength GRB afterglow spectra and light curves in the external forward shock scenario. In this code the dynamical evolution of a blastwave interacting with an external medium is reproduced and the time-evolving kinetic equations for electrons, protons and photons are solved. As a result, the afterglow spectra and the light curves at different times and frequencies can be calculated. This flexible and very complete code can be applied to GRB observational data to model the multi-wavelength afterglow emission, thus inferring constraints on several properties of the GRB physics. The code has been intensively tested with analytical prescriptions and with a similar numerical code available in literature. Such tool is able to model the observational data coming from the MAGIC and the H.E.S.S. telescopes and verify their consistency with a SSC origin.
In the second part of this thesis I will present the MAGIC data analysis of two GRBs detected in the VHE band, namely GRB 190114C and GRB 190829A. I performed the dedicated MAGIC data analysis of GRB 190114C in the context of a multi-wavelength study of the emission. The MAGIC data were analyzed in several time intervals to investigate a possible spectral evolution in the VHE band. The statistical error and several sources of systematic error were assessed in order to evaluate the firmness and the stability of the data analysis. GRB 190829A, successfully detected in the VHE band by the H.E.S.S. telescopes, was also observed by the MAGIC telescopes. Preliminary MAGIC data analysis shows a possible hint of detection. In the

context of the study and interpretation of the VHE emission coming from GRBs some applications of MUSE-GRB to GRB 190114C and GRB 190829A are also presented.
Despite these few detections, the majority of the GRBs observed in the VHE range did not show any significant signal. As a result, for these GRBs only upper limits on the γ-ray flux can be derived. I performed the MAGIC data analysis for some of these events and, for a few selected cases, I developed a novel calculation of the MAGIC de-absorbed upper limit and combined the results with the information coming from the X-ray and HE band, shown to be connected with the TeV emission.

The chapters are organized as follows: in Chapter 1 an introduction to cosmic rays and γ-ray astrophysics is presented. A detailed section is devoted to the method developed for the indirect detection of γ-rays, namely the imaging technique, and to current and future ground-based Cherenkov telescopes working in the very high energy domain. In Chapter 2 I describe the MAGIC telescopes and the standard and non-standard data analysis chains. In Chapter 3 the main properties of GRBs are presented, especially concerning the afterglow emission and the general framework of the synchrotron and Synchrotron-Self Compton (SSC) external forward shock scenario. In Chapter 4 my numerical code MUSE-GRB is described together with several tests performed to study the effects of different processes on the particle energy spectra and then on the resulting radiation. In Chapter 5 the results from the MAGIC data analysis of GRB 190114C, GRB 190829A, and a sample of GRBs observed by MAGIC without any significant detection is shown. An application of MUSE-GRB to GRB 190114C and GRB 190829A observational data is also shown. Finally, in Chapter 6 the conclusions and prospects for the future are presented.

Contents

List of Figures

List of Tables

Chapter 1

Introduction

1.1 Cosmic rays

In the wide domain of high energy astrophysics γ-rays have always been intimately linked with the physics of cosmic rays. By **Cosmic Rays** (CRs) we mean energetic particles, mostly made of protons ($\sim 90\%$), helium nuclei ($\lesssim 10\%$) and a small amount of electrons/positrons and heavier nuclei. The reason of this connection is simple: CRs accelerated in strong magnetic fields by astrophysical objects can produce the energetic γ-ray radiation. Therefore, the comprehension of the physics of CRs can be useful to investigate the emission and acceleration mechanisms as well as the origin of such powerful photons in the Universe. CRs were discovered at the beginning of the 20th century, thanks to the combined studies on the ionized radiation made by Theodor Wulf [1], Domenico Pacini [2] and especially Viktor Hess [3] who, thanks to a series of balloon flights, showed the first clear evidence of a high energy ionized radiation coming from outside the Earth.
The CR energy spectrum (Figure 1.1) spans over 12 orders of magnitude in energy, from about 10^9 eV up to 10^{21} eV with fluxes going from thousands of particles per square meter per second down to one particle per square kilometer per century. The features of the spectrum are used to classify CRs through different origin and observational techniques. Below few tens of GeV, particles coming outside the solar system are deflected by the solar magnetic field (so-called *solar modulation* phenomenon) and so the CRs are of solar origin. Above few tens of GeV the differential energy spectrum can be well fitted with a power-law $dN/dE = E^{-\alpha}$ where $\alpha \simeq 2.7$ up to $E \sim 10^{15}$ eV. At this energy a first break, called the *knee*, is present and the CR spectrum changes its slope. For energies below the knee the particles are thought to be of Galactic origin, while those above the knee are interpreted as of extragalactic origin. Then, a second break, the *ankle*, can be seen in the spectrum for $E \sim 10^{18}$ eV. Between the knee and the ankle the spectral index is ~ 3.1. After the ankle, the spectrum hardens, with an index ~ 2.6. Finally, for $E \sim 5.0 \times 10^{19}$ eV, the spectrum undergoes a severe cut-off, called **GZK cut-off** ([5, 6]), due to the interaction of CRs with photons of the Cosmic Microwave Background (CMB).
The sources responsible for CR production and acceleration are still quite under debate. For the Galactic ones the best candidate sources for standard models are Supernova Remnants (SNRs) [7], even though recent ideas have proposed different sources like young Pulsar Wind Nebulae (PWNe) [8]. For the extragalactic ones the most probable sources are considered to be Active Galactic Nuclei (AGN) [9].
Finally, also the acceleration mechanisms are still under debate. The main ingredients of particle acceleration processes are magnetic fields and shock waves. Nowadays, the first order Fermi mechanism (described in detail in Section 3.4.2), also called *diffusive shock acceleration*, is commonly recognized as responsible for most of the high-energy CRs in the Galaxy, even if an observational proof is still missing. For

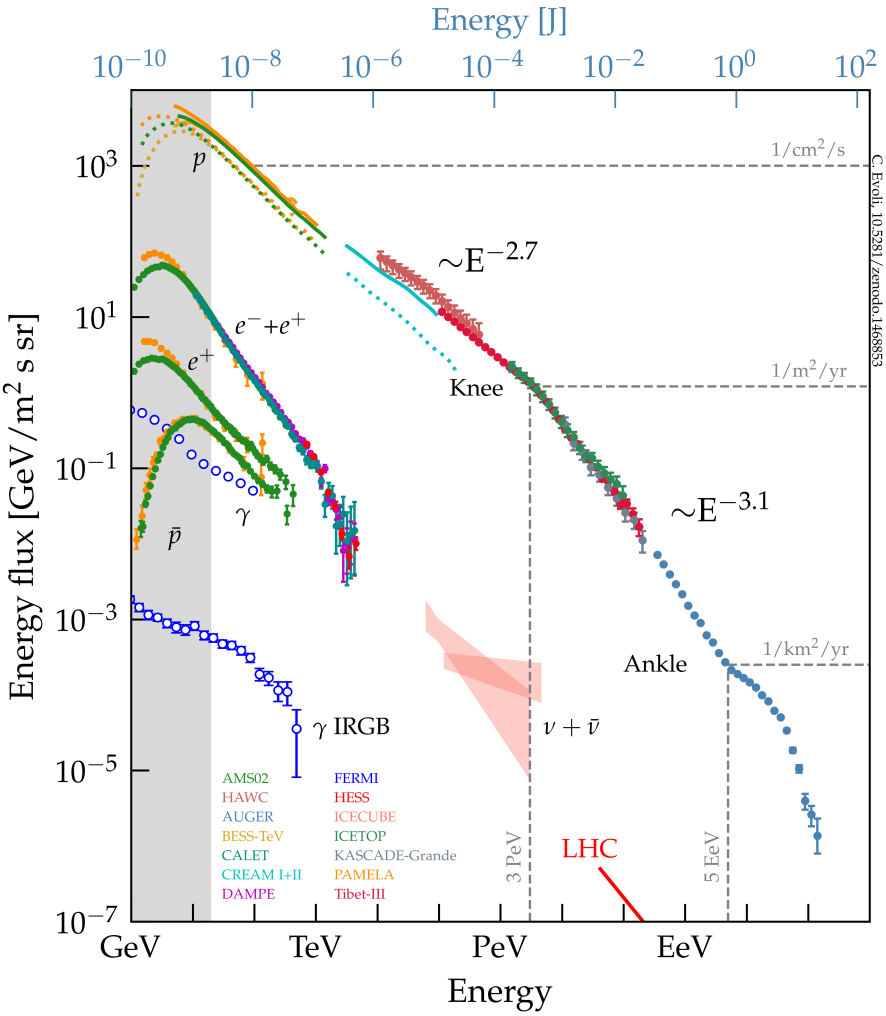

FIGURE 1.1: The CR energy spectrum measured by several experiments. Also the spectrum of the main subatomic compositions are reported. A comparison with the LHC achievable energy is also indicated. From [4].

higher energies CRs (up to 10^{20} eV) instabilities and enhanced magnetic flux density must be inferred. Hillas [10] summarized the conditions on potential acceleration sites using a relation between the maximum energy to which a particle of charge Ze can be accelerated in a diffusive shock model, the size R and the strength of the magnetic field B of the site:

$$E_{max} = \beta Ze\left(\frac{B}{1\mu G}\right)\left(\frac{R}{1kpc}\right) \quad \text{EeV} \tag{1.1}$$

where β represents the velocity of the accelerating shock wave. This relationship can be illustrated in the so-called *Hillas plot* (Figure 1.2).

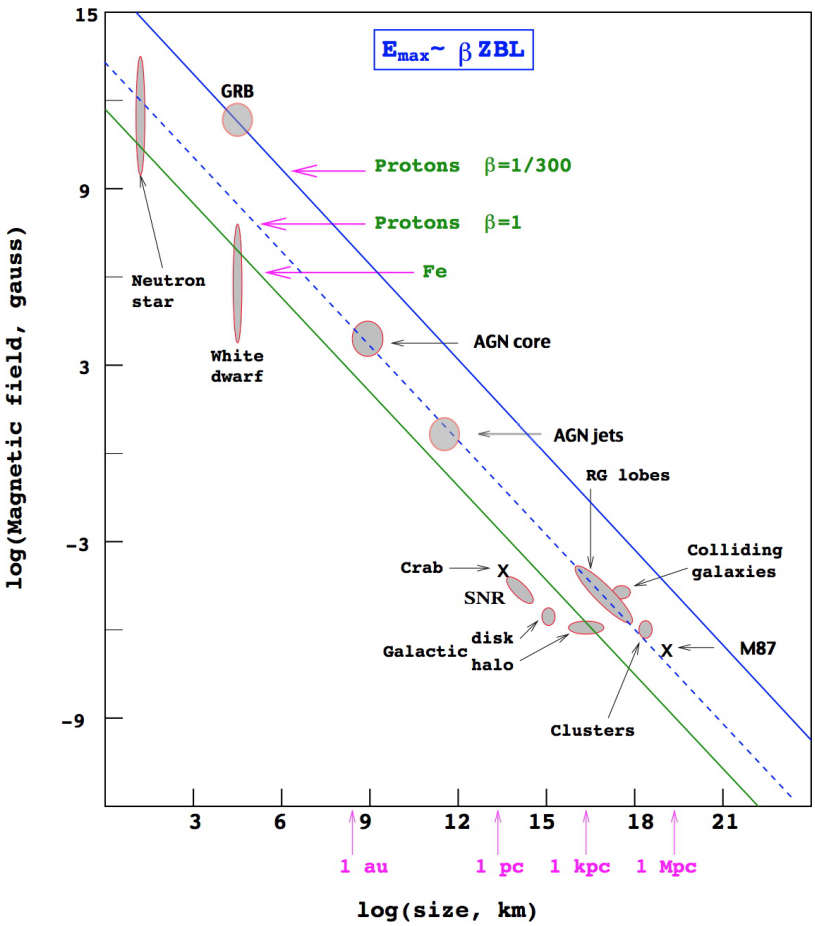

FIGURE 1.2: Hillas plot: typical source size versus magnetic field strength for several accelerator candidates. To accelerate a given particle species above 10^{20} eV objects must lie above the corresponding lines. From [9].

1.2 γ-ray astrophysics

γ-rays are the highest frequency radiation of the electromagnetic spectrum, covering a very wide energy range. Therefore, it is common to divide the γ-ray spectrum in several energetic ranges:

- High Energy (HE) (0.5 MeV - 100 GeV);
- Very High Energy (VHE) (100 GeV - 100 TeV);
- Ultra High Energy (UHE) (100 TeV - 100 PeV);
- Extreme High Energy (EHE) (above 100 PeV).

In this thesis, I will focus on the VHE band, since most of the work presented in the following sections belongs to this energy range.
In the Universe there are more than 200 **sources** that emit γ-rays in the VHE domain[1]. In the usual classification we can divide these sources into two main categories:

[1] http://tevcat2.uchicago.edu/

- **Galactic sources**: such as compact objects or complex structures produced in the final stage of of stars' life (pulsars, supernovae remnants, pulsars wind nebulae) or even γ-ray binary systems and the Galactic center;

- **extragalactic sources**: such as Active Galactic Nuclei (AGN), starburst galaxies and Gamma-Ray Bursts (GRBs).

Therefore, the Universe has plenty of astrophysical objects or environments where γ-rays are produced. Moreover, γ-rays are known to be intimately connected with other cosmic messengers such as CRs, *neutrinos* and *gravitational waves* (GWs). This is the so-called **multi-messenger** astronomy field. The recent discoveries of gravitational waves [11, 12, 13] and high-energy cosmic neutrinos [14] linked with electromagnetic radiation have shown that the exploration of the Universe through these new messengers can give us new insights into the most extreme energetic cosmic events, environments and particle accelerators.
The production of energetic radiation such as γ-rays implies the presence of *non thermal* processes. The emission mechanisms known to be involved in γ-ray production are various, including the decay of unstable particles or interactions between charged particles and nuclear targets, magnetic fields and photon fields. We can divide these processes into two classes, depending on the nature of the particles that generate the radiation:

- **leptonic processes** where high-energy electrons or positrons ($e^{\pm}$) interact with radiation fields. It is called **synchrotron process** in presence of magnetic fields. Instead, in case of interactions with low-energies photons, the latter ones are upscattered through a process called **Inverse Compton (IC)**. If the electrons are responsible both for the emission of photons through synchrotron radiation and for the upscattering of the same photons via IC, this process is referred as **Synchrotron-Self Compton (SSC)**. These processes will be discussed in detail in Section 3.4.4;

- **hadronic processes** where nucleons or mesons are involved. In case of high energy protons interacting with magnetic fields, as well as for electrons and positron, **synchrotron radiation** can produce γ-rays, even if with less efficiency with respect to $e^{\pm}$ due to their higher mass. Moreover, the interaction between hadrons and photons can also produce energetic γ-ray radiation. This can happen when CRs interact with a see of photons coming from the synchrotron radiation or the bremsstrahlung of electrons or starlight. Also mutual interaction between protons can produce γ-ray emission. This happens when CR protons interact with the interstellar gas. In such environments, mostly neutral pions (π_0) can be produced both from $p\gamma$ or pp interactions. Then, neutral pions decay into γ-rays through two possible channels:

$$\pi^0 \rightarrow \gamma + \gamma \qquad (99\%)$$

$$\pi^0 \rightarrow \gamma + e^- + e^+ \qquad (1\%)$$

  so, in most of the cases, a pair of photons are produced through the so-called **pion decay** mechanism.

Once they are produced, γ-rays can propagate freely into the space, without being deflected by magnetic fields. However, they can interact with photon fields during their travel. In such cases the interaction between γ-rays and the background

photons γ_{bkg} produces an electron-positron pair via the so-called **pair production** process:

$$\gamma + \gamma_{bkg} \rightarrow e^+ + e^- \tag{1.2}$$

The cross section of the process is given by [15]:

$$\sigma_{\gamma\gamma}(\beta) = \frac{3}{16}\sigma_T(1-\beta^2)\left[2\beta(\beta^2-2) + (3-\beta^4)\ln\left(\frac{1+\beta}{1-\beta}\right)\right] \text{ cm}^2 \tag{1.3}$$

where σ_T is the Thompson cross section and β is defined as:

$$\beta(\epsilon_{bkg}, E, \phi) = \left[1 - \frac{2m_e^2c^4}{\epsilon_{bkg}E(1-\cos\phi)}\right]^{\frac{1}{2}} \tag{1.4}$$

ϵ_{bkg} and E are respectively the background and the source photon energy, while ϕ is the scattering angle. The pair production process is allowed if the background photon energy ϵ_{bkg} is above a certain energy threshold ϵ_{thr}:

$$\epsilon_{bkg} > \epsilon_{thr}(E, \phi) = \frac{2m_e^2c^4}{E(1-\cos\phi)} \tag{1.5}$$

The cross section has its maximimum $\sigma_{\gamma\gamma} \simeq \sigma_T/4$ for $\beta \simeq 0.7$, therefore, assuming an isotropic background of photons ($\langle\cos\phi\rangle \rightarrow 0$), the cross-section is maximized for background photons of energy [16]:

$$\epsilon_{bkg}(E) \simeq \left(\frac{900\,GeV}{E}\right) \textbf{ eV} \tag{1.6}$$

For γ-rays the two main sources of background photons are the *Cosmic Microwave Background* (CMB) radiation and the *Extragalactic Background Light* (EBL). Since background photons that maximize the cross section are related to source photons as shown in equation 1.6, as a consequence UHE γ-rays mostly interact with CMB photons, while for VHE γ-rays the interaction occurs mostly with the UV/optical/infrared photons of the EBL. Indeed, the EBL consists of all the radiation accumulated by extragalactic sources throughout most of the life of the Universe. Some of this radiation is still streaming in the Universe, but now it is shifted in the UV/optical/infrared band due to absorption or re-emission by dust and cosmic expansion. So, the EBL dramatically reduces the amount of γ-rays in the energy band from $\sim$ 100 GeV to $\sim$ 100 TeV, changing the spectral shape of the sources in this range. Several numerical models have been developed to account for this effect. A plot of the present knowledge on the density of photons in the EBL region is shown in Figure 1.3. These models, with different approaches, can estimate the EBL intensities at different wavelengths and the *attenuation* factor $e^{-\tau(E_\gamma,z)}$ between the intrinsic and the observed spectrum of a source in the VHE range. The attenuation coefficient $\tau(E_\gamma, z)$ is called *optical depth* and it depends on the observed energy of the photons E_γ for a given EBL photon density $n(\epsilon_{bkg}, z)$, and on the redshift z. It is calculated as [17]:

$$\tau(E_\gamma, z) = \int_0^z \left(\frac{dl'}{dz'}\right)dz' \int_{-1}^{1} d\cos\phi \frac{1-\cos\phi}{2} \int_{\epsilon_{thr}(E,\phi)}^{\infty} d\epsilon'_{bkg}\sigma_{\gamma\gamma}(\beta')n(\epsilon'_{bkg}, z') \tag{1.7}$$

where dl'/dz' is the distance travelled by a photon per unit redshift at redshift z'.

The EBL attenuation is then a function of the photon energies and of the redshift. Therefore, distant sources with higher redshift will be more affected by EBL absorption. Moreover, photons of higher energies in the range 100 GeV - 100 TeV will be more affected by the EBL, producing a steepening of the spectral shape. This will be treated in detail for GRB spectra in Chapter 5.

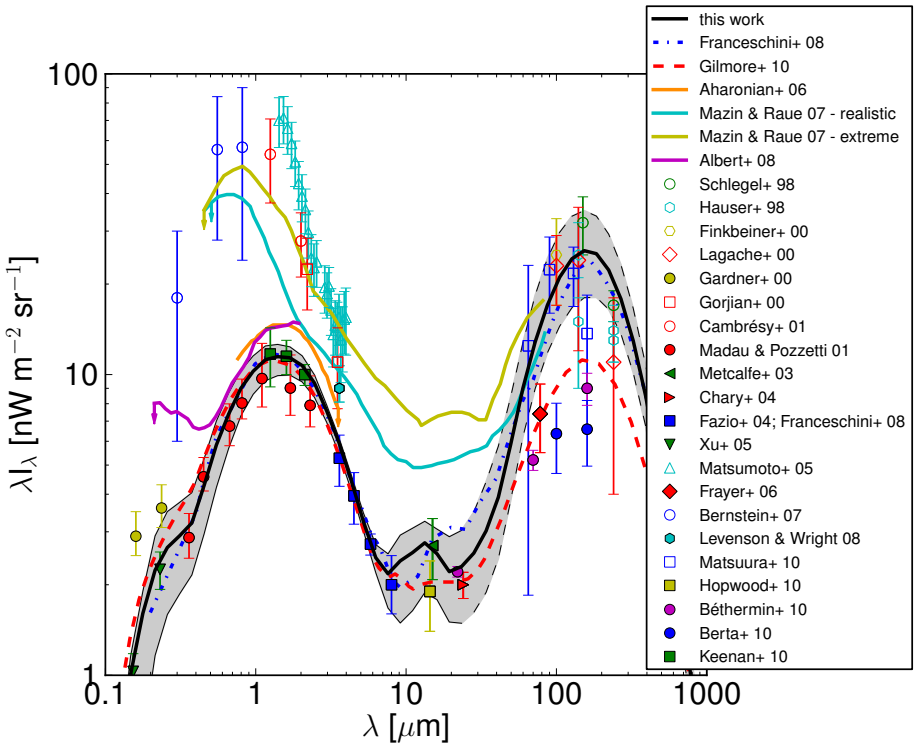

FIGURE 1.3: Spectral energy distribution of the EBL as a function of the wavelength. Open symbols correspond to lower limits from galaxy counts while filled symbols correspond to direct estimates. The curves show a sample of different recent EBL models, as labeled. From [17].

1.3 Direct detection of gamma-rays

As shown in previous sections, the radiation coming from the Universe covers the entire electromagnetic spectrum from radio to γ-rays. However, the **detection techniques** used to collect the radiation at different wavelengths are very different. This is primarily due to the interaction of the radiation with the Earth's atmosphere. In fact, the atmosphere is not transparent to high energy photons beyond the optical waveband. So, a **direct detection** of γ-rays is possible only through a satellite-based instrument. Satellites in γ-ray astronomy must face some additional challenges with respect to lower energy bands. In fact, γ-rays above some MeV cannot be focused like the soft X-rays. So their effective detection area is limited to that of the detector itself, and their detection is related only to the interaction between the incoming photons and the detector's material. Moreover, the dominant interaction process differs depending on the energies. Below $\sim$ 10-20 MeV the *Compton scattering* is the dominant process, while for higher energies the *pair production* mechanism is the most effective. A telescope developed to detect γ-rays through the Compton scattering mechanism was the *Imaging COMPton TELescope* (COMPTEL), one of the

instruments on-board the *Compton Gamma-Ray Observatory* (CGRO). This instrument worked with a two detector array: one made of liquid scintillators where the photons interact through Compton scattering, and one made of NaI crystals that absorbed the scattered photons. It was able to reconstruct images of a γ-ray source in the energy range from 1 to 30 MeV [18]. Above 30 MeV, when the pair production mechanism becomes dominant, a different kind of instrument is needed. The standard structure involves a system of tracking+calorimetry: a tracker for the determination of the direction, a calorimeter for the energy estimation of the γ-ray. The entire layout is then protected from cosmic background with an anticoincidence system. The current missions *Fermi* and *AGILE* have such on-board instruments. So, satellites detectors can overcome the atmospheric barrier, also reaching a good separation between γ and background events. They also have a large field of view and high duty cycles. Anyway, their angular resolution is not optimal due to $e^{\pm}$ multiple scattering, especially below $\sim$ 10 GeV (in best cases 0.15°, whereas soft X-ray telescopes can reach values of a few arc seconds [19]) and also their energy resolution is limited by the size of the calorimeter. However, their biggest constraint is that, as also mentioned before, the detection area is restricted to the one of the detector itself, which cannot be greater than $\sim 1\ m^2$ since they have large cost and strong requirements to be sent in the space. This limitation, joint with the intrinsically rapid decrease of flux with γ-ray energies, does not allow an efficient detection above $\sim$ 100 GeV. So, the VHE sky cannot be explored by space satellites and requires different techniques.

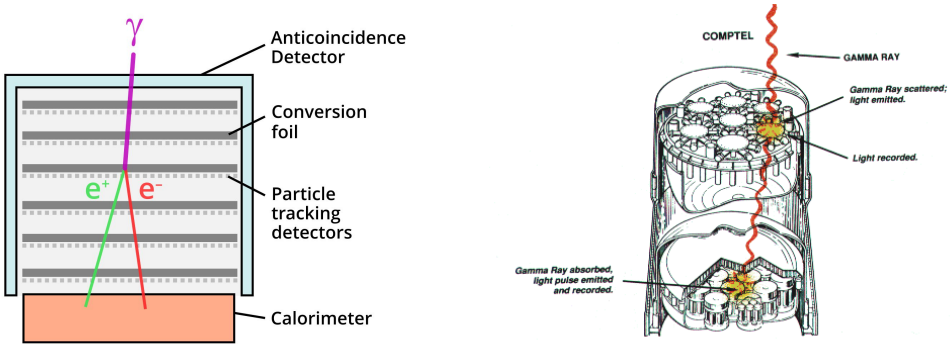

FIGURE 1.4: Left: A schematic representation of a γ-ray detector. From `https://www.nasa.gov/content/goddard/fermi-spacecraft-and-instruments`
Right: Schematic view of the COMPTEL instrument. From `https://heasarc.gsfc.nasa.gov/docs/cgro/images/epo/gallery/cgro/comptel_schematic.gif`.

1.4 Indirect detection of gamma-rays

As stated above, the collection area of satellites is not large enough to collect γ-ray radiation above $\sim$ 100 GeV. This is primarily due to low fluxes and small detector area. The VHE domain must be explored with a different technique, where γ-ray main properties are indirectly reconstructed from ground. This **indirect detection** exploits the interaction between γ-rays and the atmospheric molecules through the production of the *Cherenkov* light. Ground-based telescopes are then needed to observe the sources in the GeV and TeV energy band. There exist mainly two kinds

of instruments: **Imaging Atmospheric Cherenkov Telescopes** (IACTs) and **Extensive Air Showers (EAS) arrays**. Since my PhD work comprises several analyses of IACT data, I will now briefly outline the main physical mechanisms involved in such interactions and I will describe the ground based telescopes and their detection techniques.

1.4.1 Extensive Air Showers

The **Extensive Air Shower** is a cascade of particles generated by the interaction of high energy particles (protons, $e^{\pm}$ or γ-s) with atmospheric nuclei. From the nature of the *primary particle* that initiates the process, we can divide EAS into two groups: *electromagnetic (EM) showers* and *hadronic showers* (Figure 1.5).

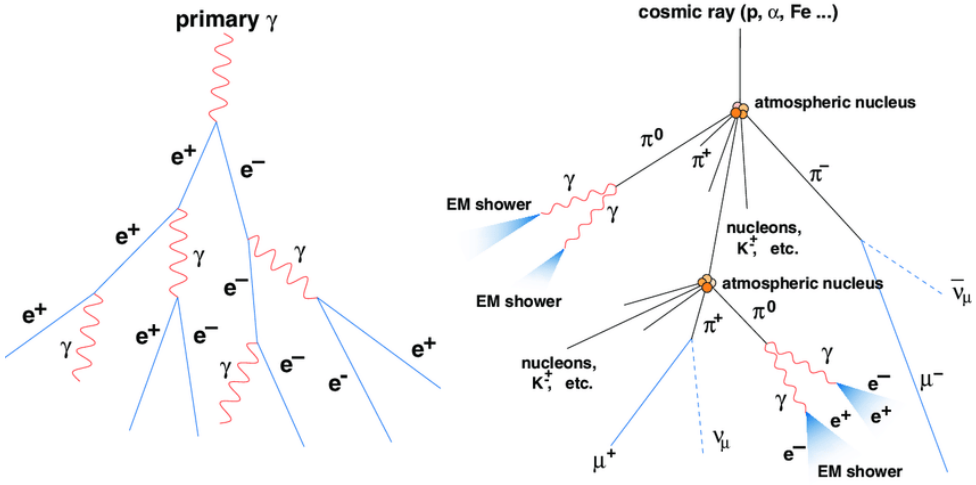

FIGURE 1.5: Sketch of the development of an electromagnetic shower (left picture) and of an hadronic shower (right picture).

An **EM shower** is generated when the primary particle is a γ-ray or a high-energy electron. This particle collides with atmospheric nuclei at a typical altitude ranging from 5 to 30 km generating a shower of secondary $e^{\pm}$ and photons. The emission mechanisms involved in the generation of this cascade are the following:

- **pair production** of $e^{\pm}$ by the conversion of high energy photons;
- **bremsstrahlung emission** when $e^{\pm}$ interact with the Coulomb field of the nuclei. It leads to the production of further high energy photons.

These processes occur alternatively generating the cascade of secondary particles and distributing the energy of the primary particle between them. The shower stops when the so-called *critical energy* E_c is reached. The value of this energy, ≈ 80 MeV in air at standard conditions (NTP, commonly defined as T = 20°C (293.15 K) and P = 1 atm), is the energy at which the radiation loss overtakes the collision energy loss. It is possible to describe the fractional energy loss due to Bremsstrahlung for a high energy electron approximately as:

$$\frac{1}{E}\frac{dE}{dx} \simeq -\frac{1}{X_0} \tag{1.8}$$

where X_0 is called the radiation length, and is characteristic of the material (e.g. it is about 300 m for air at NTP). For a typical material of mass and atomic numbers A

and Z, with Z>4, a good approximation of *radiation length* is [20]:

$$X_0 = \left[4\alpha r_e^2 \frac{N_A}{A} Z^2 \ln\left(183 Z^{-1/3}\right)\right]^{-1} \quad \text{g cm}^{-2} \tag{1.9}$$

where $\alpha = 1/137$ is the fine structure constant, r_e is the classical electron radius and N_A the Avogadro number. This quantity, for the bremsstrahlung process, corresponds to the mean distance traveled by an electron to lose all but a factor 1/e of its energy.
The radiation length for pair production $X_{0,pp}$, which is the average path after which a photon will convert into a $e^{\pm}$ pair, is strictly linked to the radiation length seen for Bremsstrahlung:

$$X_{0,pp} \simeq \frac{9}{7} X_0 \tag{1.10}$$

The development of an EM shower can be well described by a simple one dimensional analytical model where photons and electrons undergo respectively pair production and Bremsstrahlung processes after an average path equal to the radiation length X_0. A prominent model was proposed by Heitler in the late 1930s. In this approximation after i interactions in the cascade evolution, the number of particles grows exponentially as 2^i, and the energy is equally distributed between the 2^i particles as $E/2^i$ for each of them. When the energy of $e^{\pm}$ reaches the critical energy the cascade stops. The *Heitler model* [21] reproduces very well the longitudinal development of the EM cascades, but it does not take into account additional processes, like multiple scattering of charged particles, energy losses of $e^{\pm}$ by ionization or electron scattering and positron annihilation.
The **hadronic shower** is a cascade of particles generated by hadrons. The primary particles can be CRs, relativistic protons and nuclei. The shower development is more complex than EM showers since the number of secondary particles is much bigger and the interactions are governed by the strong force. In fact, the first interaction of the primary hadron produces pions, kaons and small amount of light baryons which, undergoing further collisions, produce photons, e^+, e^-, muons and neutrinos. The shower grows until the energy per nucleon reaches the minimum energy required for pion production ~ 1 GeV and the long-lived muons, that form the most penetrating component of the cascade, often reach the ground. In such a complex development, it is then possible to distinguish several components of a hadronic shower:

- **hadronic component** composed of nuclear fragments from collisions with atmospheric nuclei, isolated nucleons in very small proportion, pions ($\sim$ 90%) and kaons ($\sim$ 10%);
- **electromagnetic component** generated by the decay of neutral pions into γ rays;
- **high energy muons** generated by the decay of charged mesons (mainly $\pi^{\pm}$ and $K^{\pm}$);
- **atmospheric neutrinos** generated by the decay of mesons and muons ($\pi^{\pm}$,$K^{\pm}$ and $\mu^{\pm}$).

In summary, hadronic showers develop in a different way than EM ones: they produce more particles, the width of the shower is larger and the developing time is

longer. These differences are helpful to distinguish between them: through a morphological study of the air shower it is possible to trace back to the nature of the primary particle as will be described later.

1.4.2 Cherenkov Radiation

The **Cherenkov radiation** [22] is a beamed pulse light emitted in the UV/optical band. It occurs when a charged particle passes through a dielectric medium at a speed greater than the velocity of light in that medium. When this happens, the particle polarizes the surrounding atoms and molecules of the medium causing an emission of an EM shock wave (see Figure 1.6). This radiation is emitted along a cone with opening angle θ_c given by:

$$\cos\theta_c = \frac{1}{\beta n(\lambda)} \tag{1.11}$$

where $\beta = v/c$ and the refraction index n depends on the wavelength λ of the Cherenkov light emitted. The maximum value of the opening angle θ_c is obtained for $\beta = 1$. Then, it also follows that Cherenkov radiation is relevant if $n > 1$.

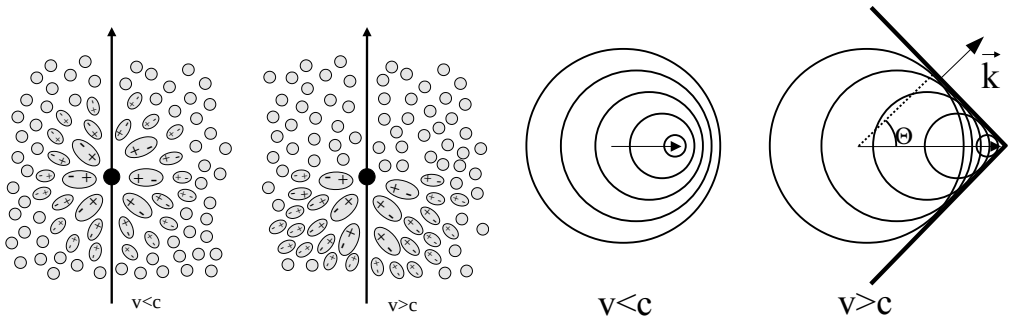

FIGURE 1.6: Left: illustration of the polarized medium by a particle with velocity v lower or greater than the speed of light. Right: the Cherenkov wave-front formation. From [20].

The number of photons produced per unit path length dx and per unit energy interval dE (or wavelength interval $d\lambda$) by a particle with charge $Z_p e$ at the maximum angle is [23]:

$$\frac{d^2N_{ph}}{dEdx} = \frac{2\pi\alpha Z_p^2}{hc}\sin^2\theta_c \approx 370\sin^2(\theta_c(\lambda))\ eV^{-1}cm^{-1} \tag{1.12}$$

or:

$$\frac{d^2N_{ph}}{d\lambda dx} = \frac{2\pi\alpha Z_p^2}{\lambda^2}\sin^2\theta_c \tag{1.13}$$

Due to the dependencies with wavelength λ it is derived that most of the photons are seen in the blue/violet and UV band. Moreover, it is shown that the number of Cherenkov photons does not depend on the altitude, since the Cherenkov yield does not depend on the local density. On the other hand, due to the variation of the atmospheric density with altitude, the Cherenkov light angle increases from $\sim 0.2^\circ$ at an altitude of $\sim$ 30 km to $\sim 1.5^\circ$ at sea level [20]. The variation of the Cherenkov angle with altitude compensates the effect of the varying distance to the ground: the result is the formation of a *light annulus* at a distance of $\sim$ 120-150 m from the shower impact on the ground, the so-called **Cherenkov ring**. Similarly, for the duration of

the shower there are two effects in competition: close to the shower axis the photons emitted at low altitude reach the detector before those emitted at high altitude, while far from the shower core the photons emitted at low altitude have a longer geometrical trajectory than those emitted at high altitude, and reach the detector after the latter. At a distance of $\sim$ 120-150 m the two effects compensate almost exactly, resulting in a duration of the shower of $\sim$ 2 ns. It can reach 5 ns on axis, and increases significantly for high impact distance (> 200 m) [20]. Finally, the Cherenkov photon density detected on the ground is proportional to the energy of the primary γ-ray photon. This relation is essential to reconstruct the main features of the incoming γ-ray.

1.4.3 Imaging Atmospheric Cherenkov Telescopes

The **Imaging Atmospheric Cherenkov Telescopes** (IACTs) are ground based instruments capable of detecting the Cherenkov pulse emitted by the air showers. Indeed, this light can be collected to generate an image of the shower, which is used to determine and study the nature and the main features (energy and incident direction) of the primary particle. The technique developed for such purpose is the so-called **imaging technique** (Figure 1.7) and it allows the indirect detection of γ-rays.

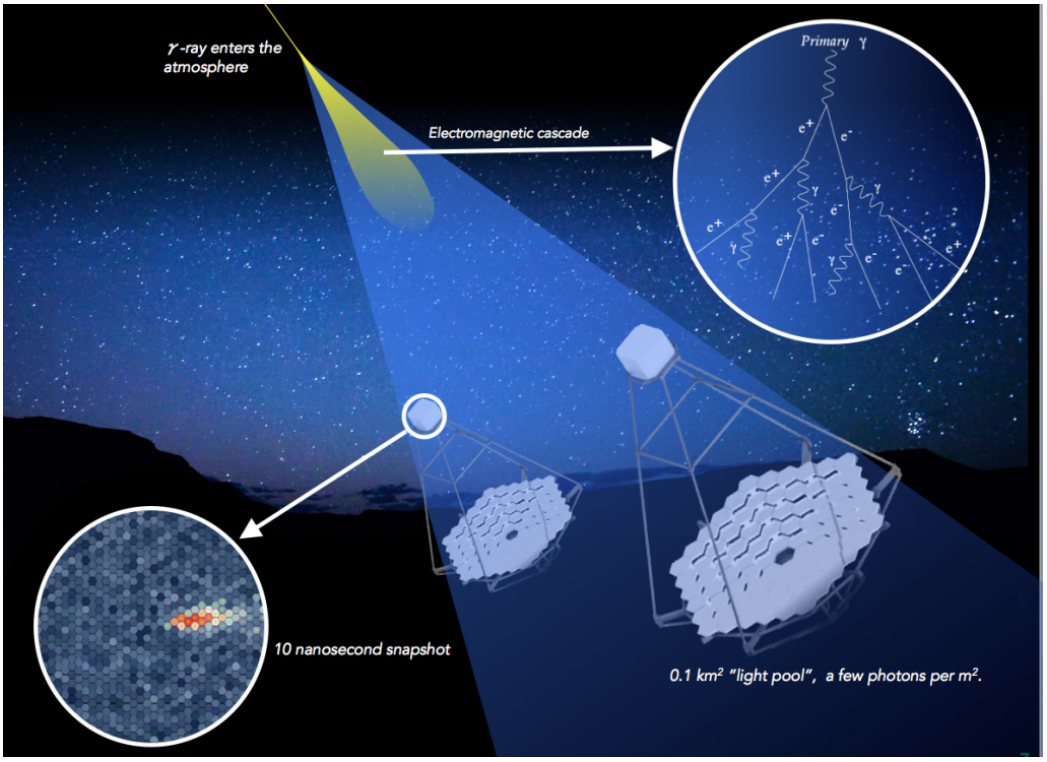

FIGURE 1.7: Scheme of the imaging atmospheric Cherenkov technique. From: `https://www.cta-observatory.org/about/how-cta-works/`.

To be efficient, this technique requires some conditions for the construction of the telescopes and on the data analysis that need to be fulfilled. The IACTs need to have large reflectors (several meters of diameter) to collect as many Cherenkov photons as possible. These photons are then focused on a camera composed usually of an array of photomultiplier tubes (PMTs) placed in the focal plane. The PMTs must be large in number to ensure that the shower image is produced with high accuracy, and

need a fast timely response to catch the fast Cherenkov flashes. Since they observe the Cherenkov light, IACTs are essentially optical telescope, so they must operate during the night, only when the contribution from the Night Sky Background (NSB) does not affect too much the observations. Their field of view is also relatively small (usually less than $\sim 5^{\circ}$) so a source to be observed must be directly pointed. Regarding the mechanical structure, the altazimutal mounts are mandatory to sustain the weight of the entire instrument. On the other hand, the rigidity of the optical system and camera support structures can be obtained with two different approaches (both used in the current operative IACTs): building the telescope structure with a steel frame or using a lightweight carbon fibre frame coupled with an active mirror system.
Despite the requirements on the hardware components, the most challenging part of the imaging technique lies on the discrimination between the γ-ray signal and the background. This is possible exploiting the recorded images of the showers. These images are cleaned from the NSB effect and then a set of *parameters* is used to reconstruct the main image properties. These features can be used to distinguish between γ-ray initiated showers and the ones of different origins. Moreover, an improvement on the reconstruction and discrimination is given by the stereoscopic technique. An array of telescopes provides a view of the same shower from a number of different perspectives, and so improves the geometrical reconstruction of the shower. This technique is described in detail in Section 2.4.
The main background contribution is given by a large distribution of hadrons arriving isotropically into the atmosphere and producing hadronic showers. These events are three orders of magnitude more than the γ-ray events, so they represent a strong source of background that must be rejected accurately. As also mentioned before, hadron showers produce irregular and wide images, while the γ-ray showers produce elliptical and narrow images on the ground. These differences are used in the data analysis technique to distinguish γ-ray events from hadronic ones. Other sources of background are muons, which are rejected since they usually produce ring-like images on the camera plane, and they are detected only by one telescope, and photons of NSB taken into account during the *cleaning* data analysis step (see Section 2.4 for details). Finally, there are also background isotropic sources that cannot be distinguished: cosmic $e^{\pm}$, that produce EM cascades identical to those produced by γ-rays, and diffuse γ-rays.
Since the IACTs are ground based instruments which use the atmosphere for the detection, their performance is dependent not only on the hardware features but also on the observational conditions. In particular, it is worth to mention the **energy threshold** and the **collection area**. They both depend on hardware properties (the dimension of the reflectors, PMTs efficiency) but also on the zenital observational angle and (for the collection area only) on the energy. These dependencies can be explained recalling that the Cherenkov light from an air shower produces a pool of $\sim$ 120 - 150 m diameter on the ground. The telescopes inside this pool will detect the Cherenkov flash and then the collection area can be (in first approach) estimated from this light pool as of the order of $\sim 10^4$ m^2. Moreover, showers coming from large zenith angle observations will travel a longer path in the atmosphere, producing a larger light pool but with a lower Cherenkov photon density and a bigger attenuation effect of the atmosphere. As a result, the low energy γ-rays can not be detected by the telescopes. Therefore, the energy threshold increases but, on the other hand, the collection area grows making possible the detection of γ-rays up to a few tens of TeV. This effect makes possible the so-called **Very Large Zenith Angle** (VLZA) observations which have been performed on the Crab Nebula by the

MAGIC telescopes [24, 25].
The instrument performances can be judged through the so-called **sensitivity**. For γ-rays telescopes it is defined as the minimum flux needed to detect a source (usually the Crab Nebula is taken as reference) with a significance of 5σ after 50 h of observation. It is called *integral sensitivity* when is calculated with a global optimized set of parameters for the shower reconstruction above different energy thresholds, while is called *differential sensitivity* when the parameter values are optimized for a small energy range.
Currently, there are three major IACT arrays fully operative:

- **VERITAS** (Very Energetic Radiation Imaging Telescope Array System) is an array of four 12 m diameter reflectors located at the F. L. Whipple Observatory in southern Arizona, USA (31° 40′ N, 110° 57′ W). The system was completed in 2007 and it went through two major upgrades on the telescope movement and on the camera to improve its performance [26]. The field of view is about 3.5° and the energy range goes from $\sim$ 85 GeV to $\sim$ 30 TeV;

- **H.E.S.S.** (High Energy Stereoscopic System) is a system of five IACTs located in the Khomas Highlands of Namibia (23° 16′ 18″ S, 16° 30′ 01″ E). In 2004 the system started operation with an array of four IACTs of 13 m diameter arranged in a square form with a side length of 120 m. Each telescope has a field of view of 5°. Then, in 2012 a fifth telescope, a 28 m reflector with a smaller field of view (3.5°), was added in the center of the array. Thus, it increased the energy coverage, sensitivity and angular resolution. Moreover, the energy threshold was decreased down to $\sim$ 30 GeV. In 2016, H.E.S.S. completed an upgrade of the cameras for the four 13 m telescopes to reduce the dead time, reduce the failure rate, and to operate smoothly with the 28 m telescope which has higher trigger rates [27];

- **MAGIC** (Major Atmospheric Gamma-ray Imaging Cherenkov) will be described in detail in Chapter 2.

The most important future project for the next generation of IACTs is the Cherenkov Telescope Array (**CTA**) [28]. It will be the major global observatory for very high energy γ-ray astronomy over the next decade and beyond. It will have two sites, one in the northern hemisphere on the Canary Island La Palma, that will cover the energy range from 20 GeV to 20 TeV and the other in the southern hemisphere near Paranal, Chile, covering γ-ray energies from 20 GeV to 300 TeV. The goal is to give a significant improvement on sensitivity, collection area, angular resolution, field of view, and energy coverage. Such improvements will be accomplished thanks to a huge number of telescopes of different sizes. The array will be formed by three different types of telescopes:

- **LSTs** (Large Size Telescopes): 23 m diameter reflectors that will cover the energy range between 20 GeV and 200 GeV and designed to be light-weighted, so to catch up GRBs with a repositioning system. LSTs will have a field of view of 4.5°. The first LST prototype (LST-I) has been completed in October 2018 in La Palma and recorded its first light in December 2018 [29]. It is now in commissioning phase;

- **MSTs** (Medium Size Telescopes): designed to have 12 m Davies-Cotton reflectors and field of view of 8°, they will be sensitive from about 150 GeV to 5 TeV;

- **SSTs** (Small Size Telescopes): designed with a dual-mirror Schwarzschild-Couder aplanatic configuration with a 4.3 m diameter primary mirror, a 1.8 diameter secondary mirror and a field of view of 9°. They will be sensitive in the energy range from 5 TeV to 300 TeV.

1.4.4 Extensive Air Shower Arrays

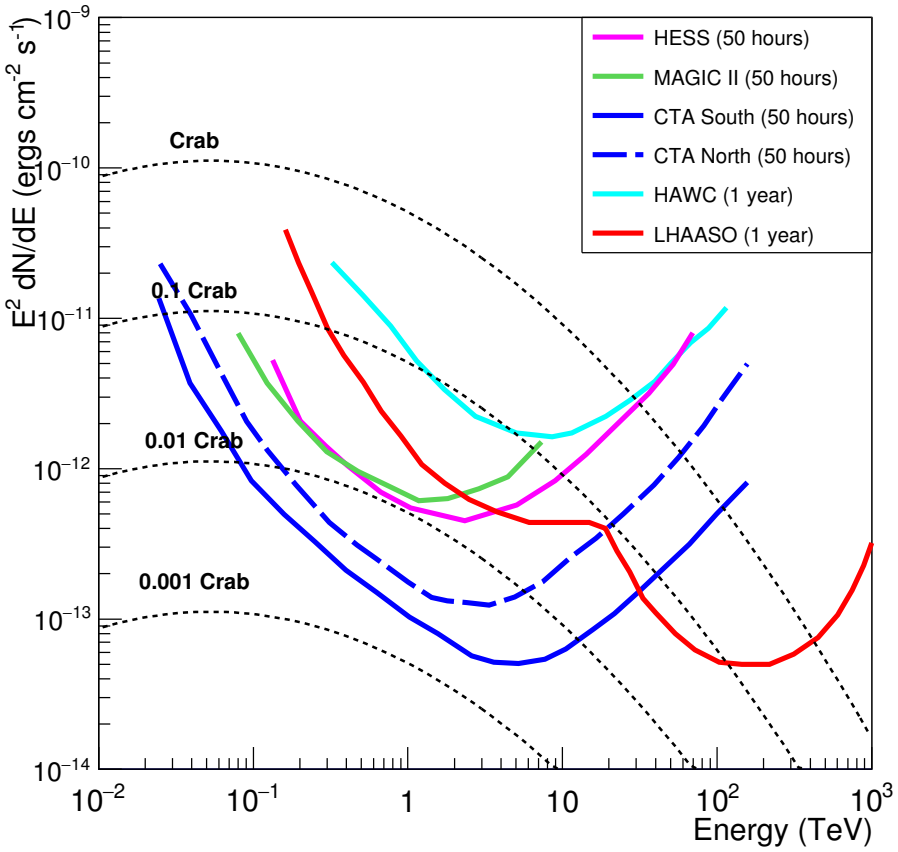

FIGURE 1.8: Differential sensitivity of LHAASO to a Crab-like point gamma ray source compared to other experiments. From [30].

The imaging technique used by IACTs is not the only method available for indirect detection of γ-rays. Ground based instruments can also exploit the so-called *particle sampling* technique. This is the approach used by the **Extensive Air Showers (EAS) arrays**. In such approach the detectors measure the secondary charged particles reaching the ground level. The detector array (sparse or covering the entire area) is distributed into a very huge area ($\sim 10^4$ - 10^5 m^2) and installed at high altitude to collect more charged particles. The particle samplers used are scintillation counters, water Cherenkov tanks or resistive-plate chambers. Since only high energy showers will produce a significant number of particles reaching the ground, the energy threshold of EAS arrays is of the order of the TeV energies, higher than for IACTs. Moreover, their ability to discriminate γ events from background, based on the reconstructed shower shape or on the muon content, is quite limited, since they only have access to the shower tails. On the other hand, these instruments may have a

100% duty cycle, a large field of view ($\sim$ 2 sr) and, as mentioned before, a huge effective area. The former two features (duty cycle and field of view) give them the capability to operate as all-sky monitors. Thanks to their large collection area, the EAS arrays are more sensitive than IACTs in the region from few tens of TeV up to hundreds of TeV.
The most important EAS arrays for γ-ray detection currently working is the **HAWC** (High Altitude Water Cherenkov, [31]) experiment. It is located at an altitude of 4100 m on Sierra Negra, in the state of Puebla, Mexico (18° 59′ 49″ N, 97° 18′ 27″W). It consists of an array of 300 water Cherenkov tanks, each with 3 PMTs covering an area of about 20 000 m^2. This instrument, completed in 2015, monitors 2/3 of the sky with an instantaneous FoV of $\sim$ 2 sr and with a duty cycle of 90%.
The future EAS array that will be completed in 2021 is **LHAASO** (Large High Altitude Air Shower Observatory). It is built in Sichuan, China, at 4410 m altitude [30]. It will be both a γ-ray and a CR detector with an unprecedented sensitivity that above a few TeV will be competitive with IACTs (see Figure 1.8). It will be composed by

- a 1.3 km^2 array divided into a central part including 4931 scintillator detectors and an outer guard-ring instrumented with 311 electromagnetic particle detectors;
- a central detector of 78 000 square meters (four times the HAWC detector) made of surface water pools equipped with PMTs;
- an overlapping 1 km^2 array of 1146 water Cherenkov tanks underground, with a total sensitive area of about 42 000 m^2 to separate γ-ray initiated showers from hadronic ones;
- 18 wide field-of-view air Cherenkov telescopes.

Chapter 2

The MAGIC Telescopes

The Major Atmospheric Gamma-ray Imaging Cherenkov (MAGIC) telescopes are a stereoscopic system of two Cherenkov telescopes located at $\sim$ 2200 m above the sea level in *Observatiorio Roque de los Muchachos* (ORM) in La Palma, Canary Island, Spain. The first telescope, MAGIC-I, started operations in 2003. Then the second one, MAGIC-II, was completed in 2009. From then on, they have been always in operation except for a major upgrade occurred in 2012 [32, 33]. They are designed to detect and collect the fast Cherenkov flashes produced when a gamma-ray interacts with the air nuclei. The aim of this system is to measure the gamma-ray flux and to reconstruct the direction of the primary particle that generates the atmospheric shower. This technique is called imaging technique, as described in Chapter 1. In this chapter I will briefly describe the main hardware structure of the system and the data taking operation procedures which were important for my PhD activities. Then, I will outline the standard and the non-standard MAGIC data analysis chains showing also an application of the analysis to two observed sources. The information presented here will be then used for the GRB data analysis shown in Chapter 5.

2.1 MAGIC Hardware

FIGURE 2.1: The MAGIC-I (left) and MAGIC-II (right) telescopes. Between the two telescopes the MAGIC counting house and the LIDAR dome are visible.

2.1.1 Structure and drive system

The structure of the MAGIC telescopes was constructed to be both rigid and light-weighted to perform fast repositioning in case of transient sources observations. The total weight of the telescopes is 67 t distributed between the camera ($\sim$ 0.89 t), the camera bow and the counter weights ($\sim$ 3.4 t), the towers ($\sim$ 20.2 t), six carriages ($\sim$ 25 t), the Al-mirrors and the active mirror control ($\sim$ 9 t) and the carbon fiber dish ($\sim$ 8 t). The carbon fiber structure is designed to avoid deformations and support the weight of the telescope. The MAGIC drive system is the hardware component which moves the telescopes in order to point and track the sources. The operation mode of the telescope are:

- **park position**: position where the telescopes can be found during the day, secured with bolts, and when no data taking is performed;
- **repositioning mode**: it is used during standard operation to skip from tracking a source to tracking a new one. In this mode the standard angular speed is $4^\circ/s$ but it can be increased up to $7^\circ/s$ in case of **fast repositioning** mode for tracking a transient source. In this mode the telescope can repoint every position in the sky in less than 30 s;
- **tracking mode**: used to track sources during observation.

The mount of the telescope is alt-azimuthal and the drive allows an angular range of movement that spans from -73° to 100° in elevation axis and of more than 400° in the azimuthal axis [34]. There are six digitally controlled industrial drive units with servo motors to allow movements on the azimuthal axis. The movement on the elevation axis is feasible thanks to one digitally controlled industrial drive unit with servo motor of 1 kW. During daytime and in bad weather conditions the telescopes are in *park position*, secured with bolts to anchor the telescopes during strong wind. Before data taking, the shifters must remove all bolts to allow switching on the motor power.

2.1.2 Mirrors

The mirror technologies used to achieve very large aperture and hence mirror area in MAGIC are the following [35]:

- MAGIC-I mounts mostly aluminum honeycomb sandwich 50×50 cm^2 mirrors produced by INFN-Padova, some aluminum honeycomb sandwich 50×50 cm^2 mirrors produced by MPI, mirrors of 1×1 m^2 at the edges with cut side and from 2011 1×1 m^2 aluminum honeycomb sandwich produced by INFN and cold-slumped mirrors produced by INAF;
- MAGIC-II has 143 1×1 m^2 aluminum honeycomb sandwich mirrors produced by INFN-Padova and 104 1×1 m^2 cold-slumped mirrors produced by INAF.

Moreover, in MAGIC-I the panels in which mirrors are mounted have a particular design called *chess-board* structure. This is due to a wrong defined mirror surface level during the design. In particular, the mirrors were touching during AMC adjustment. The problem was solved arranging the mirrors in different layers, so avoiding contact between them. Globally, the MAGIC telescopes have a diameter and a focal length of 17 m and a total reflective surface of about 236 m^2. The system is built with a small focal ratio (around 1.0 for MAGIC) in order to assure a low astigmatism over

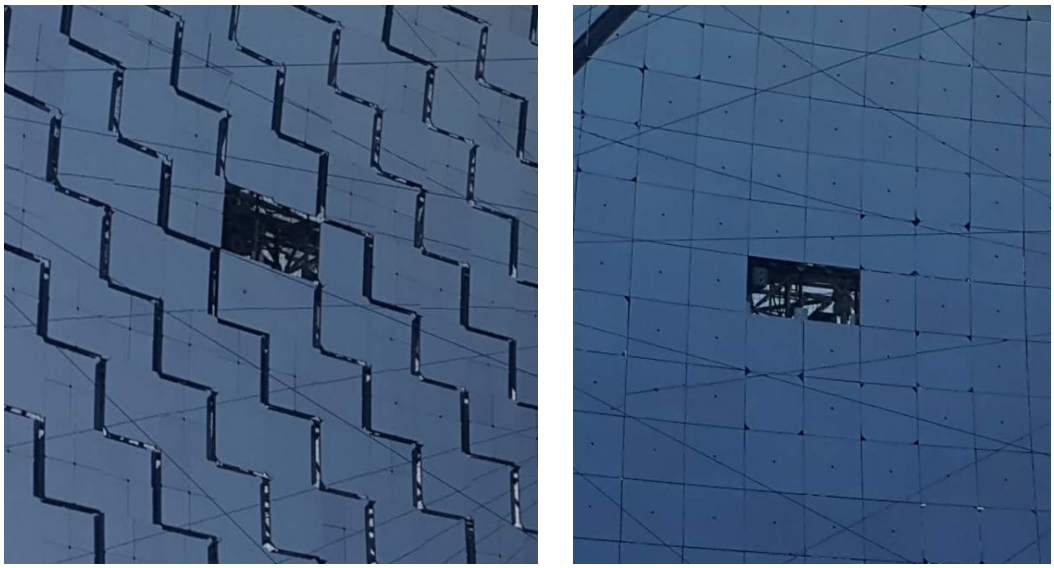

FIGURE 2.2: Mirrors of MAGIC-I (left) and mirrors of MAGIC-II (right).

the field of view. The reflectors are built in a parabolic dish design since they need to collect the fast Cherenkov flashes. Indeed, despite this shape produces strong coma effect off-axis, parabolic reflectors are favourite with respect to spherical ones because they are isochronous, so they do not induce time spread in the arrival time of Cherenkov photons at the cameras. On the other hand, parabolic mirrors have a higher cost and a more complex configuration than the spherical ones. In fact, the parabolic reflector consists of spherical individual mirrors with radius of curvatures between $\sim$ 34 - 35.6 cm. Since optics are not perfect, one of the key parameters used to evaluate the optics performance is the **Point Spread Function** (PSF). It is related to the difference between the ideal geometrical shape of the reflector and the real one. The overall PSF of the reflector is determined by the contribution of all the individual mirrors and the AMC performance. PSF affects sensitivity at low energies and worsens the pointing resolution. Every night the PSF of the telescopes are measured before the observations to check the status of the optical system.

2.1.3 Active Mirror Control (AMC)

The entire construction of the telescopes is a compromise between structure, weight and stability. When the telescopes move the gravitational load impact on the dishes changes. This generates some deformations that need to be corrected. The **Active Mirror Control (AMC)** [36] has the function to correct these effects that lead to a large defocusing of the system and then to a degradation of the PSF, as previously said. The hardware components of the AMC consist of actuators in cardan and axial joints. This system moves the panels where mirrors are mounted to correctly focus them. The scheme of AMC in the two telescopes is slightly different:

- MAGIC-I presents eight independent chains, horizontally aligned for better maintenance with eight AMC electronic boxes each;
- MAGIC-II presents seven independent chains with eight or nine boxes each. The chains are arranged in sectors to minimize the cable length from the central box.

At the beginning of every night, AMC changes the position of the mirrors to adjust their focus and to estimate the value of the PSF using the SBIG camera (see next section). To adjust the mirror position, AMC uses the so-called Look-Up Tables (LUTs) that contain the actuator positions binned in zenith and azimuth angle. During the night, when a new source is pointed, the AMC adjusts the positions of the mirrors reading them from the LUTs in agreement with the zenith and azimuth values of observation.

2.1.4 SBIG camera

The SBIG camera is a CCD camera designed with the purpose of measuring accurately the PSF of individual mirror segments and of the complete reflector and to measure the reflectivity of the reflector at different wavelengths. To perform these tasks, the camera field of view needs to include the star field and the reflected spot. It is used for long time monitoring of PSF and to check the reflectivity of the reflector.

2.1.5 Camera

The camera is the hardware component that collects the Cherenkov photons reflected by the mirrors. It is made of 1039 photomultipliers (PMTs). In particular, their photosensor module is R10408 module Hamamatsu of 25 mm diameter [37]. The overall system has a field of view of 3.5° and the PMTs are grouped in 169 clusters of 7 pixels. Each PMT is equipped with a light collector, a *Winston cone* that helps focusing the light on the PMT window and avoiding the light contribution from NSB that arrives in the PMTs from large angles. Then, the potential between photocatode, dynodes and anodes are set via Cockroft-Walton type voltage multiplier with a peak voltage of 1250 V. This system controls and sets the High Voltage (HV). After being generated by the PMTs, the electrical signal is amplified by an AC coupled pre-amplifier to improve the PMT low gain (of the order of $\sim 3\times 10^4$). Then, the *Vertical Cavity Surface Emitting Lasers* (VCSELs) convert the signal into an analog optical signal. This conversion allows a transmission of high dynamical range and high bandwidth of the analog optical signals over long distances with low dispersion. The VCSELs produce a near IR light (850 nm) with a pulse width (FWHM) of 2.5 ns. In addition, since the signal is influenced by fiber position and temperature, VCSELs should be temperature stabilized for stable gain. The signal produced is then transmitted to the electronic room into the MAGIC counting house with a system of $\sim$ 160 m long optical fibers in 19 bundels of 72 fibers.

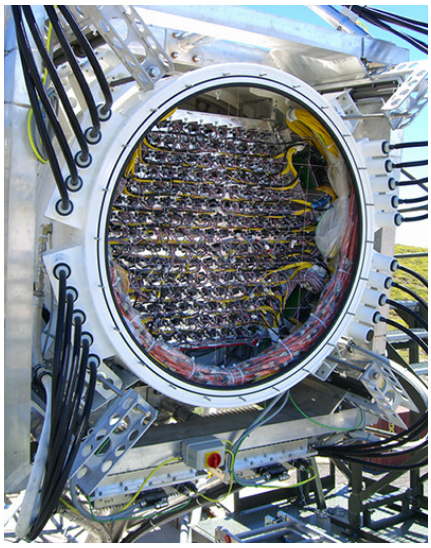

FIGURE 2.3: View of the camera from the back side with the 169 clusters of 7 pixels each. From [37].

Several auxiliary components are necessary for proper operation of the camera:

- *temperature control system*: two plates made of aluminum with horizontal water channels. They are at 20° and the control units are located on the telescope undercarriage;

- *drying unit*: it allows removing damp air from the camera, dehumidifies it and returns it back to the camera. It is available only for MAGIC-II and it is located on the right tower;
- *lids*: they protect the camera, and they are closed when no observations are performed;
- a *spectralon plate*: usually called target, approximately 3 cm in front of the plexiglass window. The star images are focused on this target, so that gamma images can be focused at the PMT plane;
- *Starguider LEDs*: placed at the intervals behind the plexiglass window. They are used by the Starguider camera to find the position of the camera relative to imaging;
- *low voltage power supplies*: each camera has two of them. They are located underneath the camera so that they can be exchanged without opening the camera. Each unit weights $\sim$ 30 kg;
- *temperature and humidity sensors*: respectively 8 and 4 sensors for a slow control of the condition of the camera;
- *Moon filters*: can be used for observations in presence of bright moon.

The user interfaces used to check the regular status of the camera are the Camera Control (CaCo1 and CaCo2) softwares.

2.1.6 Calibration System

A precise and regular calibration of the camera response with respect to the light flux is necessary. This is the aim of the **calibration system** installed in MAGIC. This system consists of two calibration boxes (one per telescope) located in the central hole in the telescope dish structure and illuminated with a defined pulsed light. The basic instrumentation of the calibration box consists of:

- a pulsed UV passively Q-switched Nd-YAG laser of 355 nm wavelength, similar to the Cherenkov light peak one ($\sim$ 350 nm) and with a pluse width of 300 ps, fast as Cherenkov light (1-2 ns);
- two filter wheels with a 6x6 filter attenuation to evaluate the linearity of the entire amplification chain;
- an Ulbricht sphere to assure the light emission homogeneity;
- a temperature and a humidity sensor and an internal heating system for controlled temperature environment.

The boxes are connected with the counting house via optical fibers. The main tasks of this instrument are:

- obtain the conversion factor between Flash Analog-to-Digital Counts (FADC) and number of photoelectrons. This is done thanks to a dedicated **calibration run** taken every time before observing a source and with **interleaved calibration events** taken at a fixed frequency of 25 Hz;
- test the linearity of the entire amplification chain from PMT to readout;

- perform the PMT HV Flat-Fielding.

The control system that monitors and checks the status of the calibration box is the Trigger Calibration Unit.

2.1.7 Readout electronics system

After being converted into an analogic optical signal by the VCSELs (see Section 2.1.5), the signal is transmitted through optical fibers from the camera to the electronics room into the MAGIC counting house. A general scheme of how the signal is treated into the electronic system is described in Figure 2.4.

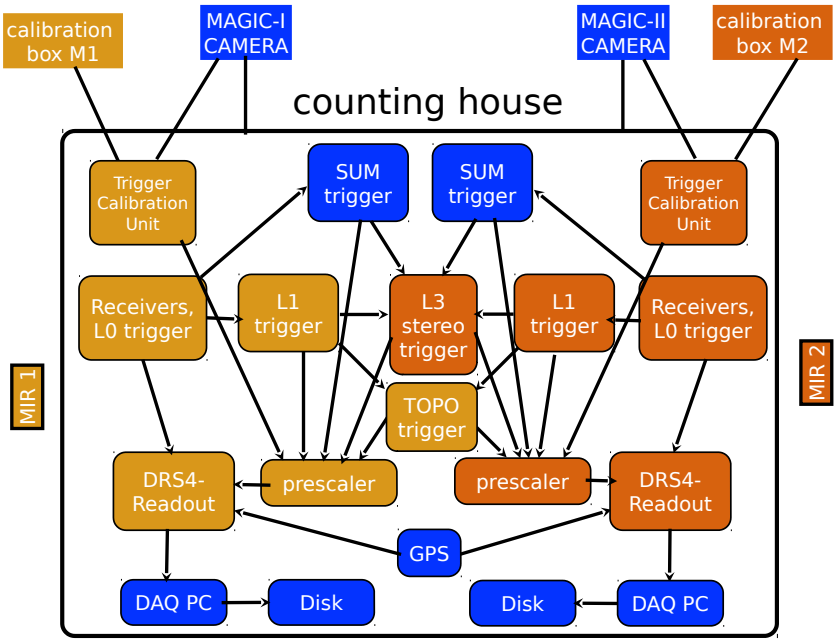

FIGURE 2.4: Overview of the MAGIC electronic readout chain. From 4th MAGIC Hardware School, Javier Herrera.

The optical fibers transmit the signal into the so-called *receiver boards*. This system converts back the signal into an electric analog signal and splits it into two branches:

- a **readout branch** where the signal is digitized and temporally stored, waiting for the trigger decision;
- a **trigger branch** where the signal passes through different trigger levels.

If the trigger levels select the signal as an interesting one, the signals of both telescopes are stored into the Domino Ring Sampler 4 (DRS4) and they are sent to the **Data AcQuisition system (DAQ)** after being digitized by a standard analog-to-digital converter.

Digital Trigger System

The standard trigger used during MAGIC observations is the **digital trigger** system. This system is based on a three level trigger scale [38]:

- the first stage, named **Level Trigger 0** (LT0) is implemented directly in the receiver boards. It performs a digitization of the analogue pulses above a discrimination threshold. Only signals exceeding the threshold can pass to the

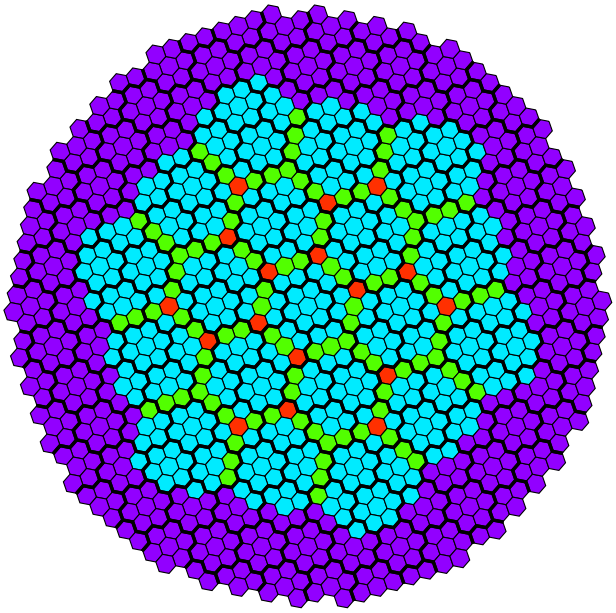

FIGURE 2.5: Color code scheme of the 1039 channels of the MAGIC camera. The cyan hexagons (36 pixels each) show the 19 L1 trigger macrocells. Pixels covered by two and three macrocells are shown respectively in green and red. From [32].

next level. In this first stage the signal's width is defined and a programmable delay is applied to synchronize the pulse. These adjustments are a useful compromise between the following Level 1 (L1) trigger rate (dependent on L0 signal width) and a good spread of the arrival times at the L1 board. The time spread is of electronic nature (e.g. intrinsic differences between the PMTs) and sometimes there can be also a physical nature (e.g. high-energy showers with large impact distance). The program that performs width and delay adjustments is called HYDRA (HYperfast Delay and Rate Adjustment);

- after the LT0 the signal is transmitted to the **Level Trigger 1 (LT1)** backplane through a 3.5 m Mini Delta Ribbon (MDR) cable. It rejects most of the accidental events due to NSB by combining temporal and spatial information at the same time. The backplane distributes the digital signals from the receiver boards (where the LT0 is implemented) to the right LT1 boards. In the path through the LT1 boards, the signals pass through 19 LVDS to LVTTL adapter boards that convert the differential signals to single ended format, compatible with the LT1 boards. To perform this second stage of trigger, each telescope has 19 LT1 boards and each camera is subdivided into 19 small regions of 37 pixels, named *macrocells*. At each macrocell corresponds a LT1 board and the goal of this second stage is to detect close compact clusters of active pixels in every macrocell using different combination of neighbour pixels (NN): 2NN, 3NN, 4NN, 5NN. The macrocells are overlapped near their border, so some pixels belong to two or three different macrocells. Then, the signals are transferred to the Trigger Processing Unit (TPU) that computes the final trigger: global logical OR of macrocells. Then, it generates the signals for the stereo trigger and for the prescaler;

- the output signals of the two LT1 (one per telescope) are given both to the

prescalers and to the **Stereo trigger (LT3)**. This last level generates a stereo trigger if the signals received are generated by the same event in both telescopes. The Global Trigger board is the LT3 core: it programs delay adjustments to synchronize the signals, which have different light paths, and stretches it to achieve 100 ns width. Then, it executes a logical combination (AND) between synchronized signals.

At the end of the trigger chain the elaborated signal is sent to the DRS4 of the two telescopes and then to the DAQ system.
The trigger system contains also, as mentioned before, a *prescaler* that accepts different kind of triggers and enables the right one using a prescaler factor, and a Trigger Calibration Unit (TCU) that sets and monitors the calibration box and emits the pedestal and calibration triggers.
Since the telescopes perform observations on different kind of sources and in different night sky conditions a proper *Discrimination Threshold (DT)* should be used in order to optimize the sensitivity of the instrument. For this reason the threshold needs to be set to a lower value if an extragalactic source is observed with respect to a Galactic one. Moreover, in presence of Moon, higher DTs will be used to avoid contamination from a higher NSB. The standard DT values used in MAGIC are: 4.25 photoelectrons (phe) for extragalactic sources, while for Galactic sources the DTs are 15% higher. In general, the DTs are set as low as allowed by the trigger rate in order to reach a low energy threshold and detect also faint events which generate few photoelectrons.

Sum-Trigger II system and Topo-Trigger system

The digital trigger system described in the previous section is not the only trigger system used in MAGIC. Other two triggers can be selected during observations: the Sum-Trigger and the Topological Trigger. The **Sum-Trigger** [39, 40] is an analog trigger developed to reach lower energy threshold (up to 30 GeV) than digital trigger. It triggers events in the few GeV domain, where a lower quantity of interactions happened with respect to higher energies. The basic principle of this trigger is to add neighbouring pixels belonging to a small area (macrocell) and then apply a threshold to the final signal. The output signals of the individual Sum-Trigger of each telescope are sent to the L3 trigger to perform the last trigger level. The software responsible for the entire system is called CRISTAL. It is a multithread program written in C language that configures, controls and monitors the Sum-Trigger system.
The **Topological Trigger** is an alternative stereo trigger with respect to standard L3 trigger that uses spatial information of the 19 L1 macrocells. The spatial information of the trigger level is used to predict which macrocells in a telescope will be triggered, if a macrocell in the other telescope is fixed, since γ-ray showers usually trigger the same macrocells in both cameras or the surrounding ones. This system can lower stereo accidental trigger and so lead to a lower energy threshold (about 8% less) and an improved collection area (up to 10-20 %) [41].
These triggers can be used to perform observation of sources like Pulsars, namely the Crab and Geminga, with the goal to catch the low energy pulsed emission. The Sum Trigger was used to detect successfully the pulsed emission from the Crab Nebula down to 25 GeV [42].

Readout system

FIGURE 2.6: The electronic room of the MAGIC telescopes where readout and trigger system are hosted. The six racks containing M1 and M2 electronics are visible. In front of them there are also two additional racks containing the Sum Trigger electronics system. From [32].

In the readout branch the signal, waiting for the trigger decision, is digitized and temporally stored. The entire readout system consists of 48 receiver boards, 12 analog PULSAR (PULSer And Recorder) boards and 2 digital boards. In each telescope, the receiver and the PULSAR boards are located in six 9U-VME crates; the trigger system, including the TCU and the Test Evaluation and Debug (TED) board implementing PRESCALER, SCALER and HYDRA functionalities, is hosted in an additional 6U-VME crates. The total readout of each telescope is hosted in seven crates. Optical fibers with LC connector allow to connect the seven crates to the control PC in a daisy chain configuration with 6VME bridge plugged in the backplane of the crates and a VME PCI card hosted by PC. In the PC the software program called MAGIC Integrated Readout (MIR) is installed. This program configures, monitors and controls the readout of both telescopes.
The signal path in the readout system starts in the Magic Optical NanoSecond Trigger and Event Receiver (MONSTER) boards, also called **receiver boards**. They are multilayer 9U boards that can receive up to 24 channels each and that perform the following tasks:

- convert optical signals from the camera back to analog electrical ones;
- bring analog signals to the digitization electronics (the so-called DRS4);
- generate the L0 individual pixel trigger signals using discriminators;
- provide LT0s to the LT1 using MDR cables;
- split the analog branch to feed a copy of the signals to the Sum-Trigger using dedicated mezzanine boards;

- integrate the Individual Pixel Rate (IPR) counters to monitor the L0 rate of each pixel.

The receiver boards have 4 outputs each: three outputs groups of 8 channels each to feed the LT1 and one analog output to feed the Sum-Trigger input.
Then, the signal from the receiver boards is transmitted into the PULSAR boards. The entire readout system consists of 12 PULSAR boards hosted in two 9U VME crates per telescope. These boards are able to digitize 96 channels each. There are also two additional digital PULSAR boards:

- the BUSY PULSAR that provides the BUSY signal that stops trigger when the readout system is busy on processing one event;
- the DIGI PULSAR that propagates the trigger arrival information to the other PULSAR boards for data readout.

The Domino mezzanine board is the one responsible to hold the **Domino Ring Sampler 4 (DRS4)** [43, 44]. This mezzanine board is a PMC card plugged on the rear side of the PULSAR board. Each mezzanine board hosts 3 DRS4 chips that control 8 channels, for a total of 24 channels per mezzanine board. The clock input is a 40 MHz clock signal that distributes 80 copies of the signals. The clock frequency determines the sampling frequency of each domino chip. Actually the sampling frequency is 1.64 GHz. The DRS4 is an array of 1024 capacitors that receive the signals coming from the receiver board. When a trigger is issued, the charge stored in the capacitors is digitized by an analog-to-digital converter. The DRS4 contains a so-called Region of Interest (RoI) so that only 60 capacitors are readout, reducing the dead time of the instrument down to 27 μs.

Data Acquisition System

The digitized data stored in DRS4 chips are transmitted via SLink protocol from the HOLA (High-speed Optical Link for Atlas) cards to the FILAR PCI (Four Input Links for Atlas Readout) cards, mounted in the **Data AcQuistion (DAQ)** computer. Additional information (time stamp of the event, trigger pattern, calibration pattern, and L3 trigger number), available through cables connected to some PULSAR boards of the readout, are also read and copied inside the data packets sent to the DAQ. Then, a multi-thread C/C++ program called Domino4Readout performs the following tasks [45]:

- readout data packets and proceed to the event building;
- online pedestal subtraction and correction and online data analysis;
- store the events in .raw data files with the MAGIC raw data format.

Finally, the events, grouped in bunches of 100, are written and stored as raw files (binary) into disks. Every raw file contains $\sim$ 14000 events with a size of $\sim$ 2 GB. The DAQ can write events up to a rate of $\sim$ 800 Hz.

2.1.8 Weather Monitoring

There are several auxiliary instruments that have been implemented in La Palma to monitor the weather conditions. The instrument used by MAGIC and other telescopes are:

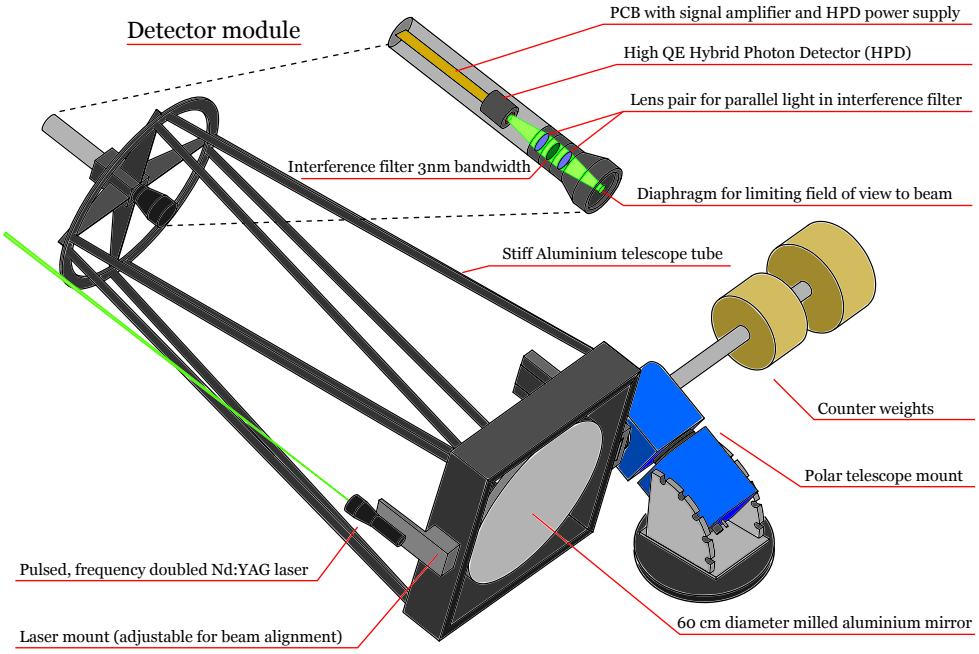

FIGURE 2.7: Scheme of the LIDAR system with some of its components. From [46].

- **TNG Dust Particle Counter**: it is an instrument at the Telescopio Nazionale Galileo (TNG). It measures the dust density in $\mu g/m^3$ through a laser scattering and it is useful in case of *calima*, a strong wind that brings Sahara sand and dust in the MAGIC site;

- **weather station**: it provides measurements of temperature, relative humidity, wind speed and direction. The data collected are available every 2 seconds and, if safety operational limits are exceeded, automatic reactions can ensure the safety of the telescope;

- **LIDAR** [46] it is used by MAGIC to measure the atmospheric transmission through backscattering on aerosols. This system is located in a specific tower on the side of the MAGIC counting house (see Figure 2.1) and it is protected by a dome. The LIDAR is formed by a Nd:YAG laser of 532 mm with a pulse energy of 5 μJ and a width of 0.5 ns, an aluminum mirror of 60 cm diameter with a focal length of 1.5 cm and an Hybrid Photo Detector (HPD) with 55% peak quantum efficiency. This system sends electromagnetic pulses that are backscattered by clouds or aerosols in the visible spectrum up to the atmosphere. Then, it records the arrival time distribution of these photons which can be used to measure the transparency of the atmosphere, assuming an extinction method. So, a value of the Transmission T from 0 to 1 is calculated at different altitude above the MAGIC site;

- **pyrometer**: the main goal of this system is to evaluate the presence of clouds in the atmosphere. It measures the sky temperature that is higher in case of presence of clouds since they reflect thermal radiation from the Earth. The output parameter of the system is called Cloudiness C and it goes from 0 to 100;

- **rain sensor**: it is an infrared LED provided by the team of the First G-APD Cherenkov Telescope (FACT) experiment and installed in May 2017. It is included in the weather report but actually it does not give any automatic reaction;
- **allSkyCamera** it is an Oculus Starlight of 1392x1040 pixels. It takes images of the sky above with a field of view of 150° every 2 minutes. These images are used to investigate the sky conditions.

2.1.9 Cooling System

A cooling system is needed to reduce the heat produced when the telescope and the readout are on and so to ensure that the entire system works properly and in safety. The cooling system of MAGIC is formed by:

- three Ritall chillers that cool down the water received from the heat exchangers and pump cold water in the circuit;
- ten heat exchangers (one per rack). They always show the temperature of the electronics. The safety range is 10-20° C if electronics is off and 22-32° if electronics is on;
- several circuits that distribute water to and from the heat exchangers and cool the air inside the racks.

2.2 Magic Software

2.2.1 MAGIC Central Control: *SuperArehucas (SA)*

MAGIC contains, as listed before, several subsystems. There are some *telescope-related* subsystems that control different hardware components like the drive system, AMC, Camera Control (CaCo) and some common subsystems that collect information for data taking and analysis like weather station, pyrometer, LIDAR. These subsystems are configured and monitored through their own programs and can be controlled from the **MAGIC Central Control (CC)** via TCP/IP. The CC program called **SuperArehucas (SA)** is a Graphical User Interface (GUI) to operate telescopes. It interfaces subsystems that do not communicate within each other. SA coordinates actions of each subsystem, automatizes some data taking procedures and avoids oversights and misuse of instruments. SA is written in LabView 8.5. The communication between CC and the subsystems occurs via TCP/IP socket connections: each subsystem opens a *read socket* to receive info from the CC and a *write socket* to send info to CC. The subsystems send a report on their status to CC every second; SA sends the report to the subsystems every ten seconds. There are only two subsystems that communicate both with weather station and SA: the CaCo and the LIDAR. This is due to the fact that it is necessary to have some automatic reactions in case the operational safety limits are not fulfilled during observations.

2.2.2 MAGIC Automatic Alert System

In case of transient alerts IACTs need an external trigger from space-born satellites to promptly repoint the position of the source. The **MAGIC automatic alert** system processes the alerts sent from the Gamma-ray Coordinates Network (GCN)

and manages also the communication with the MAGIC CC. This system is a multi-threaded C program (see [47], [48]) running in background full time in La Palma. The system handles the alerts coming from the GCN and, according to some predefined observational criteria, decides if the target is observable or not. If it is observable, it sends an alert string to the CC of the MAGIC telescopes, which automatically slew to the target position. The GRB observational strategy with MAGIC will be discussed in more detail in Chapter 5.

2.2.3 Data and Analysis products at the MAGIC site

MOLA

MOLA (Magic OnLine Analysis) is a program for real-time analysis of MAGIC data, processing events within seconds from trigger time [45]. It runs every night during observations handling a quick data analysis from low level to high one to obtain preliminary results on the flux and the significance of the observed sources. These results can be very useful in case of Target of Opportunities (ToOs), flaring sources or transient objects to deliver alerts for other observatories which can perform follow-ups of these sources.

OSA

The On-Site Analysis (OSA) program is a set of macros running in La Palma machines and performing the entire standard data analysis chain. The raw data from the DAQ and the reports from the CC are copied in a common storage (GFS2) and inserted in a MySQL database. Then, the OSA performs the standard analysis chain through several jobs and their results are transferred to the Port d'Informacio Cientifica (PIC) in Barcelona. Here, the data from every analysis step are stored, ready to be analyzed at upper levels to obtain the final graphical outputs. With this system, the data size from the raw level size of $\sim$ 1-2 GB is reduced by a factor $\sim$ 500 and so the data transfer from La Palma to PIC becomes faster. This is very useful because analyzers can have the data available in a more compact format in few hours after they were taken.

Data and Daily Check

The **Data Check System** consists of a series of scripts that start running automatically at the end of the night. They provide graphical outputs that allow to monitor several conditions that may affect data taking quality. One of the output used by analyzers to check the night conditions is the **Superplot** file. It contains four plots produced every night by a data check script:

- zenith distance (Zd) vs time;
- M2 camera current (DC) vs time;
- L3 trigger vs time;
- transmission at 9 km (T_{9km}) and cloudiness vs time.

Through a color code different observational conditions are showed (see Figure 2.8).

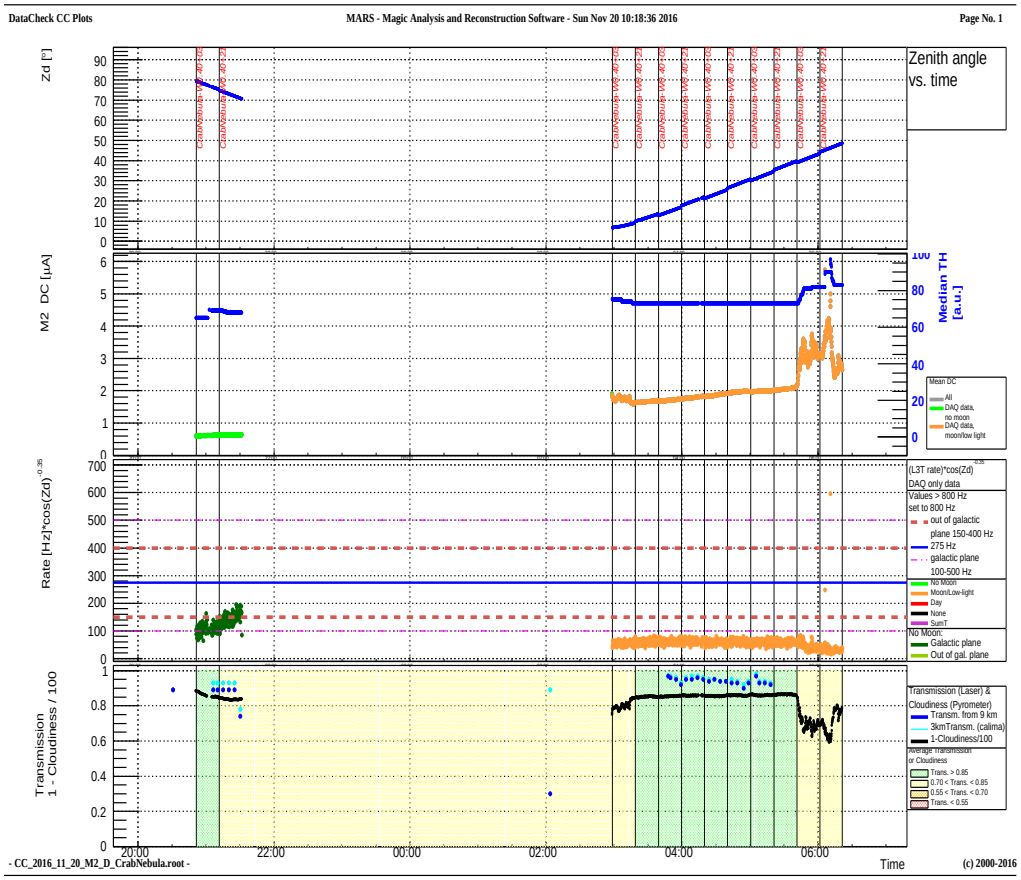

FIGURE 2.8: An example of a superplot graphical output. On the right a legenda is present for each plot. From the top to the bottom: (a) Zd vs time plot with the blue line representing the track of the observed source; (b) M2 DC vs time; (c) L3 trigger vs time; (d) T_{9km} and cloudiness vs time.

2.3 MAGIC data taking

2.3.1 Night conditions

MAGIC, as an IACT, is an instrument with a low duty cycle. In fact, the best performances are obtained in the so-called *dark time* (i.e. when the night is moonless) that represents the standard operational condition of the telescopes. The total amount per year of these nights is $\sim$ 1600 hours, that means a duty cycle of 18%. Anyway some of this time is unfortunately lost during the year because of bad weather conditions or for technical problems. The overall efficiency of the dark time observed every year is about $\sim$ 60%. For these reasons, to increase as much as possible the observational time, MAGIC is capable to observe also with the presence of the moon, in the so-called *moon time*. In these conditions the NSB is higher, so a different discriminator threshold should be set during observations and a dedicated analysis of the data should be performed (see Section 2.4.3). MAGIC can observe up to 75% of *moon time*, stopping just few days during the full moon nights.
The weather in La Palma is usually very good but there are some days in which

conditions are very harsh and it is not possible to take data. To avoid possible risk of damaging the hardware components of the system, some **safety limits** have been established. Observations are not possible if one of these conditions are not fulfilled. The limits are the following:

- humidity < 90%;
- average PMT current < 30 μA;
- individual PMT current < 47 μA;
- wind speed < 40 km/h;
- minimum zenith distance = 1.5°.

2.3.2 Pointing configurations

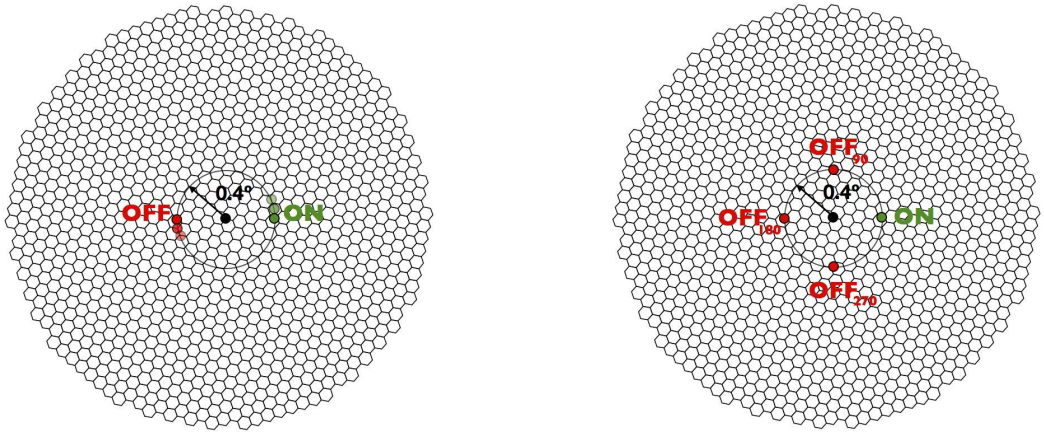

FIGURE 2.9: The WOBBLE pointing mode. The black circle represents the center of the camera. Left: WOBBLE pointing in the case of 1 OFF region. Right: WOBBLE pointing in the case of 3 OFF regions. From [41].

MAGIC takes data with two different pointing configurations:

- **ON mode:** this configuration requires two different types of observations to be performed: an ON observation where the pointed source lies at the center of the camera and an OFF observation where a position in the sky without sources is pointed, preferably under similar Zd/Az conditions and for the same time as the ON observation. This OFF observation gives an estimation of the background;
- **WOBBLE mode**: this configuration is a false source tracking method [49] where positions in the sky with a certain offset from the source are tracked. The standard offset for a point-like sources is 0.4°. During pointing, one or more OFF positions are selected in the opposite position of the camera with respect to the camera center and are used to evaluate the background sky, so no dedicated background observations have to be performed. To have an unbiased estimation of the background more than one wobble position, symmetric to the first one, are needed. These pointings, called wobble positions, are usually four, and they are denoted as W1, W2, W3 and W4. An example of a wobble pointing with 1 or 3 OFF positions can be seen in Figure 2.9.

Currently, the wobble tracking is the default pointing mode in MAGIC while the ON mode is used only in few situations, for fake sources called Dark Patch, to take data where it is sure that there is no signal. Such data, as explained in the next sections, are useful for data analysis.

2.3.3 Data taking

The MAGIC telescopes, when atmospheric conditions are fine, take data every night (except for few nights of full moon) starting after the sunset and till the sunrise. Since the instrument has no total remote control, a crew of some operators, called **shifters**, is needed to control that data are taken correctly and that all the subsystems work smoothly. Every lunar cycle (28 days) the shifters crew is changed. I have been in La Palma for a so-called *shift* two times during my PhD, one acting as shift leader, which means I was the main expert on-site responsible for the data taking operations.
During the night one of the most important parameters used to check that data taking is correctly functioning is the **event rate** of the trigger levels (L0, L1, L3). The event rate is in fact influenced by night conditions like stars in field of view, moon, atmospheric conditions or by the sky region observed (galactic or extragalactic). In a standard dark night, the typical L0 rate is around 800 kHz. As mentioned before, the mean L0 DT is set to $\sim$ 4.25 phe. However, an Individual Pixel Rate Control (IPRC) can set the DT of individual pixels and controls that the L0 rate is within the limits established. The IPRC decreases the L0 DT if the rate is below 250 kHz or increases it when the rate is above 1.2 MHz. For moon observations, the L0 typical rate is $\sim$ 500 kHz and the acceptable range of L0 where the IPRC does not change the DT value goes from 150 kHz to 700 kHz. Thanks to the IPRC system, the L1 typical rates are between 10 kHz and 20 kHz. In the end, the L3 rate is around 250-350 Hz or, using the Sum-Trigger, increases to 500-600 Hz. The rate of accidental triggers of background events is then 40 Hz. There are also, in order to ensure a correct calibration of the readout, 25 Hz of calibration events and 25 Hz of pedestal events recorded during the operation. So, MAGIC observational data containing valid triggers (e.g. cosmic events, γ-ray events, interleaved calibration and pedestal) are divided into **data runs (D)** of $\sim$ 15-20 min each and each data run is related to a specific wobble position. Before starting observation of a source also dedicated **calibration runs (C)** and **pedestal runs (P)** are taken to calibrate data and evaluate the effect of the NSB. Then, at the beginning of every night also a **pedestal subtraction run (B)** is taken to calibrate the baseline of the DRS capacitors and set the zero level to 10000 counts to correct for noise fluctuations.

2.4 MAGIC data analysis

As previously described, the output raw data files from DAQ, containing charge and arrival time information, are the input data of the MAGIC data analysis software called **MAGIC Analysis and Reconstruction Software (MARS)** [50]. It consists of a collection of programs written in C++ language that makes use, as data framework, of *ROOT* libraries [1]. The entire data analysis chain can be split into three level of data processing:

- a **low-level** stage (programs: `merpp`,`sorcerer`,`star`) where data are converted from binary raw into *ROOT* format and calibrated, image cleaning is applied

[1] `https://root.cern.ch/`

and image parametrization is calculated. It is the most time-consuming part, dealing with a huge amount of data and requiring a lot of CPU-hours. For this reason it is usually done on site by OSA and analyzers only get in touch with these steps just in case of *non-standard* analyses (e.g. moon, hardware problems, etc.);

- an **intermediate-level** stage (programs: `superstar`, `coach` and `melibea`) where data of the individual telescopes are merged and additional *stereo image* parameters are calculated, Random Forest (RF) and Look-Up Tables (LUTs) algorithms are trained and applied to data. This is the starting point of a *standard* data analysis chain;

- an **high-level** stage (programs: `odie`, `caspar`, `flute`, `fold`, `CombUnfold`) where graphical outputs for final scientific results are given.

In addition to the standard programs, there are also many small simple programs which can be useful for data selection, finding problems with the data, and automatic processing. In this work only the program `quate` has been used. It runs over input data files of `star`, `superstar` or `melibea` and generates a summary file with many useful information to make a quality selection of data. Now I will describe the main programs used for the data analysis chain in case of *standard* or *non-standard* analyses that will be presented in Chapter 5.

2.4.1 Monte Carlo γ-rays data

Monte Carlo (MC) simulations are needed for IACTs data since no source of γ-rays can be used. These simulations are performed with several softwares that do not belong to MARS (for further information see [51]). The program named `CORSIKA` (COsmic Ray Simulations for KAscade) [52] simulates the atmospheric cascades initiated by primary particles (e.g. photons, nuclei or any other particles), the transport of particles in the atmosphere and their interaction with air nuclei, as well as their decays. MAGIC simulation used a customized version of `CORSIKA` called *Mmcs*. The program calculates and stores several parameters such as particle type, energy, direction, arrival time, and location of the shower. In addition, the modified version used for MAGIC calculates the Cherenkov photons produced in the air and their transport through the atmosphere. Then, the program `reflector` simulates the atmospheric absorption of the Cherenkov photons and the *mirror response* of the telescope to the incoming Cherenkov light. It calculates also the position and the arrival time at the camera plane of the Cherenkov light. Finally, the program `camera` simulates the camera response and the effects of the entire electronic chain. Then, the output MC data files can be analyzed together with observational data since their format is the same as the raw data of the DAQ system. The MC γ-rays initial spectrum is a power law with spectral index -1.6. The MC data produced need to match as much as possible the observational and hardware conditions in order to optimize the data analysis. As a result there are different sets of MCs accounting for different pointing mode of the telescopes (Wobble, ON/OFF): the standard MC γ-rays, called *ringwobble MC*, are simulated in a ring of radius 0.4° centered in the camera center and used in case of wobble pointing. For extended sources or in case of ON observations, *diffuse* γ-rays are simulated in a circle with radius 1.5° centered in the center of the camera. Moreover, MC are produced for different ranges of zenith angle: low (5° - 35°), medium (35° - 50°), high (50° - 62°), very-high (62° -70°), ultra-high (70° - 75° and 75° - 80°). Additional MCs can be produced also in case of special sources. This

was done for GRB 190114C (see Section 5.2) where several sets of MCs have been generated to match as much as possible observational conditions and to study the effect of different DTs on the dataset. In case of hardware modifications, upgrades or if the mirror reflectivity changes during the year, new MCs sets are produced. For this reason, there exist several productions of MC recommended being used in the different analysis periods. The overall list of MCs used in this thesis is summarized in table 2.1.

Tag	Periods	Analysis details
ST.03.07	2016.04.29 - 2017.08.02	Data after PSF improvement
ST.03.08	2017.08.02 - 2017.11.02	Data affected by drop in reflectivity (dust)
ST.03.09	2017.11.10 - 2018.06.29	rain cleaned the dust, same as ST.03.07
ST.03.10	2018.06.30 - 2018.10.30	Data affected by drop in reflectivity (dust)
ST.03.11	2018.11.01 - 2019.09.15	Data with recovered reflectivity
GRB Set1	only for GRB 190114C	ST.03.11 cut in 55<Zd<63
GRB Set2	only for GRB 190114C	Same as GRB Set1 with DT $\sim$ 5 phe, NSB=0.8
GRB Set3	only for GRB 190114C	Same as GRB Set1 with DT $\sim$ 7 phe, NSB=0.8

TABLE 2.1: Summary of the MC data used for MAGIC data analysis.

2.4.2 Standard data analysis chain

Low level stage

The first action of the **low-level data analysis chain** is the conversion of raw data, output of the DAQ, into ROOT format by the program called `merpp` (MERging and Preprocessing Program) which also merges the data file and the subsystems reports. The subsystem reports come from all the MAGIC subsystems and complete the information necessary for further analysis. Then, the *calibration* and the *signal extraction* can be performed on the waveforms of the signal. The calibration program is called `sorcerer` (Simple, Outright Raw Calibration; Easy, Reliable Extraction Routines) and its main purpose is to obtain two pieces of information for each pixel in each event:

- *charge*: converted from ADC counts to number of photoelectrons;
- *arrival time* of the signal.

The signal is initially stored binned in 50 time slices of 0.5 ns each.
For the *signal extraction* the first step is to estimate the baseline which will be subtracted from the "waveform" that describes the event. The general method uses several pedestal events, taking the signal in every time slices, then the baseline value is estimated with a Gaussian fit. After that, the *sliding window* algorithm is used to extract the signal. This method takes the maximum value of the integration of the counts of five consecutive slices, moving the integration window through the slices. Once the signal is extracted the *calibration* process can be performed. The signal, given in integrated readout counts, needs to be converted in number of photoelectrons. This is done with the *F-factor method* [53]. With this method, assuming that 1 readout count corresponds to C phe and that the number of phe follows a Poisson

distribution, one can derive the conversion factor C between the number of phe N_{phe} and readout counts μ as:

$$C = \frac{N_{phe}}{\mu} = \frac{\mu}{\sigma^2_{signal} - \sigma^2_{noise}} F^2 \tag{2.1}$$

where F^2 is the excess noise factor of the PMT, σ^2_{signal} and σ^2_{noise} are the standard deviations of signal and noise. μ and σ_{signal} are computed from the calibration runs while σ_{noise} is calculated from the pedestal ones. In addition, since PMTs have different gain to the same signal, a *flatfielding* procedure is done. As a result the HV of each pixel is adjusted to have the same signal in all the pixels from a homogeneous illumination of the camera. This means that calibration is done on *equivalent* phe, so:

$$C = \frac{N_{phe,average}}{\mu} \tag{2.2}$$

where $N_{phe,average}$ is the number of phe averaged over all camera pixels.
Finally, the *arrival time* of the signal is extracted as the average time slices of the integrated window weighted with the signal in the matching slides:

$$t_{arrival} = \frac{\sum_i i \times s_i}{\sum s_i} \tag{2.3}$$

where i is the time slice number, s_i is the signal in slice i and the summing is performed over the integration window.
Once the calibration is done, the data of each telescope are processed in order to remove pixels which most likely do not belong to a given shower image (**image cleaning procedure**) and subsequently to perform a parametrization of the resulting cleaned image (**image parametrization**). The program performing all these computations is called `star` *(STandard Analysis and image Reconstruction)*. Only few pixels of the camera contain a signal that comes from the Cherenkov light of a γ-ray shower. For this reason, a proper algorithm must reject the pixels containing fluctuations of NSB or electronic noise but, at the same time, ensure that most part of the image is conserved to avoid a loss of the signal. The actual *image cleaning* algorithm is summarized in two steps [54]:

- a **sum image cleaning** procedure in which the signals are clipped in amplitude to reduce the NSB and afterpulses effect and then, for each possible combinations of 2, 3 or 4 compact neighbouring pixels in the camera, their sum is computed. If the summed charge is above a certain threshold and within a certain time interval, these pixels are considered to belong to the shower image. The charge and time thresholds are more strict for smaller groups (see [33] for details);

- a **time-constrained absolute image cleaning** is applied only for those pixels which survive first the sum cleaning. So, the *boundary* and *core* pixels are selected. First, all pixels with a number of photoelectrons above a certain threshold Q_{core} are selected. Then, a pixel is tagged as *core* pixel if at least one direct neighbour also survived the sum image cleaning step. Then, the mean arrival time from all the pixels forming the main island of the image is computed and the core pixels whose arrival time is not within a fixed time constraint of 4.5 ns with respect to this mean arrival time are rejected. Afterwards the pixels are tagged as *boundary* pixels if they are near neighbours to one core pixel with a

charge larger than a second threshold $Q_{boundary}$ and if their arrival time difference with respect to their core neighbour pixel is smaller than 1.5 ns.

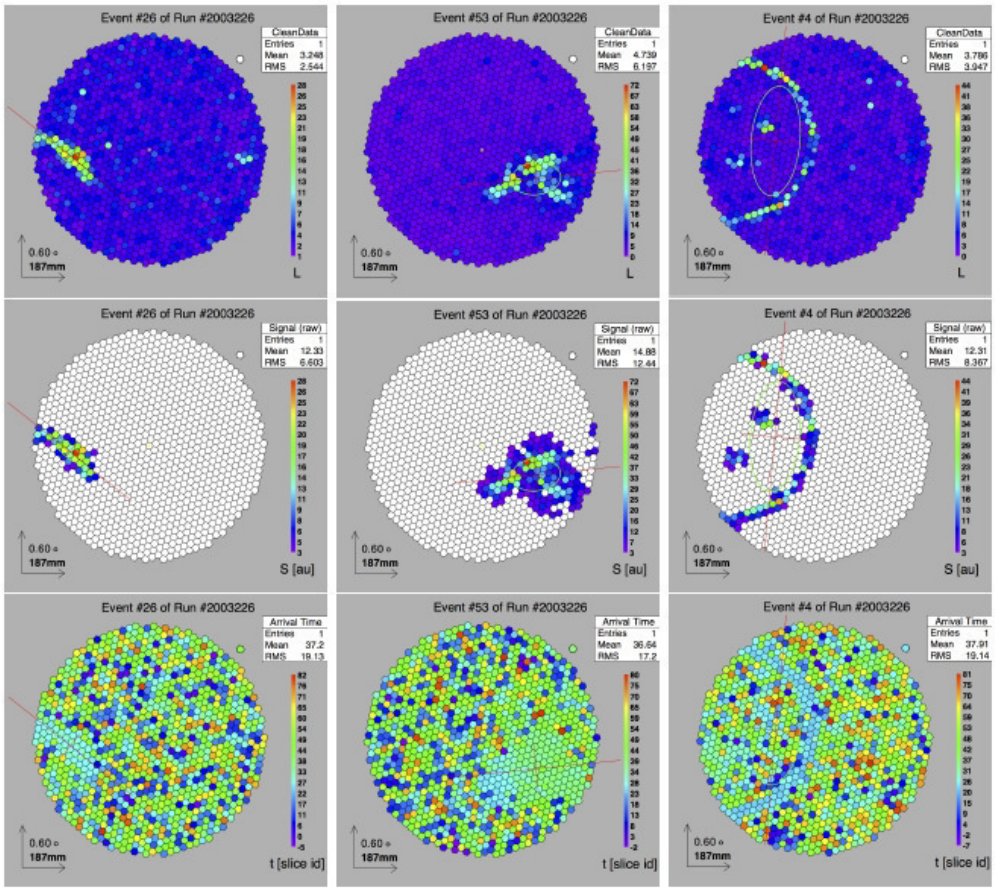

FIGURE 2.10: Examples of showers recorded by MAGIC-II. **Top panel**: charge distribution before image cleaning. **Middle panel**: charge distribution after image cleaning. **Bottom panel**: Arrival times distribution. The left panels are from a γ-ray induced shower, center panels are from a hadron induced shower and the right panels are for a muon induced shower. From [55].

In standard conditions (i.e. dark night) the chosen cleaning charge threshold for the *core* and *boundary* pixels (Q_{core} and $Q_{boundary}$) are set respectively to 6 phes and 3.5 phes. In presence of moon, the NSB effect is higher, so the analyzers have to manually change the threshold values of cleaning using higher values. Example of showers in the MAGIC camera are shown in Figure 2.10.
The last step of the low level data analysis is the *image parametrization*. In this step the stored and cleaned images are used to calculate a set of parameters, called *image parameters*. The image parameters are key tools for the data analysis chain since in the further analysis steps they allow an efficient discrimination of γ/hadron events as well as an accurate estimation of the incoming direction and energy. The parameters used can be divided into several subclasses based on their dependencies:

- **Hillas parameters** (e.g. *size*, *width*, *Center of Gravity (CoG)*): a basic set of parameters, introduced by Hillas in 1985 [56]. Their definitions are based on the

distribution of the photons in the pixels that constitute the Cherenkov image. The parameter *size* which will be used further in the analysis is given by the total number of photoelectrons in the image. In first approximation, it is proportional to the energy of the primary particle;

- **source-dependent parameters** (e.g. *alpha*, *dist*): related to the physical properties of the shower but depending on the expected position of the source;
- **time parameters** (*Time gradient*, *time RMS*): take into account the arrival time of the Cherenkov signal in the camera;
- **image quality parameters** (e.g. *leakageN*, *number of islands*): used to evaluate the noisy level of the image or if it is well contained in the camera;
- **directional parameters** (e.g. *asymmetry*, *M3Long*): discriminate between the head and tail of the shower.

An example of the image parametrization can be found in Figure 2.11.

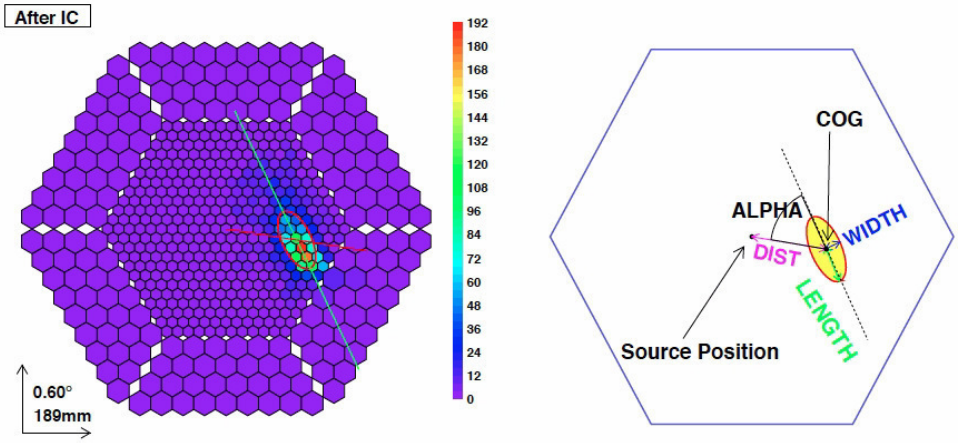

FIGURE 2.11: Some of the main image parameters. From MAGIC wiki.

Intermediate level stage

The intermediate stage of data analysis consists of several MARS executables and the final output of this level consists in a dataset containing all the relevant information to be extracted and processed into high level graphical outputs (e.g. lightcurves, spectra and skymaps). In the low level stage, the analysis is performed separately for each telescope. At this point, a ***stereoscopic* reconstruction** is needed to merge the information of both telescopes into a single file. The program responsible for this task is called `superstar`. It performs a purely geometrical reconstruction of the three-dimensional shower development. In addition, another set of parameters, called *stereo parameters*, are calculated for a better energy and direction reconstruction in the following steps. It merges, as input, the two `star` files of the same events with individual-image parameters to a *stereo* file. Some of the most important parameters are shown in Figure 2.12.

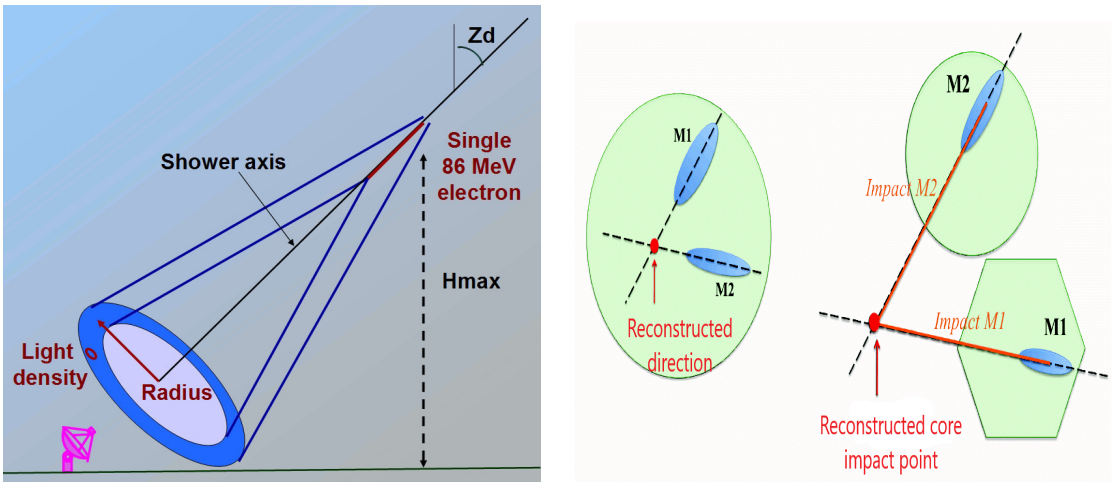

FIGURE 2.12: Scheme of some of the stereo parameters related to the Cherenkov light pool (left figure) or to geometrical reconstruction (right figure).

The *stereo* files, output of `superstar`, are the starting dataset of the analysis in case of standard conditions. Usually, the first step is to run the program `quate` to check the quality of the dataset before carrying out the analysis. This executable is useful to divide data runs that may present *non-standard* conditions to those with standard "*good*" conditions. The program simply calculates the averages of a set of parameters over runs and can perform data selection and classification. It can be applied to output `star`, `superstar` or `melibea` files. It is possible to:

- select upper and lower cut values for some parameters like Zd, Az, atmospheric transmission or Direct Current (DC) and check if there are runs out of range for these parameters;
- find data affected by technical problems like faulty subsystems, wrongly set observational configuration, data taken during hardware change or data test;
- find data with bad atmospheric conditions that can be discarded checking in the runs the mean values of the transmission at 9 km or data taken in moonlight conditions with the DC value of the telescope. This data can usually be recovered through a non-standard analysis (see Section 2.4.3).

At this point the dataset can undergo a ***characterization* process** in which the nature and the main features of the events can be estimated. MAGIC, as an IACT, is a *background*-dominated instrument since the majority of the events that trigger the telescopes are mostly hadronic-induced showers. Other sources of background are *accidental triggers* (due to NSB light, moon light or electronic shot noise), *muons* and $e^{\pm}$-induced showers. For this reason, a key point of the analysis is to identify the nature of the events and to separate γ-ray showers from the background sources. In addition, for the high level analysis is important to reconstruct the arrival direction and the energy of the events. The *Random Forest (RF)* classification algorithm is used for the γ/hadron separation, direction reconstruction, and energy estimation. The energy estimation can also be performed with the *Look-Up Tables (LUTs)* algorithm. The executable responsible to create the RFs and LUTs is `coach`. Then, the program `melibea` is responsible to apply the algorithms to the data, to obtain the final dataset that will be used for the high level data analysis.

The γ**/hadron separation** is the most crucial point of the entire data analysis chain. Indeed, even in the brightest γ-ray sources, the number of hadron events that survive the image cleaning is ~ 3 orders of magnitude larger than the γ-ray events. So, a powerful discrimination method is mandatory to correctly identify the events. In MARS, this method consists of a multi-dimensional classification algorithm based on the construction of decisional trees called **Random Forest (RF)** algorithm [57]. The RF trees (by default 100) are generated using the sample of parameters previously calculated in `star` and `superstar` since they reflect the differences between hadronic induced showers and γ-ray induced ones. The tree construction works as follows: a first parameter is selected randomly and RF searches the value of the parameter, called *cut value*, which better separates the hadron events from γ events. As a result, the events are separated in two subsamples, called *branches*, based on their value of the selected parameter. The cut value of the parameter that better separates the sample is obtained by minimizing the Gini index [58]:

$$Q_{gini} = \frac{4N_h N_\gamma}{(N_h + N_\gamma)^2} \tag{2.4}$$

where N_γ is the number of γ-ray events and N_h is the number of hadron ones. This parameter gives an estimate of the variance of the distributions of γ-ray and hadronic events. Then, the procedure is repeated: for each of the subsample the parameter that better separates hadron from γ-ray events is chosen, its optimized cut value is calculated and new branches are generated. The tree generation stops when a subsample composed only by γ-rays or hadrons events is found or if the number of events is below a predefined value. Then, at the ending subsamples (called *leaves*) a value of 1 or 0 is assigned if they contain respectively hadronic/γ-like events. This parameter is called **hadronness** and it contains the information on the nature of the particle. The RF algorithm as described, is generated by the MARS executable named `coach`. Two so-called *training samples* are given as input in `coach` to *train* the RF: one *MC train sample*, a sample of MC simulated γ-rays, and an *OFF data sample*, where data with no evidence of γ-ray signal ($\lesssim 1\%$ C.U.), so that it contains only hadronic showers, are given. At this stage the MC sample is split in two subsamples: a *train* sample, used in the RF generation, and a *test* sample that will be used later in the analysis. These subsamples must be independent in order not to have a biased result. In addition, it is essential that both samples used (OFF and MC samples) are chosen from the same analysis period and in the same zenital range of the so-called *ON data* (data taken on the source to analyze). In particular the OFF data also need to match as much as possible the observational conditions of the ON data (*dark*/*moon* nights, extragalactic/galactic sources). After its generation, the RF is applied to the data samples in the program `melibea`. The input samples of `melibea` are the *ON data* and the *MC test* sample. These data have to pass through all the separating trees generated in `coach`. As mentioned before, at the end a hadronness value of 0 or 1 for each tree is assigned. As a result, the final hadronness value h of the event is the average of all the obtained values h_i over the N trained trees:

$$h = \frac{1}{N}\sum_{i=1}^{N} h_i \tag{2.5}$$

As mentioned before, also the reconstruction of the **incident direction** of the primary γ-ray is done through an RF algorithm. The method is the so-called **DISP RF**

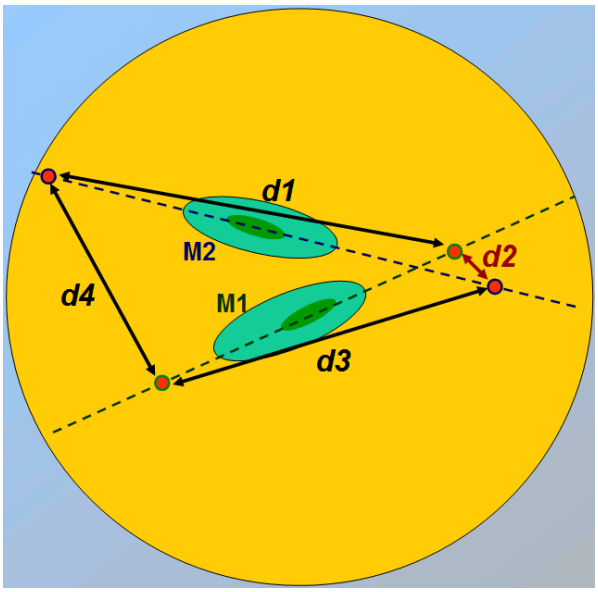

FIGURE 2.13: The *crossing method* applied for stereoscopic analysis of the source position.

method [33, 59]. The principle of the DISP method is to reconstruct the DISP parameter using a RF algorithm applied to a continue variable. Indeed, the γ-ray showers produce elliptical images at the camera. The DISP parameter represents the distance from the image Center of Gravity (CoG) to the source position and can be estimated using the following formula:

$$DISP = A(size) + B(size)\frac{width}{length + \eta(size)leakage2} \tag{2.6}$$

where A(size), B(size) and η(size) are second order polynomials of log(size). The optimization of the coefficients A, B, and η is performed with MC with a regression method using a Random Forest on a continuous quantity. As a result, the DISP is computed for each event and for each telescope, resulting in two DISP values for each event. Once DISP is calculated, four potential source position are estimated. Then, the so-called *crossing method* (Figure 2.13) is applied to solve the degeneracy. The two images of the same event are taken on the same plane and the four reconstructed source positions (2 per image) are found. The distances between each pair of source positions are estimated and the pair with the smallest distance is selected. The reconstructed direction is the average between the chosen pair of positions weighted with the number of pixels in each image. In addition, another important parameter is calculated: the angular distance between the reconstructed and the true position of the source (θ^2). Its distribution will be used later to estimate the significance of the observed signal.

The **energy estimation** of the events can be done in MARS in two different ways. The current standard method is based on the *Look Up Tables* (LUTs) [60]. The LUTs are built in `coach` through the MC training sample. The method relies on the assumption that the energy of the incident γ-ray is almost proportional to the amount of Cherenkov photons produced by the shower, and consequently to the *size* parameter. As a result, the MC training sample is divided in bins for *size* and *impact*

parameter$/r_c$, where r_c is the Cherenkov radius. Then, a two-dimensional table containing the mean energy and RMS of MC events belonging to each bin is created. However, since the amount of light detected by a telescope depends also on many other quantities (e.g. zenith angle, geomagnetic field, *leakage*) several secondary corrections are applied. At the end, for each telescope, a value of the *estimated energy* (E_{est}) of a real event is stored in the LUTs. The final value of the mean estimated energy is computed properly weighted with the RMS of the individual energies. The energy estimation can also be performed through the RF algorithm. This is not currently the standard option but it is widely used in case one wants to improve results, especially for higher energies.

High level stage

At the end of the **intermediate level** stage of data processing for each event we have evaluated *hadronness*, reconstructed energy and direction. Therefore, now the **high level** stage of data processing can be applied. In this stage the *significance* of the signal, *skymaps*, *spectrum* and *Light Curves (LCs)* are obtained. Several MARS executable are responsible for these tasks.
The program `odie` handles the extraction of the significance of the signal. It generates the so-called θ^2 **distribution plots** (Figure 2.14). Indeed the θ^2 parameter is used

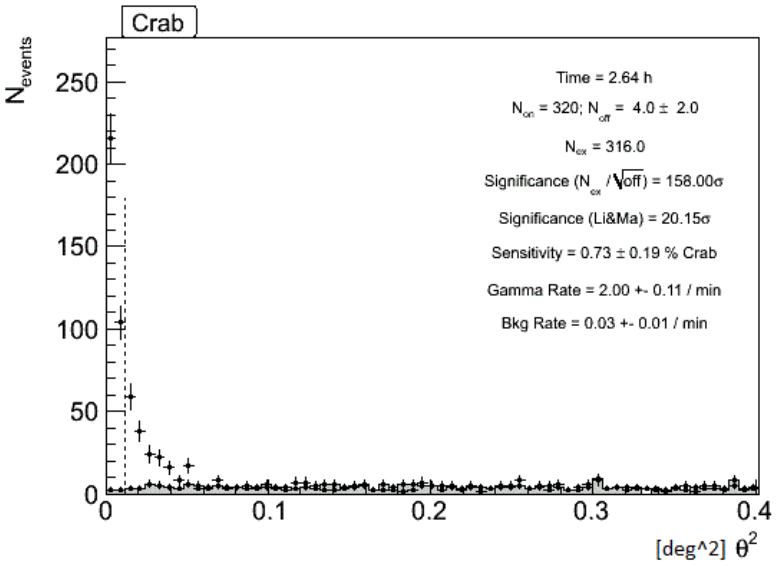

FIGURE 2.14: Example of θ^2 plot of Crab Nebula. The grey histogram is the *background histogram* while the points correspond to the value of the *signal histogram*. The cut of the *signal region* is the vertical dashed line.

to evaluate the presence of a significant γ-ray signal from a certain region in the sky. In fact, γ-ray events would accumulate at smaller values of *hadronness* and θ^2, while the hadronic events would be isotropically distributed for θ^2 and with higher values of *hadronness*. As a result a predefined set of cuts (table 2.2), optimized for different energy ranges, are applied to the parameters *hadronness*, *size* and θ^2. These three sets of cuts are used to maximize the significance in different energy ranges and they are tuned for different kind of sources. The LE cuts give the best sensitivity near the analysis threshold ($\sim$ 75 GeV after all cuts [33]). A loose cut on *size* is used in order to include also the lower energy events at a price of an higher level of background.

They are tuned for sources with a VHE *soft*-spectrum, i.e. most of the emission concentrated in the 0.1-1 TeV range, or with a cut-off at higher energies. The FR cuts provide the best sensitivity for the intermediate energy range, using stronger cuts than the LE set. It gives the best performances for sources with a Crab-like spectrum (-2.6 spectral index). Then, the HE cuts are instead thought to maximize the significance for events above 1 TeV. They also include an additional cut on the value of estimated energy E_{est}.

Energy Range deg^2	θ^2	Hadronness	*Size*M1 phe	*Size*M2 phe	E_{est} GeV
Low Energies (LE)	< 0.02	< 0.28	> 60	> 60	–
Full Range Energies (FR)	< 0.009	< 0.16	> 300	> 300	–
High Energies (HE)	< 0.007	< 0.1	> 400	> 400	> 1000

TABLE 2.2: Standard cuts optimized for the different energy ranges.

The cut value of the θ^2 parameter (θ^2_{cut}) is the upper bound of the so-called *signal region*. Then, two histograms where events are binned according to their θ^2 value are built. From the ON region histogram, also called *signal histogram*, the number of events in the signal region N_{on} are calculated. These events are potentially γ-like candidates but there are also hadronic events, diffuse γ-rays or $e^{\pm}$ events that survive the cuts. The other histogram is the OFF region histogram, also called *background histogram*. It contains events coming from the OFF region, and they are binned in θ^2, now calculated as the angular distance between the event arrival direction and the OFF region position. This histogram gives an estimate of the number of background events. The number of events in the signal region in this histogram is called N_{off}. The overplot of these two histograms is the so-called θ^2 plot. The number of excess events N_{ex} can be calculated as:

$$N_{ex} = N_{on} - \alpha N_{off} \tag{2.7}$$

where α is the ratio between the OFF and the ON regions. Finally, the **significance** of the signal can be estimated using the Li & Ma equation [61]:

$$\sigma_{LiMa} = \sqrt{2\left(N_{on} \ln\left[\frac{1+\alpha}{\alpha}\left(\frac{N_{on}}{N_{on}-N_{off}}\right)\right] + N_{off} \ln\left[(1+\alpha)\left(\frac{N_{off}}{N_{on}-N_{off}}\right)\right]\right)} \tag{2.8}$$

For a Gaussian distribution, if $\sigma_{LiMa} > 5\sigma$ the result is not consistent with the background, and a γ-ray source detection can be claimed.
Together with the signal significance also the sensitivity can be used to quantify the performances of an instrument. The sensitivity for the MAGIC telescopes after its major upgrade is reported in [33]. As mentioned in Chapter 1, the IACTs sensitivity is usually defined as the minimum flux needed to detect the Crab Nebula with a significance of 5σ after 50 h of observation. The *integral sensitivity* of the MAGIC telescopes, calculated for sources with a Crab-like spectrum, is currently 0.55% Crab Units (C.U.) at few hundreds of GeV (Figure 2.15, left plot). The MAGIC differential sensitivity, which is indeed valid for sources with any spectral shape since the cuts optimization is performed in narrow bins of energy, is 6.7% C.U. in the lowest energy

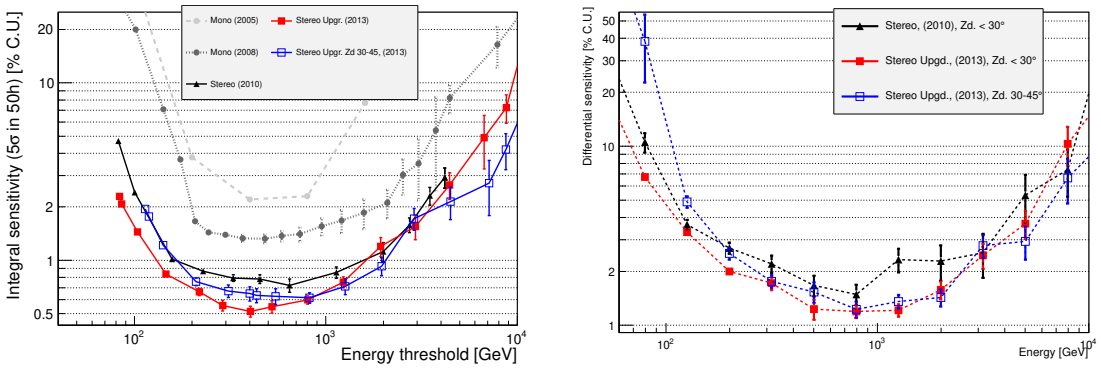

FIGURE 2.15: **Left plot**: Evolution of the MAGIC integral sensitivity versus energy threshold. Performances in stereo mode for zenith angles lower than 30° (blue squares) and between 30° and 45° (red squares) are reported. Also mono performances with Siegen (grey dots) and MUX readouts (dark grey dots) are reported. **Right plot**: differential sensitivity of the MAGIC telescopes as a function of energy and for different periods. The same colors and symbols are used as in the left figure with the same meaning. From [33]

bin 60-100 GeV and improved in all the energy range up to few TeV (Figure 2.15, right plot).

Two dimensional **sky maps** are produced in the MARS executable `caspar`. These histograms contain the γ-ray candidate events surviving the analysis cuts. Skymaps are generated first through a camera exposure model to take into account non homogeneity of the camera acceptance. From this model, an OFF background map is created. The data coming from the events are instead used to generate a ON map. These histograms are then smoothed using the PSF of the instrument added in quadrature with a Gaussian kernel to smear the number of excesses obtained. Usually the Gaussian kernel is taken equal to the PSF, so that $\sigma_{smooth} = \sqrt{2}\sigma_{PSF}$. The significance of a signal in sky maps is calculated through the Test Statistics (TS) method, which is the Li&Ma significance applied on a modelled and smoothed background estimate. This significance is not used to establish the detection of a signal in the observed region due to the complexity and the uncertainties of the background estimate.

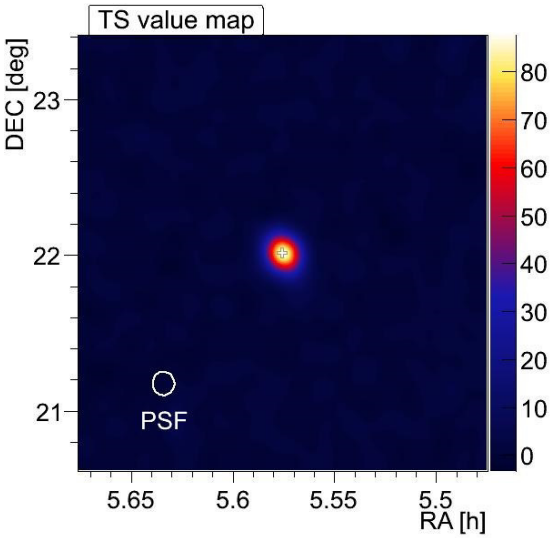

FIGURE 2.16: Example of a TS map of the Crab Nebula.

The generation of **specrum** and **light curve** in MAGIC involves several MARS executables and quantities to be calculated. The first step in the standard data analysis chain is handled by the program `flute`. The *differential spectrum* of a given source can be defined as the number of photons emitted per unit of energy, area and time, so:

$$\frac{d\phi}{dE} = \frac{dN_\gamma(E)}{dE\, dA_{eff}(E)\, dt} \tag{2.9}$$

then, the *integral flux* in a certain energy range $[E_{thr}; E_{max}]$ can be written as:

$$\Phi_{E_{thr}<E<E_{max}} = \int_{E_{thr}}^{E_{max}} \frac{d\Phi}{dE} dE \quad \mathrm{cm}^{-2}\,\mathrm{s}^{-1} \tag{2.10}$$

The LC evaluates the time evolution of the integral flux in the selected energy and time range while the Spectral Enerrgy Distribution (SED) is:

$$E^2 \frac{d\Phi}{dE} = E \frac{d\Phi}{d(\log E)} \quad \mathrm{TeV}\,\mathrm{cm}^{-2}\,\mathrm{s}^{-1} \tag{2.11}$$

where the units are the one used by MAGIC. The quantities needed for these calculations are the total number of γ-rays N_γ, the collection area of the instrument A_{eff} and the effective observation time spent on the source t. All these quantities are computed by the executable `flute` in several energy bins so that each energy bin returns a point or an Upper Limit (UL) on the differential energy spectrum from which, as explained above, SED and LC are calculated.
The total **number of γ-rays** N_γ corresponds to the number of excess events N_{ex} calculated similarly as described in the `odie` program. An important difference is that in `flute` the set of cuts on *size*, *hadronness* and θ^2 are optimized for each energy bin imposing a default efficiency value.
The **effective observation time** t_{eff} is calculated simply subtracting the *dead time d* of the DAQ to the total observational time. Assuming that the arrival time of events follows the Poissonian statistics, the effective observation time can be estimated as:

$$t_{eff} = \frac{t_{elapsed}}{1 + \lambda d} \tag{2.12}$$

where the elapsed time $t_{elapsed}$ is the time between the beginning and the end of the observation.
The effective **collection area** can be seen as the area of an ideal detector which detects the same rate of γ-rays as MAGIC. In first approximation it is determined by the size of the Cherenkov light pool. The collection area depends mainly on the energy of the γ-rays and on the zenith angle. It is calculated using MC γ-rays surviving from previous analysis cuts as:

$$A_{eff}(E; E + dE) = A_{sim} \frac{N_{sel}(E; E + dE)}{N_{sim}(E; E + dE)} \tag{2.13}$$

where A_{sim} is the simulated geometrical area of MC data, N_{sim} are the number of simulated events in the given energy bin $[E; E + dE]$ and N_{sel} is the number of survived events. This calculation is dependent on the spectrum assumed for MC γ-rays (ideally equal to the one of the observed source) and on the width of the energy bins. Considering an observed source with a spectrum $d\Phi/dE$ the collection area is weighted on the spectrum as:

$$\langle A_{eff} \rangle_{[E_1;E_2]} = \frac{\int_{E_1}^{E_2} \frac{d\phi}{dE} A_{eff}(E) dE}{\int_{E_1}^{E_2} \frac{d\phi}{dE} dE} \tag{2.14}$$

This implies that for the effective area calculation, a *tentative energy spectrum* is a needed input. The more it differs from the actual spectrum of the observed source, the wider the energetic bins, the less accurate the result will be.
In reality the average A_{eff} in a given energy bin is done with energy-dependent

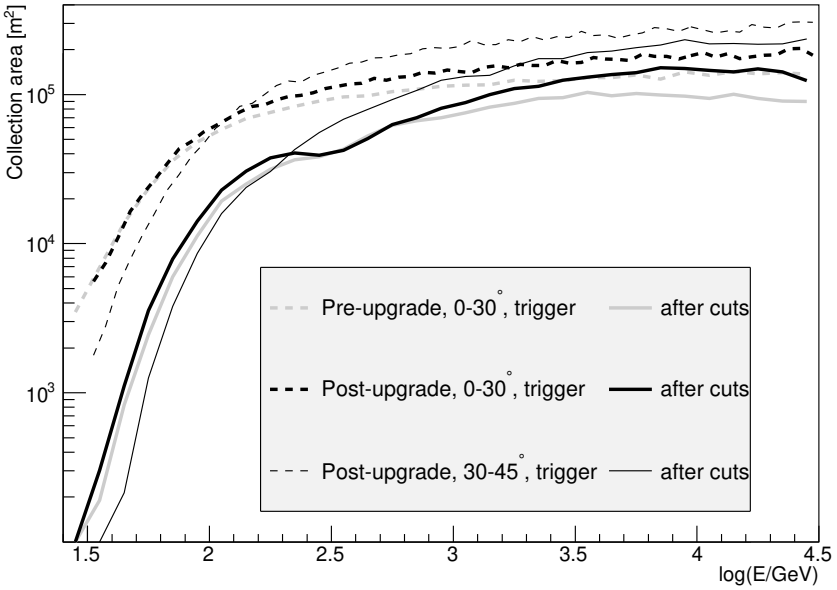

FIGURE 2.17: Collection area of the MAGIC telescopes after and before the major upgrade at the trigger level (dashed lines) and after all cuts (solid lines). From [33].

weights on $A_{eff}(E)$ in narrow bins. In the same way as for energy bins, the collection area is calculated in bins of zenith angle and its average can be calculated as:

$$\langle A_{eff} \rangle_{[Zd_1;Zd_2]} = \int_{Zd_1}^{Zd_2} A_{eff}[Zd] f(Zd) d(Zd) \tag{2.15}$$

where $f(Zd)$ is the fraction of the observation time spent at zenithal angle Zd. In `flute` the calculation is always performed separately in bins of energy and of zenith angle.

A secondary dependence of the collection area is on the *azimuth angle*. This is due to the variation of the effective distance between the telescopes and to the effect of the geomagnetic field. Taking into account the azimuth dependence in `flute` is optional and depends on the dataset to be analyzed. Indeed, binning in azimuth leads to a reduction of the MC statistics and, as a result, to an increase of the statistical fluctuation of the calculated collection area. On the other hand, as we will show later for GRB 190114C, it can improve the results for lower energies, especially in medium or high zenith angle observations.

Once N_γ, t_{eff} and A_{eff} are computed, the differential energy spectrum is calculated in bins of *estimated energy*, since we have no knowledge on the true energy of the events. However, the effective area is calculated in bins of true energy of the MC γ-rays. This can lead to the so-called *spillover* or *migration* of the events. It can happen that some events contained in the $E_1 < E_{true} < E_2$ bin fall outside the $E_1 < E_{est} < E_2$ bin and then the flux is wrongly reconstructed. To overcome this problem an **unfolding method** is needed. In `flute` the *simple unfolding* is applied. In this basic approach, the number of events surviving the analysis cuts for the collection area calculation is given in bins of estimated energy instead of the true one. This simple approach can improve the results in first approximation. However, the spectrum obtained so far was not corrected for several additional problems:

- **limited acceptance**: the acceptance of the detector is limited and energy-dependent;
- **limited resolution**: the energy estimation has a statistical uncertainty, in the case of MAGIC it depends on the energy and is of around 15%;
- other effects like *detection efficiency of the non-ideal detector*, *binning of variables*, *systematic distortion*.

The unfolding method is then needed to solve these issues. Mathematically, the problem is described by the Fredholm integral equation:

$$g(y) = \int M(x,y)f(x)dx + b(y) \tag{2.16}$$

where $g(y)$ is the distribution of the measured parameter, i.e. E_{est}, $f(x)$ is the distribution of the sought parameter, i.e. E_{true}, $M(x,y)$ is the *Migration matrix*, $b(y)$ is the background distribution occurred in the measurement process. In discretized form, the equation can be written as:

$$g_i = \sum_j M_{ij} f_j + b_i \tag{2.17}$$

where the migration matrix M_{ij} in this case represents the probability that an event in bin j of E_{true} is reconstructed in bin i of E_{est}. The most intuitive approach to solve this problem is the inversion of the migration matrix but sometimes is not possible. A second approach is the least square minimization method. Considering:

$$\chi_0^2 = (\vec{g} - \mathbf{M}\vec{f})^T \mathbf{V}[\vec{g}](\vec{g} - \mathbf{M}\vec{f}) \tag{2.18}$$

written in matrix form, the minimum value of χ_0^2 yields the solution for $\vec{f}$ which shows the best agreement with the data. This approach accounts only for Gaussian distributed data points, so it is not efficient for bins with a low number of events, where Poisson statistics has to be taken into account. In addition the solution leads to strong oscillations in $\vec{f}$ and *regularization* methods are unavoidable to produce acceptable results. One possible regularization is done adding a regularization term to the expression which is minimized during the unfolding process, so:

$$\chi^2 = \chi_0^2 \frac{\omega}{2} + Reg(\vec{f}) \tag{2.19}$$

where $Reg(\vec{f})$ is the regularization and ω is its strength: large values produce spectra with fluctuations, small values produce results that can deviate from the data. In MAGIC, the *ROOT* macro `CombUnfold` performs the entire unfolding procedure and the analyzers can choose between different regularization methods: Tikhonov, Schmelling and Bertero methods. ([62, 63, 64])
Moreover, a simpler and alternative approach to solve the Fredholm equation is the method of *forward unfolding*, where a certain model with only few free parameters for the solution $f(x)$ is assumed. First, a spectral shape is assumed and then χ_0^2 is minimized with respect to these parameters. This method is not sensitive to distinct features and should be applied as a useful check of the unfolding results as it is robust and no regularization strength has to be adjusted. The *forward unfolding* in MAGIC can be performed with `CombUnfold` or with the MARS executable `fold`. The latter one uses a different approach with respect to `CombUnfold` to obtain spectra with a *forward-folding Poissonian likelihood maximization*. It takes the output of `flute`

and it calculates the best fitting parameters of the intrinsic source spectrum. Several input information can be provided as the redshift, the energy range in which the fit is performed, the EBL model and the spectral function to be fitted. Several spectral shapes are allowed like power-law (PWL), log-parabola (LP), power-law with exponential cut-off (EPWL), log-parabola with exponential cut-off (ELP) and power-law with super-exponential cut-off (SEPWL). In addition, a `-LightScaleFactor` option can be applied to the data to simulate mismatch of MC and real data light scale. It was used for GRB 190114C to investigate the overall amount of the statistical error on the dataset.
Finally, as mentioned before, in case of energy bins in which there is no *significant* excess of events, `flute` will calculate **Upper Limits (ULs)** on the flux using the Rolke method [65]. In standard analysis, the UL on the differential energy flux is calculated if the energy bin has a relative error in the estimated flux larger than 0.5. The ULs are at the 95% Confidence Level (C.L.), and a systematic uncertainty in the overall signal efficiency of 30% is assumed. An UL can also be calculated for the integral flux with the same conditions. The calculation is dependent on the *assumed spectrum* specified as input. Assuming a γ-ray differential energy spectrum written as:

$$\frac{d\Phi}{dE} = KS(E) \tag{2.20}$$

it is the product of a normalization constant K and a function of the energy $S(E)$, also called *spectral shape*. Considering as N_{UL} the maximum number of expected events according to the measurements performed and to the confidence level defined, it can be translated into an UL for K. For a cut on the measured energy $E' > E_{min}$:

$$K_{UL} = \frac{N_{UL}(E' > E_{min})}{t_{eff} \int_0^\infty S(E) A_{eff}(E; E' > E_{min}) dE} \tag{2.21}$$

analogous in case of an upper cut on maximum energy. K_{UL} represents a limit to the flux normalization as a whole, under the assumption that the assumed spectral shape is the correct one.
In an analogous way, we can write the integral flux as:

$$\Phi(E > E_{min}) = K \int_{E_{min}}^\infty S(E) dE \tag{2.22}$$

Substituting K with the expression K_{UL} obtained previously, we get:

$$\Phi_{UL}(E > E_{min}) = \frac{N_{UL}(E' > E_{min}) \int_{E_{min}}^\infty S(E) dE}{t_{eff} \int_0^\infty S(E) A_{eff}(E; E' > E_{min}) dE} \tag{2.23}$$

2.4.3 Non-standard analyses

MAGIC data taking is performed in optimal standard conditions when a known γ-ray point-like source is observed during *dark* nights with good weather conditions. When this situation is not satisfied additional steps to the standard analysis are needed to treat correctly the data taken in the so-called **non-standard** conditions. In case of **bad atmospheric condition** the strategy is the one described in [66]. The presence of clouds and a low atmospheric transmission can degrade the shower image and then lead to a wrong estimation of the shower parameters, especially the

energy estimation. Corrections to these effects can be applied thanks to the information about the atmosphere state collected by the LIDAR. To evaluate possible corrections to the data, the value of transmission of the atmosphere at 9 km is taken into account. For $T_{9km} > 0.85$ the data are considered with good weather and so no correction is applied. For $0.55 < T_{9km} < 0.85$ data correction must be performed. For $T_{9km} < 0.55$ the data cannot be recovered and so no data analysis can be performed. The corrected energy E_{corr} can be simply calculated from the previously estimated energy E_{est} as:

$$E_{corr} = \frac{E_{est}}{\bar{\tau}} \tag{2.24}$$

where $\bar{\tau}$ is the average attenuation of Cherenkov light in the air-shower calculated directly from the integral aerosol transmission profile $T_a(h)$ and the emission profile $\epsilon(h)$ as:

$$\bar{\tau} = \int_0^\infty \epsilon(h) T_a(h) dh \tag{2.25}$$

Another important correction needed is the one on the *collection area* calculation. Indeed, events reconstructed in case of bad atmospheric conditions look like events of lower energies to the telescopes. The correction makes the events migrate from the wrong energy bin to the correct one so that a migration matrix can be built. Then, this resulting matrix is used to calculate a new collection area for each bin, averaging the collection area over all events.

Data taken in presence of the Moon, the so-called **moon conditions**, need a careful treatment. Indeed, the Moon in the sky increases the NSB and so the rate of photoelectrons continuously detected by every pixel. As a result, the average DC of the PMTs and the mean number of background photoelectrons detected increase, leading to a more noisy signal and to a higher accidental trigger rate. To compensate for this effect, the DTs are increased and, consequently, the energy threshold will be higher. This noisy signal will also affect the overall shape of the recorded images and mainly the weak event images, since they have few photoelectrons that may be lower than the NSB. Moreover, in case of bright Moon, MAGIC PMTs can be also operated at lower voltage, in the so-called *Reduced HV* configuration, to lower the DC levels in this case, observations with NSB up to 20 times dark conditions can be performed. Furthermore, UV-pass filters can be installed in the MAGIC cameras, allowing observations up to 100 times dark NSB. For these reasons also the analysis of such data is treated separately with respect to data collected in *dark nights*. The main advantages of performing Moon observations are an increase of the total observation time and a better time coverage at the cost of larger systematics and higher energy threshold of the performed analysis. An accurate technique has been developed to take care of all these drawbacks and a study of the performance of the MAGIC telescope can be found in [67]. The analysis of moon data taken in *nominal HV* begins from calibrated data, output of the MARS executable `sorcerer`. Indeed, at `star` level the cleaning levels must be increased. The new cleaning levels depend on the sky brightness, and they are chosen so that the percentage of pedestal events that survive the cleaning is less than 10%. So, depending on the sky brightness, different *moon levels* can be identified. Standard settings and cleaning levels, optimized on the Crab Nebula, for the different *moon levels* have been calculated in [67] and are summarized in Table 2.3. As well as source data, also MC and OFF data must take into account the presence of the Moon. Usually the provided MC have a NSB level for dark observations, so in this case a *tuning* of the data is needed. An easy way for that is to use the option `AddNoise` in program `star`. This option adds artificially

extra noise in the data to mimic the effect of a higher NSB level. Then, MC data and OFF data, if taken in dark nights, must be reprocessed with the same image cleaning of the source data and with the *AddNoise* option. Afterwards, in the high level stage, a higher cut on the parameter *size* must be applied to the data.

Sky brightness NSB_{dark}	HV Settings	DC_{M1} (μA)	*NoiseLvl* mean/RMS	Cleaning Lvl1-Lvl2	Size Cut [phe]
1	NomHV	1.1	$2.0 - 1.0$	$6 - 3.5$	50
$1 - 2$	NomHV	$1.1 - 2.2$	$2.5 - 1.2$	$6 - 3.5$	60
$2 - 3$	NomHV	$2.2 - 3.3$	$3.0 - 1.3$	$7 - 4.5$	80
$3 - 5$	NomHV	$3.3 - 5.5$	$3.6 - 1.5$	$8 - 5$	110
$5 - 8$	NomHV	$5.5 - 8.8$	$4.2 - 1.7$	$9 - 5.5$	150
$5 - 8$	RedHV	$3.2 - 5.2$	$4.8 - 2.0$	$11 - 7$	135
$8 - 12$	RedHV	$5.2 - 7.8$	$5.8 - 2.3$	$13 - 8$	170
$12 - 18$	RedHV	$7.8 - 11.6$	$6.6 - 2.6$	$14 - 9$	220
$8 - 15$	UV Filters	$2.2 - 4.1$	$3.7 - 1.6$	$8 - 5$	100
$15 - 30$	UV Filters	$4.1 - 8.3$	$4.3 - 1.8$	$9 - 5.5$	135

TABLE 2.3: Suggested noise, cleaning levels and size cuts calculated from Crab Nebula subsamples for NSB up to 18. From table in [67].

The last non-standard analysis that will be described in this section is the **analysis of GRB observations** or, in general, of transient unknown sources. In these cases a particular procedure is needed where some additional steps with respect to standard data analysis are performed. Due to their nature, transient phenomena cannot be identified a priori before their first appearance. Thanks to its fast repositioning system and the GCN coordinates network, MAGIC can anyway observe transient sources in less than $\sim$ 30 s after their first detection. During its repositioning the DAQ is not stopped, so the first subrun of observation needs to be treated separately. In fact, this first subrun, recorded during the repositioning of the telescope, can contain some events related to the transient event but it will be named as the previous source observed before the repositioning. So to extract only the events related to the transient event, calibrated data have to be downloaded for the first run, and then the analysers need to run `star` and `superstar` over first subrun specifying RA and DEC of the source. This is essential because in the first sub run, the run headers coordinates are still the ones of the source observed when the alert arrived. Then, standard analysis can be performed on the entire data set simply imposing on the configuration file of programs `odie`, `caspar`, `flute` the source coordinates. In the program `odie` a graphical output can also be performed, called significance evolution, that shows the progresses of σ_{LiMa}, excess events, background events and signal over background ratio with time.

2.5 Fast analysis of interesting targets

MAGIC observations are usually decided following a precise schedule which guarantees that all the research projects have enough data for their scientific purposes. Nevertheless, observations of transient or flaring sources, for their nature, cannot be scheduled well in advance. In case of flaring AGNs, information coming from space satellites can help to understand which sources are flaring and can be then tagged

as *interesting targets* worth to be observed during the following nights. In case of GW events, the LIGO/Virgo collaboration sends alerts which are processed by the MAGIC automatic alert system. For AGNs there is no need for an automatic reaction for an instantaneous observation, but a decision can be taken after discussing within the working group. For GWs the semi-automatic observational strategy developed for MAGIC follow-ups can be described as follows [68]:

- **autonomous MAGIC follow-up**: this follow-up strategy is applied in case a valid alert (in terms of visibility, zenith angle and telescope operational status) is received by the MAGIC automatic alert system and the GW candidate is well localized ($\sim 10^\circ$ at 90% CL). The starting point is given by the LIGO localization skymap. From this map, the visibility of the sky positions from the MAGIC site at different times is computed. Then, the selected sky regions with good visibility are scanned with an ordered list of pointings. The scan list takes into account the galaxies included in the available catalogues [69] or following the strategy proposed in [70]. Finally, the telescopes are repositioned to the target positions using the automatic procedure through the automatic alert system;

- **follow-up of identified transients**: in this case a transient is detected and localized by other facilities. The position is pointed following the alert of the instrument. In case this happens during the night the standard automatic follow-up procedure is followed, otherwise a dedicated observation is scheduled.

Therefore, in absence of an automatic reaction, both for AGNs and for GWs, a Target of Opportunity (ToO) must be requested to observe the source during the night. As a result, the schedule will be rearranged allowing the observation of these sources in the observational time windows requested.
Once the observation is performed, it is important to understand if a significant signal is detected and further observations in the following nights would be useful. For this reason, MAGIC needs some people (at least two for each month) to act as *Flare Advocates* (FAs). When a ToO observation is performed, the following day the FAs should:

- check the MOLA results;

- check the OSA high level results;

- perform preliminary analysis of the data.

The analysis has to be performed as soon as the `star` or `superstar` files are available (usually in the late morning). The MC files and RFs trained on recent data are prepared well in advance so that they are ready when the new lunar cycle starts. Finally, the analysis results are distributed to the collaboration and used to decide if the ToO observation should be continued. I acted as FA a few times during my PhD. In these occasions I had the possibility to analyze a flaring AGN (3c279) and to search for a possible counterpart of GW events (AT2017gfo). I will here briefly report the results I obtained from these analyses.

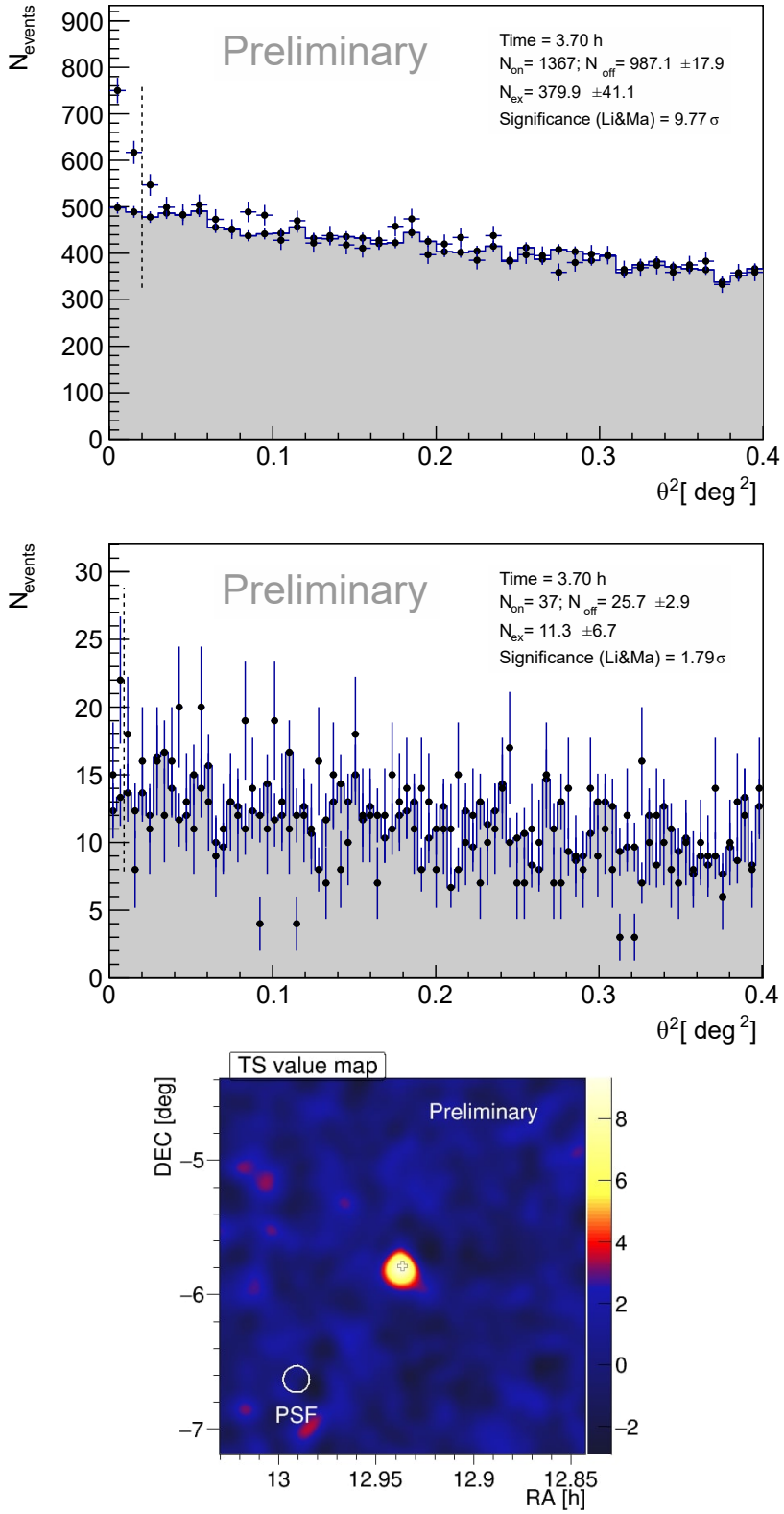

FIGURE 2.18: Fast analysis of the flaring AGN 3c279. The results are combined including the first three nights of observations when the source was clearly detected. **Upper figure**: θ^2 plot, LE cuts. **Middle figure**: θ^2 plot, FR cuts. **Bottom figure**: TS map, LE cuts.

3c279 is a very bright and highly variable *blazar*, an AGN with one of the jets pointing toward the Earth. This object has an estimated redshift of $z = 0.536$ [71] and is classified as a Flat-Spectrum Radio Quasar (FSRQ). It exhibits complex multi-wavelength variabilities with yearly radio variability, and daily optical, X-ray and γ-ray flares. MAGIC detected a VHE emission component from 3c279 for the first time in 2006 [72]. Since then, its emission was monitored several times in the following years [73, 74]. From 2nd June 2018 to 6th June 2018 this source was monitored as a ToO by MAGIC. In the following mornings I performed the analysis of the data collected over the previous night. The results from my analysis are summarized in Table 2.4 and in Figure 2.18. The day-by-day analyses are reported in Appendix A.1.

Date	Significance LE [σ]	Significance FR [σ]
02-06-2018	6.51	1.01
03-06-2018	5.51	1.23
05-06-2018	5.65	0.63
Combined	9.77	1.79
06-06-2018	0.81	0.40

TABLE 2.4: Summary of the resulting significance from the fast analysis performed on 3c279. The Combined results include the first three nights of observations when the source was clearly detected.

The θ^2 plots in the first three nights show a clear detection of the source applying LE cuts. Moreover, the corresponding skymap shows a bright hotspot at the source position. These results were used to extend the observations until the 6th June, when the source was no longer detected.

Date	T_{eff} [s]	Significance LE [σ]	Significance FR [σ]	Significance HE [σ]	UL [$\mathrm{cm^{-2}\ s^{-1}}$]
15-01-2018	0.97	1.58	1.68	1.65	1.01×10^{-11}
19-01-2018	0.43	0.94	1.68	0.00	5.15×10^{-12}
23-01-2018	0.70	1.24	0.59	-0.84	9.68×10^{-12}
25-01-2018	0.98	-0.48	-1.28	-2.28	1.48×10^{-11}
26-01-2018	0.34	1.89	0.61	-1.31	1.03×10^{-11}
27-01-2018	0.41	0.50	1.27	-1.07	9.92×10^{-12}
11-03-2018	0.81	1.45	1.03	-1.49	5.97×10^{-12}
12-03-2018	1.02	0.59	0.96	0.21	9.76×10^{-12}
24-03-2018	1.83	0.84	0.14	0.84	4.19×10^{-12}
14-06-2018	1.75	-0.47	-1.07	-1.72	4.81×10^{-12}
Combined	9.24	2.26	1.42	-0.99	–

TABLE 2.5: Summary of the results from the fast analysis performed at the loacation of the GW optical counterpart AT2017gfo. The ULs are calculated for $E > 300$ GeV. The Combined results include all the observations.

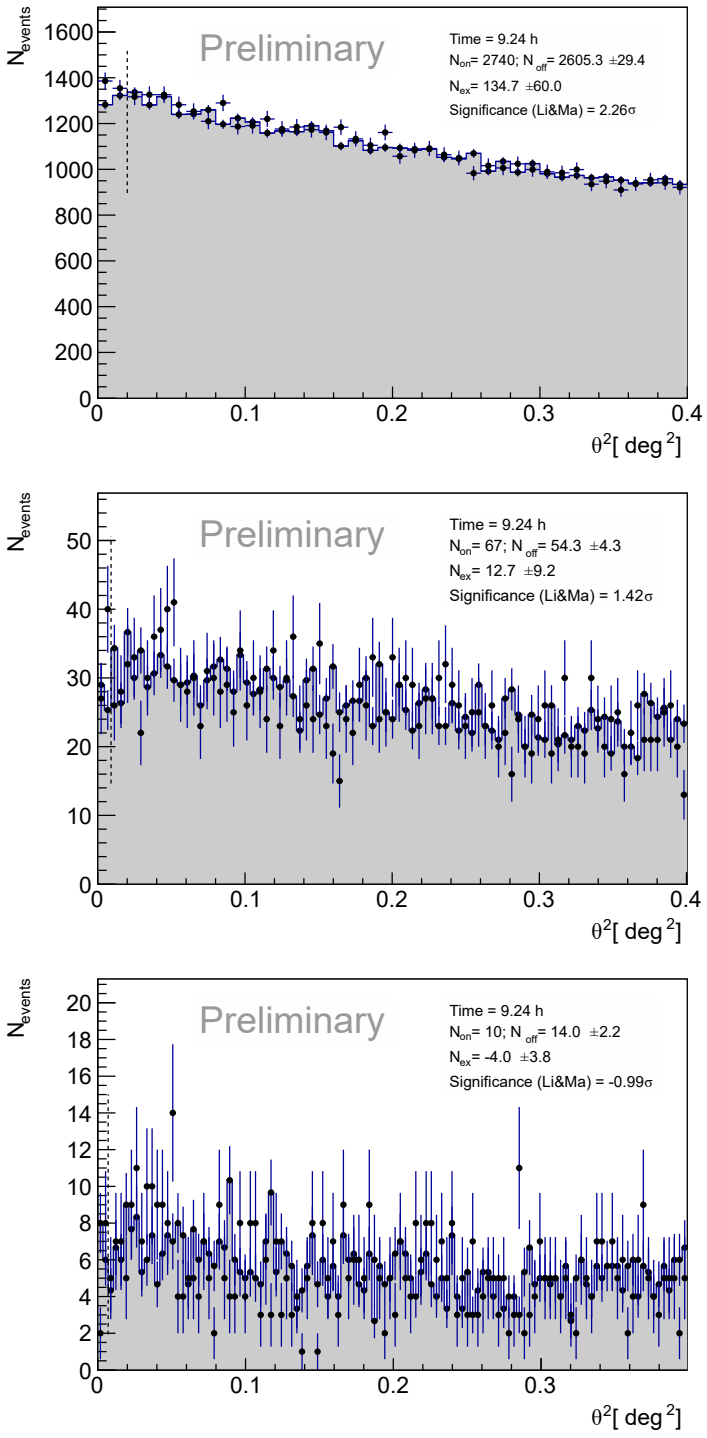

FIGURE 2.19: Fast analysis of the flaring AT2017gfo. The results are combined including all the observational nights. **Upper figure**: θ^2 plot, LE cuts. **Middle figure**: θ^2 plot, FR cuts. **Bottom figure**: θ^2 plot, HE cuts.

AT2017gfo is the optical electromagnetic counterpart of the GW event GW170817. It is the first electromagnetic counterpart of a GW event ever detected (and the only one clearly identified, so far). Its emission was detected in the optical and near-infrared band during the first 12 hrs after the trigger time. The evolution is consistent

with predictions for the behavior of a kilonova, expected in case of mergers of NS-NS systems [75, 76]. Such results led to intensive follow-up campaigns also in the radio and X-ray bands which detected the source (associated with the jet component and called GRB 170817A) from $\sim$ 10 days after the trigger time with an unusual and unprecedented raising flux up to $\sim$ 100 days after the merger [77]. Such behaviour makes it an interesting case also for γ-ray detection.
MAGIC observed the source for $\sim$ 9.5 hrs in 10 different nights from January to June 2018. The data were taken in dark conditions. I selected for the analysis those ones taken in good weather conditions ($T_{9km} > 0.85$). I analyzed the data night by night as well as stacked together. No significant detection was seen in the dataset. The results from the analysis are listed in Table 2.5 and in Figures 2.19.

Chapter 3

Gamma-Ray Bursts

The Universe is full of events which show rapid and irregular emission of electromagnetic radiation in a short time scale. In this class of sources, the so-called *transient* sources, we find the powerful explosions called **Gamma-Ray Bursts** (GRBs). Their name reveals the first temporal and spectral properties observed when they were discovered. The term "*burst*" here refers to a sudden release of radiation lasting from milliseconds to thousands of seconds, while "*gamma-ray*" stands for the energy range of the spaceborn GRB detectors, going from tens of keV to several MeV. Nowadays, we know that such features describe only the first phase of emission of a GRB, the so-called *prompt* emission. Indeed, extensive multi-wavelength observations have shown that GRB emission extends in the temporal domain, lasting from minutes, hours to weeks, months or even years, and in the energy domain where they are detected in the radio, millimeter (mm), infrared (IR), optical, ultraviolet (UV), X-rays, HE and VHE range. This is the second phase of emission of GRBs, called *afterglow* emission. This emission phase is usually fainter than the *prompt* and it shows a rapidly fading behaviour.
Considering their physical features, GRBs are the most luminous explosions in the Universe, with a typical isotropic γ-ray luminosity of the order of $\sim 10^{50}$–10^{53} erg s^{-1}. Their outflow is highly relativistic and afterglow observations have revealed that they are cosmological objects.
The usual classification separates the GRBs in two different classes according to the duration of their prompt emission: *short* GRBs last less than 2 s while *long* GRBs last longer than 2 s. This classification also reflects the different origin of such events. Long GRBs are believed to be associated with the death of some special massive stars while short GRBs with the merging of compact objects such as Neutron Stars (NS) and Black Holes (BH).
The investigation of GRB main properties is still ongoing and while several questions on their physics have been answered, a lot of unknowns are still present. For this reason, even after more than 50 years from their discovery, they are still a hot topic in astrophysics.
In this chapter I will briefly outline the historical development in the comprehension of GRB physics, both from observational and theoretical point of view, especially focusing on the HE and VHE emission component and on the afterglow emission phase which have been the two main topics of my work during the PhD. I will describe the dynamical evolution, the acceleration process and the radiation mechanisms involved in such events.

3.1 History of GRBs

The history of the discoveries and the progress in the comprehension of the GRB physics can be described through several *eras*. Such discrete description is explained since key observational breakthroughs can be made only when new detectors or telescopes become operative. Therefore, each of these *eras* can be linked with the instruments that were active and the observational data available from them.
GRBs were discovered in the late 1960s by the military satellite system *Vela*, a constellation of 12 satellites used by the USA to monitor possible nuclear explosions within and outside the atmosphere of the Earth. The first paper, announcing the discovery of 16 events, was published in 1973 [78]. This opened the so-called *dark* era (1973-1991), when GRBs were discovered and several theoretical models were developed. However, the small amount of data collected and the poor localization capability of the detectors let no possibility to reveal the mysteries beyond these events detected only for tens of seconds and exclusively at soft γ-ray energies.
The first leaps in the understanding of the nature of GRBs were done after the *Compton Gamma-Ray Observatory* (CGRO) was launched in 1991. Two of the on-board instruments which contributed to such improvements were the *Burst And TranSient Experiment* (BATSE) and the *Energetic Gamma-Ray Experiment Telescope* (EGRET).

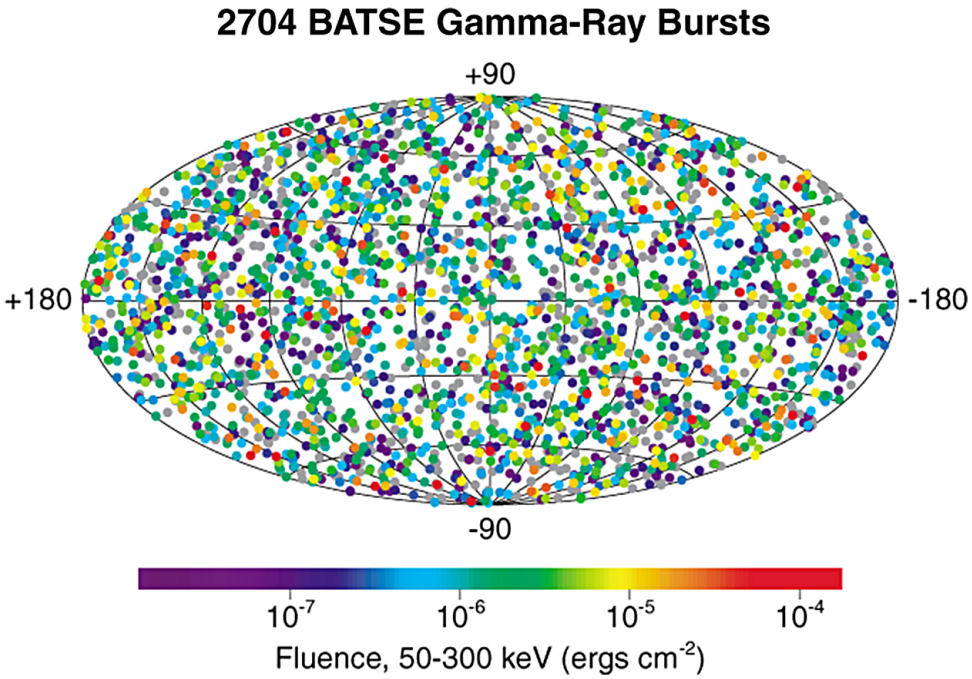

FIGURE 3.1: Spatial distribution of the GRBs observed by BATSE.
From `https://heasarc.gsfc.nasa.gov/docs/cgro/batse/`

The *BATSE* instrument, working in the energy range 20 keV - 2 MeV with an all-sky field of view, detected 2704 GRBs. In the so-called *BATSE* era (1991-1997) the most important progresses were:

- the angular distribution of GRBs was found to be highly isotropic (Figure 3.1). Such result gave a significant support to a cosmological origin interpretation of GRBs [79];

- two categories of GRBs were firmly identified [80] based on the duration time: *long-duration* GRBs and *short-duration* GRBs with a separation value of roughly 2 s;
- the first spectra were collected revealing a non-thermal behaviour (details in 3.2.1).

Moreover, the EGRET instrument, whose energy range was 30 MeV - 30 GeV, detected a few GRBs, one of which, GRB 940217[1], was found to have long-lived GeV emission extending for 1.5 hours [81]. Despite the great discoveries in the γ-ray band, no follow-up observations at lower energies were successful. The reason is that the BATSE instrument had a coarse spatial resolution and the error-boxes on the positions of GRBs contained too many candidate counterparts.
This problem was finally overcome thanks to the following generation satellites, in the so-called *Beppo-SAX/HETE* era (1997-2004). In the Italian-Dutch satellite *Beppo-SAX* [82], launched in 1996, three main on-board instruments where devoted to search for GRBs:

- a GRB Monitor (GRBM), working in the 40-700 keV range, for the detection of the GRB prompt emission;
- two Wide Field Cameras (WFCs) working in the 2-30 keV range to search and localize the X-ray counterpart of the GRB;
- a set of Narrow Field Instruments (NFIs): X-ray focusing telescopes, sensitive in the 0.1-200 keV range used to investigate the X-ray counterpart.

Therefore, when a GRB was triggered by the GRBM, the WFCs could promptly monitor the GRB error boxes to localize the X-ray counterpart with a resolution of the order of the arcmin. In addition, the spacecraft could be reoriented to observe GRBs with the NFIs to investigate the time evolution of the X-ray emission. This strategy led to the discovery of the *X-ray afterglows* of many GRBs. Moreover, follow-up observations revealed also the afterglow emission in the optical, radio and infrared energy bands. The detection of optical counterparts allowed the identification of the host galaxies and the estimation of the redshifts, establishing the *cosmological origin* of GRBs. Such discoveries produced a major step forward in the comprehension of the GRB physics. The amount of energy associated with such events was calculated opening several questions on the GRB emission structure. The decaying behaviour of the multi-wavelength afterglows were predicted with several emission models (e.g. [83]) or used to constrain the GRB physics [84, 85] . These subjects will be treated in detail in the next sections.
Another space instrument, launched in 2000, was the *HETE-II* (High Energy Transient Explorer) satellite [86]. It was the first space mission entirely dedicated to GRBs with three on-board instruments covering a broad energy range (1-400 keV). The main improvement with respect to Beppo-SAX was that the GRB position was computed on-board, in a few tens of seconds. Then, the position of the counterpart was immediately distributed to the scientific community through the Gamma-ray Coordinates Network (GCN) [87] to allow fast multi-wavelength follow-up observations. Therefore, Beppo-SAX and HETE-II provided precise localizations of more than 100 GRBs and they discovered the association between supernovae and some long GRBs [88, 89, 90], supporting the general thought that such objects could be the *progenitors*

[1] In GRB names nomenclature the number represents the date in which the GRB has been detected. In the current rule the date is followed by a letter, in the past it was omitted.

of GRBs. Moreover, HETE-II allowed the detection of the first optical afterglow from a short GRB [91] and confirmed the nature of X-Ray Flashes (XRF) (see Section 3.2.2) as soft GRBs [92].
The following breakthrough discoveries were achieved with the telescopes *Swift* and *Fermi*. These space satellites are currently the most important operative missions for GRBs hunting. It is then common to refer to these years as the *Swift* era and the *Fermi* era. These time intervals are overlapped and they started when the respective missions were launched. The Swift observatory [93] was built by an international team from the USA, UK and Italy. It started data taking in 2004 and it carries three instruments: a wide-field Burst Alert Telescope (BAT), a narrow-field X-Ray Telescope (XRT), and a UV-Optical Telescope (UVOT). While the BAT detector, covering the energy range 15-350 keV, is able to trigger and localize the GRB with an error box of a few arc-minutes, the satellite can quickly slew to the GRB position and catch the X-ray afterglow with the XRT instrument with a typical time delay from the trigger of less than one minute. XRT can also provide a position with an accuracy of the order of a few arc-seconds. Then, the UVOT with a typical time delay of less than two minutes can quickly search for a UV/optical counterpart. As for HETE-II, the burst positions are immediately sent to the GCN for prompt follow-ups from other instruments. The rapid slewing capability of Swift (e.g. for Beppo-SAX repointing was possible only hours after the trigger) allowed detections of the afterglow of the vast majority of the detected GRBs. The main Swift results up to now are:

- the detection of the faint afterglows of short GRBs, confirming the first past evidence that they might be related to different progenitors than the long GRBs;
- the high number of detected afterglows allowed to identify a "*canonical*" shape for the X-ray afterglow light curve [94] (for details, see Section 3.2.2);
- the extension of the redshift range, observing GRBs up to $z = 9.4$ [95]. Such distant objects could be useful for cosmological studies.

Together with the Italian space mission AGILE (*Astro-rivelatore Gamma a Immagini LEggero*) [96], launched in 2007, the space satellite *Fermi* provides useful data for the investigation of GRB emission in the HE band. The *Fermi* satellite [97] was launched in 2008 and it carries two instruments: a Large Area Telescope (LAT) which covers the energy range 20 MeV - 300 GeV and a Gamma-ray Burst Monitor (GBM) operative in the 8 keV - 40 MeV energy band. GBM is able to monitor the whole unocculted sky triggering $\sim$ 200 GRBs/y, while LAT can scan the entire sky every three hours with a good angular resolution at higher energies (0.15° at 10 GeV). These instruments, covering more than seven orders of magnitude in energies, were able to reveal and describe several main properties of the HE emission component in GRBs. Indeed, the LAT instrument detected a HE emission component in $\sim$ 10-15% of the GRB seen by Fermi-GBM, making also possible to perform temporal and spectral analyses of the bursts. This was a major improvement with respect to the few detections achieved by EGRET.
Finally, in the last few years, new breakthrough discoveries have been achieved in two research fields of the GRB physics: the *VHE emission* and the *multi-messenger* observations. In the last decades searches for emission from GRBs in the VHE energy band have been carried out by several ground based observatories but no TeV counterpart was identified. In 2019 such researches have finally led to an unprecedented discovery: the MAGIC and H.E.S.S. telescopes have revealed the presence of a VHE emission component in GRBs [98]. These results opened a new spectral window in

GRB research which could probably improve the comprehension of the physics of GRBs. Moreover, on 17 August 2017 a NS-NS merger event GW170817 was detected by the Advanced LIGO and Advanced Virgo GW detectors [12]. The association of this event with the GRB 170817A detected in X-ray, optical and radio bands [13] has opened the so-called *multi-messenger* era for GRBs.

3.2 GRB phenomenology

The general understanding of GRBs advanced through years thanks to the huge amount of data collected on these events from several telescopes both from space and from the ground. Beside the theoretical models developed, a phenomenological approach was essential to reveal the underlying physical processes ongoing at the GRB site. Despite some breakthrough discoveries, in most of the cases one can only infer the most plausible scenario based on the available information at hand. In this section I will summarize the main observational clues on GRBs regarding the *prompt* emission (Section 3.2.1), the *afterglow* emission (Section 3.2.2) and the *HE and VHE* emission component (Section 3.2.3).

3.2.1 The *prompt* emission

As mentioned before, the **prompt emission** is generally considered as the initial bright and rapid emission phase going from tens of keV to several MeV which triggers the GRB detectors. Their main temporal and spectral properties have been initially studied by BATSE and in the last $\sim$ 10-15 years by Swift-BAT and Fermi-GBM. Quantitatively, the duration of a burst is usually described through the "T_{90}" parameter, the time interval in which the detector collects from 5% to 95% of the total fluence. It ranges from milliseconds to thousands of seconds and the T_{90} duration distribution is bimodal (Figure 3.2) with two peaks, one at 1 s and the other at about 30 s, and a separation around 2 s. Such distribution allows to roughly classify GRBs into two different categories: **short GRBs** with $T_{90} < 2$ s and **long GRBs** with $T_{90} > 2$ s.

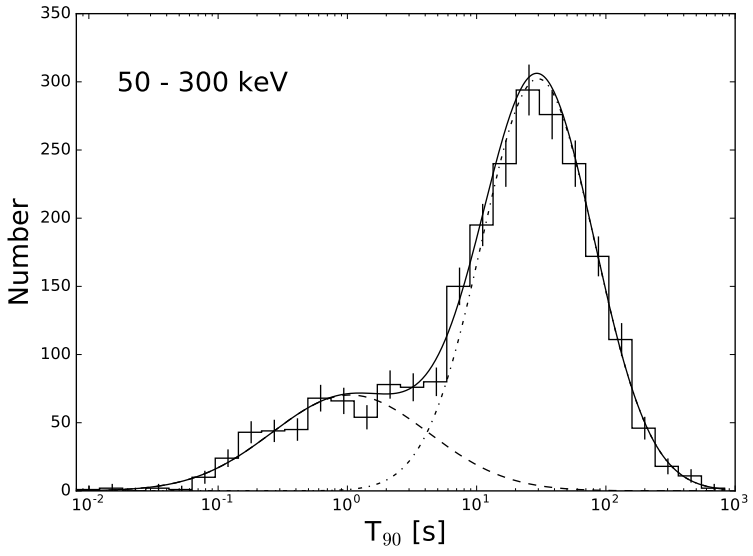

FIGURE 3.2: T_{90} distribution of GBM-triggered GRBs. Lines show the best-fitting gaussian models. From [99].

Another parameter useful to describe the burst features is the *Hardness Ratio* (HR). It is the photon count ratio in two fixed observational energy bands (higher energy band divided by a lower energy band). Usually, long GRBs have a lower value of HR than short GRBs. As a result, the two classes of GRBs are also termed respectively as *long-soft* and *short-hard*. These observational-based definitions have several limitations: they depend on the energy bandpass and on the sensitivity of the detectors. Therefore, different instruments will measure their own value of T_{90} and HR. Moreover, the T_{90} gives a correct estimation of the prompt duration only in case of a single pulse emission. On the contrary, most GRB prompt light curves show very irregular and unique patterns with multi-episode pulses, long quiescent phases or weak precursor emission. A more detailed study is then mandatory to understand the unique behaviour of these emission episodes.
Regarding their spectra, GRB prompt spectra are non-thermal. BATSE observations showed that usually they can be fitted with a smooth broken power law, known as the *Band Function* [100] (Figure 3.3). The photon number $N(E)$ spectrum in this model is:

$$N(E) = \begin{cases} A\left(\frac{E}{100keV}\right)^{\alpha} \exp\left(-\frac{E}{E_0}\right), & \text{if } E < (\alpha-\beta)E_0 \\ A\left[\frac{(\alpha-\beta)E_0}{100keV}\right]^{\alpha-\beta} \exp(\beta-\alpha)\left(\frac{E}{100keV}\right)^{\beta}, & \text{if } E \geq (\alpha-\beta)E_0 \end{cases} \tag{3.1}$$

where α and β are the photon spectral indices, respectively for low and high energies, E_0 is the transition energy and A is a normalization factor.

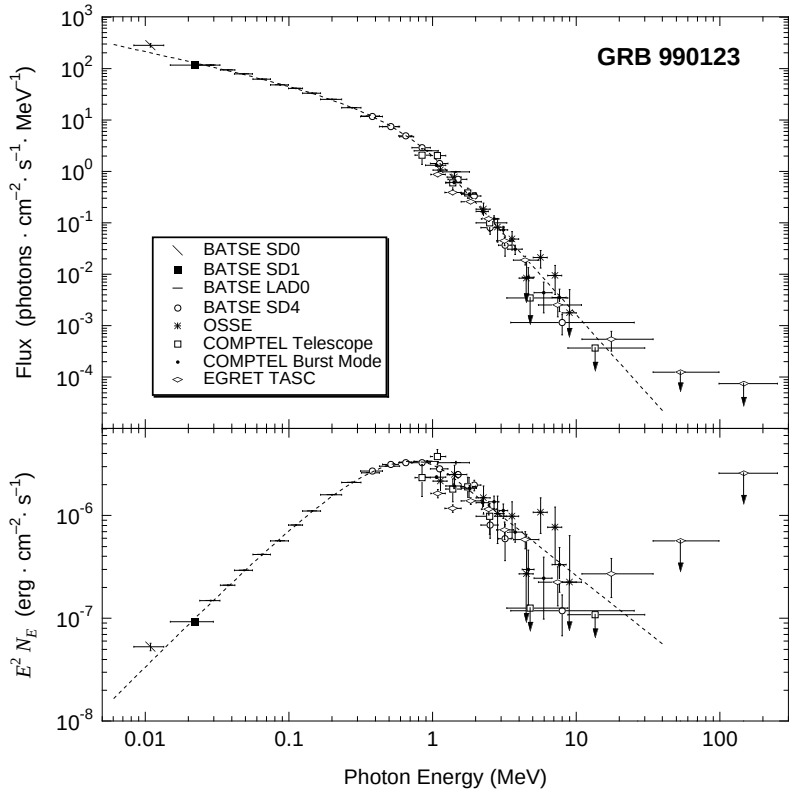

FIGURE 3.3: A typical Band-function spectrum of GRB 990123. From [101].

The peak of the spectral energy distribution $E^2N(E)$, called E_p, is given by:

$$E_p = (2+\alpha)E_0 \tag{3.2}$$

The values of E_p show a very wide distribution, so that a classification is difficult: the bright BATSE sample of GRBs (156 GRBs) has E_p clustered around 200-300 keV range but bursts with lower E_p have been found by HETE-II, Swift and Fermi. From the bright BATSE sample, the two spectral indexes of the Band function have a distribution of $\alpha \sim -1 \pm 1$ and $\beta \sim -2^{+1}_{-2}$ [102]. Such a distribution is also confirmed for the GRBs detected by other instruments such as Fermi and the INTErnational Gamma-Ray Astrophysics Laboratory (INTEGRAL) [103, 104].
Observations from HETE-II, Swift and especially Fermi have shown that the Band function is not sufficient to describe all the prompt spectra. Sometimes GRB spectra are described with simple cut-off power law spectrum, in the form:

$$N(E) = A\left(\frac{E}{100keV}\right)^{\Gamma} \exp\left(-\frac{E}{E_C}\right) \tag{3.3}$$

This function has been used when the detector energy band is not wide enough and then the high-energy photon index β of the Band function is not well constrained. Moreover, additional components are sometimes required to explain certain GRB spectra. In a fraction of GRBs a *thermal component* is found to contribute to the observed spectra. In this picture, the peak energy of the spectrum is interpreted as the peak of the thermal component defined by its temperature. Besides the Band and thermal components, also an additional *high-energy spectral component* is required to fit the prompt spectra of some GRBs. This component was clearly detected in several Fermi LAT GRBs (for details, see Section 3.2.3). Summarizing the latest results, a prompt emission spectrum may include three *elemental spectral components* (Figure 3.4) [105]:

- a non-thermal Band component;
- a quasi-thermal component;
- another non-thermal component extending to high energies.

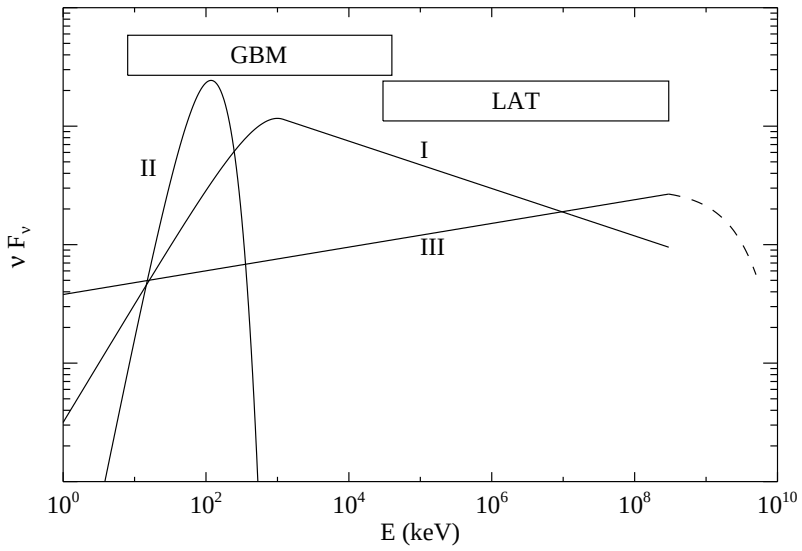

FIGURE 3.4: Scheme of the three *elemental spectral components* seen in GRB prompt spectra. The energy range of GBM and LAT are also reported. From [105]

In some spectra one component can be dominant (usually the Band component) or there can be superposition between two components. The components show distinct features and behaviours and their physical origins have not been fully identified. While the Band component can be attributed to non-thermal synchrotron radiation in optically thin regions, the thermal component can be related to the photosphere emission from the ejecta. The additional non-thermal high energy component looks more mysterious and its exact physical origin is subject to debate. In conclusion, such new discoveries have opened several questions on the nature and the properties of the prompt emission, whose current picture is currently under heavy discussions.

3.2.2 The *afterglow* emission

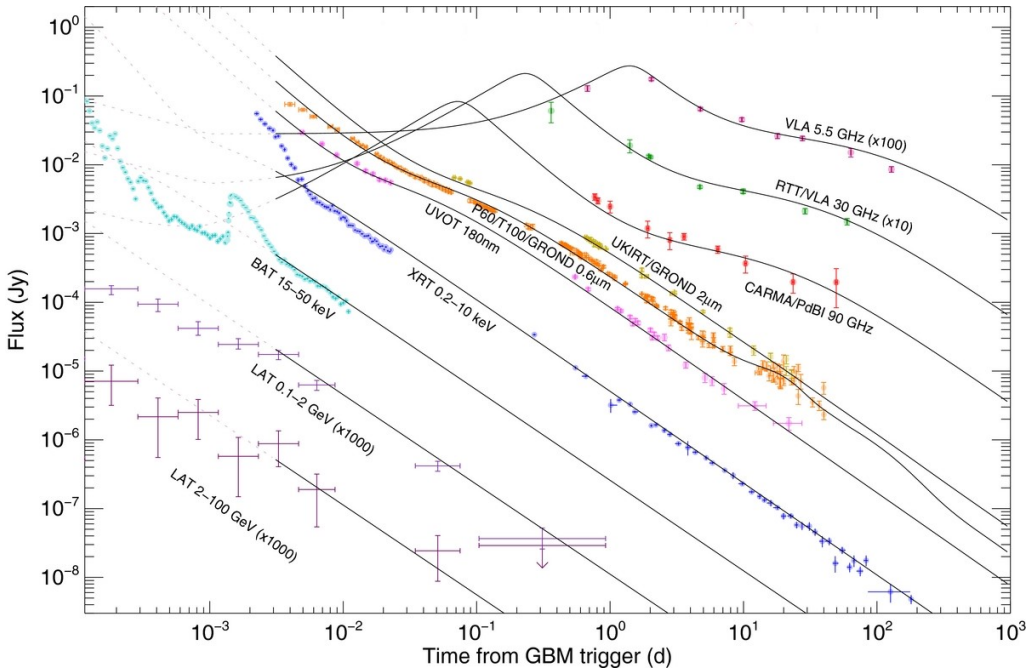

FIGURE 3.5: Multi-wavelength afterglow emission from GRB 130427A from radio to HE range. Analytical light curves are also reported (black lines). From [106]

While the prompt phase describes the first instants of GRB emission, the long-lasting and broadband following phase is known as **afterglow emission**. Since its discovery, made by Beppo-SAX on 28 February 1997 [107], it is extensively studied. Indeed, its *multi-wavelength* nature allows to perform intense campaigns, searching for this broadband emission from radio to HE and VHE range (see Figure 3.5). Moreover, its long duration allows to follow the evolution of the emission usually for several days and so to collect a huge amount of data. The afterglow emission is generally described, as a first approach, with multi-segment broken power laws. Therefore, its flux density $F(\nu, t)$ can be conventionally described as:

$$F(\nu, t) \propto t^{-\alpha} \nu^{-\beta} \tag{3.4}$$

where α and β are respectively the *temporal* and *spectral* index. Such description is in any case not sufficient to account for the several features (e.g. bumps, flares) observed during the afterglow emission at different wavelengths. Nevertheless, it is

a good simplification to describe the standard picture of the afterglow emission and the predicted radiation components. Indeed, the multi-wavelength afterglow light curves can be in general well described with the synchrotron external forward shock scenario, which will be described in detail in Section 3.4.
Thanks to the huge number of GRB X-ray afterglows detected by Swift, a ***canonical X-ray light curve*** has been defined [94]. It consists of a five segments curve, not all of them always simultaneously present. Each of these segments represents a different behaviour observed during the emission and it can be linked with a particular physical origin. The five pieces that compose this curve are the following (Figure 3.6):

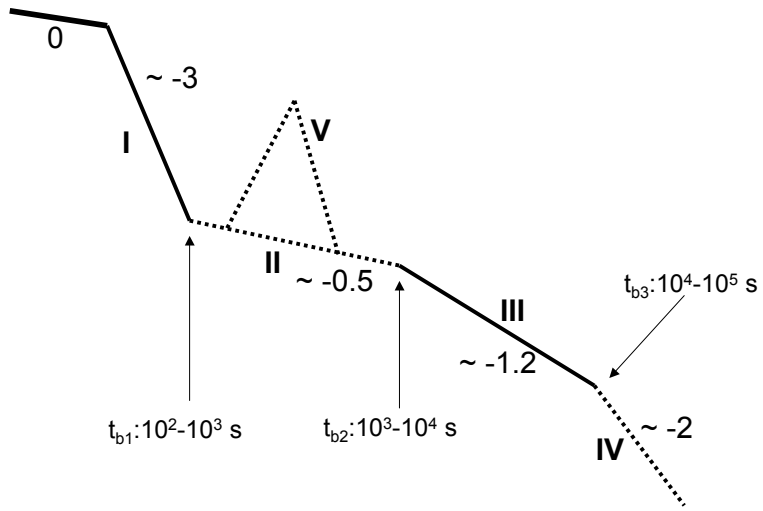

FIGURE 3.6: Graphical representation of the X-ray canonical light curve. From [94]

- **steep decay phase** (I) is the earliest power-law decay segment. The temporal decay slope is steep, with a typical index $\sim$ -3. XRT/BAT joint observations [108] have shown that this phase is the so-called "*tail*" of the prompt emission, lasting up to 10^2 - 10^3 s;
- **shallow decay phase** or **plateau** (II) with a typical slope of $\sim$ -0.5 up to 10^3 - 10^4 s. The origin of this phase almost constant in flux is the less understood;
- **normal decay phase** (III) where the decay slope $\sim$ -1 is the typical value predicted in the synchrotron external forward shock model (see Section 3.4.4);
- **late steep decay phase** (IV) the decay steepens with a slope of $\sim$ -2 or steeper. This is also expected in the external forward shock model due to the so-called *jet break* effect (see Section 3.3.4);
- **X-ray flares** (V) discovered by HETE-II and characterized by Swift (half of Swift GRBs' have one flare). Such narrow flares usually appear during the shallow decay phase, superposing the power law decay behaviour. This suggests that such events should have a different origin with respect to the power-law decay segment. Temporal and spectral analyses have shown that they share

several properties with prompt emission and that they are directly linked with it [109, 110].

Despite a smaller sample of events, also the **optical afterglow** light curves have been deeply studied. At earlier times (first hours) the optical light curves show a complicated behaviour with humps, shallow or steep decays or plateau. At late times (more than a couple of hours after GRB trigger) their behaviour is more "regular" and the light curve is well described with a single power-law decay with a decay index of $\sim$ -1. For bright afterglows, a break in the slope can be also seen at later times. Such steepening, as mentioned before, is also visible at the same time in the X-ray light curve (phase IV). Therefore, such *achromatic break* is not of *spectral* origin (i.e. when a spectral break passes across a particular observational band) but, in this case, of *geometrical* origin. This break is the proof of the collimation of the GRB emission into narrow jets (see Section 3.3.4).
There is also a substantial fraction (30-50%) of GRBs where the optical afterglow is not detected. These are the so-called *dark GRBs*. The most accepted interpretation of such events is a large amount of dust extinction between the GRB and the observer.
About 30% of GRBs are detected also in the **radio** band. The radio light curve usually starts with an early rising phase, reaching a peak $\sim$ 3-6 days after the trigger. Then, it starts to fade usually following the synchrotron external forward shock model predictions described in Section 3.4.

3.2.3 The HE and VHE emission component

The search for **HE emission** from GRBs started with EGRET, one of the instruments on board the CGRO satellite. This instrument, sensitive in the 30 MeV - 30 GeV band, detected a few GRBs which revealed different spectral and temporal properties in the HE range. In particular, GRB 940217 [81] shows a HE emission component lasting much longer than the prompt phase and detected up to 5400 s after the trigger time T_0, with a 18 GeV photon arrived at $\sim T_0$ + 4500 s. Such features suggest the possible presence of a distinct emission component, different from the prompt emission and responsible for this HE radiation. This was then confirmed with the event GRB 941017 [111] detected by EGRET, BATSE and COMPTEL which clearly revealed an additional spectral component up to 200 MeV. These detections opened several questions on the nature of this new spectral component and on its physical implications. However, the small number of detections did not allow to give a robust interpretation of these results.
A deeper study of the HE emission component was then possible thanks to the satellites AGILE and especially Fermi with its on-board instrument LAT. AGILE detected a dozen of GRBs with emission above 30 MeV. The LAT instrument released its second GRB catalog in 2019 [112] covering 10 years of observations. A total of 186 GRBs were detected: 91 show emission in the range 30–100 MeV and 169 are detected above 100 MeV. This wide sample of GRBs shows several observational features, not always in agreement, which help in the comprehension of the nature of this emission component. Most of the main results that will be now listed are summarized in this catalog and in [113].
For several GRBs, the *onset* of the high energy emission component is observed to be *delayed* with respect to the low energy one by a few seconds (Figure 3.7). The observation of this delay in bright LAT events, where the photon statistic is high, supports the intrinsic nature of this feature rather than a purely instrumental effect.

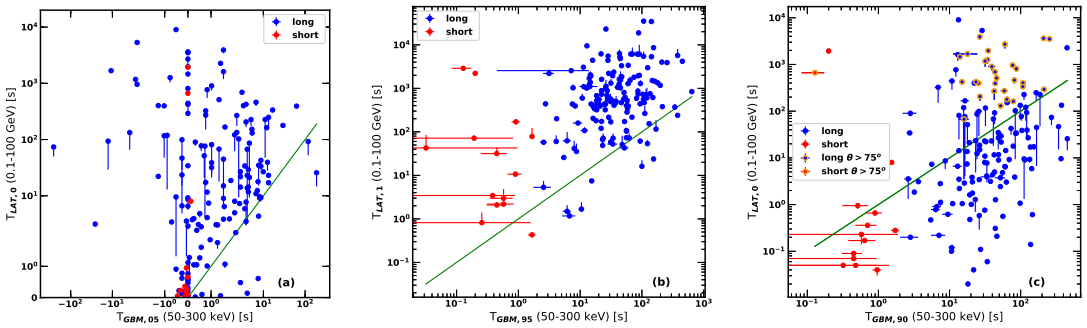

FIGURE 3.7: **Left**: onset times estimated in the LAT energy band $T_{LAT,0}$ (i.e. the time when the first photon with probability $p > 0.9$ to be associated with the GRB is detected) (100 MeV–100 GeV) vs onset times estimated in the GBM energy band $T_{GBM,05}$ (i.e. time at which GBM measures 5% of the total GRB flux) (50–300 keV). **Center**: burst duration comparison between LAT $T_{LAT,1}$ (i.e. time when last event with $p > 0.9$ is received) and GBM $T_{GBM,95}$ (i.e. time at which GBM measures 95% of the total GRB flux). **Right**: onset time $T_{LAT,0}$ of the LAT emission vs the burst duration $T_{GBM,90}$ (T_{90} calculated by GBM) (50–300 keV). The solid line denotes where values are equal. Blue and red circles represent long and short GRBs, respectively. In right panel GRBs outside FoV at trigger time are marked with a thick orange contour. From [112].

Moreover, the *duration* of this delayed HE emission is *longer* compared to the keV-MeV prompt emission and usually extends up to 10^2 - 10^3 s after the trigger. A few bursts show features and temporal variability in the light curves, especially at early times, and in some cases an evidence of temporal correlation with the prompt component was found [114]. However, such indication is still quite under debate since it could be driven by a contamination of photons coming from the prompt component with energies less than 1 GeV. At *late time* the HE emission decay follows usually a power law behaviour $t^{-\alpha}$, similar to the one observed in the X-ray, optical and radio afterglows. From the second Fermi-LAT catalog, the mean value of the decay index α calculated for a sample of 86 long GRB with a Gaussian fit is 0.99 ± 0.04 with a standard deviation of 0.80 ± 0.07. In few cases, a break is present in the data and the broken power law shape gives significant improvements in the fit results.
Regarding their *spectral properties*, a variety of different behaviours can be seen. During the prompt phase, the HE emission in several cases is the natural continuation of the HE component of the Band spectrum observed in the keV-MeV band. Sometimes also an exponential cut-off is seen in the HE tail of the spectrum. Such feature can be explained likely as generated by pair production [115]. In some cases, the HE emission cannot be simply described by a Band function and an *additional component* (as mentioned in Section 3.2.1) must be invoked. This component can be usually modelled with a power law with photon index $\gtrsim$ -2. The late time component of the HE energy emission is usually modelled with a single power law component with index $\sim$ -2 and with no spectral evolution in time.
Other aspects which were noted about GRBs detected by LAT are their flux, their fluence defined as the flux integrated over a certain time period, and the energy radiated, especially in comparison with the GRBs detected by GBM or other instruments working at lower energies. From Figure 3.8 it is clear that LAT detections are

biased towards the brighter GRBs of the GBM population. Moreover, the comparison between the energy radiated in the LAT energy range and in the keV-MeV band during the prompt phase shows that typically this ratio is smaller than 1 for long GRBs and larger than 1 for short GRBs (see Figure 3.8).

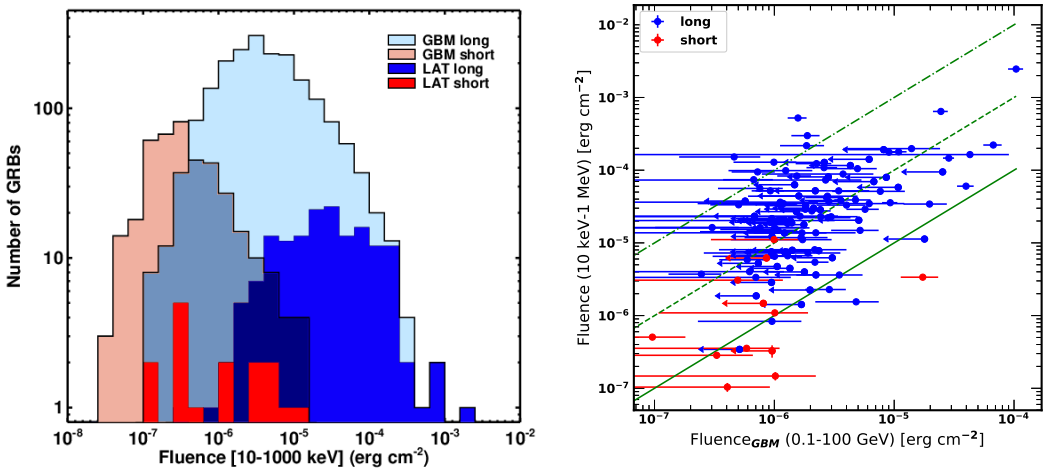

FIGURE 3.8: **Left**: comparison of the energy fluence (10–1000 keV) of GRBs detected by LAT and GBM. **Right**: GBM fluence (10–1000 keV) vs LAT fluence (100 MeV–100 GeV). Both fluences are calculated in the $T_{GBM,90}$ interval. The solid green line denotes where values are equal. The dashed and dot-dashed green lines are shifted by factors of 10 and 100, respectively. From [112].

Some studies concerning the *highest energy* photons observed by LAT and their possible nature were also carried out. The highest energy photon recorded so far by LAT is a 94.1 GeV photon coming from the event GRB 130427A [116]. At least $\sim$ 30% of LAT GRBs have a photon with energy $\geq$ 5 GeV in the observer frame and almost 80% of LAT GRBs with known redshift have a maximum source-frame photon energy $\geq$ 5 GeV [112]. Such events were fundamental to test the synchrotron forward shock models and to investigate the possible radiation mechanism responsible for the HE emission component. Indeed, these photons can have an energy that is higher than the estimated maximum one in case of synchrotron radiation, which is $\simeq$ 50 MeV$\times\Gamma/(1+z)$ in the observer frame, where Γ is the bulk Lorentz factor, decreasing with time. Therefore, the interpretation of these photons as synchrotron radiation is challenging.
Figure 3.9 shows a comparison between the maximum energy for synchrotron photons from two different configurations and assumptions and the most energetic photons of several GRBs detected by LAT. Several photons lie above these limiting curves. Although different assumptions can change the estimation of the limiting curves, this result was the first evidence that a different radiation mechanism is needed to explain the HE emission observed by LAT.
The discovery and the features observed in the HE emission component, especially with LAT, point to the possibility that a **VHE component** in GRBs is present. The search for this component was performed in the last decades with ground based Cherenkov telescopes. Despite several observations were performed, before 2019 there was only a hint of TeV emission coming from the Milagrito experiment [117]. The first announcement of a GRB detected in the TeV energy domain arrived from the MAGIC telescopes with the event GRB 190114C [118]. Afterwards, also the H.E.S.S. collaboration announced the detection of two GRBs in the VHE domain:

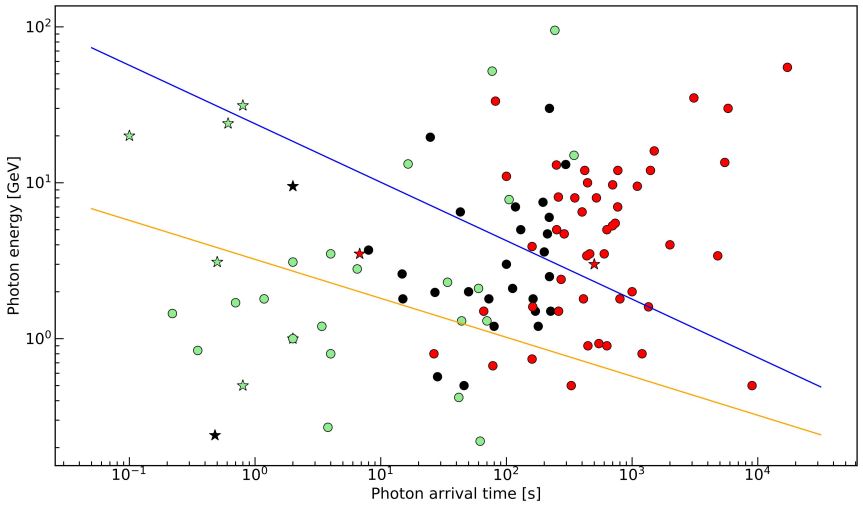

FIGURE 3.9: Maximum photon energy detected by LAT for several GRBs vs arrival time. Both quantities are plotted in the observer frame. Photons detected during the prompt phase are denoted with green symbols, while the ones detected during the afterglow phase are denoted with red symbols. Intermediate cases in which photons arrived near the end of the prompt phase are plotted with black symbols. Short GRBs are marked with stars, long GRBs with dots. The blue and the orange lines are the estimated maximum energy for synchrotron photons in case of homogeneous or wind-like medium. From [113]

GRB 180720B [119] and GRB 190829A [120]. These detections have firmly established the existence of a newly observed emission component in GRBs. The broadband spectrum of GRB 190114C, which collects afterglow data from radio up to TeV energies, shows clearly a *double-hump* structure where the VHE emission is produced via the SSC mechanism [121]. The analysis details and results from this event will be described in Chapter 5. GRB 180720B was detected almost ten hours after the end of the prompt phase in the 0.1-0.44 TeV band. Such late time detection demonstrates that VHE emission can be found also several hours after the trigger, opening to future intriguing possibilities for ground-based Cherenkov observations.

3.3 Theoretical models for GRBs

The origin and the nature of GRBs have been a hot topic for theoretical studies already from the first years after their discovery. Indeed, in parallel with the first observations several theoretical papers were released. Unluckily, it took decades before observational clues could reveal main features of the GRB physics such as the afterglow emission, the collimated outflows or the HE and VHE emission. Therefore, many of the past theoretical models have failed in explaining the GRB physics since they did not have knowledge of several important properties of these events. Nevertheless, this huge effort was certainly crucial in shaping the current GRB theoretical framework. As a result, after several decades of observational and theoretical studies, a general understanding of the origin and the nature of GRBs was reached, even though many details are still unclear. In this section, I will present the most supported models for GRB progenitors (Section 3.3.1), the so-called *fireball* model

(Section 3.3.2), the jet effect (Section 3.3.4) and the models developed to explain the HE and VHE emission component (Section 3.3.5).

3.3.1 Progenitors of GRBs

The sudden and powerful explosions that are named GRBs are caused by astrophysical objects, the **progenitors**. We can infer possible GRB progenitors based on observational evidence or theoretical modelling. The fundamental observational conditions that a candidate progenitor must fulfill are the following:

- it must release a huge amount of energy (generally in the range 10^{49} - 10^{53} erg);
- the emitted radiation should exhibit variability in time scale δt of the order of milliseconds.

Therefore, these features point towards a huge catastrophic event which leaves behind a stellar-size compact object, the so-called *central engine*. Multiwavelength GRB data have led to the identification of two progenitor systems: the death of **massive stars** and the merger of a **compact binary system**. These two categories are thought to explain respectively long and short GRBs. Several observational pieces of evidence lead to believe that the death of **massive stars** can cause long GRBs. We can summarize them as:

- some long GRBs are associated with supernovae of type Ib/c;
- most host galaxies have been identified as star-forming irregular galaxies.

These features usually describe a core-collapsing massive star. The most promising star candidate is a *Wolf-Rayet* (WR) star [122]. The WR stars are indeed evolved, massive stars with mass M > $20M_{\odot}$ at birth which lose their outer envelope by means of a strong stellar wind. Therefore, the WR stars can lose both the hydrogen and helium envelopes prior to the explosion. This may explain why the supernovae associated with long GRBs do not have hydrogen and helium lines in their spectra. The theoretical model which explains the generation of a long GRB in such environment is called *collapsar* model [123]. To power the relativistic jet, one critical requirement of this model is a high angular momentum at the stellar core. A credible picture [124, 125] to obtain and sustain a rapidly rotating stellar core at the end of a star's life suggests that the progenitor stars are rapidly rotating already at birth. In such condition, the hydrogen and helium envelopes are mixed from the main-sequence phase. These stars burn this mixed envelope on the main sequence and evolve directly to WR stars skipping the red giant phase. This scenario requires a low metallicity [126] that favors the presence of a rapidly rotating core. In conclusion, the *collapsar* model can be summarized as follows: a rapidly rotating star (probably a WR star) collapses into a black hole generating an accretion disk from which, via neutrino-anti neutrino annihilation jets can be launched in opposite directions.
Besides, the WR stars, there have been several other objects which have been proposed as candidate progenitors of long GRBs, e.g. supramassive NSs [127], merger of helium star and BH or NS [128, 129] or pulsars [130].
The preferred model used to explain short GRBs involves the merger of a **compact binary system** including NSs or BHs. Before 2017, observational evidences were not as strong as in the case of long GRBs. The main clues were [131]:

- a fraction of short GRBs is found in elliptical or early-type galaxies with little star formation;

- many short GRBs have a large offset from the center of their candidate host galaxies. Some short GRBs are even "hostless", i.e. no candidate host is found at the afterglow location;
- constraining upper limits for an associated SN have been placed in case of nearby short GRBs.

Such features point towards a different environment with respect to the one observed for long GRBs. The low star formation rate of some host galaxies suggests that no massive stars are involved. The large offsets or the absence of credible host galaxies led to believe that the progenitor could have been "kicked" out of the galaxy or that the GRB is very far away so that its host galaxy is not easy to identify. The most credible model indicated that short GRBs can be caused by NS-NS or NS-BH mergers. The NS-NS merger was definitely confirmed as progenitor of short GRBs (or at least of one class of short GRBs) with the associated GW-GRB event detection made on 17^{th} August 2017. The general picture of such merger events (NS-NS or NS-BH) states, as in the collapsar model, the formation of a BH surrounded by a dense disk or a torus. The jets can be then powered thanks to the accretion of the torus material into the BH. In this case, the magnetic mechanism is preferred with respect to the neutrino-anti neutrino annihilation. From [132] in the former mechanism a broad outflow with a half-opening angle $\sim 30^{\circ}$ may be launched. The neutrino-anti neutrino annihilation will instead require small collimation angles (32.82 deg^2) to account for an isotropic energy of 10^{52} erg. In some conditions, simulations have shown that different objects than a BH can be generated from the merger: in NS-NS systems a supra-massive NS or even a stable NS can be produced if the masses of the two NSs are small enough [133, 134]. In NS-BH systems when the mass ratio $M_{NS}/M_{BH} < 0.1$ the NS is completely swallowed by the BH without making a GRB since the tidally disrupted NS is within the BH event horizon [135].
Before merging, the tidally distorted NSs or a neutrino-driven wind from the accretion disk can eject dynamically some material. This neutron-rich ejected material, thanks to the rapid neutron capture process, can produce rare heavy elements like gold and platinum. Moreover, the radioactive decay of these unstable nuclei can also power a near-isotropic supernova-like signal in the optical/IR band. This signal is also known as "*macronova*" or "*kilonova*". An optical/IR transient with a blue [136, 137] and a red [138, 139] component was associated to the GW event GW170817. The general behaviour was found to be consistent with a macronova/kilonova origin [140, 141].

3.3.2 The fireball model

The energy released during the progenitor explosion undergoes several processes before being observed on Earth as radiation. A general theoretical picture on the GRB jet evolution can be built starting from the observational evidences. As mentioned before, GRBs release a huge amount of energy, of the order of 10^{52} - 10^{53} erg with a variability time scale δt of the order of ~ 10 ms. This implies that the emitting region $R < c\delta t \sim 3000$ km. Such a huge amount of energy constrained in a source of few kilometers gives rise to a so-called **fireball** of $e^{\pm}$, γ-rays and possibly baryons. In this environment the γ-rays cannot escape and they are lost due to the pair production mechanism. Indeed, considering the pair production optical depth

$\tau_{\gamma\gamma}$ estimated for a GRB with observed flux F at a distance d and redshift z is:

$$\tau_{\gamma\gamma} \simeq \frac{d^2 F \sigma_T f}{R^2 \epsilon_\gamma (1+z)} >> 1 \tag{3.5}$$

where f is the fraction of the emitted energy above the pair threshold $\epsilon_\gamma \gtrsim m_e c^2$. Therefore, high energy photons cannot escape from the source and should not have been observed. This is clearly in contrast with the observed GRB non-thermal spectrum. To overcome this so-called *compactness problem* and explain the observed GRB emission, the relativistic motion must be introduced. Indeed, considering the GRB outflow moving relativistically with a Lorentz factor Γ the main effects are:

- the size of the emission region R increases of a factor Γ^2;
- the observed photons are blueshifted with respect to the ones in the outflow frame.

As a result, the correct equation to calculate the relativistic optical depth is [142]:

$$\tau_{\gamma\gamma} = \frac{11}{180} \frac{\sigma_T d^2 (m_e c^2)^{-\alpha+1} F}{c^2 \delta t (\alpha - 1)} \left(\frac{E_{max}}{m_e c^2} \right)^{\alpha-1} \Gamma^{-(2\alpha+2)} (1+z)^{-(2\alpha+2)} \tag{3.6}$$

where α is the spectral index of the γ-ray spectrum and E_{max} is the maximal photon energy. The requirement that $\tau_{\gamma\gamma} < 1$ leads to the condition $\Gamma \gtrsim 100$.

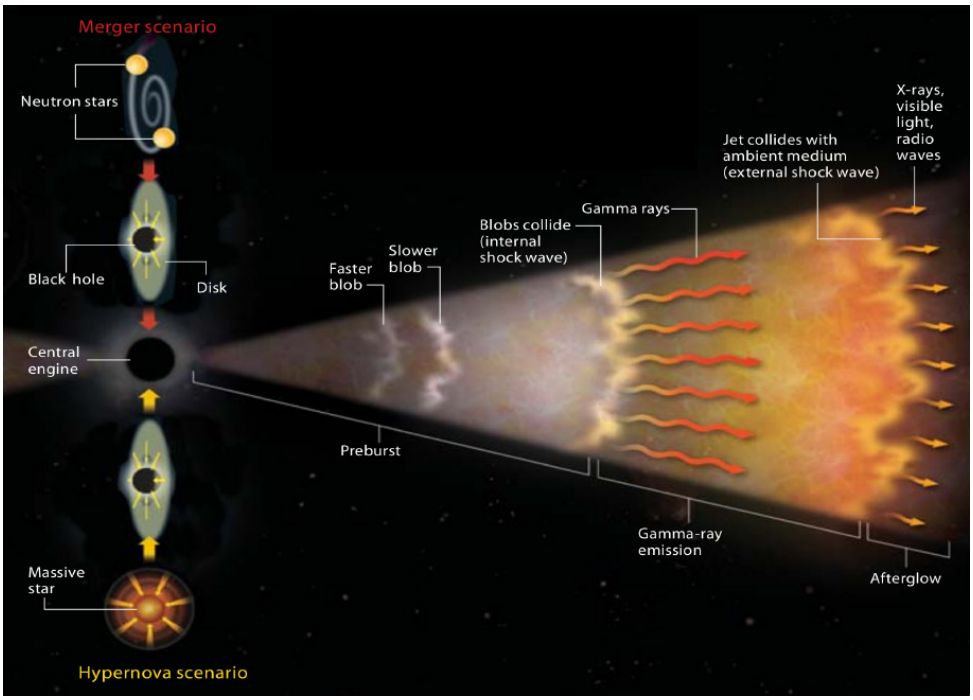

FIGURE 3.10: An artist's view illustrating the various steps of the basic standard model with the internal and external forward shocks and the various radiations emitted. On the left are indicated also the two progenitors which lead to the formation of the central engine. From [143]

Therefore, the GRB fireball propagates relativistically towards the Earth. Its *dynamical evolution* follows different phases and depends on the initial condition at the central engine. Assuming the initial energy of the fireball E_0 and the baryon loading

M_0, the energy-to-mass ratio is defined as $\eta = E_0/M_0c^2 \gg 1$. In the "initial" radius R_0, the position from which the fireball starts to expand, particles are in equilibrium almost at rest, with a mean Lorentz factor $\gamma \sim \eta$. The presence of a small amount of baryons in the fireball is crucial to explain the observed non-thermal spectrum. Indeed, when the fireball expands and cools down, the temperature decreases and the electrons and positrons start to annihilate. As a result, the fireball loses its initial equilibrium and it becomes transparent. Therefore, the radiation can escape and results in a thermal spectrum, in contrast with observations. Adding a small amount of baryons in the fireball content prevents this radiation to escape since they can carry the bulk of the fireball energy, transforming the initial radiative energy into kinetic energy. When the fireball becomes transparent, the baryons hold most of the energy and the observed spectrum is non-thermal. The dynamical evolution of the fireball includes three phases: *acceleration*, *coasting* and *deceleration*.
In the *acceleration* phase, the fireball begins to expand adiabatically with the internal thermal energy converted into kinetic energy. Therefore E_0 is constant and the temperature of the fireball in the rest frame $T' \propto R^{-1}$ where R is the fireball radius. Since the internal energy is still the dominant component, $E_0 \propto \Gamma T' \sim const$. As a result, the Lorentz bulk factor $\Gamma \propto R$ increases linearly with the fireball radius in the acceleration phase [144]. This relation holds until Γ reaches a maximum value $\Gamma_{max} \sim \eta$. The corresponding radius is called the *saturation* radius $R_{sat} = \eta R_0$ which marks the end of the *acceleration* phase and the onset of the *coasting* phase.
During the *coasting* phase the fireball propagates with a constant Lorentz bulk factor. This phase lasts until the so-called *deceleration* radius R_{dec} is reached. For $R > R_{dec}$ the fireball starts to decelerate due to its interaction with the surrounding medium which during the coasting phase was negligible. During the *coasting* and the *deceleration* phases, shocks occur. The basic assumption is that outflows are likely to generate **shocks** that reconvert the bulk kinetic energy of the flow into internal energy of non-thermal particles and then radiation. In this model two types of shocks are expected (Figure 3.10):

- **internal shocks** due to interactions between shells with different Lorentz factor sequentially ejected by the central engine. They are expected to occur during the coasting phase and they are linked with the prompt emission phase since they can explain its fast time variability [145];
- **external shocks** due to the interaction between the fireball blastwave and the circumburst ambient medium. They are usually invoked to explain the multi-wavelength afterglow radiation [146].

The *internal* shocks are so-called since the flow is interacting with itself. Such phenomena are naturally expected when dealing with an erratic central engine that may launch an unsteady ejecta. When this happens, a faster shell can easily reach a slower shell emitted at earlier times. From this collision, the emission of a highly variable non-thermal radiation occurs. Nevertheless, internal shocks are expected to be quite inefficient in converting bulk kinetic energy into radiative one. The efficiency η is typically $\lesssim 20\%$ [147]. Therefore, a large part of the blastwave energy survives and is involved in the following *external* shocks. At this point, thanks to the collision between shells, the blastwave can be seen as a unique shell propagating into the external medium. At first, the interstellar medium (ISM) has no influence on the expanding shell. As the shell propagates, it cools and drives a shock into the ISM. While the shock radius R increases, more ISM matter is shocked and the shell is progressively influenced by it. This influence becomes significant when the energy of the "shocked" ISM becomes comparable to the initial energy of the fireball.

Therefore, the deceleration phase begins and the fireball starts reconverting its bulk energy into radiation. This describes the formation of the so-called *external forward* shock component. At early times, the interaction can also give rise to a *reverse* shock component propagating into the jet itself and crossing the jet in a finite time. Here a qualitative description of the **internal-external shock** scenario has been given. The particle acceleration mechanism involved in the shocks, the dynamical evolution of the fireball as well as the radiation mechanism involved in the afterglow phase will be treated in detail in Section 3.4.4.
The *fireball* model and the *internal-external shock* scenario here described are one of the most credible picture developed to explain the GRB emission. There are anyway several other models where the GRB observed radiation is explained with various forms of energy or different mechanisms than shocks. In particular, the origin and the radiation mechanisms involved in the prompt emission are still quite under debate. Several so-called *magnetic* models (see for example [148]) invokes a Poynting-flux dominated outflow. In these models the prompt emission is explained through magnetic reconnection in an optically thin region. A category of models, the *photosphere* models (see for example [149, 150]) claim for a *quasi-thermal Comptonized* emission to account for, at least, part of the prompt spectra.

3.3.3 Relativistic and cosmological effects

Describing the dynamics involved in the GRB means dealing with a cosmological object that produces an outflow moving at ultra-relativistic velocities. Therefore, a correct treatment of this system needs to take into account the *Lorentz transformations*, the *beaming effects* and the *cosmological expansion*. As a result, some correction factors must be introduced in the description of the evolution of the outflow considering the reference system at rest with the outflow (the so-called *comoving frame*), the frame of the progenitor (the so-called *rest frame*) and the frame of the observer on Earth (the so-called *observer frame*). For convention, quantities expressed in the comoving frame will be primed while in the rest frame will be left unprimed. Quantities in the observer frame will be labeled with "obs". The transformations between these reference systems can be derived from relativistic and cosmological considerations.

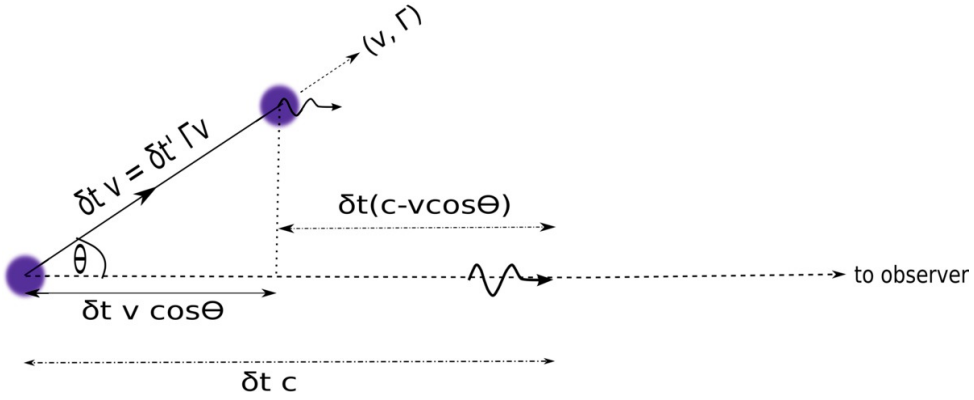

FIGURE 3.11: Scheme of the transformation of a pulse duration from the comoving to the observer frame. The following calculation is expressed in equation 3.7. From [151]

Consider a source moving with speed v, corresponding Lorentz factor Γ and at an angle θ with respect to the line of sight to an observer. Two photons are emitted in the direction of the observer in a time interval $\delta t'$ in the comoving frame. Such time

interval in the rest frame is $\Gamma\delta t'$ due to relativistic time dilation and in the observer frame can be expressed as (see Figure 3.11):

$$\delta t_{obs} = \delta t' \Gamma(1 - \beta\cos\theta) = \frac{\delta t'}{\mathcal{D}} \tag{3.7}$$

where $\beta = v/c$ and $\mathcal{D} = [\Gamma(1-\beta\cos\theta)]^{-1}$ is the so-called *Doppler factor*. For a source moving along the line of sight of the observer ($\theta = 0$) with $\beta \approx 1$, we have $D \approx \Gamma(1+\beta) \approx 2\Gamma$. Using similar arguments, also the frequency in the comoving frame ν' is affected by the standard Lorentz transformations. In this case, the Doppler shift formula is expressed as:

$$\nu = \frac{\nu'}{\Gamma(1-\beta\cos\theta)} = \nu'\mathcal{D} \tag{3.8}$$

Other relativistic effects which must be considered when dealing with the emission from relativistic particles are the *aberration* and the *relativistic beaming*. When a photon is emitted from a source at an angle θ' with respect to the observer line of sight in the source comoving frame, the emission angle in the rest frame θ is calculated from:

$$\tan\theta = \frac{\sin\theta'}{\Gamma(\cos\theta' + \beta)} \tag{3.9}$$

Therefore when moving from the comoving to the rest frame the emission angle is different. Considering an isotropic distribution of the emission, half of the total radiation will be then emitted for $\theta' < 90^\circ$. Thus, $\theta' = 90^\circ$ in equation 3.9 gives a $\tan\theta = 1/\Gamma\beta$. For highly relativistic sources like GRBs, $\Gamma \gg 1$ hence $\beta \sim 1$ and we can approximate for small angles $\tan\theta \approx \theta$. As a result, the observer sees the emission beamed in a forward cone with half-opening angle $\theta \approx 1/\Gamma$. Applying this approximation to the Doppler shift factor $\mathcal{D}$, it results $\mathcal{D} \approx \Gamma(1-\beta^2) \approx \Gamma$ since $\cos\theta \approx \beta$.
Finally, also a correction factor for the *cosmological expansion* must be introduced when considering quantities in the observer frame. The factor $1+z$ where z is the cosmological redshift, accounts for this correction. As a result, a time interval in the rest frame δt is seen in the observer frame as:

$$\delta t_{obs} = (1+z)\delta t \tag{3.10}$$

and similarly for the frequency:

$$\nu_{obs} = \frac{\nu}{1+z} \tag{3.11}$$

3.3.4 Non-spherical relativistic ejecta: jets

Several considerations, both theoretical and observational, suggest that GRB outflows are collimated into **narrow jets**. Indeed, there are some GRBs with a γ-ray isotropic energy $E_{iso} \sim 10^{55}$ erg, which is higher than the rest mass energy of the Sun ($\sim 2 \times 10^{54}$ erg). Since stellar mass progenitors are involved in the GRB explosions it is very difficult to explain such amount of energy released in γ-rays. This condition is relaxed if we consider that GRBs radiate into a narrow jet. Introducing a beaming correction reduces the total energy budget of a factor $f_b = 1 - \cos\theta_j$ with θ_j being the jet opening angle. As a result, the corrected collimated energy E_γ can be written

as:

$$E_\gamma = (1 - \cos\theta_j) E_{iso} \tag{3.12}$$

where the energy budget is reduced by one to three orders of magnitude for $2^\circ \lesssim \theta_j \lesssim 25^\circ$.

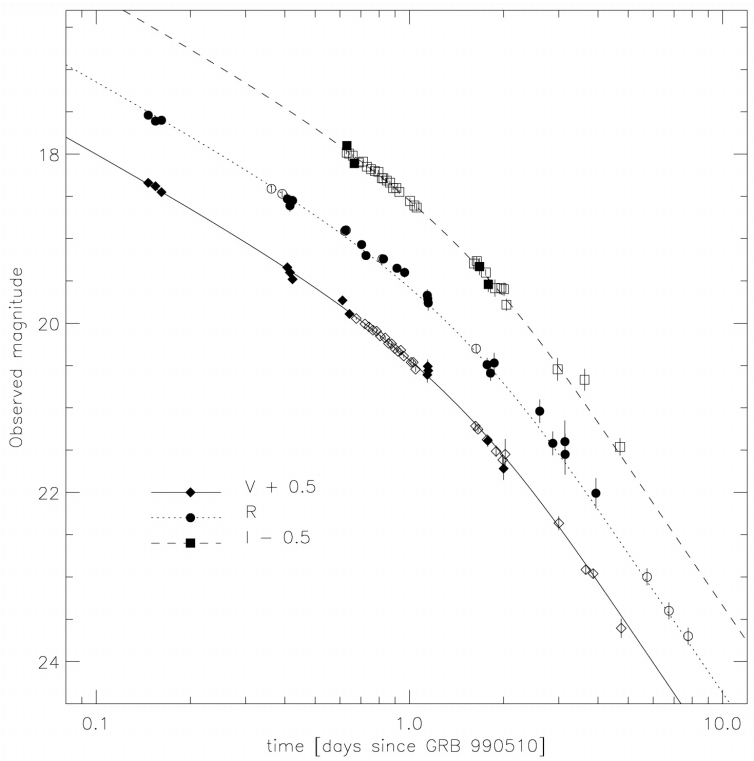

FIGURE 3.12: The jet break seen in the optical lightcurves of GRB 990510 in the V, R and I bands. From [152].

In addition, several afterglow light curves exhibit a steeping at late times which is independent from the observational frequency (see Figure 3.12). Therefore, it can be explained as a feature of *geometrical* origin. This is the so-called **jet break**. It can be described as follows: considering a conical jet with an opening angle θ_j lying in the line of sight of the observer, for relativistic beaming only the emission inside a $1/\Gamma$ cone contributes to the observed flux. Therefore, as the blastwave decelerates and so Γ decreases, a break in the light curve will appear when $1/\Gamma > \theta_j$. The light curve steepening arises in principle as the sum of two effects:

- the **edge effect** which arises when $\theta_j = 1/\Gamma$, therefore when the jet break happens. Indeed, for $\theta_j \ll 1/\Gamma$ an observer has no knowledge of the jet collimation since the radiation within the $1/\Gamma$ cone around the line of sight dominates. The isotropic and the collimated jets cases cannot be distinguished. When $\theta_j > 1/\Gamma$ the observer sees a decrease in the flux with respect to the isotropic fireball case, and the light curve starts to fall off more steeply than the previous phase. The edge effect is a pure geometrical and relativistic effect which does not affect the blastwave dynamics. It just introduces for $\theta_j > 1/\Gamma$ an additional factor of $\theta_j^2/(1/\Gamma^2)$ which reduces the observed flux with respect to the isotropic fireball case;

- the **sideways expansion** of the jet with time [153]. This effect further steepens the light curve decay index in the post jet-break phase more than the edge effect

prediction. The resulting decay slope is $\propto t^{-p}$ with $p \sim 2.2$ is the electron spectral index. Nevertheless, numerical simulations have shown that sideways expansion is not significant for $\Gamma < 2$ [154]. On the other hand, the post-break light curves obtained from numerical simulations show a steeper decay slope than the simple analytical result derived from the edge effect only. Therefore, the t^{-p} behaviour seems to be a reasonable approximation [154].

3.3.5 High and very high energy emission models for GRBs

Several theoretical models have been developed to explain the HE and VHE radiation component from GRBs. This large variety of models include leptons and/or hadrons accelerated in shocks with different environmental conditions. Observations from AGILE, LAT and in the last years from MAGIC and H.E.S.S. have helped in understanding which could be the most credible scenarios. Indeed, the current results are difficult to explain only with a single theory. The plausible picture may need to invoke different origins for the *early* emission phase and the *late time* long lasting component. The former one, which appears to be correlated with the prompt component, attributes the emission to processes of **internal origin** occurring in the jet. The latter one, related to the afterglow emission, is thought to have an **external origin** that is to be generated from external shocks.
The *early time* emission component origin is quite under discussions. There is general agreement regarding its internal origin, since it is able to explain the fast time variability, but no firm conclusion on which could be the responsible radiation mechanisms. This is also due to the fact that, as described in Section 3.2.3, a variety of contradictory different behaviours has been observed. The GRB prompt emission in the keV-MeV domain is often attributed to synchrotron emission from electrons accelerated in internal shocks or magnetic reconnection events. Despite several observational features challenge this model, the synchrotron mechanism is still the most credible radiation process for prompt emission (see for example [155]). In GRBs in which the HE component cannot be explained as the natural continuation of the keV-MeV emission but as an additional different component, additional radiation mechanisms must be introduced. The SSC mechanism is one of the most popular explanations for these cases. It is anyway not clear if SSC can reproduce the delayed onset of the HE component [156] and the low flux excess sometimes observed at energies below 50 keV [157].
Also hadronic models have been invoked [158, 159]. Indeed, synchrotron emission from protons and photohadronic interactions can explain the low energy excess observed. The prompt spectrum is described as generated by synchrotron emission and IC from secondary $e^{\pm}$ pairs [160]. Moreover, the HE temporal delay naturally arises as the time needed to accelerate protons to high energies. On the other hand, the main drawback of hadronic models is that they require a high energy budget which is hard to integrate with the observations.
The *late time* component is thought to be generated from the interaction between the decelerating fireball and the circumburst external medium. The usual behaviour observed in the GRBs detected by LAT, a simple power law decay with no temporal variability, is the same observed in the afterglow emission at lower frequencies. Therefore, the entire broadband emission can be explained by a unique radiation mechanism. The most plausible one is the synchrotron radiation from electrons energized at the external shock, with a possible contribution from SSC accounting for the HE and VHE component [161]. Indeed, broadband modeling of some GRBs detected by LAT [162] have shown that the synchrotron emission from electrons is

able to account for GeV data. On the other hand, in several cases [163] X-ray and GeV fluxes led to contradictory estimates of the blastwave total energy and of the prompt efficiency. This inconsistency can be solved introducing the effect of the SSC cooling which modifies the high-energy part of the synchrotron spectrum. The SSC mechanism is also able to explain the late-time LAT emission as well as the origin of the photons which exceed the synchrotron maximum energy [113]. The firm confirmation of the existence of the SSC component was given with the VHE emission detected by MAGIC and H.E.S.S. [164, 165]. In particular, the broadband afterglow modeling of GRB 190114C detected by MAGIC was successfully interpreted as synchrotron plus SSC emission from electrons accelerated by external shocks.
Other models developed to explain the HE and VHE emission component from GRBs within the external forward shock scenario were the hadronic models (see for example [166]). Indeed, a mixture of proton synchrotron and electron synchrotron and SSC from secondary pairs is able to reproduce the emission of γ-rays in the afterglow. On the other hand, the energy budget requirement is still very hard to explain, as will be also shown later in Chapter 4.

3.4 The Afterglow radiation

The *afterglow* radiation phase, as explained in the previous section, is interpreted as the emission resulting from the interaction between the decelerating relativistic fireball and the external medium. Its time evolution is usually well described with simple decaying power laws in contrast with the temporal variability and the various spectral features found in the prompt spectra. As a result, the afterglow models include "generic" physical assumptions which are independent from the progenitors, the central engine and the jet composition. In this section I will outline the physics involved in the **afterglow forward shock scenario**, namely the dynamical evolution of the blastwave in a self-similar regime (Section 3.4.1), the Fermi acceleration mechanism (Section 3.4.2), the assumptions on the accelerated particle distribution (Section 3.4.3) and the radiation mechanisms involved (Section 3.4.4). I will introduce these topics in detail since they have been the fundamental theoretical ingredients I used to develop a numerical code for the simulation of GRB afterglow emission in the external forward shock scenario (see Chapter 4).

3.4.1 The blastwave dynamics

The description of the dynamical evolution of the blastwave consists in following its bulk motion, described by the bulk Lorentz factor Γ and how it evolves with the radius R while encountering a circumburst interstellar material of density $n(R)$. After an initial acceleration phase, the blastwave propagates freely with a constant Lorentz factor Γ_0 (coasting phase). In this phase the effect of the swept-up shocked interstellar material is negligible. This changes when the internal energy of the shocked swept-up matter approaches the initial energy (i.e. $\Gamma_0 m(R)c^2 \sim E_0$, where $m(R)$ is the swept-up shocked interstellar mass at a radius R). This is the beginning of the deceleration phase, when the blastwave and the shocked material start to decelerate, converting their kinetic energy into random internal energy that will be partially radiated away.
A very famous approach to the relativistic blastwave dynamics in the deceleration phase is the one presented by Blandford & McKee in 1976 [167] (BM76 hereafter). Here, a self-similar solution of the evolution of relativistic blastwave, i.e. a solution

which does not depend on initial values of Γ and R, is presented. The solution is obtained assuming an adiabatic evolution of the shock wave into a medium with mass density $\rho(R)$ and solving the continuity equations to obtain the radial profile of the hydrodynamic quantities. The adiabatic assumption can be considered reasonable since it is believed that only a small fraction (10% or even less) of the energy dissipated in external shocks will be given to particles and therefore radiated away. The circumburst medium mass density profile is given by:

$$\rho(R) = m_p n(R) = m_p A R^{-s} \tag{3.13}$$

where m_p is the proton mass, R is the distance of the shock from the centre of the explosion, A and s describe respectively the normalization and the radial profile parameter of the medium particle density $n(R)$. The two common cases considered for the circumburst medium are:

- *homogeneous medium* (or ISM) with $s = 0$ and $A = A_0$ measured in cm^{-3};
- *stellar wind medium* with $s = 2$ and $A = 3.0 \times 10^{35} A_*$ which is the typical value for a WR star coming from the equation [168]:

$$A = \frac{1}{4\pi} \frac{\dot{M}}{m_p v} = 3.0 \times 10^{35} A_* \quad cm^{-1} \tag{3.14}$$

  where A_* is a dimensionless normalization factor, $\dot{M}$ is the mass loss rate of a massive star ejecting a wind at a constant speed v. The factor 3.0×10^{35} is calculated assuming $\dot{M} = 10^{-5}\ M_\odot/yr$ and $v = 10^3\ km/s$.

Under these assumptions, the blastwave internal energy E_0 in BM76 is given by:

$$E_0 = \frac{12 - 4s}{17 - 4s} \Gamma^2 mc^2 = \frac{16\pi A m_p c^2}{17 - 4s} R^{3-s} \Gamma^2 \tag{3.15}$$

Since for adiabatic assumption $E_0 = \text{const}$, it follows:

$$\Gamma \propto R^{-\frac{3-s}{2}} \tag{3.16}$$

Therefore for the ISM case $\Gamma \propto R^{-3/2}$ and for the stellar wind case $\Gamma \propto R^{-1/2}$. The BM76 solution gives a reliable description of the blastwave dynamics only during the ultrarelativistic deceleration phase and does not describe the coasting and the non-relativistic phase ($\Gamma \sim 1$). From the relation $\Gamma_0 m(R) c^2 \sim E_0$ it is possible to estimate a value of the deceleration radius R_{dec} after which the BM76 solution holds:

$$R_{dec} \simeq \left(\frac{3 - s}{4\pi} \frac{E_0}{m_p c^2 A \Gamma_0^2} \right)^{1/(3-s)} \tag{3.17}$$

where:

$$m(R) = \int_0^R 4\pi \rho(R) R^2 dR \tag{3.18}$$

For a complete description of the evolution of a relativistic blastwave a more general approach should be taken into account. I will now briefly present the one proposed in [169]. This model is based on the *homogeneous shell approximation* where the fluid hydrodynamical properties behind the shock are assumed to be uniform. It is able to describe the coasting and the non-relativistic phases and it reproduces the BM76 solution during the deceleration phase. The radial evolution of the bulk Lorentz

factor Γ is directly derived from the energy conservation equation. Considering the energy density ε of the blastwave in the rest frame:

$$\varepsilon = \Gamma^2(\rho' c^2 + u' + p') - p' = \Gamma^2 \rho' c^2 + (\hat{\gamma}\Gamma^2 - \hat{\gamma} + 1)u' \tag{3.19}$$

where ρ' is the comoving mass density, u' is the comoving internal energy density and $p' = (\hat{\gamma} - 1)u'$ is the corresponding comoving pressure and $\hat{\gamma}$ is the adiabatic index of the shocked plasma. As a result, the total energy in the shocked medium region of comoving volume V' is:

$$E_{sh} = \varepsilon V = \varepsilon \frac{V'}{\Gamma} = \Gamma m c^2 + \Gamma_{eff} U' \tag{3.20}$$

where $\rho'(R)V' = m(R)$ is the total swept-up mass of the external medium at the radius R, $U' = u'V'$ is the internal energy in the comoving frame and $\Gamma_{eff} = \frac{\hat{\gamma}\Gamma^2 - \hat{\gamma} + 1}{\Gamma}$ is defined to properly describe the Lorentz transformation of the internal energy. Then, adding the energetic contribution of the "*cold*" ejecta (i.e. without internal energy) E_{eje} of mass M_0:

$$E_{eje} = \Gamma M_0 c^2 \tag{3.21}$$

The total energy of the blastwave E_{bw} is:

$$E_{bw} = \Gamma(M_0 + m)c^2 + \Gamma_{eff} U' \tag{3.22}$$

Thus, at each step dR the system will acquire a dmc^2 rest-mass energy from the circumburst medium and will lose via radiation a portion $dU_{rad} = \Gamma_{eff} dU'_{rad}$. The energy conservation equation in the rest frame is then:

$$dE_{bw} = d[\Gamma(M_0 + m)c^2 + \Gamma_{eff} U'] = dmc^2 + \Gamma_{eff} dU'_{rad} \tag{3.23}$$

The acquired comoving internal energy dU' will go into shock heating dU'_{sh}, adiabatic losses dU'_{ad} and radiative losses dU'_{rad}:

$$dU' = dU'_{sh} + dU'_{ad} + dU'_{rad} \tag{3.24}$$

with $dU'_{sh} = (\Gamma - 1)dmc^2$. As a result, the equation of the evolution of the bulk Lorentz factor Γ can be derived:

$$\frac{d\Gamma}{dR} = -\frac{(\Gamma_{eff} + 1)(\Gamma - 1)c^2 \frac{dm}{dR} + \Gamma_{eff} \frac{dU'_{ad}}{dR}}{(M_0 + m)c^2 + U' \frac{d\Gamma_{eff}}{d\Gamma}} \tag{3.25}$$

For an adiabatic expansion ($dU'_{ad} = 0$) with $\Gamma_{eff} \approx \Gamma \gg 1$ and $dm/dR = 4\pi\rho(R)R^2$ the BM76 relation $\Gamma \propto R^{-\frac{3-s}{2}}$ is resumed.

3.4.2 The Fermi acceleration mechanism

The bulk energy of the decelerating blastwave is gradually converted into random kinetic energy produced at a shock from the interaction with the circumburst material. As a result, the particles will be accelerated. The most promising acceleration mechanism in shocks is the so-called **first-order Fermi acceleration mechanism**. In this picture (see Figure 3.13) the shock system can be seen as composed by an *upstream region* which includes the fluid preceding the shock front and a *downstream*

region which includes the fluid behind the shock front. The particles will gain energy by crossing multiple times the shock front from either region. Multiple crossing of the shock front are possible thanks to strong magnetic fields near the shock front which allow particles to gyrate around the field lines. This interaction can be seen as a diffusion process where the fluid particles scatter with inhomogeneities of the magnetic field and cross the shock front. The energy gained by particles after crossing the shock in both directions is:

$$\langle \frac{\Delta E}{E} \rangle \simeq \frac{4}{3}\beta \tag{3.26}$$

where $\beta = v/c$ and v is the propagation velocity of the shock wave in a reference system where the upstream fluid is stationary.

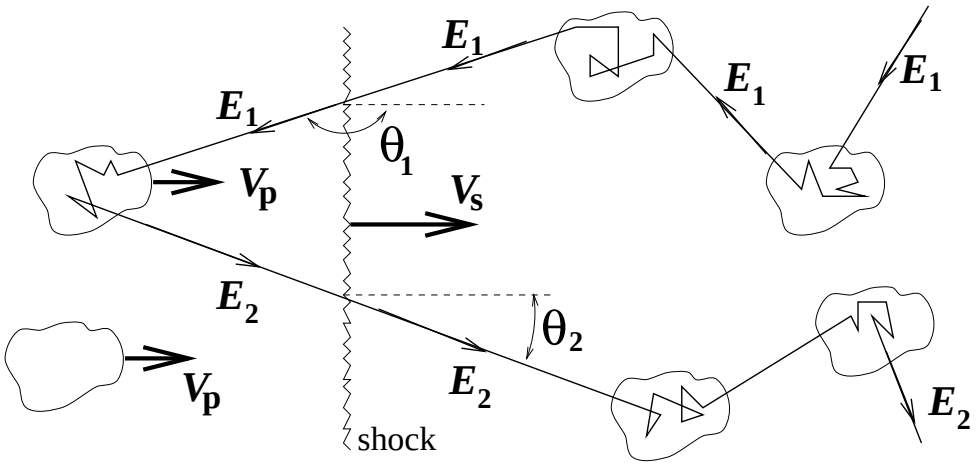

FIGURE 3.13: Graphical sketch of the first-order Fermi acceleration mechanism. V_s is the velocity of the shock, V_p is the velocity of the particles reaching the shock. From [170].

Once a round-trip from the upstream and downstream region is completed, particles usually are not able to leave the acceleration region and they can be further accelerated. Let us consider a system with initially N_0 particles with energy E_0 and P is the probability for the particles to remain in the acceleration region after one round-trip. After k round-trips the number of particles will be $N = N_0 P^k$ and they have a typical energy of $E = (1 + \frac{4}{3}\beta)^k$. Therefore, equating for k:

$$k = \frac{\ln(E/E_0)}{\ln(1+\frac{4}{3}\beta)} = \frac{\ln(N/N_0)}{\ln P} \tag{3.27}$$

Then, it is possible to derive:

$$\frac{N}{N_0} = \left(\frac{E}{E_0}\right)^{(\ln P/\ln(1+\frac{4}{3}\beta))} \tag{3.28}$$

Or, in terms of particle energy distribution $N(E) = dN/dE$:

$$N(E)dE = KE^{-p}dE \tag{3.29}$$

with $p = 1 - (\ln P/\ln(1+\frac{4}{3}\beta))$ is the spectral index of the particle energy distribution. Therefore, this implies that particles through the Fermi acceleration mechanism will be accelerated into a power-law energy distribution.

3.4.3 Shocks microphysics

From Section 3.4.1 the acquired random kinetic energy for shock heating dU'_{sh} can be written as:

$$dU'_{sh} = (\Gamma - 1)dmc^2 = (\Gamma - 1)4\pi R^2 n' m_p c^2 dR \tag{3.30}$$

considering that $dm = 4\pi R^2 \rho'(R)dR$. The number density in the comoving frame n' can be written as:

$$n' = \frac{N'}{V'} = (4\Gamma + 3)n \tag{3.31}$$

where the factor Γ comes from the volume contraction $V' = V/\Gamma$ and the numerical factors derive from the assumption $\hat{\gamma} = 4/3$ valid for a relativistic gas. Then, the comoving internal energy density u' can be written as:

$$u' = \frac{dU'_{sh}}{dV} = (\Gamma - 1)n' m_p c^2 = 4(\Gamma - 1)(\Gamma + \frac{3}{4})n m_p c^2 \tag{3.32}$$

This is the available energy dissipated through the shock. A fraction ϵ_e of this energy will go to the swept-up electrons, a fraction ϵ_p to the swept-up protons and a fraction ϵ_B will be gained by the magnetic field. These parameters (ϵ_e,ϵ_p,ϵ_b) are the *microphysical parameters* which describe the properties of the shock. As a result, it is possible to derive the energy density of each of these components. The magnetic field energy density u'_B can be written, working in cgs unit, as:

$$u'_B = \epsilon_B u' = \epsilon_B 4(\Gamma - 1)(\Gamma + \frac{3}{4})n m_p c^2 = \frac{B^2}{8\pi} \tag{3.33}$$

Then, the magnetic field strength B is:

$$B = \sqrt{32\pi\epsilon_B m_p n}(\Gamma - 1)(\Gamma + \frac{3}{4})c \tag{3.34}$$

For the electrons, assuming a neutral circum-burst medium so that $n = n_p = n_e$:

$$u'_e = \epsilon_e u' = \epsilon_e 4(\Gamma - 1)(\Gamma + \frac{3}{4})n m_p c^2 = \langle\gamma\rangle m_e c^2 4(\Gamma + \frac{3}{4})n_e \tag{3.35}$$

where electrons are assumed to move randomly in the medium with an average Lorentz factor $\langle\gamma\rangle$. It is then possible to derive:

$$\langle\gamma\rangle = \epsilon_e \frac{m_p}{m_e}(\Gamma - 1) \tag{3.36}$$

Electrons in the shock are accelerated through the Fermi mechanism. As a result, their energy distribution can be described by a power law $N(\gamma)d\gamma \propto \gamma^{-p}d\gamma$ for $\gamma \geq \gamma_m$ where γ_m is the minimum Lorentz factor at which electrons can be accelerated. Therefore, it can be derived:

$$\langle\gamma\rangle = \frac{\int_{\gamma_m}^{\gamma_{max}} N(\gamma)\gamma d\gamma}{\int_{\gamma_m}^{\gamma_{max}} N(\gamma)d\gamma} \tag{3.37}$$

So, solving the integrals (for $p \neq 2$ and $p \neq 1$) and equating 3.36 and 3.37, it is possible to derive γ_m as:

$$\gamma_m = \epsilon_e \frac{m_p}{m_e}\frac{p-2}{p-1}(\Gamma - 1) \tag{3.38}$$

In solving the integrals in equation 3.37 it was assumed $\gamma_{max} \gg \gamma_m$. In a more general and complete treatment the maximum energy γ_{max} at which electrons can be accelerated in shocks must be taken into account. Nevertheless, equation 3.38 still holds for $\gamma_{max} \gg \gamma_m$ which is often a reasonable assumption. Without this assumption, solving the integrals in equation 3.37 will lead to:

$$\left[\frac{p-1}{p-2}\frac{\gamma_m^{-p+2}-\gamma_{max}^{-p+2}}{\gamma_m^{-p+1}-\gamma_{max}^{-p+1}}\right] = \epsilon_e \frac{m_p}{m_e}(\Gamma-1) \tag{3.39}$$

where γ_{max} can be calculated as will be described in 3.4.4. This equation cannot be solved analytically for γ_m and therefore a root-finding algorithm is needed to estimate an approximate value of γ_m.
A similar treatment can be done also for protons simply substituting ϵ_e with ϵ_p, m_e with m_p and assuming a power law energy distribution with spectral index q. As a result, the minimum Lorentz factor for protons can be derived as:

$$\gamma_{m_p} = \frac{\epsilon_p}{\xi_p}\frac{q-2}{q-1}(\Gamma-1) \tag{3.40}$$

where the fraction of accelerated protons ξ_p is introduced. This factor is neglected for electrons since it is generally thought to be $\simeq 1$. Similarly solving the equations without assuming that $\gamma_{max_p} \gg \gamma_{m_p}$ lead to:

$$\left[\frac{q-1}{q-2}\frac{\gamma_{m_p}^{-q+2}-\gamma_{max_p}^{-q+2}}{\gamma_{m_p}^{-q+1}-\gamma_{max_p}^{-q+1}}\right] = \frac{\epsilon_p}{\xi_p}(\Gamma-1) \tag{3.41}$$

which is analogous to equation 3.39.

3.4.4 Emission processes

Once particles are accelerated they will react emitting electromagnetic radiation. In the afterglow scenario, where particles are accelerated in external shocks with the presence of strong magnetic fields, the main responsible radiation mechanisms are thought to be the **synchrotron emission** and the **Inverse Compton (IC)** emission of the up-scattered synchrotron photons. Considering the assumptions previously outlined on the blastwave dynamics and on the particle acceleration, it is possible to derive analytical spectra and lightcurves of GRB afterglow emission for different observational frequencies. In this section I will briefly describe the synchrotron and IC radiation mechanisms. Then, the corresponding analytical spectra and lightcurves for GRB afterglows will be presented. Such analytical prescriptions have provided a useful comparison for the results of my numerical code (see Chapter 4).

Synchrotron Radiation

The synchrotron radiation is produced when a relativistic charged particle interacts with a magnetic field. As a result, the particle will be accelerated, moving in spiral trajectories around the magnetic field lines, and it will emit electromagnetic radiation. First, some key features of synchrotron emission will be reviewed following [171] and [172]. The total emitted power P' from a particle with charge q, mass m, velocity v and Lorentz factor γ gyrating in a magnetic field with energy density

$u_B = B^2/8\pi$ and an incident angle α with respect to the field line is:

$$P'(\gamma, \alpha) = 2\sigma_T \left(\frac{m_e}{m}\right)^2 c\gamma^2\beta^2 u'_B \sin^2\alpha \tag{3.42}$$

where σ_T is the Thompson cross section. As it can be seen this is a generic formula valid for every charged particle. Nevertheless $P' \propto 1/m^2$, therefore the synchrotron emission is more efficient for electrons with respect to protons. For convenience, in the following calculation we will consider the synchrotron emission from electrons substituting in the above equation $m = m_e$ but the same conclusions can be derived also for protons simply including the factor $(m_e/m_p)^2$. Therefore, considering an electron and assuming an isotropic distribution and mediating over the pitch angles, the averaged emitted power can be written as:

$$P'(\gamma) = \frac{4}{3}\sigma_T c\gamma^2\beta^2 u'_B \tag{3.43}$$

Considering the non-relativistic case ($\gamma = 1$), the radiation is all emitted at the *gyrofrequency*:

$$\nu'_g = \frac{qB'}{2\pi m_e c} \tag{3.44}$$

which is the corresponding frequency of the charged particle moving perpendicular to the direction of the magnetic field and feeling only the centripetal force and the magnetic Lorentz force. Increasing the electron velocity the aberration and beaming effects start to arise and the emission spreads over a broader frequency range with $\nu'(\gamma) \approx \gamma^2\nu'_g$. As a result, for relativistic electrons $v \sim c$ the spectrum results in a continuum. The power emitted per unit of frequency by a single relativistic electron with pitch angle α is given by:

$$P'_\nu(\gamma, \alpha) = \frac{\sqrt{3}e^3 B' \sin\alpha}{m_e c^2} F\left(\frac{\nu'}{\nu'_c}\right) \tag{3.45}$$

where the characteristic synchrotron frequency ν_c is given by:

$$\nu'_c = \frac{3}{4\pi}\frac{eB' \sin\alpha\gamma^2}{m_e c} \tag{3.46}$$

and $F\left(\frac{\nu'}{\nu'_c}\right)$ is:

$$F\left(\frac{\nu'}{\nu'_c}\right) = \frac{\nu'}{\nu'_c}\int_{\nu'/\nu'_c}^{\infty} K_{5/3}(x)dx \tag{3.47}$$

where $K_{5/3}(x)$ is the modified Bessel function. The shape of this spectrum can be seen in Figure 3.14.
It has a broad maximum centered near the frequency $\nu' \approx \nu'_c$ while it exhibits the following behaviours:

$$P'_\nu(\gamma, \alpha) \propto \begin{cases} \nu'^{1/3} & \nu' \ll \nu'_c \\ \nu'^{1/2} e^{-\nu'/\nu'_c} & \nu' \gg \nu'_c \end{cases} \tag{3.48}$$

Therefore, a sharp exponential cut-off is observed for $\nu' \gg \nu'_c$ which means that very little power is emitted beyond the characteristic synchrotron frequency. For $\nu' \ll \nu'_c$ the spectrum rises as $\propto 1/3$.

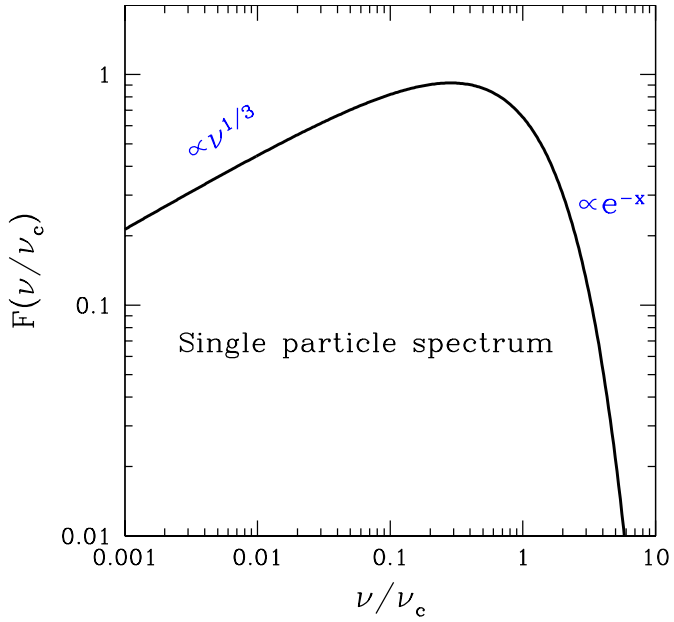

FIGURE 3.14: Synchrotron spectrum emitted by a single relativistic electron. From [173]

Extending these conclusions to a population of electrons $N_e(\gamma)$, a convolution of the single particle power spectrum is needed:

$$P'_\nu = \int P'_\nu(\gamma, \alpha) \frac{dN_e(\gamma)}{d\gamma} d\gamma \tag{3.49}$$

assuming a power law electron distribution $\frac{dN_e(\gamma)}{d\gamma} \propto \gamma^{-\delta}$ with $\gamma_i < \gamma < \gamma_f$ and $\gamma_f \gg \gamma_i$, after some algebra from equation 3.49 the following relation is obtained (Figure 3.15):

$$P'_\nu \propto \nu'^{-\frac{\delta-1}{2}} \quad \text{for } \nu'_i < \nu' < \nu'_f \tag{3.50}$$

where $\nu'_i \equiv \nu'(\gamma = \gamma_i)$ and $\nu'_f \equiv \nu'(\gamma = \gamma_f)$. Therefore, the spectral shape is linked with the shape of the electron energy spectrum δ.
When a relativistic particle radiates, it loses part of its energy. As a result, when the energy lost becomes significant the particle starts to *cool*. It is possible to derive a characteristic *cooling* time scale τ'_{cool} from the ratio between the particle energy and its emitting power. Thus, the **synchrotron cooling time scale** of an electron with energy $E' = \gamma mc^2$ and loss rate $P' = dE'/dt'$ is:

$$\tau'_{cool} = \frac{E'}{|dE'/dt'|} = \frac{6\pi m_e c}{\gamma \sigma_T B'^2} \tag{3.51}$$

valid in the relativistic case, therefore $\beta \sim 1$.
Since $\tau_{cool} \propto \gamma^{-1}$ more energetic particles have shorter cooling time scales. With the same assumptions it is also possible to derive the **cooling Lorentz factor** γ_c of particles which lose most of their energy in a timescale t' as:

$$\gamma_{cool} = \frac{6\pi m_e c}{\sigma_T B'^2 t'} \tag{3.52}$$

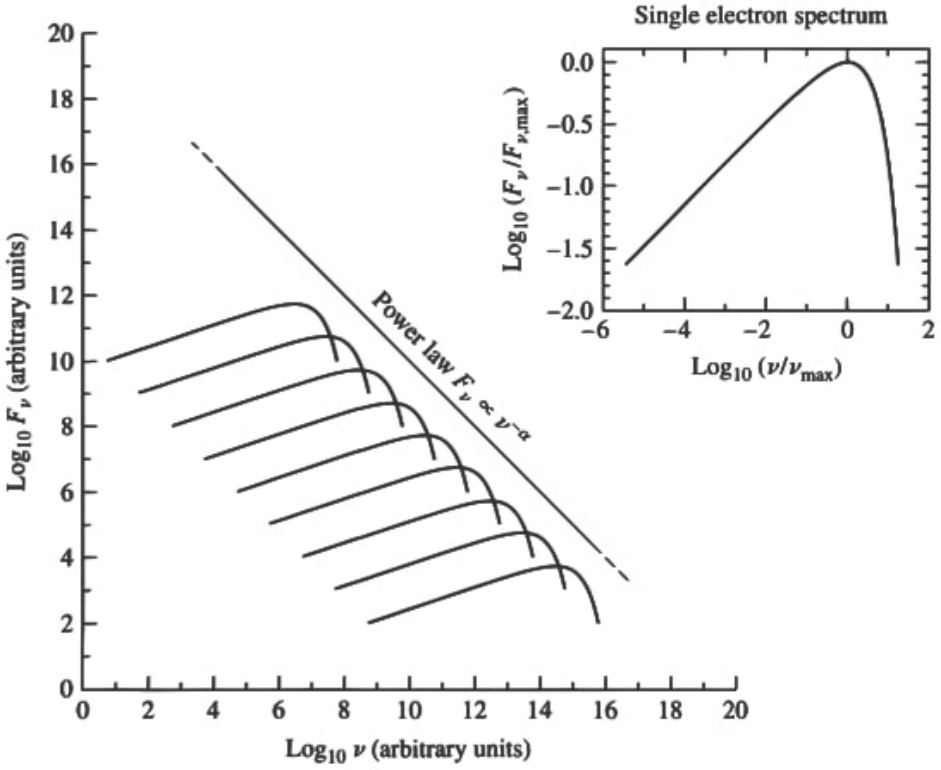

FIGURE 3.15: Synchrotron spectrum emitted by a power law distribution of relativistic electrons. From [174]

assuming that the total emitted power P' is constant with time. This effect will produce a modification in the synchrotron spectrum calculated in equation 3.48. Defining $\nu'_{cool} \equiv \nu'(\gamma = \gamma_{cool})$ as the corresponding frequency calculated for an electron with a Lorentz factor equal to γ_{cool}, an additional regime in the synchrotron spectrum will arise, following the relation:

$$P'_\nu \propto \nu'^{-1/2} \quad \text{for } \nu'_{cool} < \nu' < \nu'_c \tag{3.53}$$

As the electrons are emitting photons, there is also the possibility that they re-absorb low energy photons before they escape from the source region. This is the so-called **synchrotron self-absorption (SSA)** mechanism. Since it is an absorption process, the SSA is characterized by its absorption coefficient α_ν [171]:

$$\alpha_\nu = -\frac{1}{8\pi\nu'^2 m_e} \int d\gamma P'(\gamma, \nu') \gamma^2 \frac{\partial}{\partial \gamma} \left[\frac{N(\gamma)}{\gamma^2} \right] \tag{3.54}$$

valid for any radiation mechanism at the emission frequency ν', with $P'(\gamma, \nu')$ being the specific power of electrons with Lorentz factor γ at frequency ν' and assuming $h\nu' \ll \gamma m_e c^2$. Thus, the SSA mechanism will affect mostly the low frequency range. This results in a modification of the lower frequency tail of the synchrotron spectrum as:

$$P'_\nu \propto \begin{cases} \nu'^{5/2} & \nu'_i < \nu' < \nu'_{SSA} \\ \nu'^2 & \nu' < \nu'_{SSA} < \nu'_i \end{cases} \tag{3.55}$$

assuming a power law distribution of electrons, with $\nu'_i = \min(\nu'_m, \nu'_{cool})$ and ν'_{SSA} the frequency below which the synchrotron flux is self-absorbed and the source becomes

optically thick.
Electrons in relativistic shocks can be accelerated via Fermi mechanism up to a **maximum Lorentz factor** γ_{max} set by the condition that radiative losses between acceleration episodes should be smaller than the energy gain. As a result, also the emitting radiation will have a cut-off frequency ν'_{max} above which photons cannot be emitted. Considering electrons emitting synchrotron emission, the maximum energy can be estimated equating the timescale for synchrotron cooling and the acceleration timescale. The following calculation is presented in [175]. The acceleration timescale is the time it takes for a particle to cross the shock front, also known as the Larmor time, so:

$$t'_L = \frac{r_L}{c} = \frac{\gamma m_e c}{eB'} \tag{3.56}$$

where r_L is the Larmor radius. For each crossing the electrons gain energy by a factor ~ 2. On the other hand, the energy losses for synchrotron radiation in this timescale are:

$$\delta E' = t'_L P' = \frac{\gamma m_e c}{eB'} \frac{\sigma_T c \gamma^2 B'^2}{6\pi} = \frac{1}{6\pi} \frac{\sigma_T m_e c^2 B' \gamma^3}{e} \tag{3.57}$$

The particle stops to gain energy when:

$$\delta E' = \gamma m_e c^2 \tag{3.58}$$

Therefore, the maximum Lorentz factor for electrons can be derived:

$$\gamma_{max} = \sqrt{\frac{3\pi e}{\sigma_T B'}} \tag{3.59}$$

The corresponding maximum synchrotron photon energy is:

$$h\nu'_{max} = \frac{eB'\gamma^2_{max} h}{2\pi m_e c} \tag{3.60}$$

which for electrons is ~ 50 MeV in their rest frame.
Similar considerations regarding the cooling and the maximum Lorentz factor can be done also for protons. Following the same arguments presented below one obtains:

$$\gamma_{cool,p} = \frac{6\pi m_p^3 c}{\sigma_T m_e^2 B'^2 t'} \tag{3.61}$$

for the cooling Lorentz factor and:

$$\gamma_{max,p} = \sqrt{\frac{3\pi e m_p^2}{\sigma_T m_e^2 B'}} \tag{3.62}$$

for the maximum Lorentz factor. Synchrotron emission is less efficient for protons so they are less affected by cooling and they can reach higher maximum Lorentz factors than the electrons.
In the relativistic external shock scenario fresh electrons are continuously injected and then accelerated at the shock front. As a result, the synchrotron spectrum emitted by this distribution of electrons $N(\gamma, t)$ will variate with time. The temporal evolution of an electron population can be described through the *continuity equation*:

$$\frac{\partial N(\gamma, t)}{\partial t} = \frac{\partial}{\partial \gamma}\left[\dot{\gamma} N(\gamma, t)\right] + Q(\gamma) \tag{3.63}$$

where $\dot{\gamma} = \frac{\partial \gamma}{\partial t}$ is the cooling rate and $Q(\gamma)$ is the source term which describes the new injected particles. Assuming a power-law injection described by:

$$Q(\gamma) \propto \gamma^{-p} \quad \text{for } \gamma > \gamma_m \tag{3.64}$$

two different regimes can be identified:

- **slow cooling regime**: when $\gamma_m < \gamma_{cool}$ and so only the electron with $\gamma > \gamma_{cool}$ significantly cool. The electron distribution is described by:

$$N_\gamma \propto \begin{cases} \gamma^{-p} & \gamma_m < \gamma < \gamma_{cool} \\ \gamma^{-p-1} & \gamma > \gamma_{cool} \end{cases} \tag{3.65}$$

- **fast cooling regime**: when $\gamma_{cool} < \gamma_m$ and all the electrons cool down to roughly γ_{cool}. The electron distribution is described by:

$$N_\gamma \propto \begin{cases} \gamma^{-2} & \gamma_{cool} < \gamma < \gamma_m \\ \gamma^{-p-1} & \gamma > \gamma_m \end{cases} \tag{3.66}$$

Since the electron distribution is described by broken power laws, also the resulting synchrotron spectra will be expressed in the form of a multi-segment broken power law. Analytical spectra under these conditions and assumptions were derived by Sari, Piran and Narayan (hereafter SPN98) [176]. These formulas, toghether with the ones calculated in Panaitescu and Kumar (hereafter PK00) [168] have been used as reference models to test the spectra obtained in my numerical code. Following the SPN98 treatment, the emitted power for a single electron in the rest frame is:

$$P(\gamma) = \frac{4}{3}\sigma_T c \gamma^2 \Gamma^2 u'_B \tag{3.67}$$

which is the same of equation 3.43 with $\beta = 1$ and multiplied by a factor Γ^2. Therefore, the characteristic synchrotron frequency is:

$$\nu(\gamma) = \Gamma \gamma^2 \frac{eB}{2\pi m_e c} \tag{3.68}$$

Therefore, assuming the total number of swept-up electrons in the post shock fluid as $N_e = 4\pi R^3 n/3$ and the peak spectral power $P_{\nu,max} \approx P(\gamma)/\nu(\gamma)$ it is possible to calculate the flux normalization factor as:

$$F_{\nu,max} = \frac{N_e P_{\nu,max}}{4\pi D^2} \tag{3.69}$$

where D is the luminosity distance. As a result, the synchtron spectra in the *fast* and *slow* cooling regime are:

- **slow cooling regime** ($\nu_m < \nu_c$):

$$F_\nu = \begin{cases} F_{\nu_i max}\left(\frac{\nu_{SSA}}{\nu_m}\right)^{1/3}\left(\frac{\nu}{\nu_{SSA}}\right)^2 & \nu < \nu_{SSA} \\ F_{\nu_i max}\left(\frac{\nu}{\nu_m}\right)^{1/3} & \nu_{SSA} < \nu < \nu_m \\ F_{\nu_i max}\left(\frac{\nu}{\nu_m}\right)^{-(p-1)/2} & \nu_m < \nu < \nu_{cool} \\ F_{\nu_i max}\left(\frac{\nu_{cool}}{\nu_m}\right)^{-(p-1)/2}\left(\frac{\nu}{\nu_{cool}}\right)^{-p/2} & \nu > \nu_{cool} \end{cases} \tag{3.70}$$

- **fast cooling regime** ($\nu_c < \nu_m$):

$$F_\nu = \begin{cases} F_{\nu_i max}\left(\frac{\nu_{SSA}}{\nu_{cool}}\right)^{1/3}\left(\frac{\nu}{\nu_{SSA}}\right)^{2} & \nu < \nu_{SSA} \\ F_{\nu_i max}\left(\frac{\nu}{\nu_{cool}}\right)^{1/3} & \nu_{SSA} < \nu < \nu_{cool} \\ F_{\nu_i max}\left(\frac{\nu}{\nu_{cool}}\right)^{-1/2} & \nu_{cool} < \nu < \nu_m \\ F_{\nu_i max}\left(\frac{\nu_m}{\nu_{cool}}\right)^{-1/2}\left(\frac{\nu}{\nu_m}\right)^{-p/2} & \nu > \nu_m \end{cases} \tag{3.71}$$

where F_ν is the flux in the rest frame. The SPN98 spectra are derived considered only the ISM case but the results are valid also in the stellar wind case since the assumption on the external medium does not affect the spectral shape but just the flux normalization and its evolution over time.

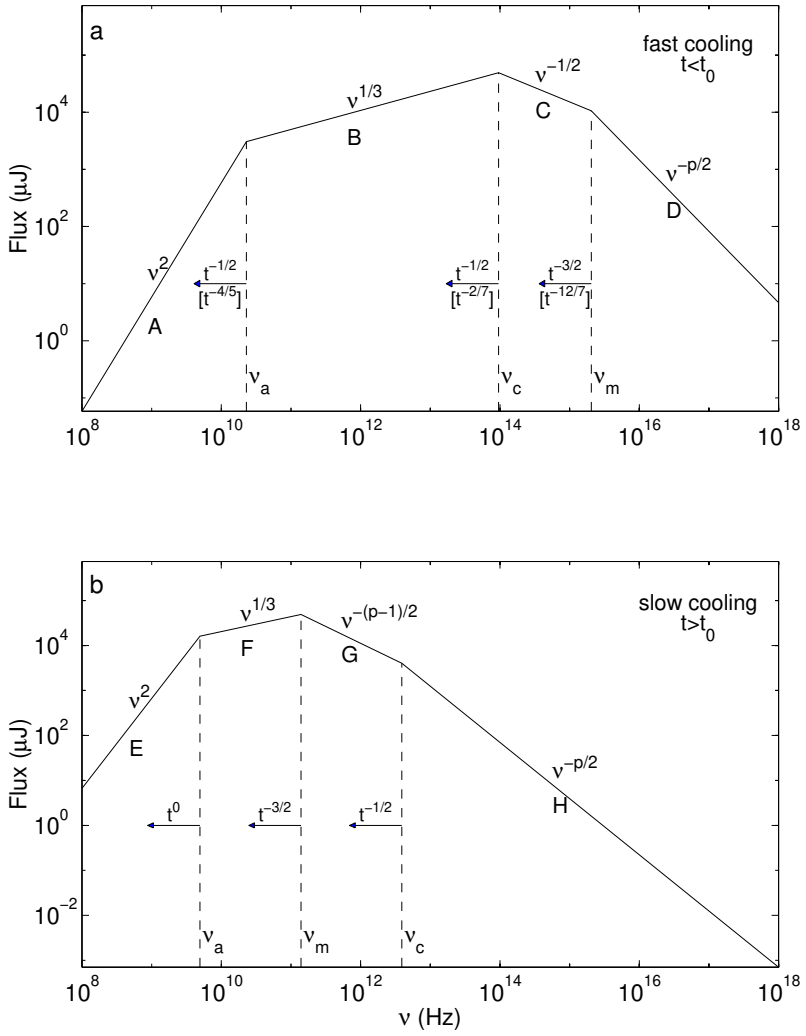

FIGURE 3.16: Synchrotron spectra in the relativistic external shock scenario from a power law distribution of electrons in the *fast cooling* regime (a) and in the *slow cooling* regime (b). The time scaling of the break frequencies is also shown. The scaling above the arrows correspond to an adiabatic evolution, and the scalings below, in square brackets, to a fully radiative evolution. From [176]

The same conclusions can be derived also for protons, as described in [177]. Compared to electrons, protons are inefficient emitters because of their much larger mass, but their spectral slopes follow the same behaviours shown in equations 3.70 and 3.71. Variations in the spectra can be seen for the *break* position and for the flux normalization. Indeed, the ratio between the minimum and the cooling frequency of protons to electrons is:

$$\begin{aligned} \frac{\nu_{m,p}}{\nu_m} &= \left(\frac{\epsilon_p/\xi_p}{\epsilon_e}\right)^2 \left(\frac{m_e}{m_p}\right)^3 \\ \frac{\nu_{cool,p}}{\nu_{cool}} &= \left(\frac{m_p}{m_e}\right)^6 \end{aligned} \tag{3.72}$$

and the flux normalization ratio is:

$$\frac{F_{\nu,max,p}}{F_{\nu,max}} = \xi_p \frac{m_e}{m_p} \tag{3.73}$$

Inverse Compton Radiation

The diffusion process to which electrons and photons undergo when they interact is called *scattering*. Depending on the interaction properties, there may be different types of scattering.
Considering an electron at rest interacting with a photon with frequency ν_i, after the interaction a photon with a frequency ν_f is released at angle θ with respect to the initial direction. Then, the energy-momentum conservation results in:

$$h\nu_f = \frac{h\nu_i}{1 + \frac{h\nu_i}{m_e c^2}(1 - \cos\theta)} \tag{3.74}$$

- for a low energy photon (so that $h\nu_i \ll m_e c^2$) one has $h\nu_f \sim h\nu_i$. This is the *Thompson* scattering where the electron scatters the incoming photon into a random direction without transfer of energy;
- for a high energy photon $h\nu_i/m_e c^2$ is not negligible anymore and as a result $h\nu_f < h\nu_i$. This is the *Compton* scattering, where the electron receives part of the photon energy.

Considering an electron moving with a Lorentz factor γ and a photon with a frequency ν_i, the equation 3.74 can be written in a more generic form as:

$$h\nu_f = h\nu_i \frac{1 - \beta\cos\alpha}{1 - \beta\cos\phi + \frac{h\nu_i}{\gamma m_e c^2}(1 - \cos\theta)} \tag{3.75}$$

where $\beta = v/c$, α and ϕ are respectively the angles between the incoming and the outcoming direction of electrons and photons. In this case the electron is not at rest and can transfer part of its energy to the photon. This is the so-called **Inverse Compton (IC)** mechanism. The IC mechanism can occur in two possible regimes:

- The *Thompson* regime when $h\nu_i < \gamma m_e c^2$ and the electron recoil is negligible. The scattering cross section is defined by the so-called *Thomson cross section*:

$$\sigma_T = \frac{8\pi}{3} r_0^2 = \frac{8\pi}{3}\left(\frac{e^2}{m_e c^2}\right)^2 \tag{3.76}$$

where r_0 is the classical radius of the electron.

In this regime the equation 3.75 can be simplified as:

$$h\nu_f = h\nu_i \frac{1-\beta\cos\alpha}{1-\beta\cos\phi} \tag{3.77}$$

Therefore, the maximum frequency $\nu_{f,max}$ at which a photon can be up-scattered can be calculated assuming $\alpha = \pi$ and $\phi = 0$ (i.e. head-on collision):

$$\nu_{f,max} = \nu_i \frac{1+\beta}{1-\beta} = \nu_i \gamma^2 (1+\beta)^2 \approx 4\nu_i\gamma^2 \tag{3.78}$$

for $\beta \approx 1$.

- The *Klein-Nishina* regime when $h\nu_i > \gamma m_e c^2$ and the electron recoil becomes relevant. Therefore, a more general cross section should be taken into account:

$$\sigma = \frac{3}{4}\sigma_T \left[\left(\frac{1}{2x} - \frac{1+x}{x^3} \right) \ln(1+2x) + \frac{2(1+x)^2}{x^2(1+2x)} - \frac{1+3x}{(1+2x)^2} \right] \tag{3.79}$$

where $x = h\nu/(m_e c^2)$.

For $x \ll 1$ one obtains:

$$\sigma \sim \sigma_T (1+2x) \tag{3.80}$$

The formula approaches the Thompson cross section, while for $x \gg 1$:

$$\sigma \sim \frac{3\sigma_T}{8x}(\ln 2x + \frac{1}{2}) \tag{3.81}$$

the cross section decreases and in the ultra relativistic case is strongly suppressed.

The maximum energy that can be given to the photon is:

$$E_{f,max} = h\nu_{f,max} \lesssim \gamma m_e c^2 + h\nu_i \tag{3.82}$$

Following the physical arguments present in [171] or [178], it is possible to derive the IC emission power in the Thompson regime as:

$$P = \frac{4}{3}\sigma_T c \gamma^2 \beta^2 u_{rad} \tag{3.83}$$

where u_{rad} is the energy density of the radiation in the observer frame. Then, considering an incident monocromatic isotropic photon field of frequency ν_0 and number density $N(\nu_0)$, the IC spectrum is derived as:

$$F_\nu d\nu = \frac{3\pi\sigma_T c}{4\gamma^4} \frac{N(\nu_0)}{\nu_0^2} \nu [2\nu \ln\left(\frac{\nu}{4\gamma^2\nu_0}\right) + \nu + 4\gamma^2\nu_0 - \frac{\nu^2}{2\gamma^2\nu_0}] d\nu \tag{3.84}$$

The spectrum (Figure 3.17) exhibits a rising behaviour $\propto \nu$ up to the maximum IC frequency in Thompson regime $\nu_{f,max}$. Moreover, it is notable to calculate the average frequency of the IC scattered photons as:

$$\langle \nu \rangle \approx \frac{4}{3}\gamma^2\nu_0 \tag{3.85}$$

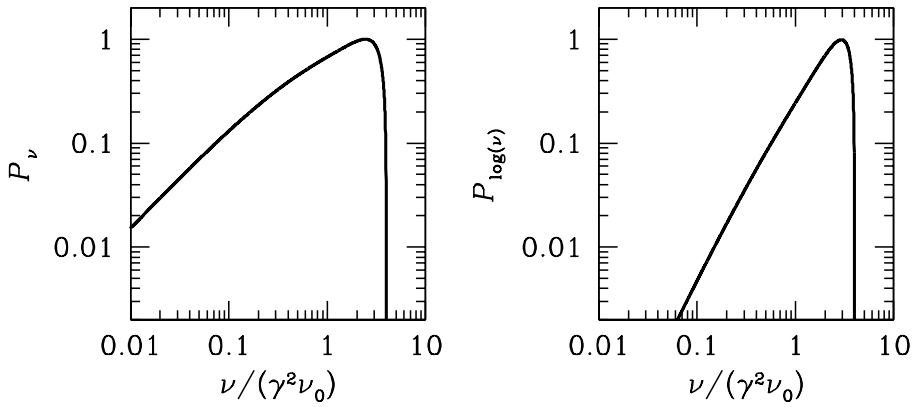

FIGURE 3.17: IC spectrum of electrons with energy γ irradiated by an incident monocromatic photon field of frequency ν_0. The logarithmic scale plot on the right shows that the spectrum is more peaked than the synchrotron spectrum of monoenergetic electrons. From [178].

This means that the scattered photons gain a factor γ^2 in energy and the spectral shape is sharply peaked near the average frequency since $\nu_{f,max} \approx 3\langle\nu\rangle$.
Assuming that the photons are radiated by a power law energy distribution of electrons the resulting spectrum will have the same shape derived also for synchrotron emission:

$$F(\nu) \propto \nu^{-(p-1)/2} \tag{3.86}$$

and the break frequency ν_b^{IC} of the scattered photons is:

$$\nu_b^{IC} \approx \gamma^2 \nu_b \tag{3.87}$$

where ν_b is the break frequency of the seed photon spectrum.
Similarly as for synchrotron radiation, it is possible to define an *IC cooling timescale* and the *IC cooling Lorentz factor*:

$$\begin{aligned} \tau_{cool}^{IC} &= \frac{m_e c}{\frac{4}{3}\sigma_t \gamma \beta^2 u_{rad}} \\ \gamma_{cool}^{IC} &= \frac{3}{4}\frac{m_e c}{\sigma_T \beta^2 u_{rad} t} \end{aligned} \tag{3.88}$$

The relevant IC process in the GRB afterglow environment is the **Synchrotron-Self Compton (SSC)**. In this process the synchrotron photons produced by electrons in the emission region act as seed photons that will be up-scattered via IC by the same population of electrons. Such scenario will generate a very high energy spectral component which have been detected and successfully modelled in the GRBs detected by MAGIC and H.E.S.S.. The importance of the IC emission component can be estimated through the so-called *Compton parameter Y* which is defined as:

$$Y = \langle\frac{\Delta E}{E}\rangle\langle N_{es}\rangle \tag{3.89}$$

where $\langle \frac{\Delta E}{E} \rangle$ is the average fractional energy change per scattering and $\langle N_{es} \rangle$ is the mean number of scatterings. In the relativistic case this will correspond to:

$$Y = \frac{4}{3}\tau_{es}\langle\gamma^2\rangle \tag{3.90}$$

since $\Delta E = \frac{4}{3}\langle\gamma^2\rangle E$ as also seen from equation 3.85 and $\langle N_{es} \rangle \sim \tau_{es}$ with τ_{es} the optical thickness for the electron-photon interaction. On the other hand, the Compton parameter Y can also give an estimate of the efficiency of IC and synchrotron emission component in extracting energy from a population of electrons:

$$Y = \frac{P_{SSC}}{P_{SY}} \simeq \frac{u_{syn}}{u_B} \tag{3.91}$$

The two formulas can be equated since:

$$u_{syn} = \int dr \int d\gamma \frac{P_{syn}}{c}\frac{dN(\gamma)}{d\gamma} = \frac{\sigma_T R B^2}{6\pi}\int d\gamma\gamma^2\frac{dN(\gamma)}{d\gamma} = \frac{\sigma_T R N(\gamma) B^2}{6\pi}\langle\gamma^2\rangle \tag{3.92}$$

Therefore, for $Y \geq 1$ the SSC will have relevant effects on the evolution of the electron energy distribution changing also the resulting spectra. As a result, the total emitted power can be expressed as:

$$P_{tot} = P_{SY} + P_{SSC} = (1 + Y)P_{SY} \tag{3.93}$$

and the electron cooling will be then enhanced resulting in a *cooling timescale*:

$$\tau_{cool} = \frac{6\pi m_e c}{\sigma_T \beta^2 B^2 (1 + Y)\gamma} \tag{3.94}$$

and in a *cooling Lorentz factor*:

$$\gamma_{cool} = \frac{6\pi m_e c}{\sigma_T \beta^2 B^2 (1 + Y)t'} \tag{3.95}$$

Since $Y \propto \gamma^2$ it is clear that SSC will play an important role especially in shaping the highest energy emission. Analytical spectra for the SSC component were calculated by Sari, Esin (hereafter SE01) [161]. In their approach they make the same assumptions for the synchrotron emission seen in SPN98. Then, the synchrotron photons are up-scattered with a single interaction, while multiple scattering are ignored because the energy gain is highly suppressed by electron recoil and Klein-Nishina effects. Therefore, the inverse Compton volume emissivity for a power-law distribution of scattering electrons is calculated as [171]:

$$j_\nu^{IC} = 3\sigma_T \int_{\gamma_m}^{\infty} d\gamma N(\gamma) \int_0^1 dx g(x) \tilde{f_{\nu_s}}(x) \tag{3.96}$$

where $x = \nu/(4\gamma^2\nu_s)$, $\tilde{f_{\nu_s}}$ is the incident specific flux at the shock front, and $g(x) = 1 + x + 2x\ln x - 2x^2$ evaluate the angular dependence of the scattering cross section in the relativistic limit from [178]. Then, the corresponding fluxes for the synchrotron

and IC component can be calculated as:

$$F_{\nu_s}^{syn} = 4\pi R^2 \frac{\tilde{f}_{\nu_s}}{4\pi D^2}$$
$$F_{\nu}^{SSC} = \frac{4}{3}\pi R^3 \frac{j_{\nu}^{IC}}{4\pi D^2} \tag{3.97}$$

where R is the size of the shocked region and D is the distance to the observer. Then, we can write equation 3.96 as:

$$F_{\nu}^{SSC} = R\sigma_T \int_{\gamma_m}^{\infty} d\gamma N(\gamma) \int_0^{x_0} dx F_{\nu_s}^{syn} \tag{3.98}$$

considering $g(x) = 1$ for $0 < x < x_0$ and $x_0 = \sqrt{2}/3$ to ensure the energy conservation. The break frequencies ν_b^{IC}, which identify a change in the spectral slope, are approximated as:

$$\nu_b^{IC} = 4\gamma_b^2 \nu_b^{SY} x_0 \tag{3.99}$$

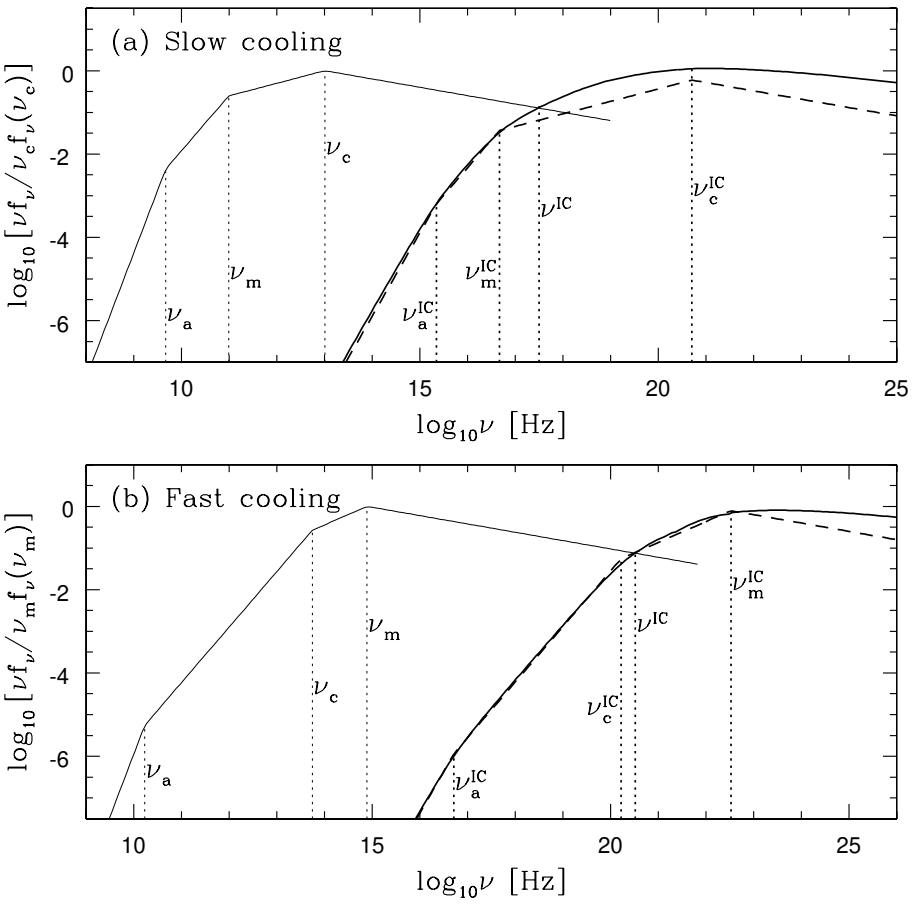

FIGURE 3.18: The synchrotron and SSC spectra in slow and fast cooling regimes. The synchrotron component and the IC spectrum from equations 3.100 and 3.101 are shown as a thick solid lines. A broken power law approximation to the IC spectrum is plotted as a dashed line for comparison. From [161]

Therefore, the resulting SSC spectra are (Figure 3.18):

- **slow cooling regime**:

$$f_\nu^{IC} \simeq R\sigma_T n f_{max} x_0 \begin{cases} \frac{5}{2}\frac{p-1}{p+1}\left(\frac{\nu_a}{\nu_m}\right)^{1/3}\frac{\nu}{\nu_a^{IC}} & \nu < \nu_a^{IC} \\ \frac{3}{2}\frac{p-1}{p-1/3}\left(\frac{\nu}{\nu_m^{IC}}\right)^{1/3} & \nu_a^{IC} < \nu < \nu_m^{IC} \\ \frac{p-1}{p+1}\left(\frac{\nu}{\nu_m^{IC}}\right)^{\frac{1-p}{2}}\left[\frac{4(p+1/3)}{(p+1)(p-1/3)} + \ln\left(\frac{\nu}{\nu_m^{IC}}\right)\right] & \nu_m^{IC} < \nu < \sqrt{\nu_m^{IC}\nu_c^{IC}} \\ \frac{p-1}{p+1}\left(\frac{\nu}{\nu_m^{IC}}\right)^{\frac{1-p}{2}}\left[2\frac{2p+3}{p+2} - \frac{2}{(p+1)(p+2)} + \ln\left(\frac{\nu_c^{IC}}{\nu}\right)\right] & \sqrt{\nu_m^{IC}\nu_c^{IC}} < \nu < \nu_c^{IC} \\ \frac{p-1}{p+1}\left(\frac{\nu}{\nu_m^{IC}}\right)^{\frac{-p}{2}}\frac{\nu_c}{\nu_m}\left[2\frac{2p+3}{p+2} + \frac{2}{(p+2)^2} + \frac{p+1}{p+2}\ln\left(\frac{\nu}{\nu_c^{IC}}\right)\right] & \nu > \nu_c^{IC} \end{cases} \tag{3.100}$$

- **fast cooling regime**:

$$f_\nu^{IC} \simeq R\sigma_T n f_{max} x_0 \begin{cases} \frac{5}{6}\left(\frac{\nu_a}{\nu_c}\right)^{1/3}\frac{\nu}{\nu_a^{IC}} & \nu < \nu_a^{IC} \\ \frac{9}{10}\left(\frac{\nu}{\nu_c^{IC}}\right)^{1/3} & \nu_a^{IC} < \nu < \nu_c^{IC} \\ \frac{1}{3}\left(\frac{\nu}{\nu_c^{IC}}\right)^{-\frac{1}{2}}\left[\frac{28}{15} - \ln\left(\frac{\nu}{\nu_c^{IC}}\right)\right] & \nu_c^{IC} < \nu < \sqrt{\nu_m^{IC}\nu_c^{IC}} \\ \frac{1}{3}\left(\frac{\nu}{\nu_c^{IC}}\right)^{-\frac{1}{2}}\left[2\frac{p+5}{(p+2)(p-1)} - \frac{2(p-1)}{3(p+2)} + \ln\left(\frac{\nu_m^{IC}}{\nu}\right)\right] & \sqrt{\nu_m^{IC}\nu_c^{IC}} < \nu < \nu_m^{IC} \\ \frac{1}{p+2}\left(\frac{\nu}{\nu_m^{IC}}\right)^{\frac{-p}{2}}\frac{\nu_c}{\nu_m}\left[\frac{2}{3}\frac{p+5}{p-1} - \frac{2}{3}\frac{p-1}{p+2}\ln\left(\frac{\nu}{\nu_m^{IC}}\right)\right] & \nu > \nu_m^{IC} \end{cases} \tag{3.101}$$

where R is the size of the shocked region and F_{max} is the flux normalization factor calculated for the synchrotron spectral component. The SSC spectrum is obtained with a convolution of the electron distribution and the incident photon spectrum. Both electrons and incident photon spectra are described through multi-segment broken power laws. However, the resulting SSC spectrum will contain also a logarithmic factor.
So far, the results have been obtained without including the Klein-Nishina (KN) regime. A full treatment of the *KN effect* including modifications in the synchrotron and IC spectra can be found in [179]. As previously mentioned, in the KN regime the energy gained by the up-scattered photons is no longer related to the initial photon frequencies and it is roughly $\sim \gamma m_e c^2$. Such effect is relevant when the photon energy in the rest frame of the electron is higher than $m_e c^2$. The main modifications to the IC spectrum due to photons in the KN regime are:

- the suppression of the high energy up-scattered photons of the SSC component which generate a so-called *KN cut-off*;
- when the SSC dominates the energy output ($Y > 1$) a large part of the electrons are able to cool. Electrons with different Lorentz factors will cool on a different fraction of the synchrotron radiation field. The reason is that which photons are in the KN regime depend on the energy of the electrons that they will consequently interact with different parts of the seed photon spectrum.

As a result, in the KN regime, the Compton parameter Y is no longer a constant but it is $Y = Y(\gamma)$. The resulting electron distribution taking into account the KN effects is:

- **slow cooling regime**:

$$N_\gamma \propto \begin{cases} \gamma^{-p} & \gamma_m < \gamma < \gamma_{cool} \\ \gamma^{-p-1}\frac{1}{1+Y(\gamma)} & \gamma > \gamma_{cool} \end{cases} \tag{3.102}$$

- **fast cooling regime**:

$$N_\gamma \propto \frac{1}{1+Y(\gamma)} \begin{cases} \gamma^{-2} & \gamma_{cool} < \gamma < \gamma_m \\ \gamma^{-p-1} & \gamma > \gamma_m \end{cases} \tag{3.103}$$

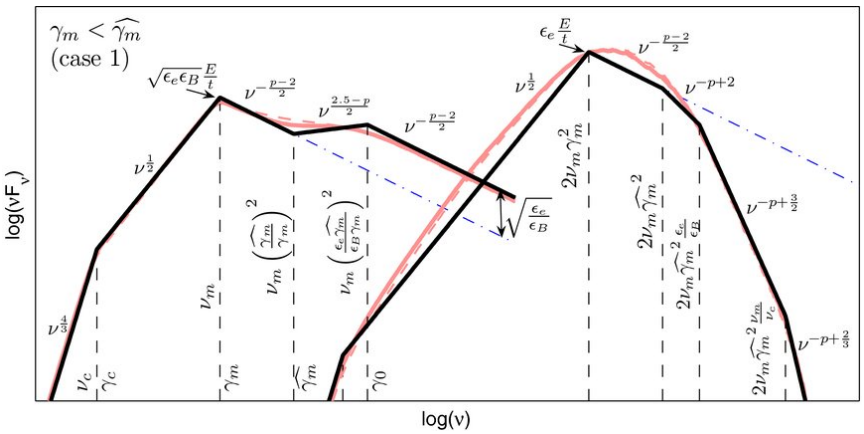

FIGURE 3.19: Example of synchrotron and SSC spectra modified by KN effects. The black solid line is the analytical spectrum, while the red solid and the red dashed lines are calculated numerically. Vertical dashed lines correspond to the break frequencies. From [179]

Then, the resulting spectra with the predicted slopes are shown in Figure 3.19. The *KN cut-off* is clearly evident in the high energy part of the spectrum as well as a hardening of the high energy tail of the synchrotron component with an increased flux with respect to the synchrotron only analytical model.

Chapter 4

Numerical code for the modeling of gamma-ray burst afterglow radiation

A substantial amount of time during my PhD was dedicated to the investigation of the theoretical framework and of the main radiation processes involved in the GRB afterglow phase. As a result, I developed a numerical code able to reproduce the multi-wavelength afterglow emission in the external forward shock scenario. The main theoretical ingredients of the topic were already presented in Section 3.4. In this chapter I will summarize the different approaches for modeling the external shock radiation available in literature (see Section 4.1) and I will describe my numerical code, called `MUlti-wavelength Simulated Emission from GRBs (MUSE-GRB)` (see Section 4.2). Then, the main tests and checks performed to verify the robustness of the code will be described in Section 4.3.

4.1 Modeling of GRB afterglows

Afterglow modeling is often performed adopting analytical prescriptions. In this section I will mention the main articles which were fundamental for the development of the general framework on which my calculation are based, namely the synchrotron-SSC external forward shock scenario. In SPN98 the broad band spectra and corresponding light curves of synchrotron radiation from a power-law distribution of electrons in an expanding relativistic shock were derived. The dynamical evolution was limited to the case of a spherical shock propagating into a constant-density surrounding medium. The light curves were derived assuming two extreme cases for the dynamical evolution: a fully adiabatic system and a fully radiative system. In PK00 the adiabatic evolution of a blast wave interacting with an external medium was taken into account. Break frequencies and fluxes were derived both assuming an homogeneous ISM and a wind-like environment. The effect of the IC scattering on the electron cooling and the signatures on the synchrotron spectrum were also studied. In Granot and Sari [180] a complete description for the synchrotron radiation emitted from relativistic blast waves expanding into an external medium was presented. The slopes of all the spectra in the possible regimes, derived depending on the ordering of the break frequencies, the dependencies of break frequencies and fluxes were calculated. In SE01 the IC spectra of synchrotron photons upscattered by relativistic electrons in GRB afterglows were computed. The modification of the synchrotron spectra due to the presence of a strong IC component were derived. In Nakar, Ando and Sari [179] the modification to the synchrotron and SSC spectra due to the KN effects were calculated when considering a continuos injection of a

power-law energy distribution of relativistic electrons. In parallel with these works, and especially when the Fermi-LAT discoveries revealed the presence of a HE component, models including also the contribution of the hadronic components were revisited. [166, 177, 181].

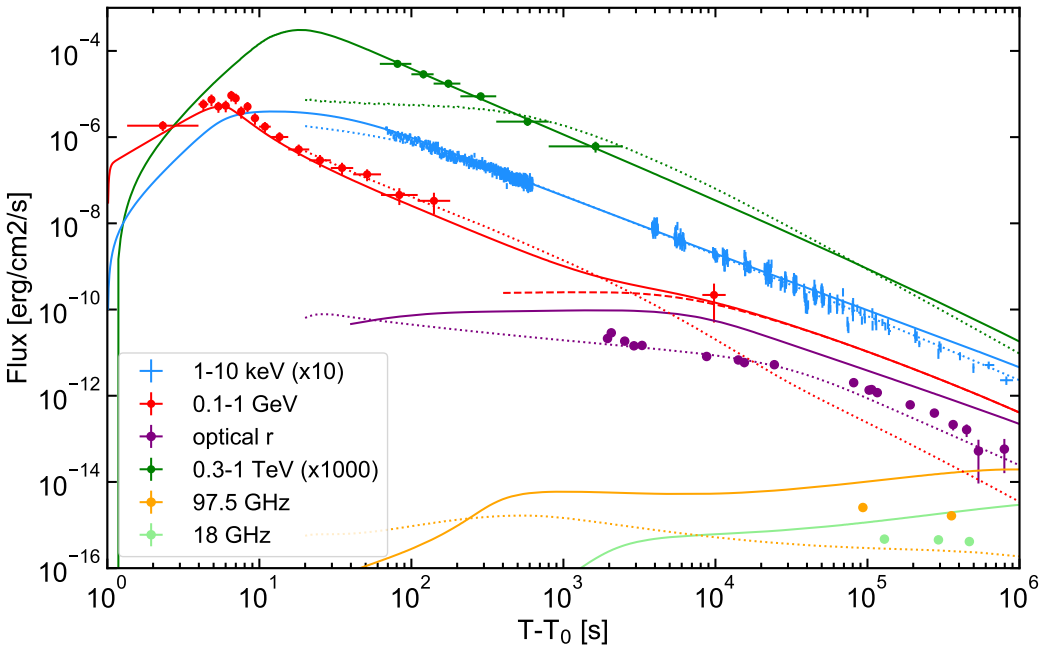

FIGURE 4.1: Multi-wavelength modelling of GRB 190114C observed data within the external forward shock synchrotron and SSC afterglow scenario. Two different models are shown in the plot: solid and dashed lines are obtained with a model optimized for X-ray, GeV and TeV radiation. The overall flux, including synchrotron and SSC, is described by the solid line, while the SSC contribution only is given by the dashed line. Dotted lines refers to a better modelling for the optical and radio observations. From [121].

Numerical calculations of the synchrotron and SSC external forward shock scenario in GRB afterglows were also performed. The ingredients needed are the dynamical evolution of a decelerating blast wave interacting with an external medium coupled with the calculation of the emission generated from the involved radiation processes. Numerical evolution of the synchrotron, IC and pair production emission from a distribution of accelerated electrons is presented in Petropoulou & Mastichiadis (PM09) [182]. For the blast wave evolution the BM76 solution was used assuming a constant-density ISM. A similar treatment is also presented in Pennanen, Vurm and Poutanen (PVP14) [183] where in addition to PM09 the electron heating due to synchrotron self-absorption was taken into account and the wind-like environment was introduced. Further studies also including the difference between the forward shock radiation due to Maxwellian and power-law electron injection were described. The modelling for GRB 190114C was also performed with a numerical code for the synchrotron and SSC radiation emitted from electrons accelerated at the forward shock within the external-shock scenario. An example of such modeling on the GRB 190114C data can be found in Figure 4.1. A numerical code including hadronic processes such as proton synchrotron and secondary particles emission

was also developed through a series of GRB studies [159, 160]. Nevertheless it accounts for the emission in the prompt phase and not in the standard afterglow scenario.
Finally, an open source code, written in Python, was presented in Ryan et al. [184]. To date, it accounts for the calculation of GRB afterglow synchrotron spectra and light curves, also considering the evolution of a structured jet. It has a limited support for IC treatment, initial energy injection and early coasting phase and it does not account for synchrotron self-absorption and external medium density.
In this context, the numerical code MUSE-GRB is a new tool including the most credible leptonic and hadronic processes which are thought to be involved in the GRB afterglow emission. With respect to the aforementioned analytical prescriptions it has the advantage of including the general treatment of the KN effects with no limitations to only some particular cases of interest. The advantage with respect to the other numerical models is that MUSE-GRB can be easily accessed and it is open to several future developments including detailed GRB morphologies and jet structures as well as variable assumptions on the environmental conditions and particle acceleration. In the next section I will describe in detail the structure of the code and the several routines implemented so far.

4.2 MUlti-wavelength Simulated Emission (MUSE) from GRBs

MUSE-GRB is a new elaborate numerical code developed during my PhD. This tool is able to simulate GRB afterglow spectra and light curves at different frequencies and time intervals. In this code I modeled the dynamical evolution of the fireball and I numerically solved the relativistic kinetic equations for electrons, protons, and photons to calculate their time-evolving distributions in the emission region. Several physical processes have been included in this description, namely **synchrotron emission** and **self-absorption**, **adiabatic losses**, **Compton scattering**, **pair production**, and **proton synchrotron radiation**. The code predicts the spectral and temporal properties of the emission from radio to TeV energies and it accounts for two different density profiles of the surrounding medium (constant-density or wind-type). In this section I will describe in detail the general structure of the code and the functions and routines implemented to simulate the dynamical evolution of the blast wave and the emission coming from the aforementioned radiation mechanisms.

4.2.1 General structure

MUSE-GRB is a numerical code for GRB afterglows written in Python. It consists of a series of routines (see Figure 4.2) which make large use of the Scipy and Numpy Python libraries. Every routine has a particular task necessary to calculate the final outputs, namely the GRB afterglow light curves and spectra in the external forward shock scenario. In order to run the simulation and perform these calculations a set of input values in the code are needed. Indeed, the physics involved in the afterglow forward shock scenario contains some assumptions due to unknown properties of the acceleration process, of the shock microphysics, of the external medium and of the jet as described in Section 3.4. As a result, a set of *free parameters* are introduced. For these parameters an input value must be given in the code. Moreover, input values are also needed for the quantities which describe the initial conditions from which the simulation should start. Some other input parameters are needed for

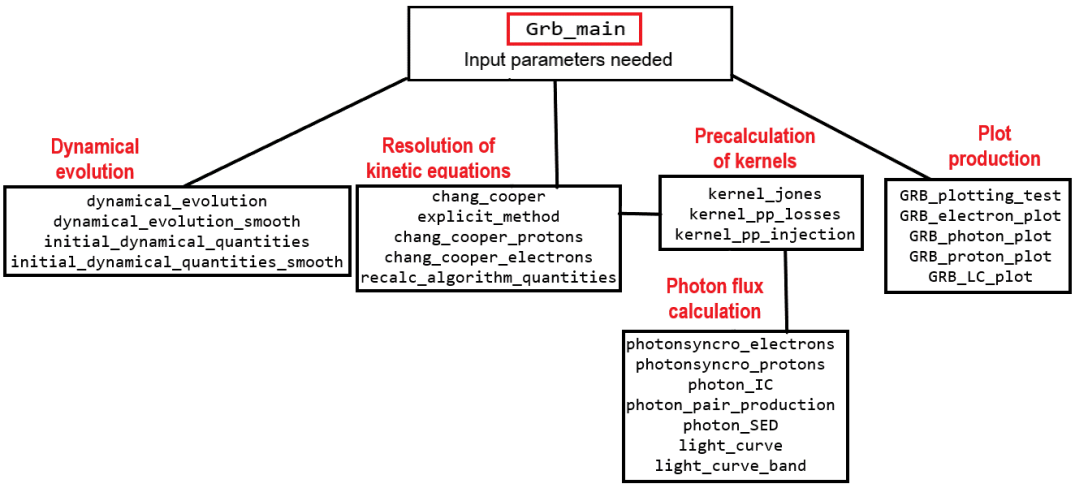

FIGURE 4.2: Chartflow of MUSE-GRB.

computational reasons or for tests. In total, there are 15 input parameters. The ones concerning the GRB physics and the initial conditions are:

- p: spectral index of the distribution of injected accelerated electrons;
- q: spectral index of the distribution of injected accelerated protons;
- ε_e: fraction of energy given to the swept-up electrons;
- ε_p: fraction of energy given to the swept-up protons;
- ε_B: fraction of energy gained by the magnetic field;
- A_0 or A_*: normalization factors of the medium particle density $n(R)$ respectively for the homogeneous ISM and the wind-like scenario;
- s: radial profile index of the medium particle density $n(R)$;
- Γ_0: bulk Lorentz factor for the coasting phase;
- z: redshift;
- E_k: initial kinetic energy in the afterglow;

while the parameters which describe the computational requirements are:

- `smoothing_value`: smoothing parameter for dynamical evolution (see next sections)
- `start_t_obs`: starting time for the simulation in the observer frame;
- `log_gamma`: logarithmic step width for the γ-grid;
- `log_frequency`: logarithmic step width for the ν-grid in the observer frame;
- `test`: boolean variable to activate or deactivate the dynamical evolution described in PVP14, for test purposes.

Currently, in the code the protons and the electrons are mutually exclusive, therefore it must be chosen, at the beginning of the simulation, which of the two distribution must be taken into account. A coupled treatment of the particles in a lepto-hadronic distribution is planned as a future development of the code. As a result, the parameters describing the proton distribution and microphysics (q and ε_p) are mandatory only if the hadronic distribution is chosen. On the other hand, the parameters describing the electron distribution (p and ε_e) are needed when the leptonic processes are considered. I will describe more in detail the physical assumptions and the main routines written by me which constitute the core of the numerical code.

4.2.2 Dynamical evolution

The numerical simulation of the dynamical evolution consists in describing the evolution in space (and therefore in time) of the bulk velocity of the blast wave interacting with the circumburst ambient density. The physical quantities which describe such evolution are the bulk Lorentz factor of the fluid just behind the shock front Γ and the circumburst interstellar density n. For the calculation of these quantities in the code a discrete grid in time t' (fluid comoving frame) and in radius R are calculated. Then, for each value of time/radius, the corresponding value of $\Gamma(R)$ and $n(R)$ can be calculated. The equations which describe the evolution of the bulk Lorentz factor Γ and the interstellar density n have already been described in Section 3.4.1. During the coasting phase the blastwave propagates freely with a constant Lorentz factor Γ_0, while for $R > R_{dec}$ the BM76 self-similar solution is valid, therefore:

$$\Gamma(R) = \left(\frac{(17-4s)E_0}{16\pi A m_p c^2 R^{3-s}} \right)^{\frac{1}{2}} \tag{4.1}$$

The interstellar medium density evolution is described by the equation:

$$n(R) = AR^{-s} \tag{4.2}$$

where $s = 0$ and $A = A_0$ describe the homogeneous constant-density scenario and $s = 2$ and $A = 3.0 \times 10^{35} A_*$ describe the wind-like medium. A_0 for $s = 0$ or A_* for $s = 2$ are the normalization parameters given as input in the code.
The relationship connecting the fluid comoving time t' and the radius R is:

$$dt' = \frac{dR}{\Gamma \beta c} \tag{4.3}$$

which can be also expressed in the rest frame and in the observer frame, following the equations described in Section 3.3.3. In the code it is assumed that the observer is on-axis with the GRB jet. The emission is collimated in a cone of half opening angle $\theta = 1/\Gamma$. For relativistic effects, photons received by the observer at the same time were instead emitted at different comoving times. Since it is not possible to introduce this effect, a good approximation is that all the radiation received at a certain time comes from a ring with $\sin\theta = 1/\Gamma$. Therefore, the following transformations between reference systems are valid:

$$dt_{obs} = (1+z)dt = \frac{1+z}{\Gamma} dt' \tag{4.4}$$

During the coasting phase, since $\Gamma = \Gamma_0$ it is possible to write equation 4.3 as:

$$t_{obs} = \frac{R(1+z)}{\Gamma_0^2 \beta c} \tag{4.5}$$

In `MUSE-GRB` the dynamical evolution can be simulated with two possible routines: `dynamical_evolution` and `dynamical_evolution_smooth`. Both the functions require two input quantities which define when the simulation should stop, namely:

- `condition`: a numerical parameter which identifies the quantity responsible to stop the simulation of the evolution. Possible values and corresponding quantities are 0 for *number of simulation steps*, 1 for Γ, 2 for t_{obs}, and 3 for R;
- `Variable_stop` is the value of the defined quantity at which, when reached, the simulation stops.

The simulation accounts for the two possible values of the radial profile of the external density `s`, which is defined at the beginning of the code, and consequently simulates the blast wave evolution in the chosen environment. If the parameter `test` is activated (i.e. `test` = 1) the dynamical evolution described in PVP14 is followed. Indeed in PVP14 a factor $1/2$ is introduced in the transformations between dt and dt' (equations 4.4) since they account for the radiation received only from the center of the jet emission, i.e. $\theta = 0$. Moreover, the dynamical evolution does not follow the BM76 solution but a similar description which differs for a numerical factor. When activating the parameter `test` these modifications are introduced. Such description was used for comparison checks between PVP14 results and my code.
In the `dynamical_evolution` routine, equation 4.1 is solved at each step i and the corresponding solution, called $\Gamma_{BM}(R_i)$, is calculated. Then, the bulk Lorentz factor evolution is defined as:

$$\Gamma(R_i) = \begin{cases} \Gamma_0 & \Gamma_{BM}(R_i) > \Gamma_0 \\ \Gamma_{BM}(R_i) & \Gamma_{BM}(R_i) < \Gamma_0 \end{cases} \tag{4.6}$$

for $i = 1, \ldots, N$ where N is the total number of simulation steps. With such implementation the Γ evolution is splitted into two distinct regimes. First, during the coasting phase it has a costant value Γ_0. Then, during the deceleration phase it follows the BM76 solution, therefore $\Gamma \propto R^{-\frac{3-s}{2}}$ (see Figure 4.3). The drawback of the evolution described with these assumptions is that it produces a sharp break at the position of the transition between the two regimes. This unphysical feature will be reflected in all the physical quantities which have a dependence on Γ. As a result, the calculations of the code near the transition will not be very reliable and the quantities estimated will not follow the behaviour expected from the theory. To overcome this problem a different equation which includes a smoother transition between the two regimes of the bulk Lorentz factor evolution can be introduced. This is what is done by the function `dynamical_evolution_smooth`. As a result, the bulk Lorentz factor Γ is calculated through the formula:

$$\Gamma(R_i) = \Gamma_0 \left[1 + \left(\frac{R_i}{R_{tr}} \right)^{\frac{3-s}{2}\chi} \right]^{-\frac{1}{\chi}} \tag{4.7}$$

where $\chi =$ `smoothing_parameter` is an input parameter of the code, and:

$$R_{tr} = \left(\frac{(17-4s)E_0}{16\pi A m_p c^2 \Gamma_0^2} \right)^{\frac{1}{3-s}} \tag{4.8}$$

is the radius at which the transition between the two regimes occurs, therefore $\Gamma_{BM}(R_{tr}) \equiv \Gamma_0$. Equation 4.7 reproduces a smoother evolution of the bulk Lorentz factor near the transition, while for $R_i \ll R_{tr}$ it follows $\Gamma(R_i) = \Gamma_0$ and for $R_i \gg R_{tr}$ $\Gamma(R_i) = \Gamma_{BM}(R_i)$. Such behaviour is visible in Figure 4.3 where a comparison between the two methods developed for the Γ evolution is shown.

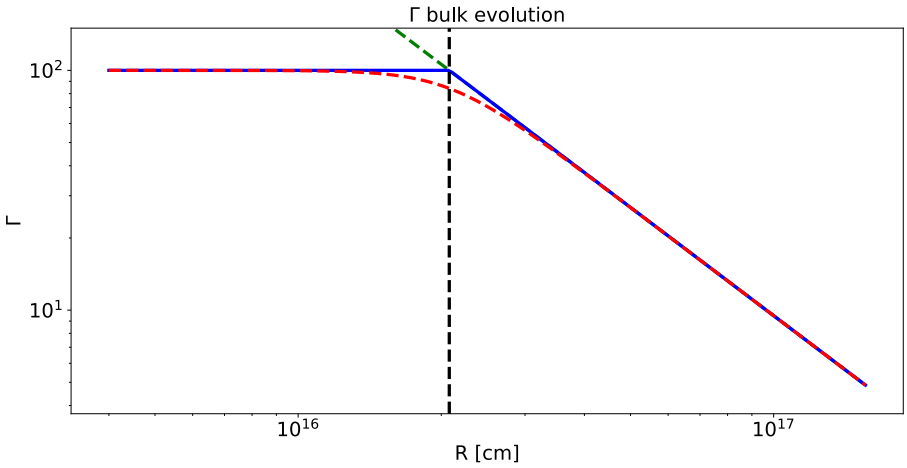

FIGURE 4.3: Evolution of the bulk Lorentz factor Γ in `MUSE-GRB` with different assumptions. The coasting and the deceleration regimes are clearly evident. The dashed black vertical line is R_{tr}, where $\Gamma_0 = \Gamma_{BM}$. The dashed green line is the BM76 solution. The blue line is the Γ evolution obtained from equation 4.6, while the red dashed line is the smoother formula described in equation 4.7.

One of the input parameters given in the code, `start_t_obs`, is the time in the observer frame at which the simulation should start. Indeed the goal of the code is to compare the numerical modeling results with the observational afterglow data, which are always taken with some time delay with respect to the GRB trigger time. For this reason, there is no need to reproduce the dynamical evolution starting from $t_{obs} = 0$ which would also have the effect to increase the computational time of the simulation. It is more convenient to define as input parameter the time from which we are interested to evaluate the dynamical evolution. Once a starting time in the observer frame $t_{obs,init}$ is given, it is necessary to evaluate the corresponding values of radius r_{init} and bulk Lorentz factor Γ_{init}. In the code this is done with the function `initial_dynamical_quantities` and `initial_dynamical_quantities_smooth` respectively for the methods previously explained. Equations 4.3 and 4.4 describe the relationship between time and radius but they are valid only in differential form when $\Gamma = \Gamma(R)$. During the coasting phase integration of the differential form is possible since $\Gamma = \Gamma_0$ and therefore equation 4.5 holds. As a result, to assure that the correct values of r_{init} and Γ_{init} are calculated the functions generate a wide grid spaced in logarithmic scale of radius values r_{grid} assuring that the first value of the grid $r_{grid,0} \ll R_{tr}$. Then, from $r_{grid,0}$ is possible to estimate the corresponding observer time with equation 4.5. Once the radius, the time and the bulk Lorentz factor

of the first point of the grid is known, it is possible to use equations 4.1, 4.3, 4.4, 4.7 to calculate for each value of the radius grid the corresponding values of the bulk Lorentz factor $\Gamma(r_{grid})$ and of the time in the observer frame $t_{obs,grid}$. The values obtained for $t_{obs,grid}$ are then compared with the chosen starting time $t_{obs,init}$. The i-th point of the grid for which $t_{obs,grid,i} = t_{obs,init}$ is taken as starting point for the simulation and therefore $r_{grid,i} = r_{init}$ and $\Gamma(r_{grid,i}) = \Gamma_{init}$. At this point the initial values of radius, time and bulk Lorentz factor are correctly calculated and the dynamical simulation can start. Another variable which is calculated during the dynamical simulation is the strength of the magnetic field B'. Such calculation is performed at this stage since $B' = B'(\Gamma, n)$. Indeed, B' is calculated following the equation 3.34. The physical quantities calculated are then stored into NumPy arrays ready to be used for further calculations.

4.2.3 Kinetic equations

Once the dynamical calculation is performed, the environmental framework set-up is built. The system is assumed to be adiabatic, therefore the dynamical evolution is decoupled from the particle evolution and the radiation emission. As seen from the theory, in the afterglow phase the blast wave propagates and decelerates when interacting with an external circumburst medium. The bulk energy of the blast wave is converted into random kinetic energy of the swept-up particles which are therefore accelerated and emit the afterglow radiation. The accelerated particles injected continuously in the system will radiate photons loosing energy. In order to evaluate the evolution of the particle energy distributions in time and in space taking into account the energy losses and the source terms, their **kinetic equations** should be solved. The equation, valid for protons and electrons, can be written as:

$$\frac{\partial N(\gamma, t')}{\partial t'} + \frac{\partial}{\partial \gamma}[\dot{\gamma}(\gamma, t')N(\gamma, t')] = Q(\gamma, t') \tag{4.9}$$

or written in terms of the radius R, recalling equation 4.3:

$$\frac{\partial N(\gamma, R)}{\partial R} + \frac{1}{c\Gamma\beta}\frac{\partial}{\partial \gamma}[\dot{\gamma}(\gamma, R)N(\gamma, R)] = Q(\gamma, R) \tag{4.10}$$

where $N(\gamma, R)$ (or $N(\gamma, t')$) is the number distribution for particles with Lorentz factor γ measured at a radius R (comoving time t'), the second term of the left hand side takes into account the energy losses $\dot{\gamma}(\gamma, R)$ of the particles due to the different radiation mechanisms and $Q(\gamma, R)$ is the particle injection term. In `MUSE-GRB` several radiation mechanisms are taken into account. Therefore, there will be several losses and the injection terms accounting for such mechanisms. When expliciting all these terms, the **kinetic equation for electrons** can be therefore written as:

$$\frac{\partial N_e}{\partial R} + \frac{1}{c\Gamma\beta}\frac{\partial}{\partial \gamma}[(\dot{\gamma}_{e,syn} + \dot{\gamma}_{ad} + \dot{\gamma}_{IC})N_e] = Q_e^{inj} + Q_e^{pp} \tag{4.11}$$

while for **protons** we have:

$$\frac{\partial N_p}{\partial R} + \frac{1}{c\Gamma\beta}\frac{\partial}{\partial \gamma}[(\dot{\gamma}_{p,syn} + \dot{\gamma}_{ad})N_p] = Q_p^{inj} \tag{4.12}$$

where N_e and N_p are respectively the electrons and protons number distributions. The subscripts in the losses and injection terms denote the different radiation mechanisms involved, namely the electron synchrotron (e,syn), adiabatic losses (ad), IC scattering (IC), proton synchrotron (p,syn) and pair production (pp). The terms Q_e^{inj} and Q_p^{inj} are the injection functions for electrons and protons. Once the particles distribution function is calculated, the corresponding observed photon flux accounting for the different emission and absorption terms is estimated.
In order to perform these calculations the particle energy distributions and the photon flux are discretized. Therefore, two logarithmic spaced grids are introduced in the system: one for the electrons/protons Lorentz factor γ and one for photon observed frequencies ν_{obs}. The γ-grid for electrons ranges from $\gamma = 1$ to $\gamma = 10^8$. The γ-grid for protons ranges from $\gamma = 1$ to $\gamma = 10^{10}$. The number of points in the grid can be calibrated with the input code parameter `log_gamma` which defines the logarithmic step width. The ν_{obs}-grid ranges from $\nu_{obs} = 10^8$ Hz to $\nu_{obs} = 10^{30}$ Hz. Corresponding grids also for the rest frame and the comoving frequencies can be obtained simply recalling the relationship:

$$\nu_{obs} = \frac{\nu}{1+z} = \frac{\Gamma}{1+z}\nu' \tag{4.13}$$

The number of points in the grid can be calibrated with the input code parameter `log_frequency` which defines the logarithmic step width. Usually, stable and accurate results are obtained with grids of more than 200 points. In case better precision is needed (especially for the γ-grid) it is possible to increase the number of points in the grid at the cost of larger computational time. Since the γ-grid is limited to 10^8 for electrons and 10^{10} for protons, the maximum energy for particles injection is calculated for electrons as:

$$\gamma_{max} = \min\left(\sqrt{\frac{3\pi e}{\sigma_T B'}}, 10^8\right) \tag{4.14}$$

and in a similar way for protons:

$$\gamma_{max,p} = \min\left(\sqrt{\frac{3\pi e m_p^2}{\sigma_T m_e^2 B'}}, 10^{10}\right) \tag{4.15}$$

4.2.4 The Chang-Cooper numerical scheme

The kinetic equations presented above can be solved using numerical algorithms. Several schemes are used to find numerical approximated solutions for such class of equations, called *Fokker-Planck* equations, including implicit or explicit methods. *Explicit methods* calculate the state of a system at a later time from the state of the system at the current time, while *implicit methods* find solutions by solving an equation involving both the current state of the system and the later one. In `MUSE-GRB`, the differential equations are solved with the numerical implicit finite difference scheme proposed by **Chang and Cooper** (CC) [185]. Despite a more complicated implementation, an implicit scheme was chosen since it ensures a numerical stability and an accuracy for which the explicit methods would require impractically small steps. As a result, the computational time for the simulation is reduced with the use of implicit methods. Moreover the CC method yields more stable, non-negative and particle number conserving solutions. In comparison with other schemes, it requires less meshpoints to reach satisfying precision [186]. For test purposes I also implemented

in the code the function `explicit_method`. A comparison of the computational times of the explicit and CC methods are shown in Figure 4.4. For simplicity, only the synchrotron radiation mechanism has been included. For the explicit method, the time step was calculated using the Courant–Friedrichs–Lewy (CFL) condition [187]. For the CC method the CFL condition has been relaxed: larger simulation steps can be used but still preserving the accuracy of the solution. From this test, it is evident that the CC method is much faster than the explicit method (up to a factor ~ 5 for this test) and the difference increases when more simulation steps are required.

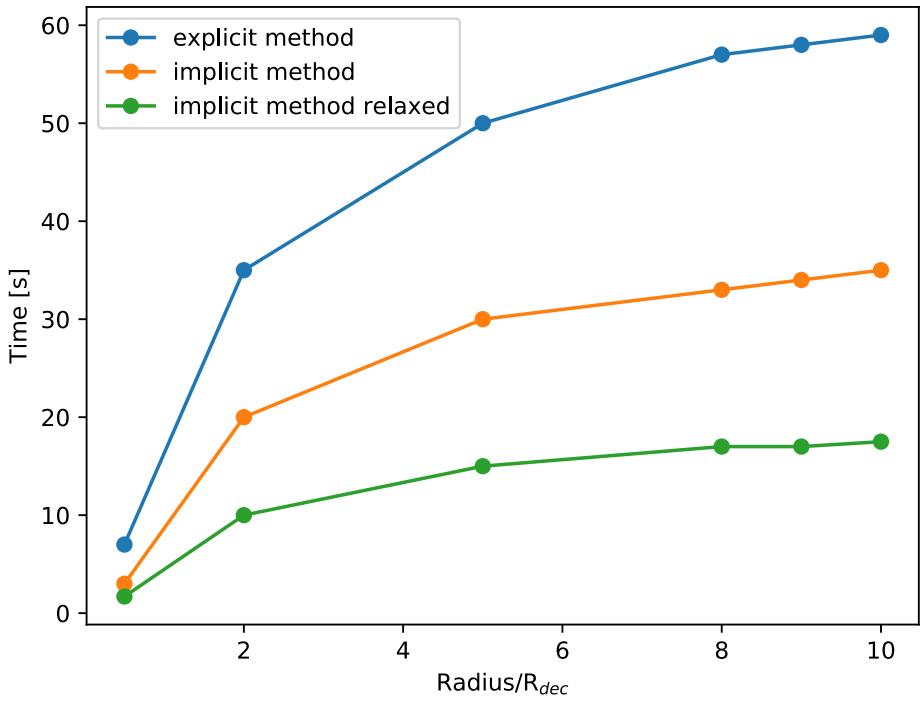

FIGURE 4.4: Comparison of simulation time needed for resolution of kinetic equations when applying an implicit (orange and green) or an explicit method (blue). The x-axis is the last value of radius in the simulation normalized for R_{dec}. The orange points were obtained applying the implicit method and the CFL condition, while the green ones are obtained relaxing the CFL condition.

In `MUSE-GRB` the CC method is implemented in the function `chang_cooper`. The kinetic equation can be written as:

$$\frac{\partial N(\gamma, t')}{\partial t'} + \frac{\partial}{\partial \gamma}[\dot{\gamma}(\gamma, t')N(\gamma, t')] = Q(\gamma, t') \tag{4.16}$$

and the γ-grid with logarithmic scaling is defined as:

$$\gamma_j = \gamma_{inf}\left(\frac{\gamma_{sup}}{\gamma_{inf}}\right)^{\frac{j-1}{jmax-1}} \tag{4.17}$$

where γ_{inf} and γ_{sup} are the lower and upper edge of the grid, j_{max} is the number of meshpoints and the sizes of the intervals are:

$$\Delta\gamma_j = \gamma_{j+\frac{1}{2}} - \gamma_{j-\frac{1}{2}} \tag{4.18}$$

where $j \pm 1/2$ corresponds to the half-grid points. Then, the kinetic equation is discretized as:

$$\frac{N_j^{i+1} - N_j^i}{\Delta t} = \frac{\dot{\gamma}^i_{j+\frac{1}{2}} N^{i+1}_{j+\frac{1}{2}} - \dot{\gamma}^i_{j-\frac{1}{2}} N^{i+1}_{j-\frac{1}{2}}}{\Delta\gamma} + Q_j^i \tag{4.19}$$

where $N_j^i = N(\gamma_j, i\Delta t)$ and $\Delta t = t_{i+1} - t_i$. So the j index refers to the γ-grid, while the i index represents the simulation time step. Following the CC prescriptions it is possible to assume that:

$$\begin{aligned} N_{j+\frac{1}{2}} &\equiv N_{j+1} \\ N_{j-\frac{1}{2}} &\equiv N_j \end{aligned} \tag{4.20}$$

Therefore, equation 4.19 after some algebra can be rewritten as:

$$A_j N_{j+1}^{i+1} + B_j N_j^{i+1} + C_j N_{j-1}^{i+1} = S_j^i \tag{4.21}$$

which is a tridiagonal system of equations where the coefficients are:

$$A_j = 0 \quad B_j = 1 + \frac{\Delta t \dot{\gamma}^i_{j-1/2}}{\Delta\gamma_j} \quad C_j = -\frac{\Delta t \dot{\gamma}^i_{j+1/2}}{\Delta\gamma_j} \quad S_j^i = N_j^i + \Delta t Q_j^i \tag{4.22}$$

The system can then be solved with a simple algorithm or through the Scipy package `linalg.solve_banded`.

4.2.5 Particle injection distribution

In the numerical code the swept-up particles accelerated during the blast wave evolution are reproduced assuming that at each simulation step a population of newly accelerated particles are injected in the system. Therefore, an **injection function** for the particles $Q(\gamma, R)$, where γ is the random Lorentz factor of the particles in the fluid comoving frame, is needed in the code. Such function will account at each simulation step for the particles injected in the system. Different shapes of the injection function can be chosen and introduced in the code. Following the considerations done on the particle acceleration processes in Section 3.4.2, it was decide to use a power-law distribution. When dealing with electrons the formula will be given by:

$$Q_e^{inj}(\gamma, R) = q_0(R)\gamma^{-p} \tag{4.23}$$

valid for $\gamma_{min} < \gamma < \gamma_{max}$, with p spectral index for the injected electrons given as input for the code. An analogous formula is calculated also for the protons. The normalization of the injection function $q_0(R)$ is calculated as described in PM09. Considering the rate of the accreted kinetic energy in the lab frame as:

$$\frac{dE}{dt} = 4\pi R^2 c^3 m_p n(R) \beta\Gamma(R)(\Gamma(R) - 1) \tag{4.24}$$

it follows that, for the energy conservation relation, the fraction of this energy ε_e which goes into electrons is conserved step by step, therefore:

$$\varepsilon_e \frac{dE}{dt} = \int_{\gamma_{min}}^{\gamma_{max}} Q_e^{inj}(\gamma, t)(\gamma - 1) m_e c^2 d\gamma \tag{4.25}$$

As a result, the normalization factor $q_0(R)$ can be calculated solving equation 4.25 as:

$$q_0(R) = \varepsilon_e \frac{4\pi m_p n(R) c}{m_e \left[\frac{\gamma_{min}^{-p+2} - \gamma_{max}^{-p+2}}{p-2} - \frac{\gamma_{min}^{-p+1} - \gamma_{max}^{-p+1}}{p-1} \right]} \frac{R^2(\Gamma - 1)}{c\beta} \tag{4.26}$$

where we have used the $R - t$ relationship expressed in equation 4.3 and the values of minimum and maximum injection Lorentz factors are calculated with equations 3.39, and 3.59. Since all these quantities depend on the dynamical evolution, their values must be updated at each simulation step. In the code the function called `recalc_algorithm_quantities` is responsible for the recalculation of these quantities at each step. Analogous equations and formula can be also obtained when considering protons instead of electrons. The calculation for the normalization factor presented above can be performed using ε_p instead of ε_e and m_p instead of m_e.

4.2.6 Particle energy losses and photon flux calculation

The resolution of the electron or proton kinetic equation requires the calculation of the energy losses terms $\dot{\gamma}$ for the different mechanisms taken into account. These terms are calculated directly from the theoretical considerations done in Section 3.4.4. Once the time-evolving electron or proton distribution function is estimated, the photon flux can be then computed. When taking into account the electrons, I consider synchrotron radiation, adiabatic losses, IC scattering and pair production. Therefore, the electron kinetic equation is coupled together with the photon flux calculation and computed step by step since the evolution of the electron and photon distribution functions affect each other. In the case of protons instead the proton kinetic equation is decoupled with the photon flux calculation, since only the proton synchrotron emission has been included so far. Then, in this case the resolution of the proton kinetic equation and the photon flux calculation can proceed separately. In `MUSE-GRB` the solution of the proton kinetic equation is done by `chang_cooper_protons`, while for the electrons the solution of the electron kinetic equation is performed in `chang_cooper_electrons`. The photon flux calculation is performed with a set of functions each of which taking into account a different mechanism. Thanks to this structure it is possible to decide for each simulation which mechanisms can be introduced and which can be neglected. The functions are the following: `photonsyncro_protons` for the calculation of the proton synchrotron emission, `photonsyncro_electrons` for the electron synchrotron radiation, `photon_IC` for the IC radiation, `photon_pair_production` for the pair production mechanism. The adiabatic losses are taken into account directly when solving the electron or proton kinetic equation. The overall flux is then calculated in the function `photon_SED` and the light curves are calculated in the functions `light_curve` and `light_curve_band` respectively for a given frequency and for a given frequency range.
I will outline, for each of the mechanism, the equations and the quantities calculated for the resolution of the kinetic equations and the calculation of the photon flux.

Synchrotron radiation

The synchrotron radiation terms are introduced in the code both when considering electrons or protons. The energy losses term can be calculated directly starting from equation 3.42. For the electrons, assuming an isotropic distribution of the pitch angle α, the average power is the one described in equation 3.43. From that formula it is possible to derive the energy losses as:

$$\dot{\gamma}_{e,syn} = \left.\frac{d\gamma}{dt'}\right|_{e,syn} = -\frac{\sigma_T B^2 \gamma^2 \beta^2}{6\pi m_e c} \tag{4.27}$$

and similarly for protons:

$$\dot{\gamma}_{p,syn} = \left.\frac{d\gamma}{dt'}\right|_{p,syn} = -\frac{\sigma_T B^2 m_e^2 \gamma^2 \beta^2}{6\pi m_p^3 c} \tag{4.28}$$

The photon emission term can be calculated, recalling the synchrotron power emitted per unit of frequency by a single electron from equation 3.45. The analytical formula is calculated mediating over the pitch angles, as [188]:

$$P'_\nu(\gamma, B') = \frac{2\sqrt{3}e^3 B'}{m_e c^2} x^2 [K_{4/3}(x)K_{1/3}(x) - 0.6x(K^2_{4/3}(x) - K^2_{1/3}(x))] \tag{4.29}$$

where $x = \frac{2\pi m_e c \nu}{3eB'\gamma^2}$, $K_{4/3}(x)$ and $K_{1/3}(x)$ are the modified Bessel functions. When considering a distribution of electrons as described in MUSE-GRB, the total emitted power per unit of frequency $P'_\nu(\nu', \gamma)$ can be calculated as in equation 3.49. In the code, the calculation is done over the discrete γ and ν' grids, therefore:

$$P'^{syn}_\nu(\nu'_k) = \sum_j P'_\nu(\gamma_j, B') N_e(\gamma_j) \Delta\gamma_j \tag{4.30}$$

where j runs over the γ-grid and k is the ν'-grid index. Then, the observed flux is calculated as:

$$F^{syn}_\nu(\nu_{obs,k}) = \frac{P'_\nu(\nu'_k)\Gamma(1+z)}{4\pi D^2} \tag{4.31}$$

where D is the luminosity distance and the factor $\Gamma(1+z)$ comes from relativistic and cosmological effects. Therefore for each element k of the ν_{obs}-grid the observed synchrotron flux is calculated. Analogous results are obtained when considering the proton synchrotron, simply substituing in equation 4.29 m_e with m_p.
In parallel with the synchrotron emission, also the Synchrotron-Self Absorption (SSA) mechanism is introduced in the code. Since it is an absorption process, it is characterized by an optical depth τ_{ssa} which is described as:

$$\tau_{SSA}(\nu') = \sigma_{SSA}(\gamma, \nu') n'_e \Delta R' \tag{4.32}$$

where σ_{SSA} is the SSA cross section, n_e is the number density of the target (in this case $e^\pm$) and $\Delta R'$ is the size of the region involved. Recalling the absorption coefficient calculated in equation 3.54, it is possible to estimate the SSA cross section [171]:

$$\sigma_{SSA}(\gamma, \nu') = \frac{1}{8\pi m_e \nu'^2} \frac{P'^{syn}_\nu(\gamma)}{\gamma} \left[2 - \frac{\partial \ln n'_e(\gamma, t')}{\partial \ln \gamma}\right] \tag{4.33}$$

considering that:

$$n'_e = \frac{N_e}{V'} = \frac{N_e}{4\pi R^2 \Delta R'} \tag{4.34}$$

the optical depth τ_{SSA} is calculated as:

$$\tau_{SSA}(\nu') = \sigma_{SSA}(\gamma, \nu') \frac{N_e}{4\pi R^2} \tag{4.35}$$

In the code $\tau_{SSA}(\nu')$ is calculated and then it is applied to the synchrotron observed flux:

$$F_\nu^{syn+SSA} = F_\nu^{syn} \left(\frac{1 - e^{-\tau_{SSA}}}{\tau_{SSA}} \right) \tag{4.36}$$

Adiabatic losses

Particles in relativistic blast waves may also lose their energy adiabatically through the spreading of the emission region. These are the so-called **adiabatic losses** which are taken into account in the code. To calculate the energy loss term to be inserted in the electron or proton kinetic equation let us consider the emission region $\Delta R'$ as the region between the forward shock plane and the discontinuity plane. At the comoving time t' the comoving volume V' of the emission region is defined as:

$$V' = 4\pi R^2 \Delta R' \tag{4.37}$$

and:

$$\Delta R' = \frac{R}{\Gamma} \tag{4.38}$$

Now, considering a monoenergetic population of N_e electrons with Lorentz factor γ in a volume V', their pressure P' and internal energy E are:

$$P' = \frac{N_e \gamma \beta^2}{3V'} \tag{4.39}$$

$$E = (\gamma - 1) N_e \tag{4.40}$$

From the first law of thermodynamics $dE = -PdV$ and therefore the adiabatic losses can be calculated as [183]:

$$\dot{\gamma}_{ad} = \left. \frac{d\gamma}{dt'} \right|_{ad} = -\frac{\gamma \beta^2}{3} \frac{d \ln V'}{dt'} \tag{4.41}$$

In the code the calculation of $\dot{\gamma}_{ad}$ is done at each time step and for each values of the γ-grid.

IC radiation

The introduction of a numerical treatment for the IC mechanism is not straightforward. Indeed, both the electron and the photon distributions are involved in the scattering process. Moreover, as described in Section 3.4.4 the IC mechanism can take place in different regimes, Thompson or Klein-Nishina, depending on the photons and electrons energies. A good approach for numerical calculations, which includes both regimes, is the one proposed in [189]. In such approach the energy

loss term and the emitted IC power are calculated using a kernel defined as:

$$K(\gamma,\nu',\tilde{\nu'}) = \begin{cases} \frac{E_f}{E_i} - \frac{1}{4\gamma^2} & \frac{E_i}{4\gamma^2} < E_f < E_i \\ 2q\ln q + (1+2q)(1-q) + \frac{1}{2}(1-q)\frac{(4\gamma E_i q)^2}{(1+4\gamma E_i q)} & E_i < E_f < \frac{4\gamma^2 E_i}{1+4\gamma E_i} \end{cases} \tag{4.42}$$

where:

$$E_i = \frac{h\tilde{\nu'}}{m_e c^2} \quad E_f = \frac{h\nu'}{m_e c^2} \quad q = \frac{E_f}{4\gamma E_i(\gamma - E_f)} \tag{4.43}$$

E_i and E_f are the energies of the photons before and after the scattering process. The two terms of equation 4.42 account respectively for the down-scattering (i.e. $E_f < E_i$) and the up-scattering (i.e. $E_f > E_i$) process. In `MUSE-GRB` the kernel $K(\gamma,\nu',\tilde{\nu'})$ is precalculated once on a three dimensional grid before the time evolution of the kinetic equation starts. The calculation is done in the function `kernel_jones`. Once the kernel is calculated, the energy loss term for the IC can be calculated at each simulation step with the equation:

$$\dot{\gamma}_{IC} = \left.\frac{d\gamma}{dt'}\right|_{IC} = -\frac{3h\sigma_t}{4m_e c\gamma^2}\int d\nu'\nu' \int \frac{d\tilde{\nu'}}{\tilde{\nu'}} n_{\tilde{\nu'}}(t') K(\gamma,\nu',\tilde{\nu'}) \tag{4.44}$$

where the integration is performed using the Scipy package `integrate.simps` which allows the calculation over a finite grid with the Simpson's rule. The IC power emitted is calculated as:

$$P'^{IC}_{\nu}(\nu') = \frac{3}{4}h\sigma_T c\frac{\nu'}{\gamma^2}\int \frac{d\tilde{\nu'}}{\tilde{\nu'}} n_{\tilde{\nu'}}(t') K(\gamma,\nu',\tilde{\nu'}) \tag{4.45}$$

and consequently the observed IC flux on the ν_{obs}-grid is estimated:

$$F^{IC}_{\nu}(\nu_{obs,k}) = \frac{P'^{IC}_{\nu}(\nu'_k)\Gamma(1+z)}{4\pi D^2} \tag{4.46}$$

in the same way as calculated for the synchrotron radiation. In both equations 4.44 and 4.45 the photon number density $n_{\tilde{\nu'}}(t')$ is required for the calculations. Considering a spherical shell of radius R and comoving volume $V' = 4\pi R^2 \Delta R'$ continuously emitting at a power $P'_{\nu'}(\nu')$ at a certain frequency ν', the radiation energy density $u'_{rad}(\nu')$ can be written as:

$$u'_{rad}(\nu') = \frac{P'_{\nu'}(\nu')}{V'} t_{esc} \tag{4.47}$$

where t_{esc} is the mean escape time for photons from the emission region $\Delta R'$. Such value is on average $\langle t_{esc}\rangle \sim \Delta R'/c$. Therefore the radiation energy density can be rewritten as:

$$u'_{rad}(\nu') = \frac{P'_{\nu'}(\nu')}{4\pi R^2 c} \tag{4.48}$$

From the radiation energy density it is possible to derive the photon number density:

$$n_{\nu'} = \frac{u'_{rad}(\nu')}{h\nu'} \tag{4.49}$$

Equations 4.48 and 4.49 are included in the code and the number photon density is calculated on the frequency grid and its value is updated at each simulation step. The emitted power $P'_{\nu'}(\nu')$ is the one calculated via synchrotron radiation from equation 4.30 since the seed photons involved in the IC mechanisms are the ones emitted

via synchrotron mechanism. With the introduction of the IC mechanism in the code, the kinetic equation for electrons and the photon flux calculation are coupled. The energy losses terms for synchrotron and IC mechanisms must be updated at each simulation step. This recalculation, as can be seen from equation 4.44, requires that also the photon number density and the IC emitted power are recalculated at each step.

Pair production

The pair production mechanism can shape the GRB afterglow spectra introducing an absorption term for photon flux and an additional injection term for electrons. Indeed, in such mechanism a high energy photon interacts with a target photon of lower energy. This interaction leads to the loss of high energy photon and to the production of an electron-positron pair. The treatment presented in [190] is followed which is consistent with the one already presented in Section 1.2. Therefore, the cross section of the process $\sigma_{\gamma\gamma}$ as a function of β', the centre-of-mass speed of the electron and positron is given by:

$$\sigma_{\gamma\gamma}(\beta') = \frac{3}{16}\sigma_T(1-\beta'^2)\left[(3-\beta'^4)\ln\left(\frac{1+\beta'}{1-\beta'}\right) - 2\beta'(2-\beta'^2)\right] \tag{4.50}$$

where:

$$\beta'(\omega_t, \omega_s, \mu) = \left[1 - \frac{2}{\omega_t\omega_s(1-\mu)}\right]^{\frac{1}{2}} \tag{4.51}$$

and $\omega_t = h\nu'_t/m_ec^2$ with ν'_t being the the target photon frequency, $\omega_s = h\nu'/m_ec^2$ with ν' being the source photon frequency and $\mu = \cos\phi$, where ϕ is the scattering angle. Then, it is possible to derive the annihilation rate of photons into electron-positron pairs as:

$$R(\omega_t, \omega_s) = c\int_{-1}^{\mu_{max}} \frac{d\mu}{2}(1-\mu)\sigma_{\gamma\gamma}(\omega_t, \omega_s, \mu) \tag{4.52}$$

where $\mu_{max} = \max(-1, 1-2/\omega_s\omega_t)$ coming from the requirement $\beta'^2 > 0$. Considering $x = \omega_t\omega_s$ it is possible to derive asymptotic limits for $R(\omega_t, \omega_s) \equiv R(x)$ in two regimes. For $x \to 1$ (i.e. near the threshold condition) $R(x) \to c\sigma_T/2(x-1)^{3/2}$, while for $x \gg 1$ (i.e. ultra-relativistic limit) $R \to \frac{3}{4}c\sigma_T \ln x/x$. An accurate and simple approximation which takes into account both these regimes is given by:

$$R(x) \approx 0.652c\sigma_T\frac{x^2-1}{x^3}\ln(x)\,\mathrm{H}(x-1) \tag{4.53}$$

where $H(x-1)$ is the Heaviside function. The approximation reproduces accurately the behaviour near the peak at $x_{peak} \sim 3.7$ and over the range $1.3 < x < 10^4$ which usually dominates during the calculations.
At this point it is possible to calculate the optical depth value for the pair production mechanism $\tau_{\gamma\gamma}$ to be introduced in the simulation code. From its definition:

$$\tau_{\gamma\gamma}(\nu') = \sigma_{\nu'\nu'_t}n'(\nu'_t)\Delta R' \tag{4.54}$$

where $n'(\nu'_t)$ is the number density of the target photons per unit of volume. Introducing the cross section in terms of the annihilation rate $R(x)$ in its approximated

formula and integrating over all the possible target photon frequencies:

$$\tau_{\gamma\gamma}(\nu') = \frac{\Delta R'}{c} \int R(\nu', \nu'_t) n'_{\nu'}(\nu'_t) d\nu'_t \tag{4.55}$$

where ν' and ν'_t are the frequencies of the source and of the target interacting photons. Then, once this value is calculated, assuming that:

$$F_{syn+SSA+IC} = F_{syn+SSA} + F_{IC} \tag{4.56}$$

the overall photon flux considering synchrotron emission and self-absorption, IC and pair production is:

$$F_{tot} = F_{syn+SSA+IC} \left(\frac{1 - e^{-\tau_{\gamma\gamma}}}{\tau_{\gamma\gamma}} \right) \tag{4.57}$$

Similar considerations can be done also for the electron injection term. Assuming that the electron and positron arises with equal Lorentz factor γ and that $x_{peak} \sim 3.7$, a photon with energy $\omega_s \gg 1$ will mostly interact with a target photon of energy $\omega_t \approx 3/\omega_s$. Then, from the energy conservation condition:

$$2\gamma = \omega_s + \frac{3}{\omega_s} \approx \omega_s = \frac{h\nu'}{m_e c^2} \tag{4.58}$$

Following this assumption, the injection term can be calculated as:

$$Q_e^{pp}(\gamma, t') = 4 \frac{m_e c^2}{h} n_{\nu'}(\frac{2\gamma m_e c^2}{h}, t') \int d\nu'_t n_{\nu'}(\nu'_t, t') R(\frac{2\gamma m_e c^2}{h}, \nu'_t) \tag{4.59}$$

For the code implementation, first the annihilation rate functions $R(\nu', \nu'_t)$ and $R(\frac{2\gamma m_e c^2}{h}, \nu'_t)$ are precalculated in `kernel_pp_losses` and `kernel_pp_injection`. Then, at each simulation step the loss and the injection terms are calculated in `photon_pair_production`. The integrals are solved using the Scipy pacakage `integrate.simps` integrating over the ν-grid defined in the code.

4.3 Code Testing

During the code development, after some functions were implemented, I performed several checks in order to assure the validity of the implementation. Such tests involved comparisons with analytical results or with results from numerical modeling already published in literature. Some checks were also performed to evaluate the accuracy of the method and the error introduced in the numerical resolution of the kinetic equations when dealing with finite grids and approximate calculations.

Dynamics

In order to assure that all the quantities were correctly calculated I compared some of the code results with analytical prescriptions. One of the first test I did was to check the $R - t'$ relation. The analytical formula can be obtained with an integration of the differential equations. Recalling equation 4.3, it is possible to obtain from the

integration the analytical comoving time $t'_{an}(R)$ at a radius R as:

$$t'_{an}(R) = t_0 + \int_{r_0}^{R} \frac{dR'}{\Gamma\beta c} = t_0 + \frac{1}{\Gamma_0\beta c}\int_{r_0}^{R_{tr}} dR' + \frac{1}{\beta c}\int_{r_{tr}}^{R} \frac{dR'}{\Gamma(R')} \tag{4.60}$$

where we have splitted the integral calculation in the two regimes as described in equation 4.61. The integral can be solved assuming that R is before or after the transition radius R_{tr}:

$$t'_{an}(R) = \begin{cases} \frac{R}{\Gamma_0\beta_0 c} & R < R_{tr} \\ \frac{R_{tr}}{\Gamma_0\beta_0 c} + \frac{2}{c(5-s)}\left[\frac{R}{\Gamma(R)} - \frac{R_{tr}}{\Gamma(R_{tr})}\right] & R > R_{tr} \end{cases} \tag{4.61}$$

where in this calculation we have assumed for simplicity that $\beta \sim 1$, which is a valid approximation for $\Gamma \gg 1$.

Particle distribution

Analytical equations have been also derived for the particle energy distributions. Following the equations derived when assuming synchrotron radiation emitted by a distribution of particles $N(\gamma, t')$ injected with a power-law function, it is possible to derive analytical formulas valid in slow and fast cooling regime. From equations 3.65 and 3.66 it is possible to derive:

$$N(\gamma, t') = K_1 \begin{cases} \gamma^{-p}\gamma_{cool}^{-1} & \gamma_m < \gamma < \gamma_{cool} \\ \gamma^{-p-1} & \gamma_{cool} < \gamma < \gamma_{max} \end{cases} \tag{4.62}$$

valid in slow cooling regime, and:

$$N(\gamma, t') = K_2 \begin{cases} \gamma^{-2}\gamma_m^{1-p} & \gamma_{cool} < \gamma < \gamma_m \\ \gamma^{-p-1} & \gamma_m < \gamma < \gamma_{max} \end{cases} \tag{4.63}$$

valid in fast cooling regime. K_1 and K_2 are the normalization factors. Their values is calculated from the conditions:

$$K_1 \int_{\gamma_m}^{\gamma_{cool}} d\gamma\gamma^{-p}\gamma_{cool}^{-1} + K_1 \int_{\gamma_{cool}}^{\gamma_{max}} d\gamma\gamma^{-p-1} = N_{tot,inj}(R) \tag{4.64}$$

$$K_2 \int_{\gamma_{cool}}^{\gamma_m} d\gamma\gamma^{-2}\gamma_m^{1-p} + K_2 \int_{\gamma_m}^{\gamma_{max}} d\gamma\gamma^{-p-1} = N_{tot,inj}(R) \tag{4.65}$$

where $N_{tot,inj}(R)$ are the total number of injected particles at radius R which is calculated as:

$$N_{tot,inj}(R) = 4\pi \int_0^R R'^2 n(R) dR' = \frac{4\pi A R^{3-s}}{3-s} \tag{4.66}$$

then, the two integrals can be solved and the normalization factors can be calculated. The values of γ_m and γ_{max} are calculated as described in equations 3.38 and 3.59 or in case of protons from equations 3.40 and 3.62. For the values of γ_{cool}, recalling equation 3.52 a modified formula was used:

$$\gamma_{cool}(t') = \frac{6\pi m_e c}{\sigma_t B'^2 (t' - t'_{init})} \tag{4.67}$$

where I took into account the starting time of the simulation t'_{init} before which no electrons are injected in the system. Analogous considerations have been done also for protons, starting from equation 3.61. Despite this formula does not reproduce exactly the simulation evolution, since it is calculated assuming that the total emitted power is constant with time, it is anyway a good approximation. A comparison between the analytical electron distributions and the numerical ones in slow and in fast cooling regimes for simulations taking into account only synchrotron losses and assuming an homogeneous ISM or a stellar wind medium are shown in Figures 4.5 and 4.6. For both cases the normalizations and the slopes are well consistent and just few discrepancies can be seen. A difference which arises between the numerical and the analytical results is at the transition between the regimes. In the numerical simulations the transition between the cooled and the uncooled segments in the distribution is very gradual while in the analytical formula a sharp break is found. Moreover, in the fast cooling regime it is possible to see electrons accumulated for $\gamma < \gamma_{cool}(t')$, especially in the stellar wind case. These discrepancies are the result of the different electron populations which are injected at different times in the simulation. Each of this population will have its own cooling history, and its own cooling factor which changes with time. The sum up of these populations generates the gradual and smoothed behaviour and the accumulation of the electrons for $\gamma < \gamma_{cool}(t')$ in the fast cooling regime.

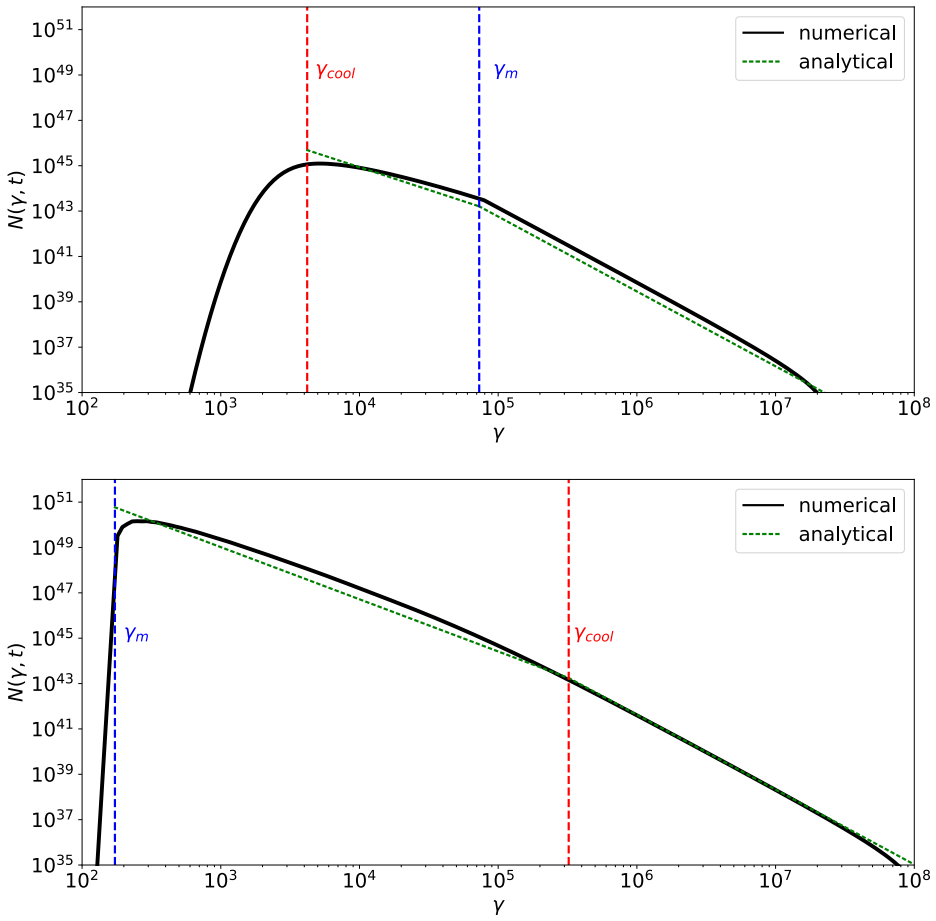

FIGURE 4.5: Electron lorentz factor γ versus electron number distribution $N(\gamma, t')$ in the homogeneous ISM case in fast cooling regime (top panel) and in slow cooling regime (bottom panel).

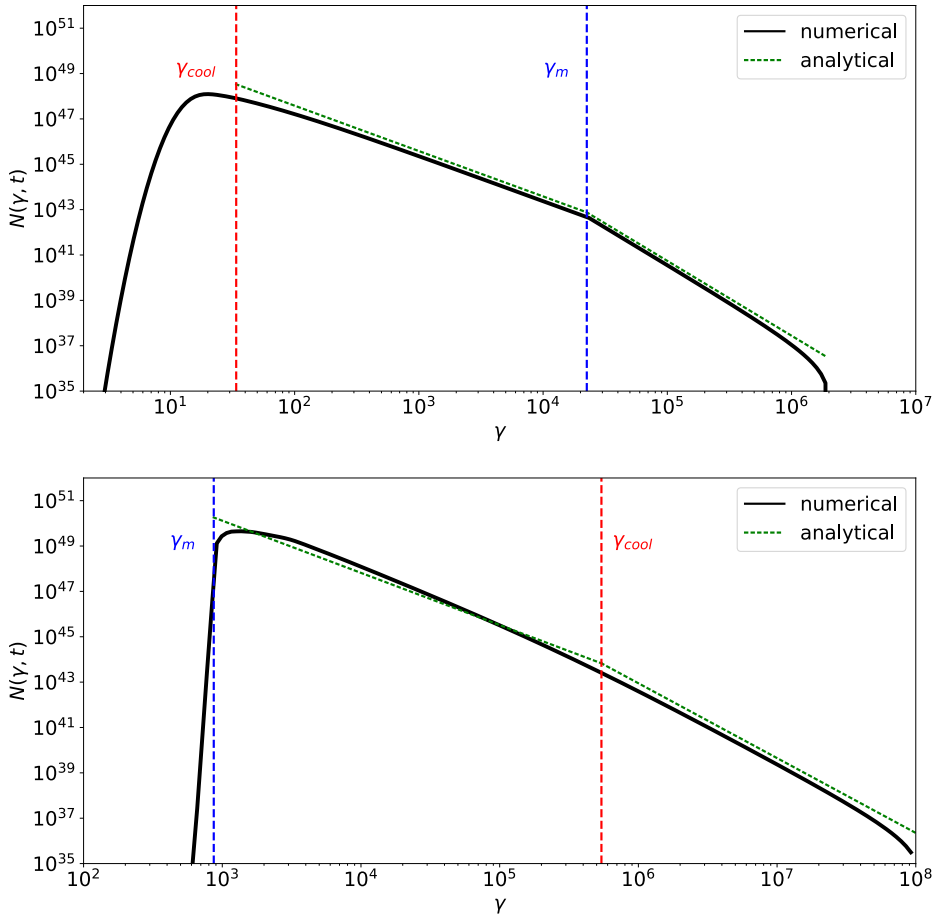

FIGURE 4.6: Electron lorentz factor γ versus electron number distribution $N(\gamma, t')$ in the stellar wind case in fast cooling regime (top panel) and in slow cooling regime (bottom panel).

Particle number conservation

An important check which is done at each step in the code to test that the evolution is behaving properly concerns the conservation of the injected particle number in the system. At the i-th step the particle number distribution $N(\gamma, R_i)$ calculated numerically and the total number of injected particles $N_{tot,inj}(R_i)$ calculated analytically are derived. $N(\gamma, R_i)$ will contain the sum of all the electrons injected from the starting radius R_{init} up to R_i distributed in γ. In order to assure that the injection works correctly and particles are not lost during the evolution it should be valid that:

$$\frac{\int_1^{10^8} N(\gamma, R_i) d\gamma}{N_{tot,inj}(R_i) - N_{tot,inj}(R_{init})} \approx 1 \tag{4.68}$$

where the integral is calculated over the γ-grid where the lower and upper edge are 1 and 10^8. $N_{tot,inj}(R_{init})$, which is the number of electrons injected for $R < R_{init}$, is subtracted since in the simulation these particles are ignored. This assumption does not affect too much the simulation results even when large values of $t_{obs,init}$ are given as input. Indeed, after some steps the number of electrons injected in the simulations are always larger and dominate with respect to the electrons which have been ignored since $N_{tot,inj} \propto R^{3-s}$. In the simulation usually the ratio calculated in

equation 4.68 ranges between 0.95 and 1.05, therefore the code conserves particles with about 5 % accuracy.

SEDs and LCs

Analytical prescriptions can also be used to test the radiation emission obtained in the code, comparing the analytical and the numerical SEDs and light curves. For this test I made use of the analytical spectra and lightcurves derived from SPN98 (for the homogeneous ISM case) and PK00 (for the stellar wind case) to test the synchrotron emission and the synchrotron self-absorption and the spectra derived from SE01 for the IC emission. A comparison between the SPN98 and the PK00 analytical curves and the numerical ones are shown in Figures 4.7 and 4.8 when synchrotron emission and self absorption only are considered in the homogeneous ISM and in the stellar wind scenario. In Figure 4.9 the corresponding light curves for three frequencies representative of the X-ray, optical and radio band observations are shown. When introducing also adiabatic losses and the IC emission, also SE01 and numerical results are compared. Such comparison is shown in Figures 4.10 and 4.11 with the same settings as before. The break frequencies are calculated from analytical prescriptions as described by equation 3.68 for SPN98, equation 3.99 for SE01 and similar equations derived in PK00.
From the comparison it can be clearly seen that the analytical results have sharp breaks which deviate from the actual curved radiation spectrum. Slopes in the different regimes are in agreement but the SEDs and the light curves obtained in the simulation show a smoother behaviour. As a result, when approaching a break frequency the curve does not exhibit a sharp break but it gradually changes the slope. This is the same effect seen in the electron distribution spectra. Regarding the flux normalization, there are small discrepancies between the numerical and analytical results. This is due to the fact that in analytical prescriptions it is assumed that radiation is entirely emitted at the characteristic synchrotron frequency. On the other hand, in the code the synchrotron spectrum of a single electron summed up over the electron distribution is taken into account. Similar considerations can be also done for the IC component when comparing with the SE01 analytical spectra. The discrepancies observed between analytical and numerical IC spectra arise naturally as the amplified effect of the differences observed in the synchrotron spectra. When introducing also the adiabatic losses it can be seen that the synchrotron spectra change slightly their shape, affecting primarily the low energy electrons.

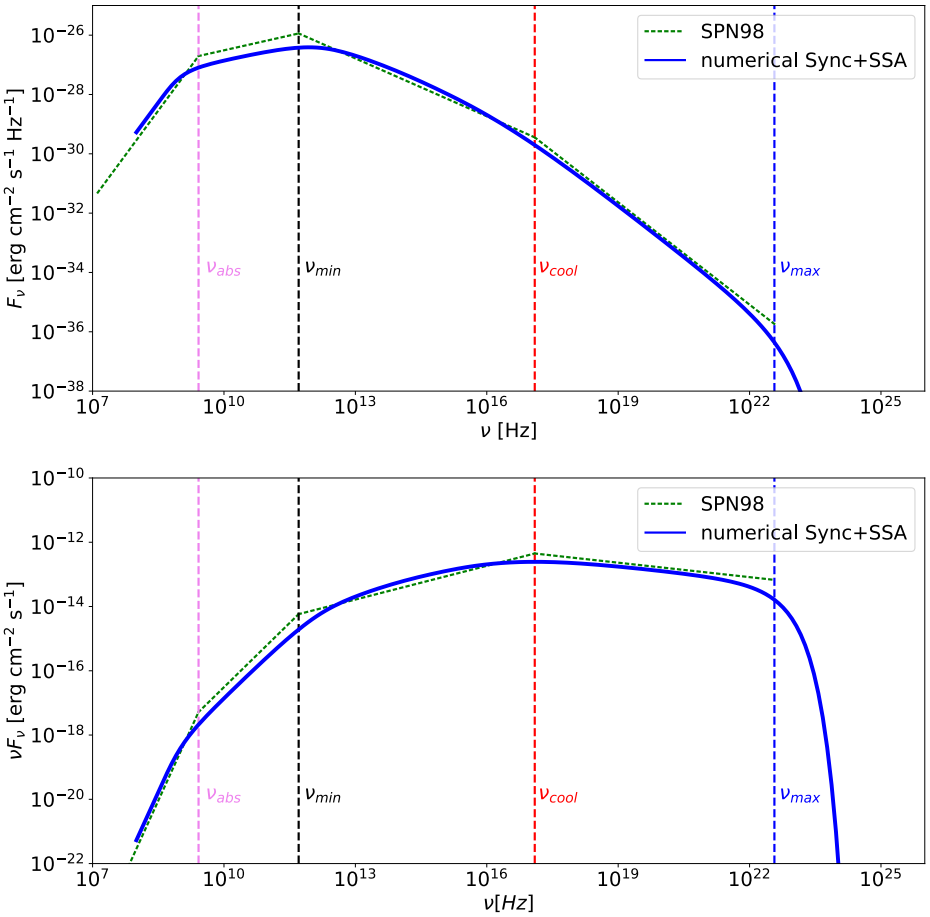

FIGURE 4.7: F_ν (Top panel) and νF_ν (bottom panel) spectra for $s = 0$ at $t = 1 \times 10^4$ s with synchrotron emission and self-absorption only. The analytical comparison is the one given in SPN98. The input parameters used for this simulation are $p = 2.3$, $\epsilon_e = 0.05$, $\epsilon_B = 0.0005$, $E_k = 10^{52}$ erg, $A_0 = 1$ cm^{-3}, $\Gamma_0 = 400$, and $z = 1$.

I performed a test for the pair production mechanism exploiting an analytical approximated result. The idea is to compare the value of the optical depth $\tau_{\gamma\gamma}(\nu')$ with a corresponding analytical approximation $\tau_{\gamma\gamma,\mathrm{an}}(\nu')$. The analytical approximation is calculated, recalling equation 4.54:

$$\tau_{\gamma\gamma}(\nu') = \sigma_{\nu'\nu'_t} n'(\nu'_t)\Delta R' \tag{4.69}$$

considering only the target photons of energy $\omega_{targ} \approx 3/\omega_s$ and corresponding frequency $\nu'_{targ} = \frac{3m_e c^2}{h\omega_s}$, this means introducing a delta function $\delta(\nu'_t - \nu'_{targ})$ in the integral in equation 4.55. As a result, equation 4.69 can be rewritten as:

$$\tau_{\gamma\gamma,\mathrm{an}}(\nu') = \frac{\Delta R' \sigma_T}{5} n'_{\nu'}(\nu'_{targ})\nu'_{targ} \tag{4.70}$$

assuming that $\sigma_{\nu'\nu'_{targ}} \approx \sigma_T/5$ which is valid at the maximum, and $n'(\nu'_{targ}) \approx n'_{\nu'}(\nu'_{targ})$ ν'_{targ} where $n'_{\nu'}(\nu'_{targ})$ is the photon number density per unit of volume and frequency. A comparison between $\tau_{\gamma\gamma}(\nu')$ and $\tau_{\gamma\gamma,\mathrm{an}}(\nu')$ is shown in Figure 4.12. The two behaviours are very similar, which confirms that the numerical approach that was defined works properly.

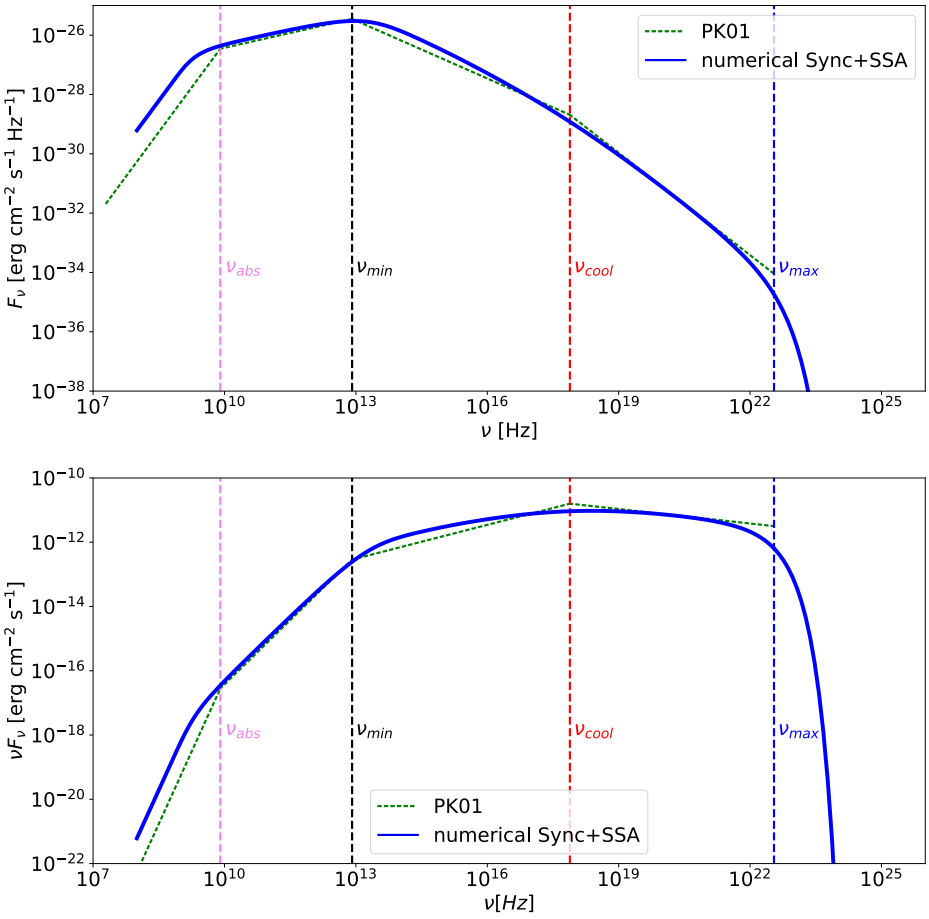

FIGURE 4.8: F_ν (Top panel) and νF_ν (bottom panel) spectra for $s = 2$ at $t = 1 \times 10^4$ s with synchrotron emission and self-absorption only. The analytical comparison is the one given in PK00. The input parameters used for this simulation are $p = 2.3$, $\epsilon_e = 0.2$, $\epsilon_B = 5 \times 10^{-6}$, $E_k = 10^{53}$ erg, $A_* = 1$, $\Gamma_0 = 100$, and $z = 1$.

Another check of the code I performed was a comparison with the results obtained in PVP14. In Figure 4.13 a set of electron and the photon spectra calculated with `MUSE-GRB` are shown. These results reproduce Figure 1 of PVP14. Several simulations with different combinations of radiation processes and the analytical results from SPN98 are presented. The same dynamical evolution presented in PVP14, which is slightly different from the one developed for my code, was followed activating the input code parameter `test` previously mentioned. The results obtained from `MUSE-GRB` are consistent both for the electrons and for the photons spectra with those shown in PVP14. The flux normalization and the spectral slopes of the different radiation components, the positions of the peak and break frequencies appear identical. Despite the IC component and the pair production mechanisms were treated with slightly different assumptions, no big differences can be seen between the results of the two codes. Morevoer, this test shows clearly that the adiabatic cooling mostly affects the low energy electrons and photons. Indeed, when this mechanism is added in the simulation, the electron and photon distributions have a more flat behaviour in the low energy side. Once again it can be seen that the analytical spectrum does not reproduce the smoothed behaviours clearly evident in the numerical simulations. As a result, fitting the observed GRB afterglow with analytical spectra may

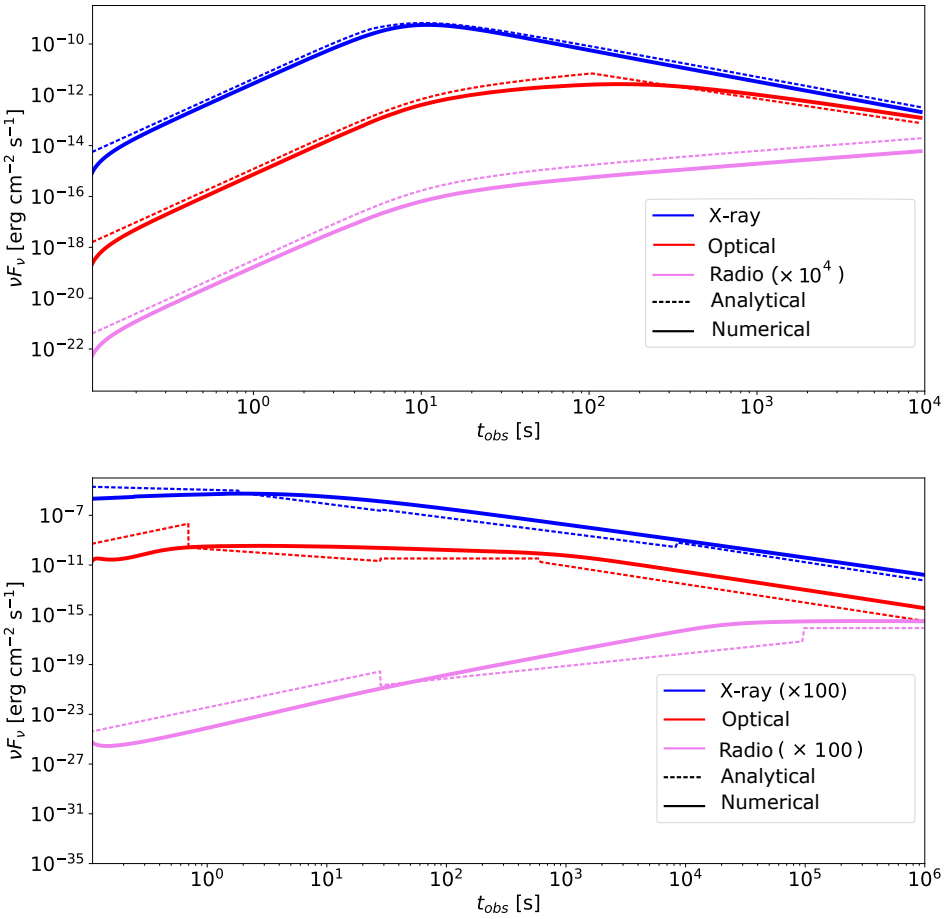

FIGURE 4.9: Light curves for $s = 0$ (top panel) and $s = 2$ (bottom panel) with synchrotron emission and self-absorption only for three different frequencies: 2.4×10^{18} Hz (X-ray), 6.46×10^{14} Hz (optical), 1.3×10^{9} Hz (radio). The analytical comparisons are the ones from SPN98 and PK00.The input parameters used are the same listed in Figure 4.7 for $s = 0$ and Figure 4.8 for $s = 2$.

lead to an inaccurate determination of the forward shock parameters. Numerical code as `MUSE-GRB` can give more precise results which can be very useful to model the observed GRB afterglow emission. The IC emission adds a second "*bump*" which is the one observed in the VHE component from GRBs. In this simulation the pair production mechanism does not affect too much the results, just slightly changing the photon spectrum behaviour for the high energy tail. These tests show that under the assumptions on which analytical prescriptions are derived, `MUSE-GRB` is able to reproduce their results consistently. On such basis, the code can be then used also to explore the conditions in which the analytical prescriptions are not valid anymore (e.g. when the KN effects become relevant). This is fundamental to test frameworks which could be of great interest to explain and investigate the nature of some of the observed GRBs.

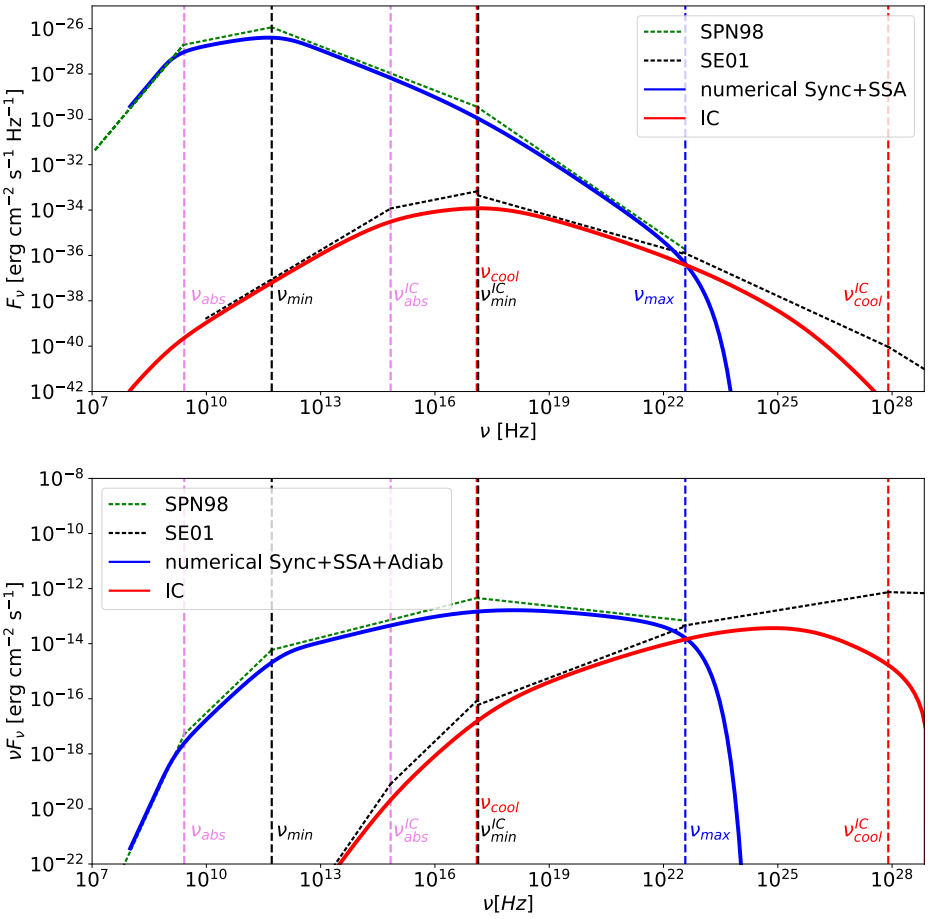

FIGURE 4.10: F_ν (Top panel) and νF_ν (bottom panel) spectra for $s = 0$ at $t = 1 \times 10^4$ s with synchrotron emission and self-absorption, adiabatic losses and IC. The analytical comparisons are the ones given in SPN98 and SE01. The input parameters used are the same listed in Figure 4.7.

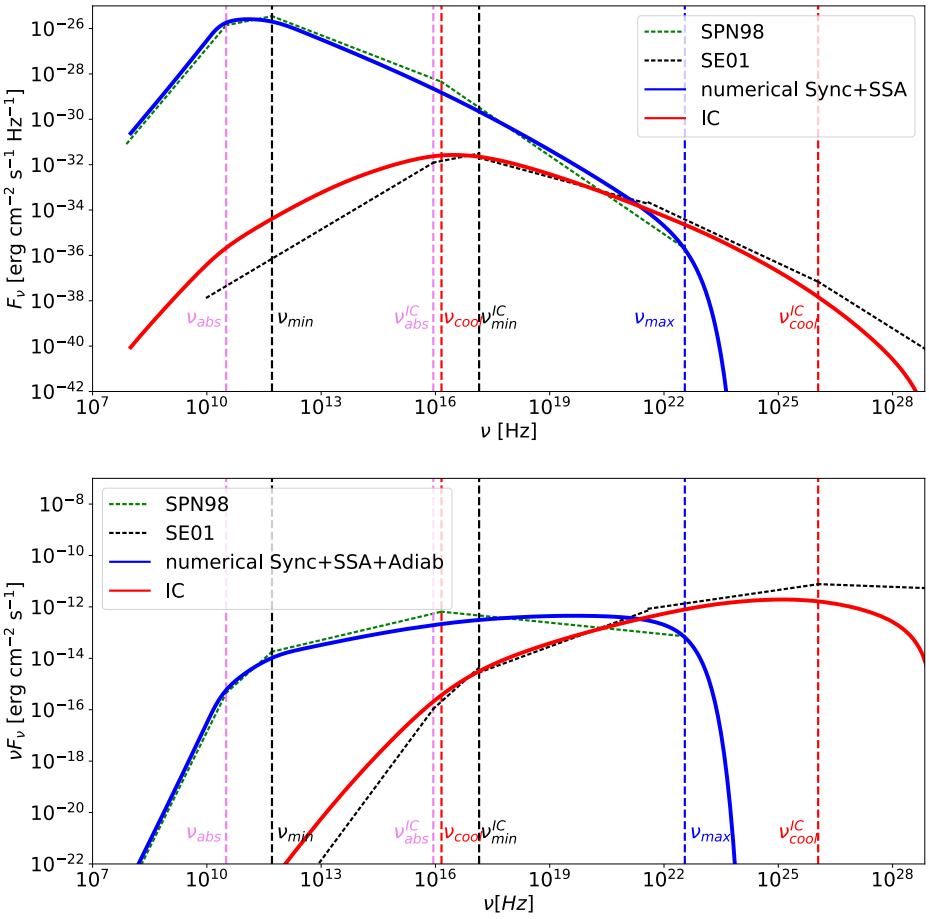

FIGURE 4.11: F_ν (Top panel) and νF_ν (bottom panel) spectra for $s = 2$ at $t = 1 \times 10^4$ s with synchrotron emission and self-absorption, adiabatic losses and IC.The analytical comparisons are the ones given in PK00 and SE01. The input parameters used are the same listed in Figure 4.8.

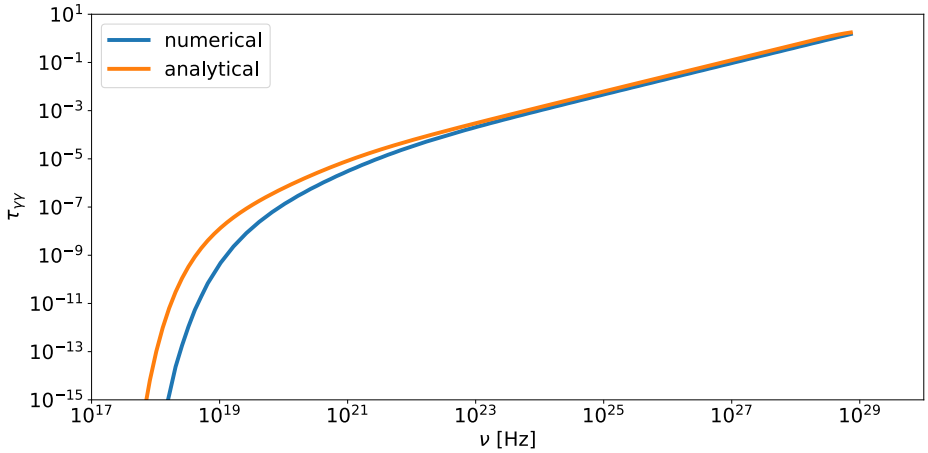

FIGURE 4.12: Frequency versus optical depth $\tau_{\gamma\gamma}(\nu')$ calculated by `MUSE-GRB` (blue line) and approximated analytical formula (orange line).

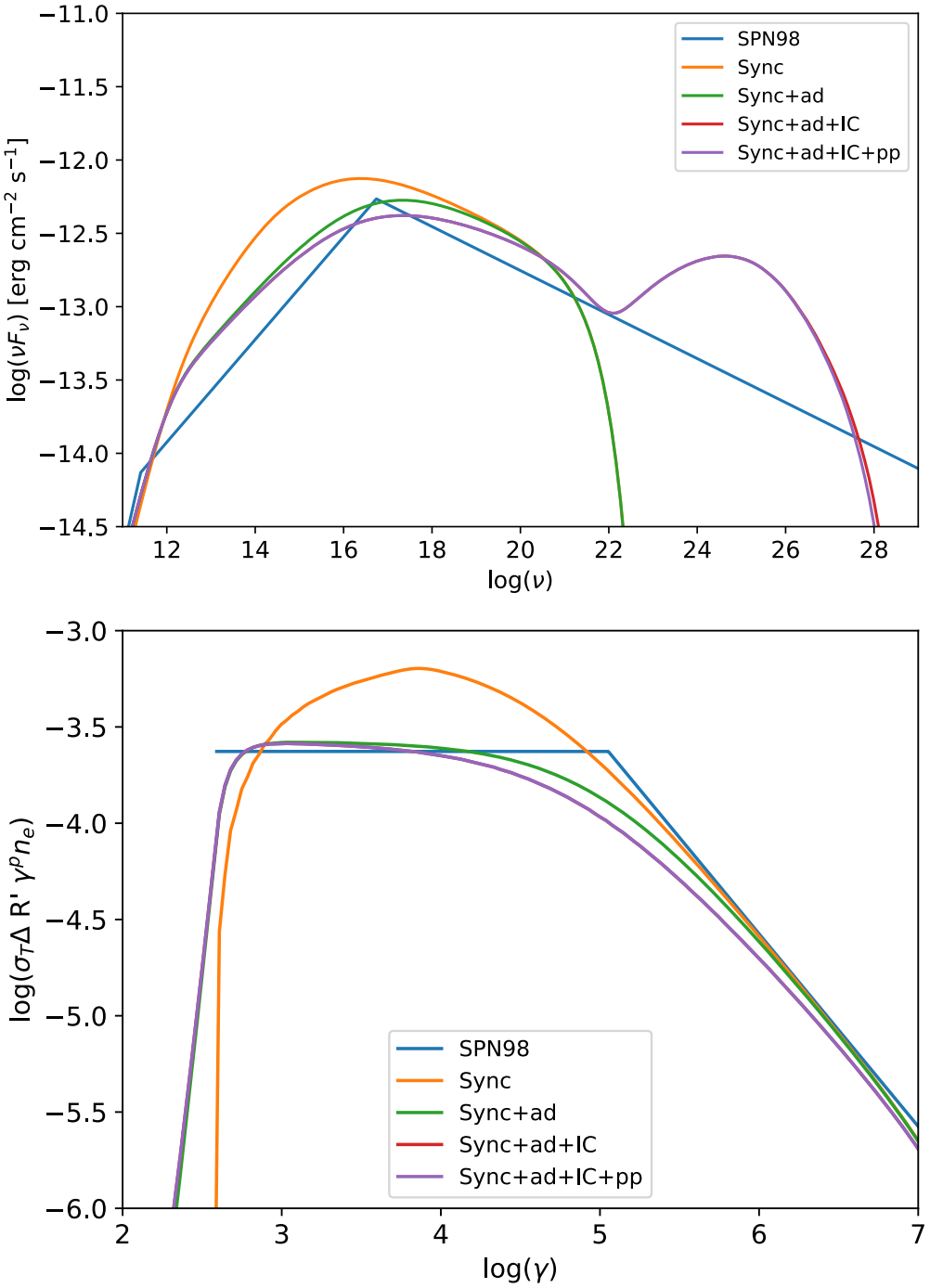

FIGURE 4.13: Simulated photon spectrum in the observer frame with `MUSE-GRB` (top panel) and electron distribution in the fluid frame (bottom panel) at $R = 3.4 \times 10^{17}$ cm. The radiation mechanisms (listed in the legend) have been added one by one to assess their effect on the electron and photon spectra. The analytical result from SPN98 has also been added. The simulation parameters are $E_k = 10^{53}$ erg, $A_0 = 1$ cm^{-3}, $s = 0$, $\epsilon_e = 0.1$, $\epsilon_B = 10^{-3}$, $\Gamma_0 = 400$, $p = 2.3$ and $z = 1$. The value of the maximum Lorentz factor for electron injection was assumed to be a constant value $\gamma_{max} = 4 \times 10^7$. The figure reproduces consistently Fig.1 of PVP14.

Chapter 5

MAGIC data analysis and modeling of gamma-ray bursts

During my PhD, as a member of the MAGIC collaboration, I performed data analysis of several **GRBs observed by MAGIC** and I interpreted some of these results by means of `MUSE-GRB`.
The results of my analysis on GRB 190114C served as a test for the final dataset published in the paper announcing the discovery of TeV radiation from GRBs [165]. In this article, I also derived the synchrotron burnoff limiting curves for GRB 190114C. In the context of the proton synchrotron radiation, a simple analytical estimate was proposed in the paper. I performed a more accurate modeling of the data in this scenario using `MUSE-GRB`. In addition, I performed a dedicated MAGIC analysis for a second companion paper where all the multi-wavelength data from this event have been collected, and the TeV emission has been interpreted as SSC radiation. I am one of the main corresponding authors of this study [121], where for the first time a SSC emission component from GRBs has been unequivocally identified. Both papers have been published by *Nature*.
More recently, my research activity has been focused on the MAGIC data analysis and multi wavelength studies of several GRBs non-detected by MAGIC. These results will be included in a *GRB catalog paper* which is currently in preparation. I am involved in this project, which is at an advanced stage, as one of the main authors.
The third project which is still ongoing involves the analysis and interpretation of GRB 190829A, an event of particular interest for the GRB community which shows a possible hint of detection from the preliminary MAGIC data analysis. The analysis I performed on such event and the public data available gave me the possibility to build a multi-wavelength observational dataset to be modeled with `MUSE-GRB`. A Preliminary modeling for GRB 190829A will be presented in this chapter.
The chapter is organized as follows: first the MAGIC observational strategy for GRBs is presented (Section 5.1). Then, the studies I performed on the event GRB 190114C (Section 5.2), on the sample of the non-detected GRBs observed with MAGIC from 2013 to 2019 (Section 5.3) and on GRB 190829A (Section 5.4) are presented.

5.1 Observation of GRBs with MAGIC

Transient phenomena as GRBs appear randomly on the celestial sphere with no possibility to know in advance their position and explosion time. Since the MAGIC telescopes, with their small field of view and low duty cycle, cannot survey the entire sky in search for these events an *external trigger* from other instruments and a fast and efficient *alert system* are needed. Therefore, observations of these sources

with MAGIC will always be affected by a time delay. Moreover, since GRBs are cosmological objects, in the VHE domain the emission is heavily affected by the EBL absorption. As a result, the number of photons reaching the Earth will be dramatically reduced, especially for $E > 100$ GeV. The use of the lowest possible energy threshold to overcome the EBL absorption is mandatory.
The external trigger is given by space-satellite instruments which can scan large fractions of the sky. The current system used to provide information regarding GRB observations to the scientific community is the **Gamma-ray Coordinates Network (GCN)**. It constitutes a link between space satellites that provide a full time GRB monitoring and the ground-based instruments. The GCN system is mainly composed by two distinct parts:

- **GCN Notices**: they are real time information packets produced by space satellites that distribute locations of GRBs and other transients. They are simple text messages and internet socket packets produced automatically into a standard format. Their generation is completely automatized and they are distributed to the community with time delays from few seconds to few minutes;
- **GCN Circulars**: they are reports of follow up observations made by ground based or space telescopes distributed to the entire GRB community. They are also used to send updated information about a specific event.

The GCN Notices distribution usually occurs through binary packets via socket, i.e. 160 bytes packet composed of 40 long words (4-byte integers). Despite the information given are very similar, there is no standard packet to be distributed, and each instrument can put different information. For a detailed list of the items contained in the different binary packets, see `https://gcn.gsfc.nasa.gov/sock_pkt_def_doc.html`.
Once the GRB position is distributed via GCN Notice, the MAGIC telescopes should be able to quickly react. The **MAGIC automatic alert system** was created to cope with this scope. This system manages the communication both with the GCN and the MAGIC CC, decoding the possible incoming GCN alerts. It substantially consists of a daemon (a multi-thread C program running in background full time in La Palma) monitoring 24 hours a day the GCN. In case of a GRB alert, it retrieves the information from the 40 long words of the GCN package using bit-masks provided by the GCN team. The alert is stored into a list and the observability of the GRB is computed according to some predefined criteria defined in the GRB observation strategy (see next paragraph). If the criteria are fullfilled and the observation is possible, it communicates to the CC the occurrence of the GRB with time and coordinates of the event and the informations are translated into human-readable language and sent by email to the GRB working group. As the alert string is received, the CC starts the full automatic procedure that stops the current observation and fast repoints the telescopes on the GRB coordinates. To lower the chance of hardware failures, the automatic procedure was revised in 2013: the DAQ is not stopped during slewing and the trigger tables are changed in the same movement.
The GRB observational criteria are constraints related to the positions of the source, the Sun and the Moon:

- the Sun must be below the astronomical horizon ($Zd > 103^\circ$);
- the Moon must have at least 30° of angular distance from the GRB coordinates;
- the Zd for GRB observation has to be smaller than 60°.

Such conditions allow to perform the observation at the MAGIC local site in La Palma and to reduce the energy threshold of the analysis. Once these conditions are fulfilled, the visibility of the target is computed. Until December 2019, the visibility was checked up to 4 hours starting from the time of the event trigger T_0. This strategy was revised after GRB detections of 2019 which show that also late-time observations can lead to detections. In the current strategy, the visibility is checked for the whole night after or within which they occur. If a GRB is tagged as observable, it will be observed for a maximum of 4 hours from the moment it becomes observable. It can happen that a GRB occurring late in one night is observable early in the following night. In this case, a standard ToO could be requested depending on the information received for the GRB.
Through the MAGIC Collaboration it was decided to appoint a person, called *Burst Advocate* (BA) who is in charge of monitoring the follow-up of transient sources. Whenever a transient observation is performed, the BA is contacted by the shifters at the MAGIC site to manage and check that the observation is performed without problems. With the help of the shifters, he/she should check that the trigger table and the DT used are fine, the mirrors are aligned and the DAQ rate is stable and within the limits. In search for a detection, he/she should monitor the MOLA results. Moreover, the BA should check the GCN Circulars for the GRB. Indeed, in case of MAGIC detection or if multi wavelength observations contain relevant physical information which could increase the possibility of a detection (e.g. low redshift) the BA can prolong the observation beyond the default maximum observation time of 4 h. Since GCN Circulars are released also hours after the trigger, the BA should check them also during the day. This is especially true for GRBs detected by Fermi-LAT which are very good candidates for MAGIC detections even several hours from the onset. In the past, some so-called *late-time* observations of Fermi-LAT detected GRBs have been performed by MAGIC. The day after, the BA should report to the collaboration the observation and perform a fast analysis of the data. The BA role, initially born for GRB observations, has now been extended to several other time-critical observations such as GW events or neutrino events. I acted as BA several times during my PhD.
Since 2005 and up to November 2020 MAGIC followed-up without hardware problems **125 GRBs** (see Figure 5.1) with 46 of them with known redshift. The number of GRBs observed with a delay lower than 100 seconds from their trigger time is 30, so 24% of the total (see Figure 5.2). The GRB with the minimum delay (GRB 160821B) was observed 24 s after T_0. Despite they constitute a good sample, in most of the cases GRBs are observed with longer delays due to bad weather conditions or observational criteria not fulfilled at the moment of the GRB alert. The number of GRBs with redshift z (see Figure 5.3) less than 1.5 is 21. The GRB observed with lowest measured redshift ($z = 0.0785$) is GRB 190829A, while the one with highest redshift ($z = 6.3$) is GRB 050904.
GRBs observed in the period 2005-2006 were published into a catalog paper [191]. Since no detections were found, flux ULs have been calculated for the first 30 minutes of observation in the energy range [0.08 - 1.0] TeV. ULs were compared, in the case of redshift estimation, with a power-law extrapolation from lower energies taking into account the EBL absorption and were found to be compatible with such assumption. For GRB 050713A, a detailed temporal analysis in search for γ-ray emission was performed since it was the first GRB observed in the prompt emission phase by an IACT [192, 191]. Despite this effort, no significant signal was found.
Other two past GRBs observed by MAGIC and published are GRB 080430 [193] and

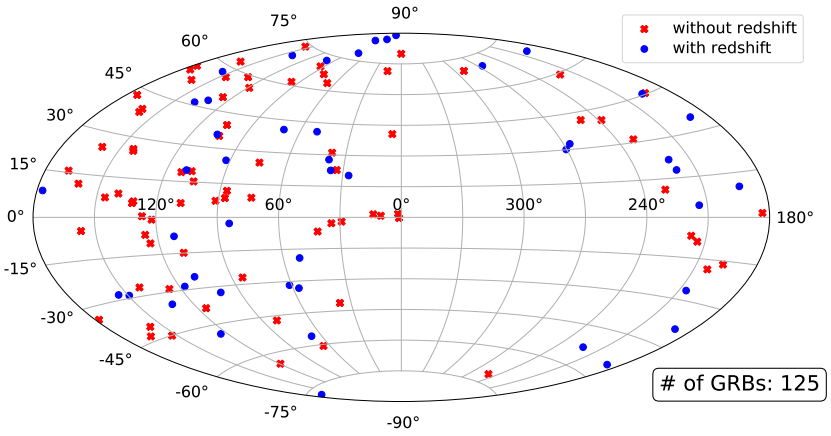

FIGURE 5.1: Skymap in galactic coordinates of the GRBs observed by MAGIC from 2004 up to November 2020. Courtesy of Alessio Berti.

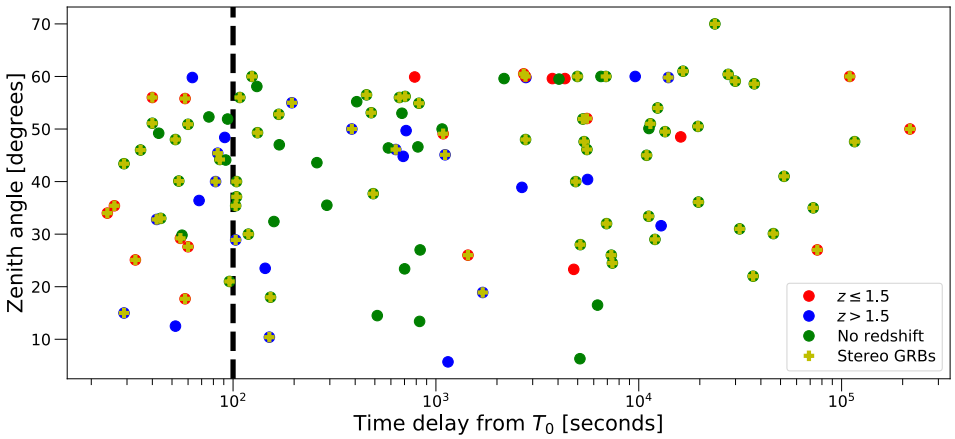

FIGURE 5.2: Time delay from trigger time of the MAGIC observed GRBs versus the zenith angle. Courtesy of Alessio Berti.

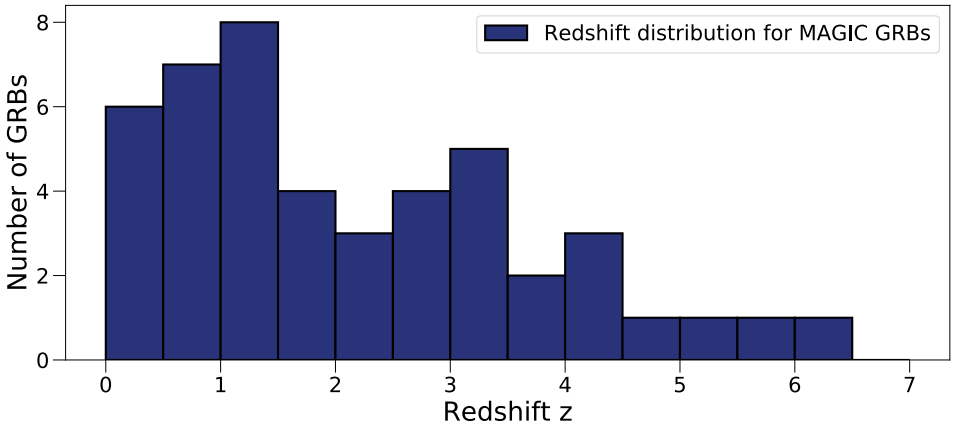

FIGURE 5.3: Redshift distribution (0.5 binning) of MAGIC GRBs observed up to November 2020. Courtesy of Alessio Berti.

GRB 090102 [194]. For both of them ULs were computed trying to reach the lowest possible energy threshold. In the latter case, GRB 090102 was observed with the Sum-Trigger system reaching an energy threshold of 30 GeV and also Fermi-LAT ULs were derived. The ULs were then compared with theoretical models of SSC from electrons and proton synchrotron. These studies conclude that it was not possible to rule out leptonic nor hadronic additional components.
After the upgrade of the automatic procedure of 2013, the MAGIC GRB group focused on several projects, some of them still in progress, namely:

- **GRB 160821B**: it is a short GRB with redshift $z = 0.16$ and evidence of a coincident kilonova, followed up by MAGIC starting from 24 sec after the burst trigger. Despite non-optimal observing conditions, hints of a gamma-ray signal are found above ~ 500 GeV a few hours after the burst. Assuming that the signal was real, the multi-wavelength observations were compared with several afterglow models. Preliminary results have been presented in conferences [195] and published in [196].

- **GRB 190114C**: the first GRB ever detected by the MAGIC telescopes. As mentioned in the previous chapter, two papers have been published regarding its discovery and the multi wavelength modeling. The results will be presented in detail in Section 5.2.

- **GRB catalog paper** it will include the overall sample of GRBs observed after the automatic procedure upgrade, in the period 2013-2019 (except for the previously mentioned GRB which will have a stand-alone publication). The details of this project will be described in Section 5.3.

- **GRB 190829A**: it is a long GRB with low redshift ($z = 0.0785$) followed-up by several instruments in the radio, optical, X-ray and HE bands and detected in the VHE domain by H.E.S.S. MAGIC followed-up the event ~ 30 hrs after the trigger time, as soon as it was visible from La Palma. Preliminary analysis showing a possible hint of detection is presented in Section 5.4. Further studies are still ongoing.

During my PhD, I actively took part to GRB 190114C, GRB 190829A and GRB catalog paper projects. I will now describe in detail these projects pointing out my contributions.

5.2 GRB 190114C

GRB 190114C was the first GRB ever detected by the MAGIC telescopes. As mentioned in the previous chapters, such discovery, together with the H.E.S.S. detection of GRB 180720B, opens a new era for the study of the GRB physics. Several auxiliary checks regarding the behaviour of the subsystems during the automatic repointing and in the first seconds of observations were done. Moreover, sets of dedicated MCs matching the GRB observation conditions as much as possible were generated. Such huge amount of work was done to verify the robustness of the dataset and to exploit as much as possible the collected data. Given the importance of such detection, detailed systematic and statistical studies on the GRB dataset were also performed. Several people from the MAGIC Transient group participated in the analysis and interpretation of the data, and in writing and editing the two resulting papers. I was part of the *analysis team* which took care of the MAGIC data analysis. The main

other people in the team, the so-called *analyzers*, were Koji Noda, Alessio Berti, Elena Moretti, Yusuke Suda, and Satoshi Fukami. Each analyzer has performed its own analysis independently. Then, the analyses have been cross-checked to assure that consistent results were obtained.

5.2.1 The GRB picture

Observations and general properties

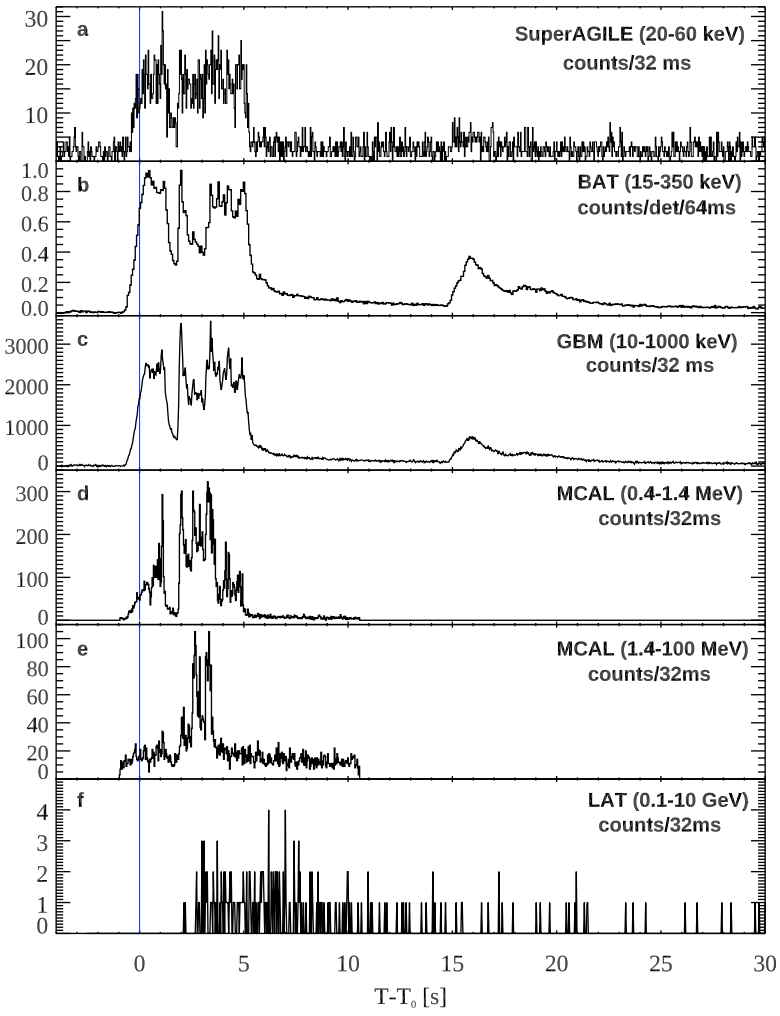

FIGURE 5.4: GRB 190114C prompt light curves from several instruments. From [121].

GRB 190114C is a long GRB triggered by Swift-BAT [197] and Fermi-GBM [198] space instruments on 14 January 2019, 20:57:03 UT. The event was detected also by several other space instruments, namely Fermi-LAT, Swift-XRT, Swift-UVOT, AGILE, INTEGRAL/SPI-ACS, Insight/HXMT, and Konus-Wind [121]. Triggered by space satellite alerts, the event was then followed-up and detected by MAGIC and several optical-NearInfraRed (NIR) and radio ground based telescopes. With such a huge multi-wavelength campaign, which covers the entire electromagnetic spectrum from 1 up to 2 $\times 10^{17}$ GHz, it was possible to estimate the general properties of this event both for the prompt and for the afterglow phases.

The prompt light curve showed a bright multi-peak structure with a total duration of about 25 s (see Figure 5.4). The duration of the burst is not unambiguously identified since $T_{90} \approx 116$ s by Fermi-GBM and $T_{90} \approx 362$ s by Swift-BAT. The total radiated energy is calculated as $E_{iso} = (2.5 \pm 0.1) \times 10^{53}$ erg (isotropic equivalent) in the energy range 1–10^4 keV [199]. The prompt light curve exhibits a quiescent phase between two prompt pulses in the time interval 5-15 s. The smooth power-law decay observed during this phase, which is similar to the one observed at the end of the last prompt pulse ($t > 25$ s), can be interpreted as the onset of the afterglow component. Support to such interpretation is also obtained from a joint spectral and temporal analysis of the Fermi-GBM and Fermi-LAT data [200].

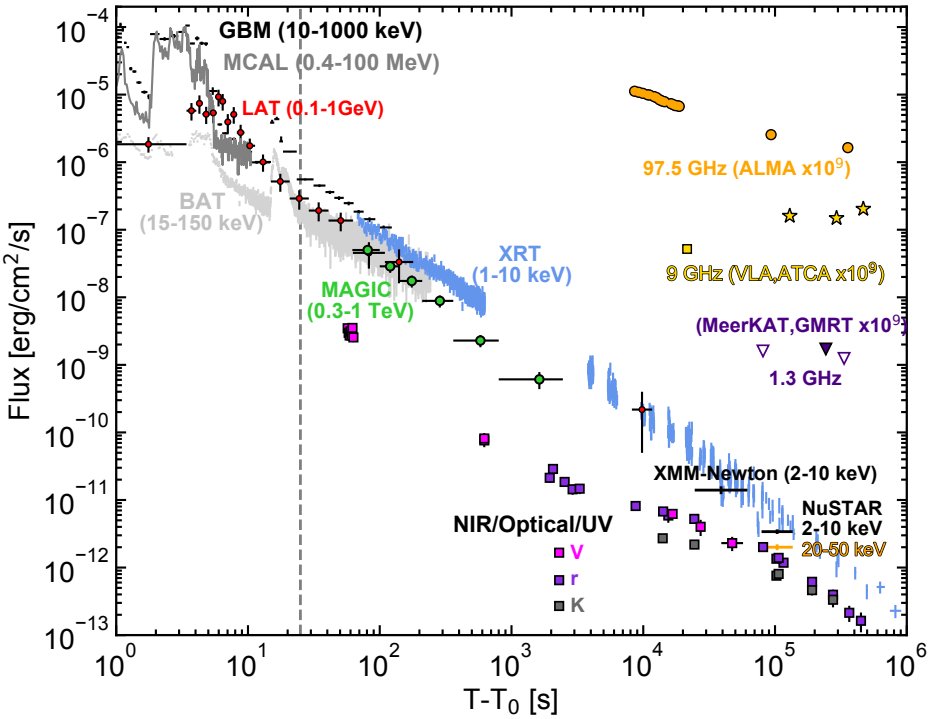

FIGURE 5.5: Broadband light curves of GRB 190114C. Data from radio up to γ-rays are included. The vertical dashed line marks approximately the end of the prompt phase, identified as the end of the last flaring episode. Adapted from [121].

In Figure 5.5 multi-wavelength light curves of GRB 190114C are reported. After ~ 60 s Swift-XRT started observations. The light curve in the 1-10 keV energy band is consistent with a power-law decay $F \propto t^{\alpha}$ with $\alpha = -1.36 \pm 0.02$ [121], consistently with expectations from the synchrotron external forward shock behaviour. XRT observation lasts until $\sim 10^6$ s. The NIR, optical and UV data were taken from around ~ 100 s. The Nordic Optical Telescope evaluate a redshift of $z = 0.4245 \pm 0.0005$ [201] which was then confirmed by Gran Telescopio Canarias [202]. The first part of the emission, characterized by a fast decay, is interpreted as dominated by the reverse shock component. Afterwards, the behaviour is consistent with the synchrotron external forward shock scenario. Radio data were taken from $\sim 10^4$ s and exhibit an initial fast decay in which the emission is most likely dominated by the reverse shock, followed by emission at late times with nearly constant flux.

MAGIC observation

The timeline of the MAGIC observation can be described as follows:

- The MAGIC observation was triggered by the Swift-BAT alert, received by the MAGIC automatic alert system at 20:57:25 UT (T_0 + 22 s). The alert was validated, the event tagged as observable and the automatic fast repositioning procedure started;
- the telescopes reached the target and started tracking respectively at 20:57:52.858 UT (for MAGIC-I) and 20:57:53.260 UT (for MAGIC-II) (T_0 + 50 s);
- the DAQ started receiving the first events at 20:58:00 UT (T_0 + 57 s);
- the DAQ system operated stably from 20:58:05 UT (T_0 + 62 s);
- observation was prolonged and lasted until 01:22:15 UT (T_0 + 15912 s) when $Zd = 81.14^\circ$ was reached.

Therefore, the automatic procedure took approximately 27 s to repoint the GRB position. After about one minute from the trigger time the data taking rate was stable. The observation was performed in *moderate* Moon conditions, with a mean DC $\sim$ 6.9 μA for M1 resulting in a NSB approximately 6 times higher than in dark conditions, and in the high zenithal range, starting from 55.8° up to 81.14°. The LIDAR was not operating during the night of the observation but the other auxiliary systems (Starguider, pyrometer, stable DAQ rates) and the shifters in La Palma reported very good weather conditions. Considering the non-standard conditions in which the observation started, several auxiliary checks were performed to investigate the behaviour of the subsystems during the automatic repointing. The main tests performed were:

- **pointing precision**: usually the Starguider camera pointing correction is applied to the data at `star` level but it sometimes failed during moon observations. For these data, a special method was applied to double the precision of the correction. The reports from the drive system, which are produced every 1 s, have been merged through `merpp` with the data. Thanks to such method, it was derived that M1 pointing deviation was $<$ 1 arcmin at $\sim$ 20:58:30 ($\sim$ 30 s after DAQ start) and M2 pointing deviation was $<$ 1 arcmin at $\sim$ 20:58:15 ($\sim$ 15 s after DAQ start);
- **camera oscillation measurements**: at the end of the slewing, the cameras on the telescopes oscillated for a short time. Subsequently, dedicated tests were performed to reproduce the movement of the telescopes. The results show that the duration of the oscillations was less than 10 s after the start of the tracking, and their amplitude was less than 0.6′ when data taking began;
- **behaviour of DTs, rates and IPRC**: the evolution of the DT, the IPR and the DAQ rate during the repointing from the previous source (which was Perseus-MA) to the GRB position were checked. The study confirmed that the system operated stably from 20:58:05 UT (T_0 + 62 s) and the DT stabilized from 20:58:21 UT (T_0 + 78 s) (see also Figure 5.7);
- **effective time check**: the first seconds of calibrated data have been checked to establish when the first events started to be stored and to exclude possible data loss. No issues were found from approximately 20:58:04 UT (T_0 + 61 s);

5.2.2 MAGIC Data Analysis

Preliminary results

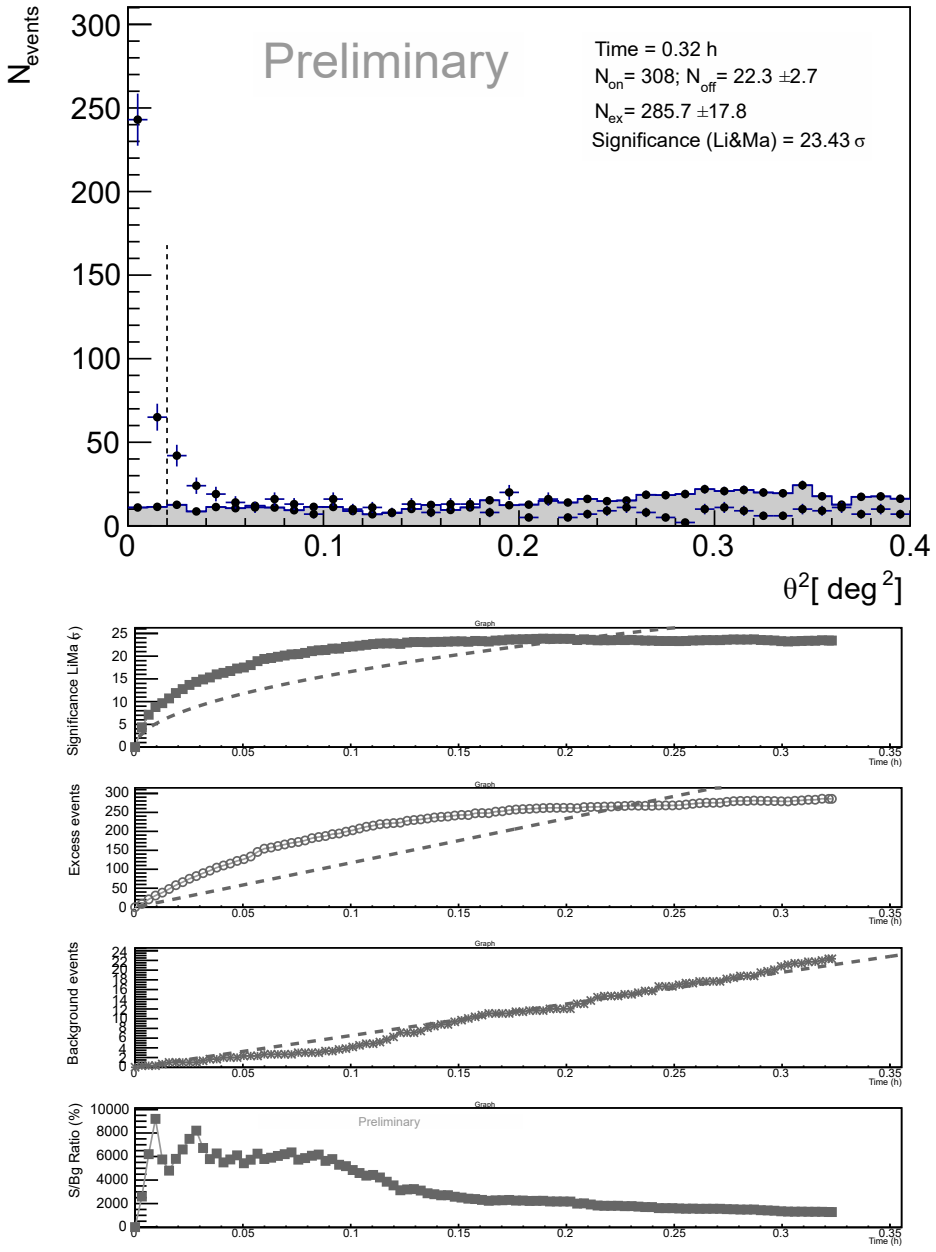

FIGURE 5.6: The results from preliminary analysis of GRB 190114C of the first $\sim$ 20 minutes of observations are shown. **Top panel**: θ^2 plot , LE cuts and moon settings ($size > 150$). **Bottom panel**: time versus significance plot including, starting from the top: the time evolution of Li&Ma significance, number of excess and background events, and signal to noise ratio.

The analysis of GRB 190114C was done with unprecedented accuracy, performing many checks and tests. Before presenting the final results from my analysis, I will outline the main steps which occurred in the first phases including preliminary fast analyses, the choice of MCs and of the best analysis settings to be used.
The standard MC sets used for the preliminary analyses were:

- **ST_03.07** available at the moment of the GRB 190114C observation. Even if they were not specifically tuned on the current observational period, they were used for fast analysis;

- **ST_03.11** produced for the MAGIC data observed in the period $\sim$ 2018.11.01 - 2019.09.15. With respect to ST_03.07 they fix a 5% miscalibration between telescopes.

Both MC sets have been produced with standard $DT = 4$ and $NSB = 0.19$. The preliminary analyses with such standard MC sets demonstrated the presence of a strong significant signal at the GRB position with a significance $> 20\ \sigma$ for $E > 300$ GeV in the first 20 minutes of observations as reported in [118]. Most of the signal was found in the first hour of observations, which is therefore the most interesting one. In Figure 5.6 the θ^2 plot and the significance versus time plot of the preliminary analysis performed by myself (and cross-checked later by the other analyzers) with ST_03.07 MCs are reported. I performed this analysis using the *moon condition* settings with cleaning levels 9-5.5, *size* > 150, and the *GRB observation* settings previously explained.
Nevertheless in the preliminary analysis performed with these MC sets the data taken in first phases (i.e. between $T_0 + 62$ and $T_0 + 78$ s) were not correctly simulated and under control, since the DTs were still adjusting (see Figure 5.7). Moreover, a larger MC sample was needed to increase the statistical robustness of the data especially since the GRB observed spectrum was expected to be quite steep. For these reasons it was decided to generate dedicated MC sets matching the GRB observational conditions in the most precise way. These sets were used not only for the data analysis but also to perform several checks and tests in order to derive the best settings to be used. The generated MC sets are the following:

- **GRB Set1**: a MC set produced with the same option of ST_03.11 ($DT = 4$ and $NSB = 0.19$) but tailored in zenith (55°-63°) and azimuth (175°-212°).

- **GRB Set2**: a MC set produced with $DT = 5$ and $NSB = 0.8$ and tailored in zenith (55°-63°) and azimuth (175°-212°).

- **GRB Set3**: a MC set produced with $DT = 7$ and $NSB = 0.8$ and tailored in zenith (55°-63°) and azimuth (175°-212°).

A summary of the MC sets main features can be found in Table 5.1. The *GRB Set1* was used to confirm the results obtained with the standard MC sets and to enlarge the statistics. Moreover, since it was tailored in zenith and azimuth it allowed to improve the reconstruction of the shower energy. On the other hand, it does not solve the problems on treating the first phases of the GRB data taking since the DT and NSB settings were the same as the standard MCs. For this reason *GRB Set2* and *GRB Set3* were produced assuming higher values of DTs and NSB. The *GRB Set2* was not appropriate for the data but was used for tests. The *GRB Set3* was indeed matching properly the observational conditions for the first 2.3 hrs until $Zd < 63°$, therefore it was used for the final data analysis.

Tag	Periods	DT (phe)	NSB	Tailored in Zd/Az
ST.03.07	2016.04.29 - 2017.08.02	4	0.19	No
ST.03.11	2018.11.01 - 2019.09.15	4	0.19	No
GRB Set1	only for GRB 190114C	4	0.19	Yes
GRB Set2	only for GRB 190114C	5	0.8	Yes
GRB Set3	only for GRB 190114C	7	0.8	Yes

TABLE 5.1: Summary of the MC data used for GRB 190114C

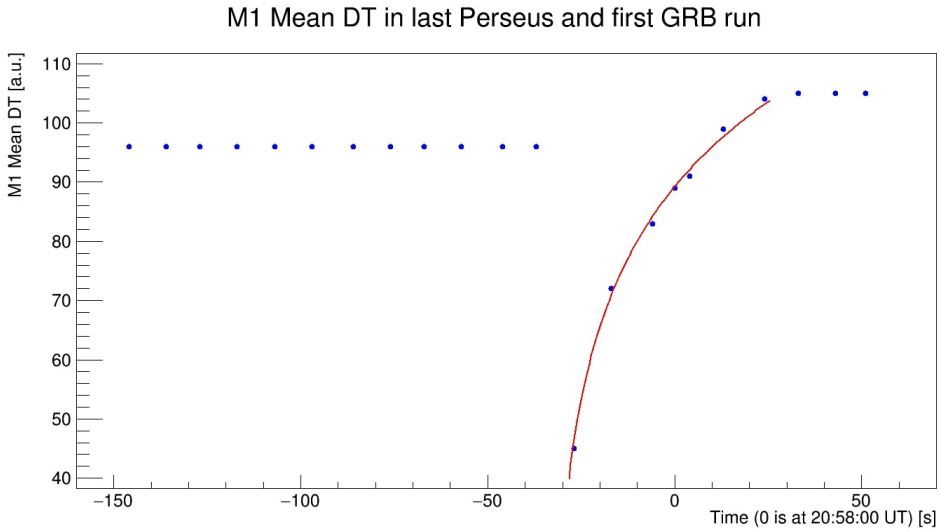

FIGURE 5.7: M1 mean DT versus time. The time axis in the plot has the 0 at 20:58:00 UT, i.e. the start of the first GRB subrun. The red line is a logarithmic function fitting the DT evolution. The DT stabilized from 20:58:21 UT (T_0 + 78 s) which in the x-axis of the plot corresponds to 21 s. Courtesy of Alessio Berti.

These dedicated MCs were also used to investigate the possibility to loosen the cut on the parameter *size* with respect to the standard one used for *moon* analysis at this level, which is 150. Indeed, the analysis results would have benefit from the usage of a loosen cut on *size* since the number of γ-like events which overcomes the cut at lower energies would increase and therefore the energy threshold would decrease. On the other hand, the drawback in case a too loose cut on *size* is used is to increase the pixels noise, which can affect the overall shape of the recorded images, the parameter reconstruction and therefore the entire data analysis chain.
Data taken in moonlight conditions have a higher accidental trigger rate which is compensated using higher DTs. On the other hand MCs are usually generated assuming standard *dark* conditions and the effect of moonlight is mimicked through the `AddNoise` option in `star`, higher cleaning levels and a higher cut on the sum of the charge of the pixels surviving the image cleaning, the so-called *size* parameter. For GRB 190114C additional MC sets with higher DTs were generated, therefore the options needed to adapt standard MCs to moon observations can be revised. In particular, a loosen cut on parameter *size* can be used. To test this possibility, the *size* distributions in energy for the three dedicated MC sets have been compared (see Figure 5.8). The idea of this comparison is to derive from which value of *size* the distributions have similar results and therefore the MC sets have usual performances

and the effect of using different DTs is negligible. Such value of *size* can be then used as cut value for the analysis with the *GRB Set3* MCs. From this study we derived that an acceptable *size* cut is found at the order $\sim$ 80-100.

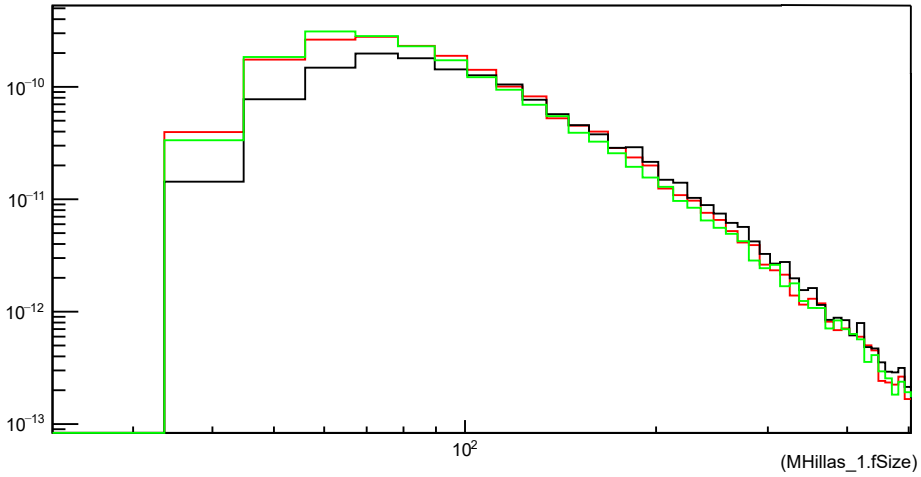

FIGURE 5.8: Size distributions for *GRB Set1* (green line, DT=4), *GRB Set2* (red line, DT=5), and *GRB Set3* (black line, DT=7) MCs normalized and weighted with a power law of index -5.0, similar to the observed spectrum.

As additional test we also compared the resulting LC obtained with *GRB Set3* applying *size* cuts of 80 and 100 (see Figure 5.9). Since the results are compatible within errors we finally decided to use a *size* cut of 80 for further analyses.

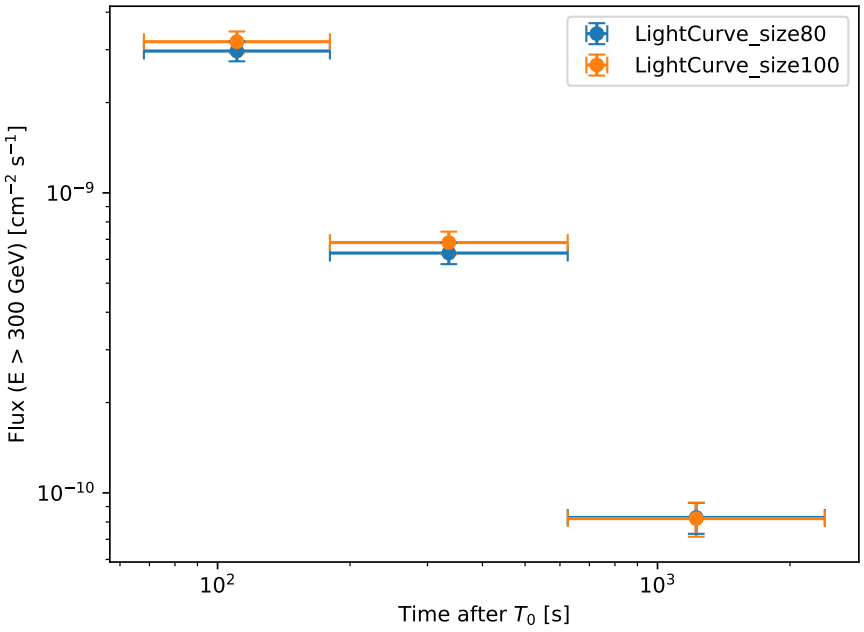

FIGURE 5.9: Light curves with time intervals: $T_0 + 68$ s - $T_0 + 180$ s; $T_0 + 180$ s - $T_0 + 625$ s; $T_0 + 625$ s - $T_0 + 2400$ s using *GRB Set 3* MCs with `flute` and different size settings.

Time-binned analysis

Once an agreement on the MCs and on the settings to be used was reached, the analysis and the high-level output results (LCs, SEDs and θ^2 plots) could be produced. In order to exploit the dataset and to maximize the manpower, it was decided to split the analyzers team into two subgroups respectively devoted to perform the specific analysis for the two resulting papers to be published. In the first paper [165], named "*Discovery* paper", the focus was to highlight the MAGIC results and announce the discovery of TeV emission from GRBs. In the second one [121], called "*Multi-WaveLength (MWL)* paper", the MAGIC data were analyzed and interpreted in the multi-wavelength context. I performed the analysis for the MWL paper together with Elena Moretti, Yusuke Suda and Satoshi Fukami. I will now present the main results obtained from my analysis.

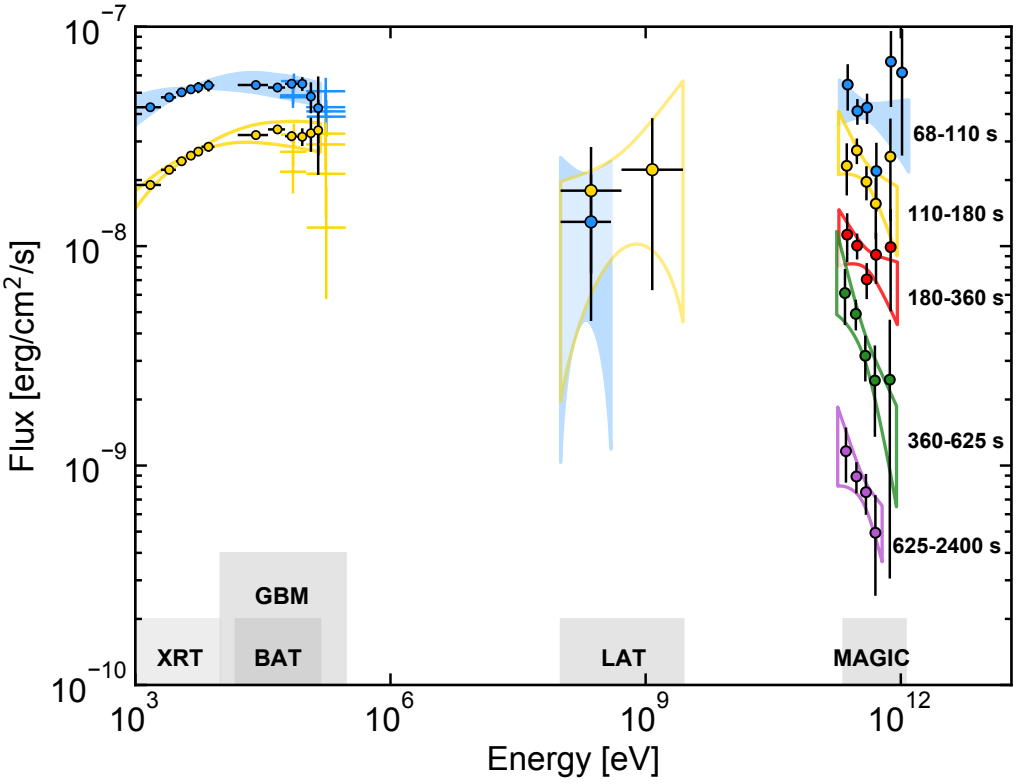

FIGURE 5.10: Multi-band SEDs in five different time intervals. MAGIC data analysis results are corrected for the EBL attenuation. MAGIC and LAT contour regions are drawn from the 1σ error of their best-fit power-law functions. For Swift data, the regions show the 90% confidence contours for the joint fit for XRT and BAT, obtained by fitting a smoothly broken power law to the data. From [121].

In the MWL paper I performed a time-binned analysis of MAGIC data. The time intervals were chosen in order to produce multi-band SEDs including also contemporaneous X-rays data and to evaluate a possible spectral evolution in the VHE band (see Figure 5.10). I followed the MAGIC standard data analysis chain from `superstar` up to `flute`. I generated the RF using the *GRB Set3* MCs. Afterwards, I ran `flute` selecting several time intervals in which SEDs and LCs must be produced. I applied the additional settings *size* > *80* and number of bins in *azimuth* = 5. Then I

applied the unfolding procedure, running `fold` and `CombUnfold`, in the selected time intervals. As a result, I obtained the unfolded spectral points and the spectral fitting parameters in the chosen time bins. The spectral fitting was performed assuming a simple power law for the intrinsic spectrum with the forward-folding method to derive the best-fit parameters. The parameters of the fit are the photon index and the flux normalization. The spectral points were derived following the different unfolding prescriptions (Tikhonov, Schmelling and Bertero) or in the forward unfolding method. All the spectra were produced taking into account the EBL effect, using the model of Domínguez et al [17]. The fitting results for various time bins (with pivot energy chosen to minimize the correlation between the normalization and photon index parameters) are shown in Table 5.2. The unfolded SEDs obtained with different prescriptions and in the different time bins are shown in Appendix A.2. From these results a hint of a spectral evolution to softer values can been seen, although the photon indices are compatible within the 1σ error with a constant value of about -2.5 up to 2400 s. The unfolding methods produce mostly consistent results.

Systematic error

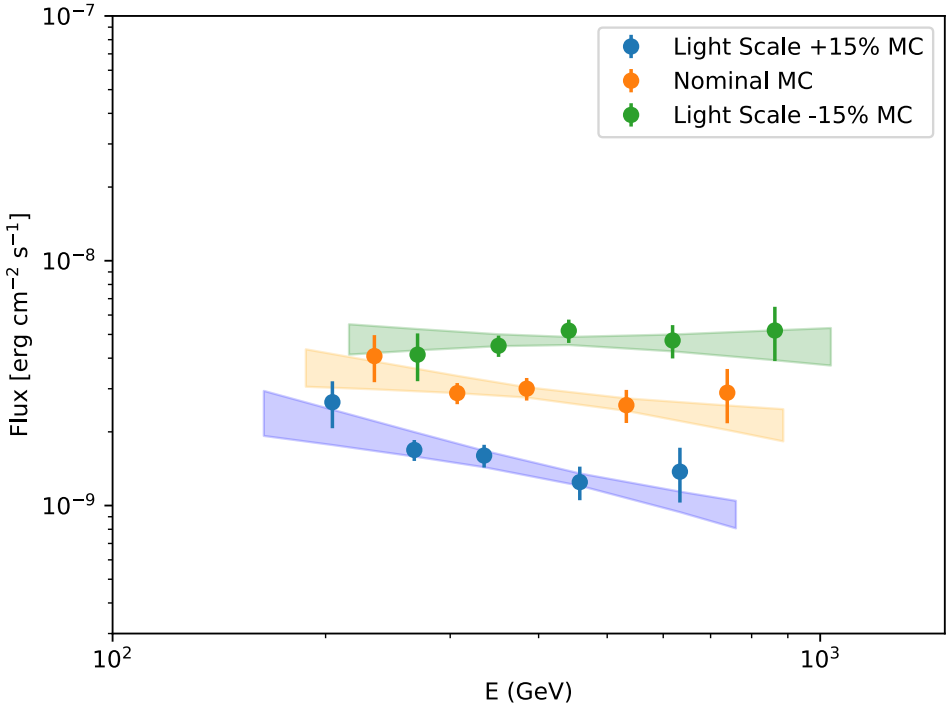

FIGURE 5.11: The orange (blue, green) points and band show the results of the Monte Carlo (MC) simulations for the nominal and the varied light scale cases (+15%, -15%), which define the limits of the systematic uncertainties. The contour regions are drawn from the 1σ error of their best-fit power-law functions. The vertical bars of the data points show the 1σ errors on the flux.

In order to test the robustness of our dataset we performed also several checks to estimate the systematic errors. Indeed, our imperfect knowledge of hardware conditions, such as the mirror reflectance or the properties of photomultipliers and of

the atmospherical transmission, systematically affect the MAGIC results. The predominant contribution to the systematic error on the energy scale is given by a possible mismatch of MC and real data light scale [33]. Indeed, such miscalibration can lead to a wrong reconstruction of the resulting spectrum affecting both the flux and the assumed spectral shape, especially at the lowest energies. An estimation of such error can be done with the `-LightScaleFactor` (LSF) option in `fold`. With this option it is possible to derive the best-fit spectral parameters and the unfolded SED assuming a light-scale variation in the MCs. Therefore, I calculated these quantities with `fold` assuming a light-scale variation of the order of $\pm$ 15%, which are the limited variations reported (see the study in [33]). The systematic errors on the spectral parameters can be then computed as the difference between the best-fit parameter values in the standard case and the best-fit parameter values obtained running `fold` with a LSF of $\pm$ 15%. The results are reported in the last two lines of Table 5.2 and the comparison between the nominal and the light-scaled SEDs are shown in Figure 5.11 for the time interval $T_0 + 62$ s - $T_0 + 2400$ s.

Time bin [seconds after T_0]	Normalization [$\mathrm{TeV}^{-1}\,\mathrm{cm}^{-2}\,\mathrm{s}^{-1}$]	Photon index	Pivot energy [GeV]
62 - 90	$1.66^{+0.18}_{-0.17} \cdot 10^{-7}$	$-1.75^{+0.34}_{-0.36}$	414.1
68 - 180	$8.97^{+0.72}_{-0.69} \cdot 10^{-8}$	$-2.16^{+0.24}_{-0.25}$	414.1
180 - 625	$2.06^{+0.18}_{-0.18} \cdot 10^{-8}$	$-2.48^{+0.27}_{-0.30}$	395.5
68 - 110	$1.36^{+0.13}_{-0.12} \cdot 10^{-7}$	$-1.94^{+0.29}_{-0.31}$	404.7
110 - 180	$7.26^{+0.79}_{-0.75} \cdot 10^{-8}$	$-2.43^{+0.34}_{-0.37}$	395.5
180 - 360	$3.02^{+0.32}_{-0.31} \cdot 10^{-8}$	$-2.45^{+0.33}_{-0.36}$	395.5
360 - 625	$1.51^{+0.19}_{-0.18} \cdot 10^{-8}$	$-2.46^{+0.39}_{-0.45}$	386.5
625 - 2400	$2.78^{+0.37}_{-0.37} \cdot 10^{-9}$	$-2.50^{+0.45}_{-0.51}$	386.5
62 - 2400 (Nominal MC)	$9.24^{+0.64}_{-0.62} \cdot 10^{-9}$	$-2.35^{+0.19}_{-0.21}$	433.6
62 - 2400 (Light scale +15% MC)	$4.39^{+0.40}_{-0.40} \cdot 10^{-9}$	$-2.63^{+0.20}_{-0.22}$	433.6
62 - 2400 (Light scale -15% MC)	$1.56^{+0.10}_{-0.09} \cdot 10^{-8}$	$-2.04^{+0.19}_{-0.20}$	433.6

TABLE 5.2: **MAGIC spectral fit parameters for GRB 190114C.** For each time bin, columns represent: start time and end time of the bin; normalization of the EBL-corrected differential flux at the pivot energy with statistical errors; photon indices with statistical errors; pivot energy of the fit (fixed).

In case of moonlight observation, an additional contribution to the systematic error on the flux is given by the higher noise in the photomultipliers and the higher DTs which are usually not simulated in the MC. However, the dedicated *GRB Set3* MC produced for this analysis mitigates such contribution to the systematic error which is therefore minor compared to that due to the light-scale variations.
Another source of systematic error comes from the choice of a particular EBL model among the many available in literature. The results previously shown are indeed obtained using the Dominguez et al. (from now on D11) model. Therefore, to estimate this contribution, I derived the best-fit spectral parameters in `fold` using other three EBL models: Franceschini et al. (F08) [203], Gilmore et al. (G12) [204] and Finke et al. (FI10) [205]. The resulting spectral indices for the different EBL models can be found in Table 5.3. The systematic error caused by the uncertainty on the EBL model

is estimated as the difference between the calculated mean values of the photon indices. Taking as reference D11, which was used in the previous analysis, the photon index calculated with the other EBL models in the several time bins is at maximum $+0.12$ softer or -0.15 steeper, which is anyway smaller than the statistical uncertainty (one standard deviation). On the other hand the systematic error due to EBL models on the flux normalization is higher. For the time interval $T_0 + 62$ s - $T_0 + 2400$ s is $\sigma_N = ^{+0.26}_{-0.07} \times 10^{-8}$ which is only partially at the same level of the statistical error (one standard deviation). Similar results are obtained also for the other time bins.

Time bin	Photon Index			
[seconds after T_0]	D11	F08	FI10	G12
62 - 90	$-1.75^{+0.34}_{-0.36}$	$-1.89^{+0.34}_{-0.35}$	$-1.66^{+0.34}_{-0.35}$	$-1.77^{+0.34}_{-0.35}$
68 - 180	$-2.16^{+0.24}_{-0.25}$	$-2.31^{+0.24}_{-0.26}$	$-2.07^{+0.24}_{-0.26}$	$-2.20^{+0.24}_{-0.26}$
180 - 625	$-2.48^{+0.27}_{-0.30}$	$-2.60^{+0.27}_{-0.30}$	$-2.37^{+0.27}_{-0.30}$	$-2.50^{+0.27}_{-0.30}$
68 - 110	$-1.94^{+0.29}_{-0.31}$	$-2.09^{+0.29}_{-0.31}$	$-1.85^{+0.29}_{-0.31}$	$-1.98^{+0.29}_{-0.30}$
110 - 180	$-2.43^{+0.34}_{-0.37}$	$-2.57^{+0.34}_{-0.37}$	$-2.34^{+0.34}_{-0.37}$	$-2.46^{+0.34}_{-0.37}$
180 - 360	$-2.45^{+0.33}_{-0.36}$	$-2.58^{+0.33}_{-0.36}$	$-2.35^{+0.33}_{-0.36}$	$-2.48^{+0.32}_{-0.35}$
360 - 625	$-2.46^{+0.39}_{-0.45}$	$-2.59^{+0.38}_{-0.43}$	$-2.35^{+0.38}_{-0.43}$	$-2.48^{+0.38}_{-0.42}$
625 - 2400	$-2.50^{+0.45}_{-0.51}$	$-2.63^{+0.44}_{-0.50}$	$-2.40^{+0.44}_{-0.50}$	$-2.50^{+0.44}_{-0.50}$
62 - 2400	$-2.35^{+0.19}_{-0.21}$	$-2.46^{+0.19}_{-0.21}$	$-2.23^{+0.19}_{-0.21}$	$-2.36^{+0.18}_{-0.20}$

TABLE 5.3: `fold` photon indices for different EBL models. The errors correspond to one standard deviation and the abbreviations refer to the EBL models used.

Statistical error

The statistical error is usually driven by the number of events simulated in the MC sample. For this reason, in this particular analysis additional MC sets were produced in order to reduce as much as possible this effect. Unfortunately producing MC events is very time consuming and therefore the number of simulated events is anyway limited. There are also additional options in the MARS software which can introduce larger statistical fluctuations. One of these options, which was used in GRB 190114C data analysis, is the azimuth binning of the collection area in `flute`. It is possible to choose from a minimum of 1 to a maximum of 12 bins for the azimuth in `flute`. A larger number of azimuth bins can improve results for the lower energies, especially when dealing with high zenith angle observations, but at the cost of higher statistical fluctuations. The reason for that is that when MC data are splitted in a larger number of azimuth bins, each bin has less MC events. I performed a test to evaluate how much the results change when performing the analysis with 5 azimuth bins or with 12 azimuth bins. In Figure 5.12 the *fold* spectra with the 1σ error contour regions of the best-fit power-law functions are shown for 5 (green) and 12 (blue) azimuth bins for the time interval $T_0 + 62$ s - $T_0 + 90$ s. Moreover, an additional spectrum (the orange one) is obtained with 12 azimuth bins but relaxing the condition on the maximum acceptable relative error in the MC-calculated exposure for each energy bin from the standard 0.2 to 0.4. With this loosen condition, `fold` is able to recover the spectral point at $E \sim 220$ GeV which for the standard 12 azimuth bins spectra was not shown because the MC statistics in the corresponding energy bin is too low. The results are well consistent but the spectra obtained with

5 azimuth bins, as expected, have clearly smaller statistical errors. For this reason we decided to use the 5 bins azimuth option for the final analysis to be delivered. I also performed a test to compare the systematic errors and the statistical ones in the same time intervals and with the same options for these three spectra. The results can be found in Appendix A.2. The systematic errors are estimated with the LSF option in `fold` as previously explained. The very similar results obtained despite these changes demonstrate the robustness of the dataset against these MC-related changes.

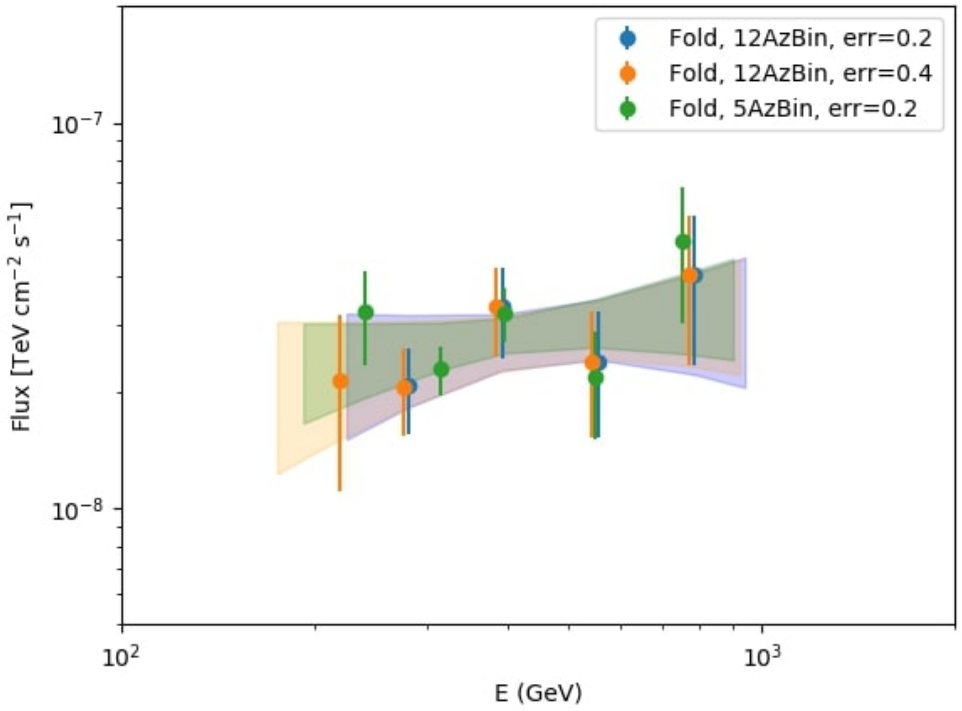

FIGURE 5.12: GRB 190114C spectra in time interval $T_0 + 62$ s - $T_0 + 90$ s with `fold` using different configuration for azimuth binning and maximum relative error for MC exposure. The countour regions are drawn from the 1σ error of their best-fit power-law functions.

5.2.3 Synchrotron burnoff limiting curves

The dynamical evolution calculated in `MUSE-GRB` was used to test the synchrotron burnoff limit for the GRB 190114C afterglow emission. As already mentioned in Chapter 3, the highest energy photons observed by LAT were used to test the synchrotron forward shock model and to investigate the possible radiation mechanism responsible for the HE emission component. It is indeed possible to compare the maximum energy for synchrotron photons expected from the theory with the energy of the events collected by the telescopes. As seen in Section 3.4.4 the maximum energy for synchrotron photons ε_{max} (equation 3.60) is derived equating the acceleration timescale with the synchrotron energy loss timescale and assuming a maximum Lorentz factor γ_{max} for the electrons. A numerical estimation in the shock comoving frame is given by $\varepsilon_{max} \approx 50 - 100$ MeV. When moving to the observer frame the

synchrotron spectrum is expected to cutoff at:

$$\varepsilon_{max}(t) \approx 100\ \text{MeV}\frac{\Gamma}{1+z} \tag{5.1}$$

since $\Gamma = \Gamma(t)$ also $\varepsilon_{max} = \varepsilon_{max}(t)$ will be a function of time. Therefore it is possible to estimate its evolution with time, which will follow the Lorentz bulk factor Γ evolution, and compare it with the estimated energy of the MAGIC detected events. Such comparison is shown in Figure 5.13 to give a robust proof of the existence of a new emission component beyond synchrotron emission in GRB afterglows. The two curves in the plot are the synchrotron burnoff limiting curves estimated with the dynamical evolution calculated in `MUSE-GRB`. The calculation was done assuming extreme values of the parameters in order to maximize the possible values of $\varepsilon_{max}(t)$. The calculation of $\varepsilon_{max}(t)$ was done assuming two different scenarios for the external medium: the homogeneous ISM (dotted curve) and the stellar wind scenario (dashed curve). In both simulations I assumed a blastwave kinetic energy $E_k = 3 \times 10^{55}$ erg. This value implies a low prompt efficiency $\eta = 1\%$ since $E_k = E_{iso}(1-\eta)/\eta$ where E_{iso} is the total isotropic equivalent energy. I used a normalization factor for the medium density $A_0 = 0.01$ cm^{-3} in the ISM scenario and $A_* = 0.01$ in the wind-like scenario. In order to perform the comparison, The MAGIC events were divided in bins of energy and time colour-coded. Despite very extreme assumptions were done for the estimation of the maximum synchrotron energy, the comparison shows clearly that the events detected by MAGIC from GRB 190114C are well more energetic than $\varepsilon_{max}(t)$ in both scenarios and therefore a new radiation mechanism must be claimed to explain the VHE emission component in GRB 190114C.

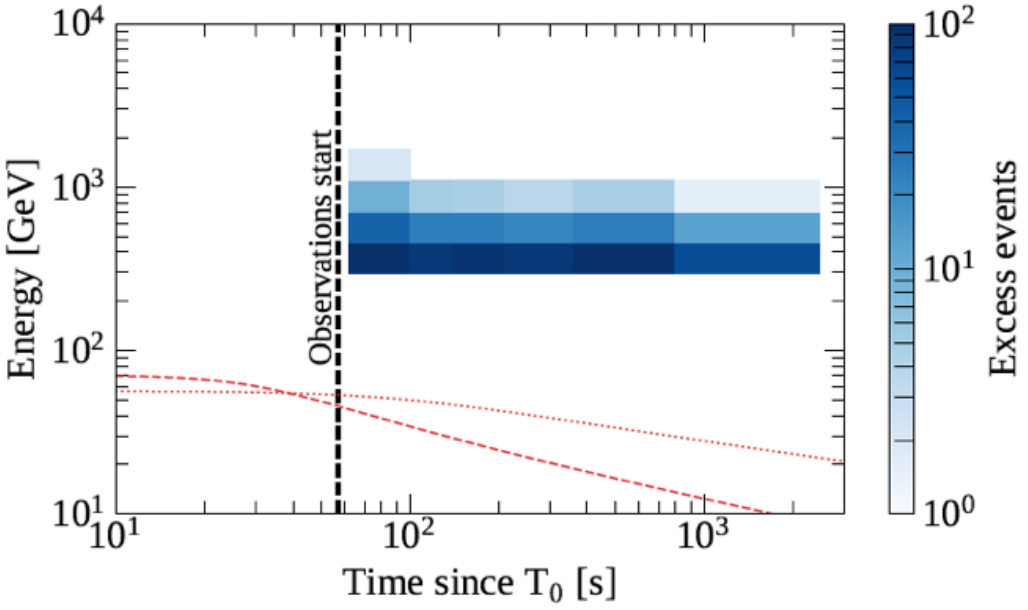

FIGURE 5.13: Distribution of the number of GRB 190114C γ-ray events observed by MAGIC binned in time and energy and colour-coded. The synchrotron burnoff limiting curves estimated from the dynamical evolution in `MUSE-GRB` are also visible in the lower side of the figure with two different assumptions for the external medium: constant-density ISM (dotted curve) and wind-like scenario (dashed curve). From [165].

5.2.4 Proton synchrotron afterglow emission with MUSE-GRB

As mentioned in the previous chapters, the proton synchrotron emission has been proposed several times in the past as possible radiation mechanism responsible for the emission of VHE photons in GRBs within the external shock scenario. Indeed, protons can be accelerated to energies which are well above the burnoff limit for electron synchrotron emission previously discussed. In order to test such mechanism I tried to model the MAGIC VHE light curve of GRB 190114C with MUSE-GRB assuming that only hadrons are responsible for such radiation. The tentative modeling is shown in Figure 5.14. The free parameters which I used for the modeling mostly follow the calculations presented in [165]. In this formulation, assuming a homogeneous ISM scenario, the maximum expected energy for proton synchrotron emission in the observer frame $\varepsilon_{max,p}$, from analytical prescriptions is derived as [206]:

$$\varepsilon_{max,p} = 7.6\,\mathrm{GeV}\eta^{-2}\epsilon_B^{3/2}(A_0 E_{k,53})^{3/4} t_{obs}^{-1/4}(1+z)^{-3/4} \tag{5.2}$$

where η is a factor of order 1 that characterizes the acceleration timescale and $E_k = 10^{53} E_{k,53}$. For GRB 190114C ($z = 0.42$) and in the optimistic case for which $\eta = 1$ and $\epsilon_B = 0.5$ in order to have $\varepsilon_{max,p} \geq 1$ TeV at $t_{obs} = 100$ s $A_0 E_{k,53} \gtrsim 10^4$ which would require a very dense environment and/or an extremely energetic event. A similar consideration, even more stringent, can be done also for the observed flux in the TeV range. It is possible to assume a proton spectral index $q = 3$, derived from the condition that the GRB photon spectral index is $\alpha \sim -2$ and for a synchrotron spectrum extending up to the TeV range is valid the relation $\alpha = -(q+1)/2$. Therefore, the observed flux at 1 TeV is estimated as:

$$F(1\,\mathrm{TeV}) = (1.1\times10^{-16}\,\mathrm{erg\,cm^{-2}\,s^{-1}})\epsilon_\mathrm{p}^2\,\xi_\mathrm{p}^{-1}\epsilon_\mathrm{B}\,A_0^{1/2}E_{\mathrm{k},53}^{3/2}\,D_{28}^{-2}\,t_\mathrm{s}^{-3/2}(1+z)^{3/2} \tag{5.3}$$

In an optimistic scenario for which $\epsilon_B = 0.5$, $\epsilon_p = 0.5$, $\xi_p = 0.1$ in order to reproduce the GRB 190114C flux $F \sim 4\times10^8$ erg cm^{-2} s^{-1} at $t_{obs} = 100$ s it is required that $A_0^{1/2}E_{k,53}^{3/2} \gtrsim 10^{11}$ which is an extremely large and non plausible value. This qualitative calculation is performed at 1 TeV while indeed in the analysis is calculated in 0.3-1 TeV energy range.

A more precise estimation of these parameters can be obtained with a numerical modeling. Indeed, it is possible to compare the MAGIC energy flux in the 0.3 - 1 TeV energy range with the simulated results calculated with MUSE-GRB. To obtain an acceptable modeling of the MAGIC light curve following the prescriptions derived above I used the following parameters: $q = 3$, $\epsilon_p = 0.5$, $\xi_p = 0.1$, $\epsilon_B = 0.5$, $E_k = 7.0\times10^{57}$ erg, $A_0 = 10^6$ cm^{-3}, $\Gamma_0 = 400$, and $z = 0.42$. Therefore, I obtained very similar parameters with those assumed from the analytical formulation presented above. The values of the normalization external density $A_0 = 10^6$ cm^{-3} and of the blastwave energy $E_k = 7.0\times10^{57}$ erg are extremely high. Even if such a high density may be explained assuming that the GRB explode at the centre of a dense molecular cloud, such a high value of the energy blastwave cannot be explained with the current GRB progenitors. The numerical modeling confirms the qualitative analytical estimation results from which the TeV emission from GRB 190114C is hardly explained with the proton synchrotron emission because of its low radiative efficiency.

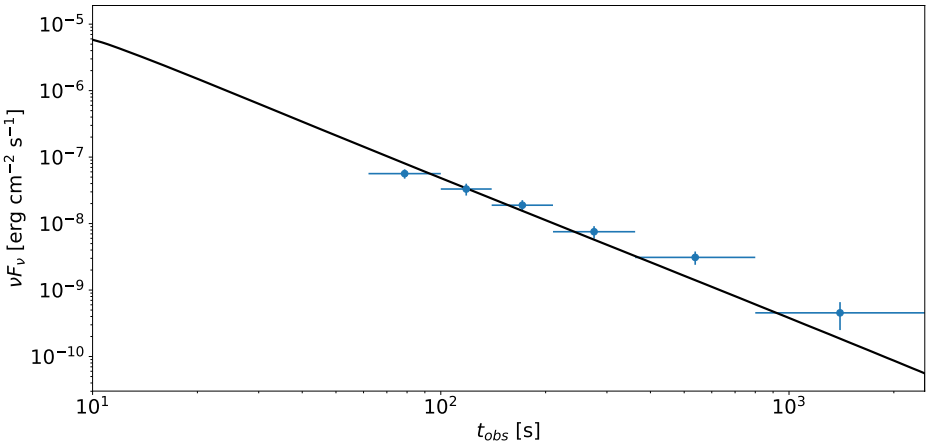

FIGURE 5.14: Modeling of GRB 190114C light curve in the 0.3-1.0 TeV energy range with `MUSE-GRB` considering only the proton synchrotron emission mechanism. The parameters used for the modeling are $q = 3$, $\epsilon_p = 0.5$, $\xi_p = 0.1$, $\epsilon_B = 0.5$, $E_k = 7.0 \times 10^{57}$ erg, $A_0 = 10^6$ cm^{-3}, $\Gamma_0 = 400$, and $z = 0.42$.

5.3 GRBs UL catalog with MAGIC

The MAGIC observational strategy, previously outlined, lead to the observation of a large sample of GRBs during these years. Despite such great efforts, only one GRB (GRB 190114C) was clearly detected by MAGIC up to 2019. The reason why most of the observed GRBs were not successfully detected arises from physical and technical considerations, as already mentioned. Besides the possible intrinsic faintness of TeV emission in GRBs, another physical factor limiting the chances of detection is the EBL. Indeed, the EBL absorption affects the GeV-TeV energy range where the MAGIC telescopes, and the IACTs in general, are sensitive. Moreover, the amount of absorption increases with the redshift and the energy, causing a cutoff in the GRB observed spectrum already evident at hundreds GeV for $z \sim 0.4 - 0.5$, and which arises at even lower energies for more distant GRBs, which constitute the majority of the MAGIC sample. The technical limiting factor for detections is instead intrinsic to the imaging technique of the ground-based Cherenkov telescopes, which always observe the events with some time delay, which can be also of the order of several hours in case of GRBs that occur during the day or under unfavorable atmospheric conditions at the site. Therefore, despite with the automatic alert system a great effort has been done to reduce as much as possible such time delay, still in several cases it is not possible to observe the first minutes of GRB emission.
GRBs observed by MAGIC constitute a heterogeneous sample comprising events with different physical features and observational conditions. In 2013 the MAGIC GRB automatic procedure was upgraded, increasing the number of GRBs followed in the prompt and early afterglow phases and decreasing dramatically hardware failures during fast repositioning. In this section I will present the work I have done for the analysis and the interpretation of several GRBs observed by MAGIC with no significant detection from 2013 to 2019. The goal of such study is to deliver a MAGIC GRB catalog. This project is presently at an advanced stage and it will be soon submitted for publication.
For this project I performed the MAGIC data analysis of several events in order to deliver for each of them a list of observed flux ULs. In addition, for some selected

GRB name	Satellite	T_{90} [s]	Redshift	Delay [s]	Zenith [deg]
130701A$^+$	*Swift*-BAT	4.4	1.155	60	27-16
131030A$^+$	*Swift*-BAT	41	1.295	26	33-40
141220A$^+$	*Swift*-BAT	7.21	1.3195	55	29-19
160623A$^+$	*Fermi*-LAT	50	0.367	75897	12-30
160625B$^+$	*Fermi*-LAT	4.60	1.4	2765	21-60
171020A	*Swift*-BAT	41.9	-	104	15-40
171210A	*Fermi*-LAT	12	-	31435	30-62
180512A	*Swift*-BAT	24	-	153	18-40
180715A	*Swift*-BAT	0.68	-	12019	29-35
180720C	*Swift*-BAT	124.2	-	108	54-56
180904A	*Swift*-BAT	5.39	-	96	21-60

TABLE 5.4: List of GRBs analyzed by myself (in bold) and GRBs for which I developed a dedicated calculation of the intrinsic ULs (marked with a cross). In the table are also reported the satellite which triggered the observation, T_{90}, redshift, MAGIC time delay from trigger and zenithal range.

GRBs of the sample I developed a special dedicated analysis to calculate the intrinsic flux UL in the MAGIC energy range and put the results in the context of the X-ray and Fermi-LAT observations. Since the project is still ongoing and the sample of GRBs is large (more than 40 GRBs), in this section I will focus only on the GRBs for which I gave a direct contribution. Such events are listed in Table 5.4. In total they are 11, 10 long and 1 short (GRB 180715A).

For the entire sample of GRBs the ULs on the observed flux were evaluated with `flute`, assuming a simple power law function for the intrinsic γ-ray differential photon spectrum $d\Phi/dE \propto E^{-\Gamma}$ using the method of Rolke et al. (2005) [65], with a confidence level (CL) of 95% and a total systematic uncertainty of 30%. Two values of the photon index Γ have been considered: 1.6 and 2.2. Their usage can be justified from a phenomenological point of view since they correspond to the best fit values obtained respectively for GRB 180720B and GRB 190114C [164, 165]. Moreover, these are also the possible photon indices expected in the SSC external forward shock scenario. Indeed, considering the radiation generated by electrons accelerated into a power law distribution $dN/d\gamma = \gamma^{-p}$ with p ranging between 2.2 and 2.4, the photon indices Γ used in this study roughly correspond to the photon indices of the SSC spectrum assuming that the peak is above or below the MAGIC energetic range. Recalling indeed from [161], the slopes of the differential flux in the slow cooling regime were $N_\nu \propto \nu^{(1-p)/2-1}$ for $\nu < \nu_{cool,IC}$ and $N_\nu \propto \nu^{-p/2-1}$ for $\nu > \nu_{cool,IC}$. Substituting respectively in the first equation $p = 2.2$ results in $N_\nu \propto \nu^{-1.6}$ and in the second equation $p = 2.4$ results in $N_\nu \propto \nu^{-2.2}$.

To estimate the observed spectrum starting from the intrinsic one, the effects of EBL absorption need to be taken into account. Moreover, when going to redshift higher than ~ 0.5 the differences between EBL models starts to be not negligible anymore and should be taken into account as a source of uncertainty. For such study I considered three different EBL models: Dominguez et al. (D11), Franceschini et al. (F18) [207], and Gilmore et al. (G12). In Figure 5.15 the attenuation factor $e^{-\tau}$, where τ is the optical depth, calculated for the three EBL models at redshift $z = 0.5, 1, 2$ is

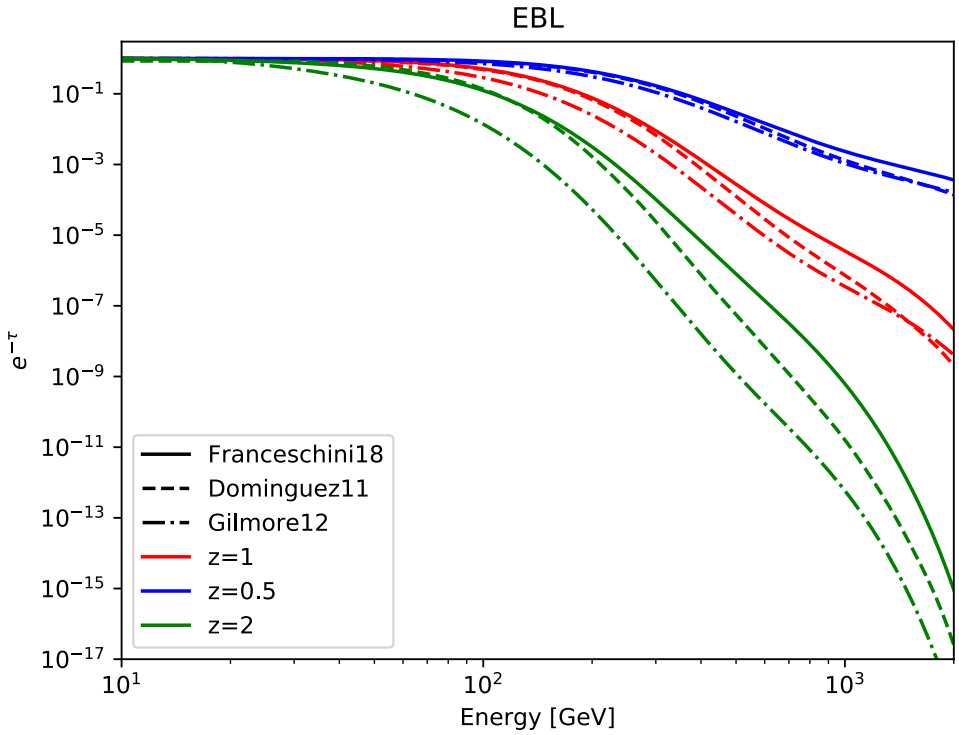

FIGURE 5.15: Energy versus attenuation factor $e^{-\tau}$ for different EBL models and different redshifts. Variations between models increase with the redshift.

compared. This plot shows clearly that when going to higher redshifts the differences between EBL models increase. In Figure 5.16 the ratio between attenuation factors of different EBL models is plotted for redshift $z = 1$ (left) and $z = 2$ (right). Such comparisons show that the D11 and F18 models behave similarly, especially for $E \lesssim 150 - 200$ GeV. Going to higher energies the difference between them is at maximum of the order of a factor ~ 2 for $z = 1$ and ~ 10 for $z = 2$. On the other hand, the G12 model shows bigger discrepancies and a higher absorption with respect to the other two models already starting from ~ 20 GeV. Differences with D11 are at most of the order of a factor ~ 4 for $z = 1$ and ~ 50 for $z = 2$. While G12 model shows clearly different values, observed ULs computed with EBL models D11 and F18 differ by no more than 30% up to $E \sim 200$ GeV, therefore it is a reasonable choice to report just one of them. For this reason, I decided to calculate the observed ULs considering two EBL models: F18 and G12 models. For those GRBs in the sample with unknown redshift z, a common value has been used for the calculation of the EBL absorption. Since most of the GRBs in the sample have been detected by *Swift*, we chose $z = 2$ for long GRBs and $z = 0.5$ for short GRBs. Indeed, these are the current average redshift values of the *Swift* long and short GRB population [208]. Therefore, according to the considerations on the intrinsic photon index and on the EBL absorption, a total of four values of observed ULs have been calculated, two for each photon index and two for each chosen EBL model. This is the analysis applied to the entire sample of GRBs. The ULs on the observed flux in several energy bins calculated from my analysis are listed in Appendix A.3. Only the energetic bins which assure a systematic uncertainty below 30% are reported.

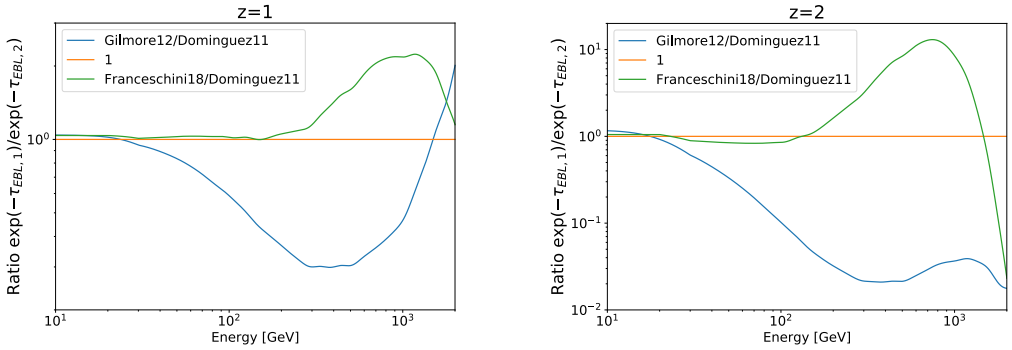

FIGURE 5.16: **Left panel**: Ratio of the attenuation factor of different EBL models for redshift $z = 1$ between 10 GeV and 2 TeV. **Right panel**: Ratio of the attenuation factor of different EBL models for redshift $z = 2$ between 10 GeV and 2 TeV

Comparison with X-ray and HE flux

Detections of GRB 190114C and GRB 180720B have shown a strong connection between emission in the soft X-ray band and in the VHE one. The luminosities in the two energy bands are comparable. In an SSC scenario, this would imply a similar amount of power in the synchrotron and in the IC components. Therefore, for a subsample of the GRBs with no detection I proposed a comparison between the MAGIC flux ULs and the flux obtained in the X-ray band by the *Swift*-XRT instrument. The GRBs chosen for this comparison have a redshift $z < 2$ and the total systematic uncertainty of the calculated ULs in the selected energy range is within 30%. The MAGIC ULs on the intrinsic flux have been estimated and compared with the simultaneous de-absorbed X-ray flux detected by XRT. The de-absorbed XRT flux is estimated in the energy range 0.3-10 keV (observer frame, from `https://www.swift.ac.uk/xrt_curves/`). For the MAGIC flux, four ULs for each GRB are calculated in a single selected energy bin $[E_{min}, E_{max}]$ following the assumptions previously outlined regarding the intrinsic spectral index and the EBL models. The low energy edge of the flux-integration window E_{min} is given by the energy threshold of each GRB or by the lowest energy value which assures a total systematic uncertainty within 30%. The energy threshold of each GRB is calculated as the peak of the MC reconstructed energy distribution weighted for the observed spectrum. The upper energy edge E_{max} is fixed to 1.5 TeV in the rest frame. This value is chosen considering that the highest photon energies observed by MAGIC from GRB 190114C are $\sim$ 1 TeV (observer frame, corresponding to $\sim$ 1.5 TeV in the rest frame).
To calculate the intrinsic ULs, first the MAGIC observed ULs Φ_{obs} are calculated with `flute` applying the same procedure previously explained for the entire GRB sample. Then, the observed γ-ray differential energy spectrum behaviour is reproduced thanks to a smoothly broken power law function as:

$$\left(\frac{d\Phi}{dE}\right)_{obs} = KE^{-\Gamma}\left[1 + \left(\frac{E}{E_c}\right)^{\frac{\Gamma_2-\Gamma}{s}}\right]^{-s} \tag{5.4}$$

where K is the normalization factor, E_c is a break energy, s is a smoothing parameter, Γ and Γ_2 are the photon indices reproducing the asymptotic behaviours for low and high energies. Since the low energy side of the spectrum is mostly unaffected by

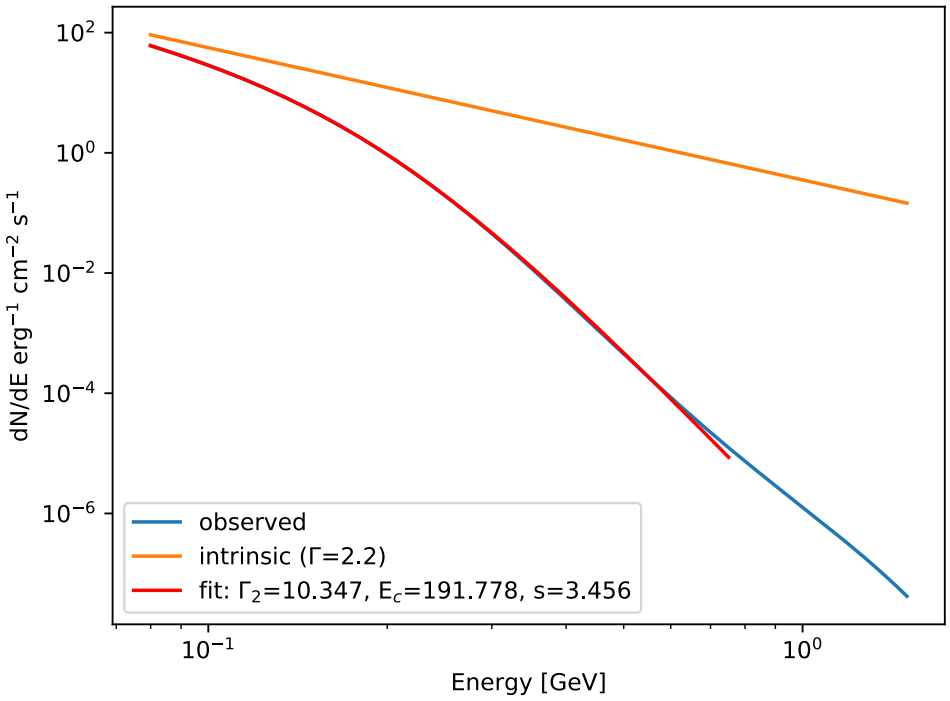

FIGURE 5.17: Fit (red line) of the observed differential energy spectrum (blue line) in the range $[E_{min}, E_{max}]$ for a generic event with redshift $z = 1$. The fit is done using the `Scipy` function `curve_fit`. The parameters of the fit are reported in the legend. The assumed intrinsic differential energy spectrum, power law with index $\Gamma = 2.2$, is also shown (orange line).

the EBL absorption, the Γ index is fixed to the assumed value of the intrinsic γ-ray differential spectrum. The parameters E_c, s and Γ_2 are instead free parameters calculated by fitting this spectral shape to the observed spectrum obtained applying the EBL absorption to the intrinsic γ-ray differential spectrum $(d\Phi/dE)_{deabs} \propto E^{-\Gamma}$ with $\Gamma = 1.6$ or 2.2 and with F18 and G12 EBL models. An example of such fitting is found in Figure 5.17. At this point, it is possible to calculate the normalization factor K from the relation:

$$\Phi_{obs} = K \int_{E_{min}}^{1.5TeV/(1+z)} E^{-\Gamma} \left[1 + \left(\frac{E}{E_c} \right)^{\frac{\Gamma_2 - \Gamma}{s}} \right]^{-s} dE \quad (cm^{-2}s^{-1}) \tag{5.5}$$

Then, the EBL correction factor can be applied to move from the observed spectrum to the intrinsic de-absorbed one:

$$\left(\frac{d\Phi}{dE}\right)_{deabs} = \left(\frac{d\Phi}{dE}\right)_{obs} * e^{(\tau(E,z))} \tag{5.6}$$

where $\tau(E,z)$ is the optical depth for a given energy E and redshift z. Finally, the intrinsic UL Φ_{deabs} is calculated in erg cm^{-2} s^{-1}:

$$\Phi_{deabs} = \int_{E_{min}}^{1.5TeV/(1+z)} E \left(\frac{d\Phi}{dE}\right)_{deabs} dE \quad (\text{erg } cm^{-2}s^{-1}) \tag{5.7}$$

In Table 5.5 the resulting ULs on the intrinsic MAGIC flux are listed for each choice

of the photon index and for the EBL models F18 and G12. The comparison plots between MAGIC ULs, XRT flux and LAT flux (in case of detection) are shown in Figures 5.18, 5.19, 5.20, 5.21, and 5.22. The events GRB 130701A, GRB 131030A and GRB 141220A were triggered by Swift-BAT and immediately repointed by MAGIC with a short time delay (respectively after 60 s, 26 s, and 55 s). For these events the ULs have been performed for the entire observational night. On the other hand, GRB 160623A and GRB 160625B were triggered by Fermi-LAT but they became observable by MAGIC only respectively 21 hrs and 0.8 hrs after the trigger. In search for a possible late-time detection, observations of these GRBs were performed for two nights. Therefore in such cases, in order to allow a comparison with the X-ray observations, I calculated separately the intrinsic ULs for each observational night. Moreover, in the first night of GRB 160625B the UL calculation method was applied only for the second half of the night. This is due to the fact that for the first part of the night it was not possible to calculate the ULs assuring a total systematic uncertainty below 30%. For all these events except GRB 160625B the MAGIC ULs are at the same level or also below the simultaneous X-ray flux. This is a first good indication that the resulting ULs can be used for further studies to derive constraints on the physics of the external shocks based on the lack of a VHE emission component as observed by MAGIC for such cases.
Some tests regarding the effect of the chosen EBL models and spectral indices on the resulting intrinsic MAGIC ULs has been performed. Results can be found in Appendix A.3.

GRB	T_{eff}	$E_{\min}$	E_{max}	F18,1.6	F18,2.2	G12,1.6	G12,2.2
				10^{-10}	10^{-10}	10^{-10}	10^{-10}
name	[h]	[GeV]	[GeV]	[erg cm^{-2} s^{-1}]	[erg cm^{-2} s^{-1}]	[erg cm^{-2} s^{-1}]	[erg cm^{-2} s^{-1}]
130701A	0.99	100	696	1.58	0.95	4.00	2.29
131030A	2.04	120	654	2.19	1.32	7.55	4.31
141220A	0.79	75	647	1.70	0.98	4.29	2.32
160623A	2.59	165	1097	0.56	0.40	0.71	0.50
160623A	2.33	140	1097	0.14	0.10	0.22	0.12
160625B	3.88	200	625	7.58	5.11	56.3	35.9
160625B	2.25	110	625	1.54	0.95	5.94	3.45

TABLE 5.5: ULs on the intrinsic flux for a selected number of GRBs in the sample. Flux ULs are in units of 10^{-10} erg cm^{-2} s^{-1}. The abbreviations refer to the EBL models (F18,G12) and the assumed intrinsic photon indices (1.6, 2.2) used. In the table also the effective time and the lower and upper energy edge for the UL calculations are reported. Since 160623A and 160625B have been observed for two nights the analyses have been performed separately and different ULs for each night have been computed.

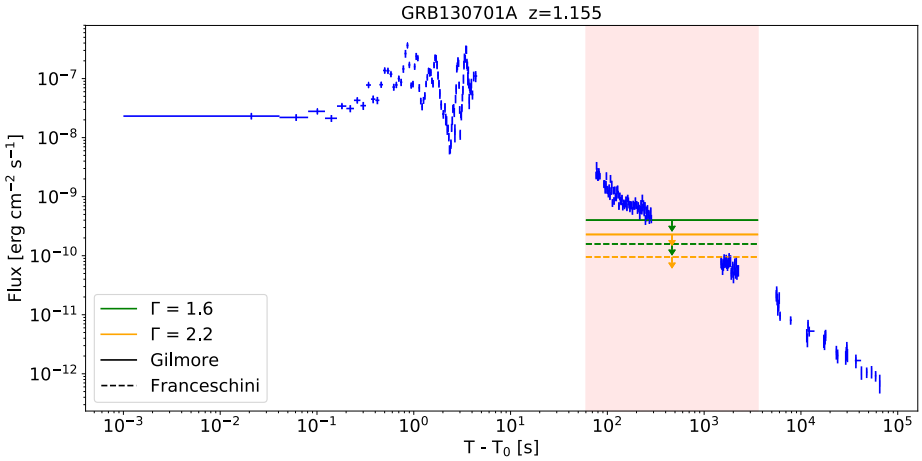

FIGURE 5.18: MAGIC UL in green and orange and Swift-XRT light curve for GRB 130701A. The vertical red bar marks the MAGIC observational window.

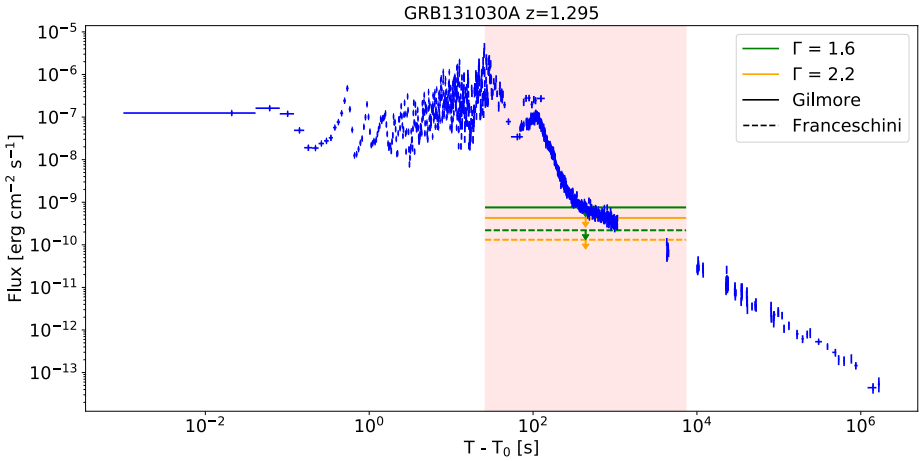

FIGURE 5.19: MAGIC UL in green and orange and Swift-XRT light curves for GRB 131030A. The vertical red bar marks the MAGIC observational window.

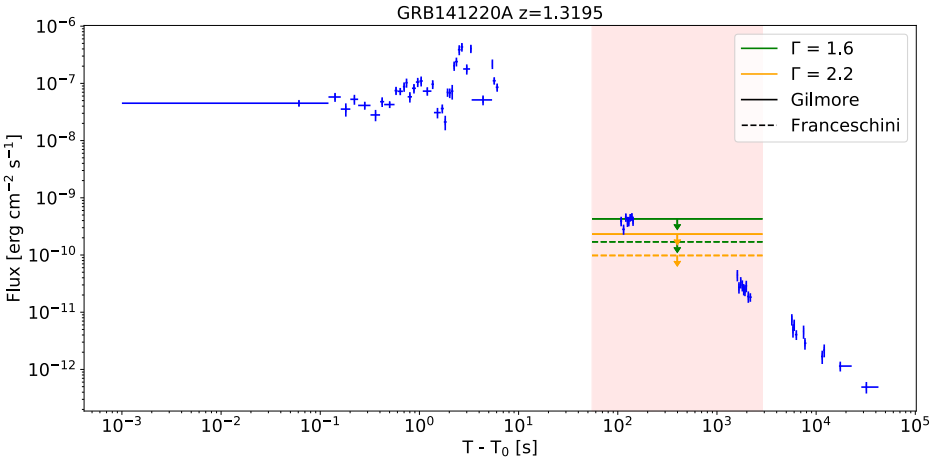

FIGURE 5.20: MAGIC UL in green and orange and Swift-XRT light curves for GRB 141220A. The vertical red bar marks the MAGIC observational window.

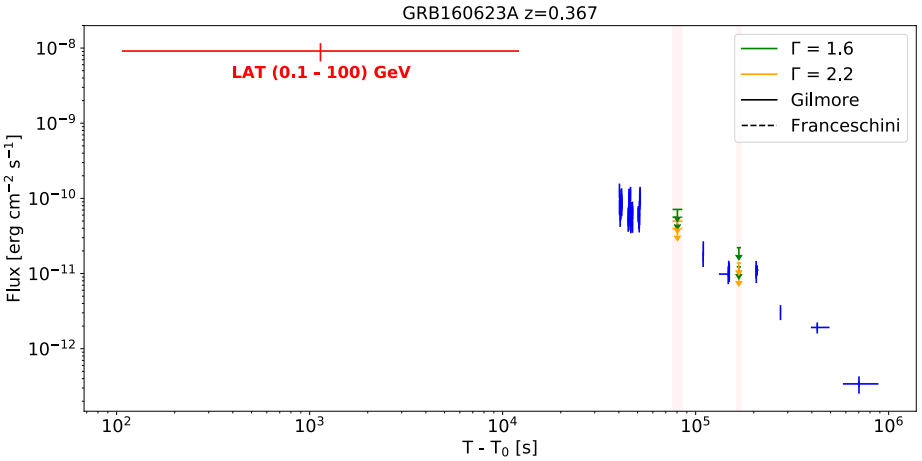

FIGURE 5.21: MAGIC UL in green and orange and Swift-XRT light curves for GRB 160623A. The vertical red bar marks the MAGIC observational window.

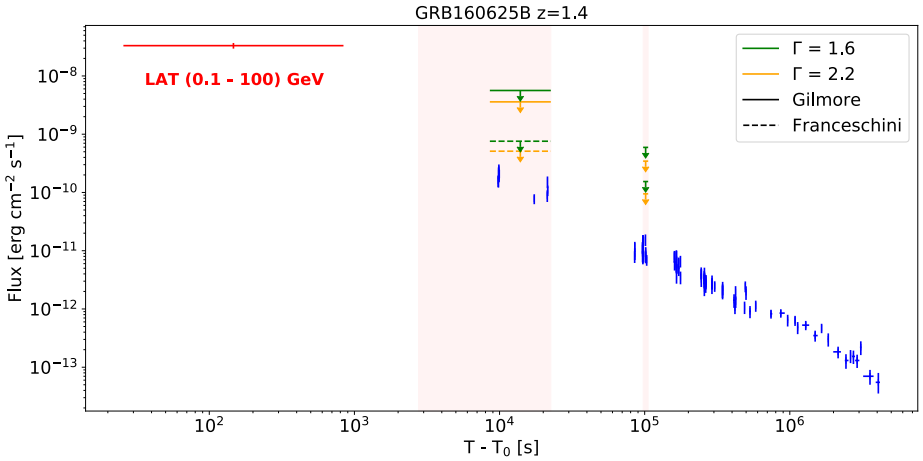

FIGURE 5.22: MAGIC UL in green and orange and Swift-XRT light curves for GRB 160625B. The vertical red bar marks the MAGIC observational window.

5.4 GRB 190829A

Despite GRB 190114C is the only GRB clearly detected by MAGIC up to now, there have been in the years few events showing a possible hint of detection. For such events it was decided to perform further dedicated analysis. In case the results are strong enough and the event is particularly interesting for the GRB community a so-called *stand-alone* publication with the MAGIC results on the event can be done. GRB 190829A fits all these conditions. In this section I will briefly summarize the importance of such event for the whole GRB community and the preliminary MAGIC analysis done. This project is still ongoing and further dedicated activities will be performed in the next future.

5.4.1 Observations and general properties

GRB 190829A is a long GRB triggered by Swift-BAT [209] and Fermi-GBM [210]. The Fermi-GBM trigger time is 19:55:53.13 UTC. The prompt emission detected by the two instruments consists of two episodes with the first one seen in the time interval T_0 - $T_0 + 4$ s and the second brighter episode from $T_0 + 47$ s to $T_0 + 61$ s. The nature of the episodes is clearly different: the first one is described by a power law with index -1.41 ± 0.08 and an exponential high-energy cutoff function with $E_p = 130 \pm 20$ keV, the second one, which shows a softer HR, can be described with a Band function with $E_p = 11 \pm 1$ keV , $\alpha = -0.92 \pm 0.62$ and $\beta = -2.51 \pm 0.01$ [211]. A multi-wavelength observational campaign of the event was performed covering the entire electromagnetic spectrum from radio to VHE. In the VHE band the H.E.S.S. telescopes reported the detection of a $> 5\sigma$ signal around ~ 4 hrs after T_0 [120]. This is therefore the third GRB up to date detected in the VHE band. Despite the VHE detection, the event was not detected in the HE range by Fermi-LAT. Nevertheless, ULs have been reported in the MeV-GeV band up to 3×10^4 s [212]. The simultaneous detection in the VHE band and non-detection in the HE band make this event unique and peculiar. The Swift-XRT telescope detected a bright X-ray afterglow starting from 97.3 s after T_0. The X-ray afterglow was monitored until $\sim 7.8 \times 10^6$ s after T_0.

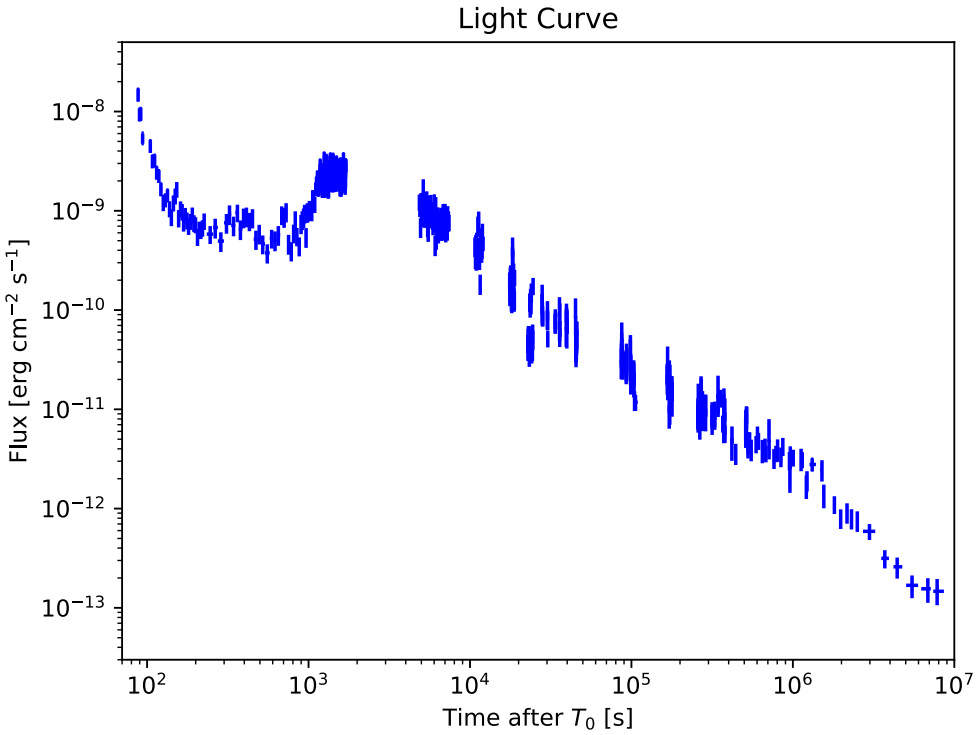

FIGURE 5.23: Swift-XRT light curve for GRB 190829A. The peculiar behaviour with several different trends can be seen.

The X-ray light curve in the 0.3-10 keV energy range (observer frame) is shown in Figure 5.23. It shows a peculiar behaviour with an initial steep decay phase followed by a plateau and a strong flare episode. After the flare the standard afterglow phase starts with a decay following a power-law or a broken power-law behaviour. In the UV/optical/NIR band the event was followed by several instruments. Thanks to these observations the redshift was estimated to be $z = 0.0785 \pm 0.005$ [213], which makes this event one of the closest GRB ever detected. Starting from 4.5 - 5.5 days after the trigger an associated supernova has been reported [214]. Also in the optical data a flare is seen contemporaneously with the one in X-rays. In the radio band the detection was reported by several instruments starting from $\sim$ 1 day after the trigger [215, 216, 217, 218]. With such a great covering in the electromagnetic spectrum, including also a VHE detection, GRB 190829A is one of the most interesting events for the entire GRB community.

5.4.2 MAGIC observation and data analysis

Observations of GRB 190829A were performed starting from $\sim$ 30.5 hours after T_0. They last for $\sim$ 3 hours and were performed in *dark* and very good weather conditions. The source was observed in the mid-high zenithal angle range, spanning from 38° up to 60°. Being these standard conditions, the data analysis was performed applying the standard data analysis chain from `superstar` data. For the analysis I used standard ST_03.11 MCs. The θ^2 plots and the significance vs time plots with the LE, FR and HE cuts are shown in Figures 5.24, 5.25, 5.26. A hint of detection may be claimed, especially when applying the HE cuts. Such hint observed especially at high energies is compatible with the observational conditions. Indeed, for such mid-high zenithal observation, the energy threshold of the event, which is calculated

as the peak of the MC reconstructed energy distribution weighted for the observed spectrum, is $\sim$ 500 GeV. Nevertheless, the estimated significance $\sigma_{Li\&Ma}$ calculated applying the HE cuts can be biased and therefore is less trustable because the number of surviving events is $\lesssim$ 10. As a result, the number of the events follows the Poissonian rather then the Gaussian distribution, and thus it does not completely fulfill the assumptions made in [61]. An intrinsic ULs have been estimated with `flute` following the same procedure as described in the MAGIC UL catalog. The results are listed in Table A.2. As can be seen for such low redshift the differences between EBL models are significantly lower. The G12 and F18 ULs differs by $\sim$ 7%.

E_{min}	E_{max}	T_{eff}	F18,1.6	F18,2.2	G12,1.6	G12,2.2
			10^{-12}	10^{-12}	10^{-12}	10^{-12}
[GeV]	[GeV]	s	[erg cm^{-2} s^{-1}]	[erg cm^{-2} s^{-1}]	[erg cm^{-2} s^{-1}]	[erg cm^{-2} s^{-1}]
500	1391	10169	4.16	3.89	4.48	4.18

TABLE 5.6: Intrinsic ULs of GRB 190829A. Flux ULs are in units of 10^{-12} erg cm^{-2} s^{-1}. The abbreviations refer to the EBL models (F18, G12) and the assumed intrinsic photon indices (1.6, 2.2) used. In the table also the effective time and the lower and upper energy edge for the UL calculations are reported.

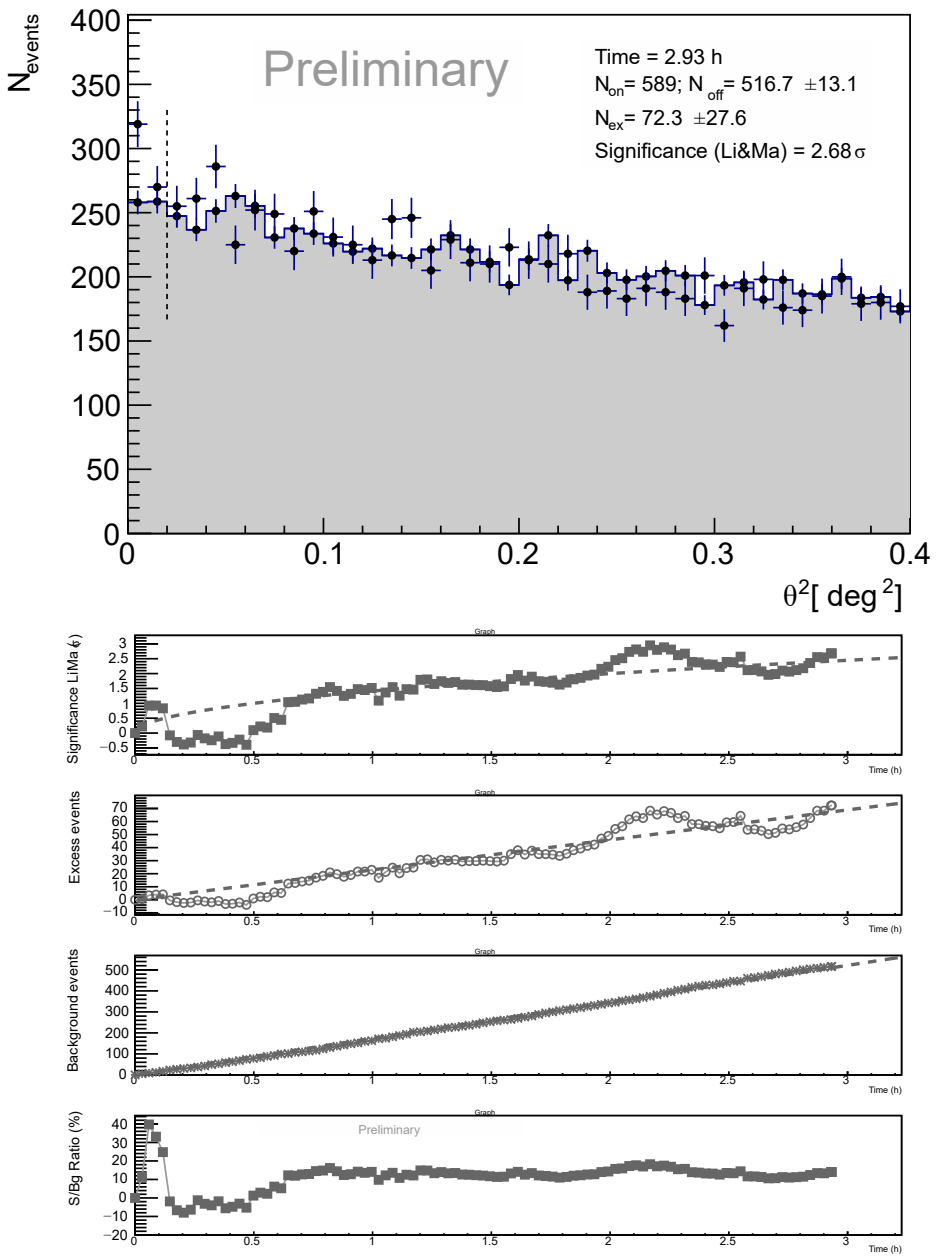

FIGURE 5.24: **Top panel**: θ^2 plot, LE cuts, for GRB 190829A. **Bottom panel**: significance versus time plot, LE cuts, for GRB 190829A.

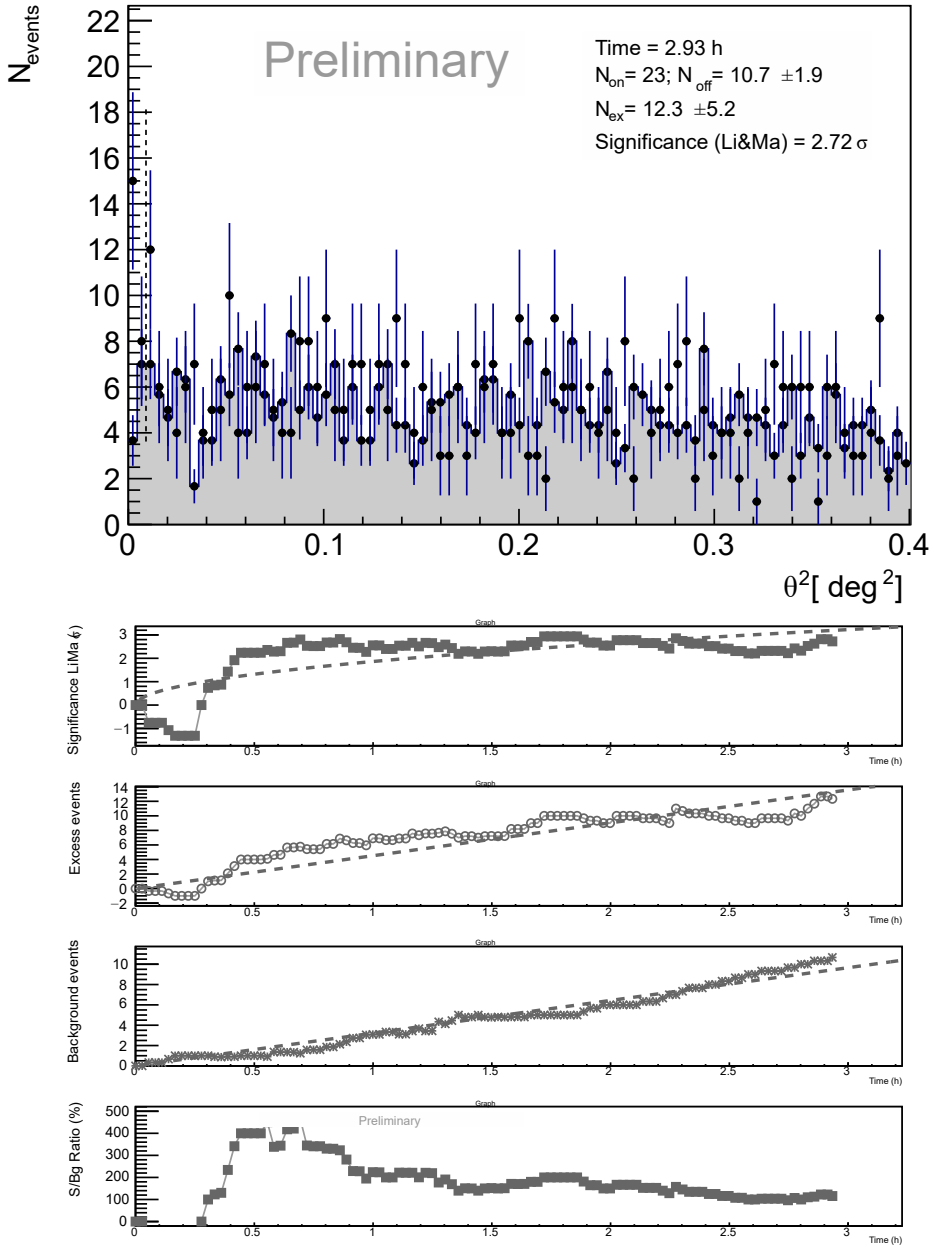

FIGURE 5.25: **Top panel**: θ^2 plot, FR cuts, for GRB 190829A. **Bottom panel**: significance versus time plot, FR cuts, for GRB 190829A.

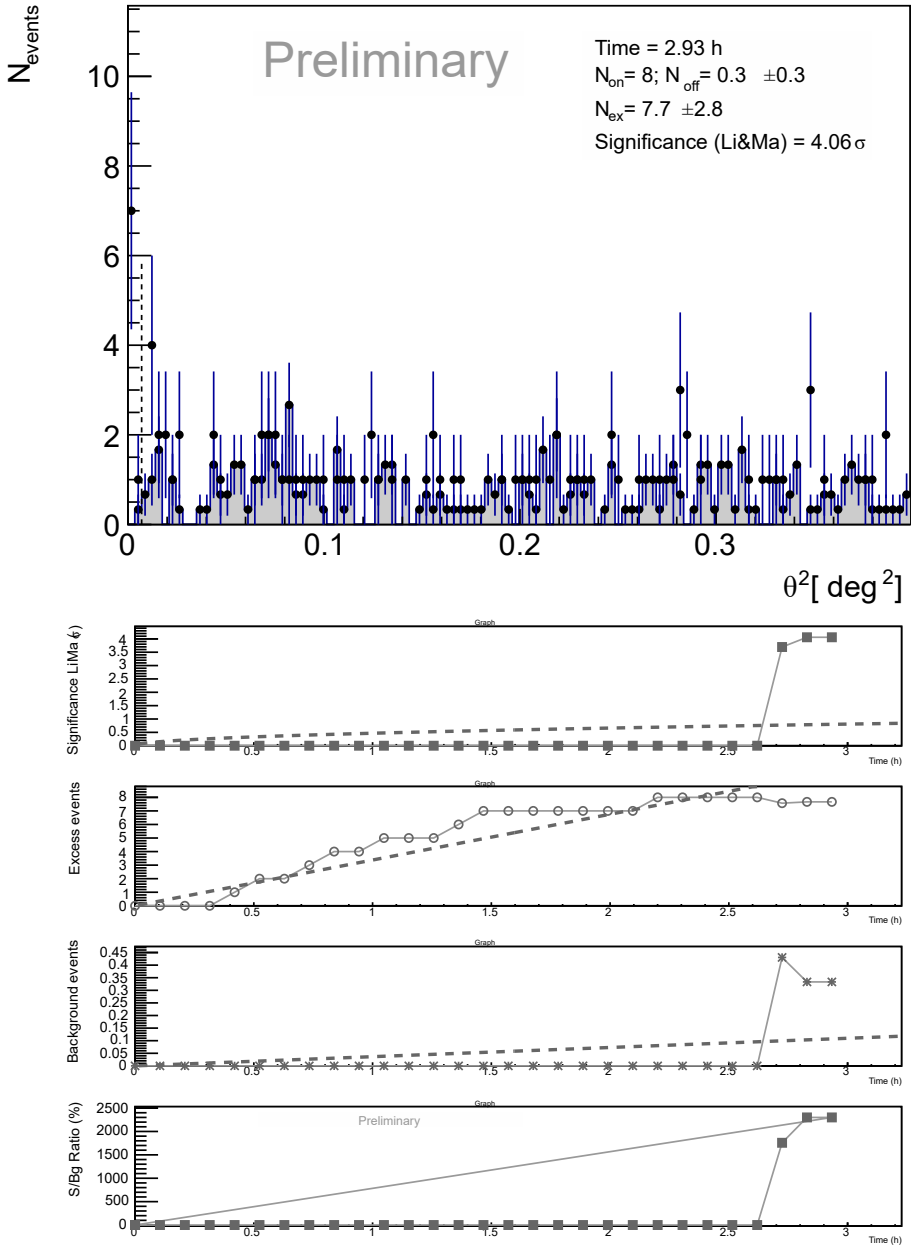

FIGURE 5.26: **Top panel**: θ^2 plot, HE cuts, for GRB 190829A. **Bottom panel**: significance versus time plot, HE cuts, for GRB 190829A.

5.4.3 Preliminary modeling with MUSE-GRB

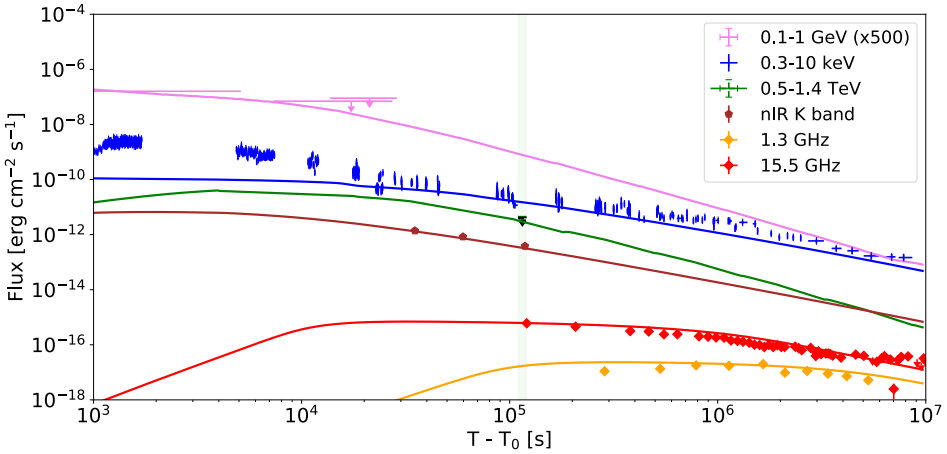

FIGURE 5.27: Modeling of multi-wavelength afterglow data of GRB 190829A with MUSE-GRB.

The broad follow-up multi-wavelength campaign of GRB 190829A allowed to collect observational data covering the entire spectrum, from radio up to the VHE band. A qualitative multi-wavelength description is provided here with a preliminary modeling obtained from MUSE-GRB including radio, near-IR, X-ray, HE and VHE data.
The radio data were published in [219]. Observations with the Meer Karoo Array Telescope (MeerKAT, 1.3 GHz), and Arcminute Microkelvin Imager - Large Array (AMI-LA, 15.5 GHz) began one day after the burst trigger and lasted nearly 200 days. The near-IR data (K band, 1.4×10^{14} Hz) used for the modeling were obtained from the GCN circulars [220, 221, 222]. Magnitudes provided in the GCN were converted into flux densities using the AB zero point flux and corrected for the Galactic extinction. The Swift-XRT deabsorbed light curve (0.3-10 keV) was downloaded from the online analysis tools (`https://www.swift.ac.uk/xrt_curves/00922968/`). The HE LAT flux ULs (0.1-1 GeV) were taken from the corresponding GCN [223] and the MAGIC flux ULs (0.5-1.4 TeV) were calculated as described in the previous section. Tentative modeling assuming a stellar-wind like scenario $s = 2$ is shown in Figure 5.27 with the following parameters: $p = 2.1$, $\epsilon_e = 0.8$, $\epsilon_B = 9 \times 10^{-4}$, $E_k = 8.5 \times 10^{50}$ erg, $A_* = 0.04$, $\Gamma_0 = 10$, and $z = 0.0785$.
The X-ray curve shows a huge flare at $\sim 10^3$ s which is difficult to be explained within the synchrotron and SSC external forward shock scenario [211]. Then, at later times it decays following a power-law behaviour with a possible steeping around $t = 10^6$ s. In my preliminary modeling (see Figure 5.27) the power-law behaviour is reproduced assuming that $\nu_{XRT} > \nu_{cool}$ until $t = 2 \times 10^4$ s. Then, the cooling frequency ν_{cool} starts to cross the XRT energy range until $t \approx 3 \times 10^6$ s, producing a smoothed steeping of the curve. In the modeling ν_m crosses the near IR frequency ν_{IR} at $t \approx 3 \times 10^4$ s causing the steeping of the modelled light curve. The observational data, which are collected from $t \approx 3 \times 10^4$ s to $t \approx 2 \times 10^5$ s, are then reproduced assuming that $\nu_m < \nu_{IR} < \nu_{cool}$. Concerning the radio band the description is summarized as follows: the absorption frequency ν_{abs} crosses the AMI-LA and the Meer-KAT frequencies respectively for $t \approx 10^4$ s and $t \approx 10^5$ s causing a flattening of the observed flux $F \propto t^0$. Then, the decay observed in the data around $t = 1 - 4 \times 10^6$ s is explained as the crossing of the break frequency ν_m. The HE and

VHE light curves are consistent with the derived flux ULs and can explain the detection by H.E.S.S.. The LAT ULs constrain the initial value of the Lorentz bulk factor to be $\Gamma_0 \lesssim 10$, while the VHE flux ULs derived by MAGIC, which are compatible with a possible hint of detection, constrain the normalization of the external density as $A_* \lesssim 0.05$. Currently, the H.E.S.S. results from the detection of GRB 190829A cannot be included in this description since they have not been published yet. Nevertheless, I made a tentative estimation of the flux seen by H.E.S.S. from the results published in [224] and I compared it with the results from my preliminary modeling. In [224] for a $\sim 9\sigma$ detection in ~ 2 hours, an observed flux $F = 8 \times 10^{-12}$ cm^{-2} s^{-1} is quoted for $E > 200$ GeV. Assuming that a similar result is obtained also for GRB 190829A, I estimated an observed flux $F = 1.6 \times 10^{-11}$ cm^{-2} s^{-1} for a ~ 4 hours observation. From this assumption, I calculated a de-absorbed flux $F \approx 1.5 \times 10^{-11}$ erg cm^{-2} s^{-1} in the energy range 0.2-1.0 TeV, considering a power-law intrinsic differential photon spectrum $d\Phi/dE \propto E^{-\Gamma}$ with $\Gamma = 2$. The flux has been corrected for the EBL absorption using the D11 model. In my preliminary modeling, at the time of the H.E.S.S. detection $t \approx 2 \times 10^4$ s, a flux $F \approx 4.5 \times 10^{-11}$ erg cm^{-2} s^{-1} in the energy range 0.2-1.0 TeV is obtained. Therefore, the preliminary modeling results are in agreement with a $\gg 5\sigma$ detection of GRB 190829A by the H.E.S.S. telescopes.

Chapter 6

Conclusions and Future Prospects

In this thesis I focused on the study of the VHE emission component from GRBs. When I started my PhD, it was still unclear if GRBs were TeV emitters or not. On the one hand, observations performed until then (fall 2017) did not reveal any significant signal. On the other hand theoretical comprehension of the physical conditions where the TeV emission should occur was still limited and did not allow any clear prediction. I tackled the problem of TeV production in GRBs, from two different sides:

- data analysis of GRBs observed by the MAGIC telescopes;
- investigation of the SSC external forward shock scenario as responsible of the VHE radiation component with `MUSE-GRB`.

During my PhD the detections of GRB 180720B, GRB 190114C and GRB 190829A have clearly shown that at least a class of GRBs has a VHE emission component which can be seen by current ground-based instruments, such as the MAGIC and the H.E.S.S. telescopes. Thanks to such discoveries, I had the possibility to perform: i) data analysis of GRBs detected in the VHE range; ii) studies dedicated to the interpretation of the detected VHE radiation in the context of the SSC external forward shock scenario by means of `MUSE-GRB`. This work gave me the possibility to draw some conclusions on VHE emission from GRBs.

The synchrotron burnoff limiting curves and the modeling of the VHE MAGIC light curve of GRB 190114C with `MUSE-GRB` presented in this thesis have shown that the electron and proton synchrotron radiation are disfavoured in explaining the TeV emission. These studies confirm that a different radiation mechanism must be introduced to explain the VHE emission component of GRB 190114C. The most viable mechanism is the SSC radiation. `MUSE-GRB` can help to support and test such claim. Indeed, assuming a set of typical parameters for a long GRB, namely $E_k = 10^{53}$ erg, $s = 2$, $A_* = 0.5$, $\epsilon_e = 0.1$, $\epsilon_B = 10^{-3}$, $\Gamma_0 = 400$, $p = 2.3$ and $z = 0.5$, or similarly for a short GRB, $E_k = 2 \times 10^{51}$ erg, $s = 0$, $A_0 = 1$ cm^{-3}, $\epsilon_e = 0.2$, $\epsilon_B = 10^{-3}$, $\Gamma_0 = 700$, $p = 2.1$ and $z = 0.1$, the observed flux in the energy range 0.2-1.0 TeV at $t = 100$ s calculated with `MUSE-GRB` is $F_{0.2-1.0TeV} \approx 3 - 7 \times 10^{-9}$ erg cm^{-2} s^{-1}, which is in the detectable range of both MAGIC (it is indeed similar to the GRB 190114C flux at $t \approx 300 - 400$ s) and H.E.S.S. telescopes, as described in [143]. Therefore, it is reasonable to conclude that *for quite standard afterglow parameters, the SSC emission from relatively nearby GRBs is detectable by current IACTs telescopes and can be detected even from a larger sample of GRBs in the future.*

Besides these few detections, most of the GRBs observed by MAGIC so far did not show any significant signal. For this sample of GRBs I have derived de-absorbed

flux ULs which I have compared with the X-ray and HE information coming from other instruments. The derived VHE MAGIC ULs were mostly at the same level of the contemporaneous X-ray flux or above, which means that *the presence of a possible VHE component with an energy budget similar to the one observed in the X-ray band cannot be excluded*. Such a result is also in agreement with the current estimation performed on the GRBs detected in the VHE range and leaves open the possibility that such SSC component might be present in a larger sample of GRBs.

Another topic which was addressed in this thesis is the study and the modeling of the VHE emission in the context of the multi-wavelength afterglow observational data. In this work I have modeled GRB 190829A multi-wavelength afterglow observations with `MUSE-GRB`. The preliminary modeling which I have obtained including radio, near IR, X-ray, HE and VHE data gave me the possibility to infer some constraints on the parameter space. A preliminary tentative modeling of the data is presented assuming a stellar-wind like scenario ($s = 2$) with the following parameters: $p = 2.1$, $\epsilon_e = 0.8$, $\epsilon_B = 9 \times 10^{-4}$, $E_k = 8.5 \times 10^{50}$ erg, $A_* = 0.04$, $\Gamma_0 = 10$, and $z = 0.0785$. In such interpretation the HE data constrain the initial value of the Lorentz bulk factor to be $\Gamma_0 \lesssim 10$, while the VHE flux ULs derived by MAGIC constrain the normalization of the external density to be $A_* \lesssim 0.05$. I also performed a raw calculation of the feasible H.E.S.S. flux. The modeling interpretation is in agreement with a $\gg 5\sigma$ detection of GRB 190829A by the H.E.S.S. telescopes. In conclusion, GRB 190829A observational data from radio to TeV range were found to be consistently explained with a synchrotron and SSC external forward shock scenario. The VHE emission component helped in providing additional information useful to constrain the parameter space. As a result, *multi-wavelength afterglow modeling including also future VHE detections will help to investigate and constrain with more detail the parameter space*.

Overall, this thesis gave the opportunity to partecipate and contribute to a breakthrough discovery for the history of the GRB physics such as the first detections of the VHE emission component. I had the possibility to investigate the responsible radiation mechanisms involved in these detections and I also developed an important tool, namely `MUSE-GRB`, which can be fundamental to study the future interesting VHE events. Indeed, in the last months the MAGIC telescopes have already announced the detection of another GRB, namely GRB 201216C [225], and the hint of detection of a VHE γ-ray signal from GRB 201015A [226]. Given the growing number of the VHE detections, I can exploit `MUSE-GRB` to perform initial population and systematic studies of GRBs detected in the VHE band and detailed modeling of the multi-wavelength observational data within the synchrotron and SSC external forward shock scenario.
Moreover, future GRB detections correlated with GW events are also expected during the next observational run (O4) of the LIGO-Virgo-Kagra interferometers. Past observations of the short GRB 170817A afterglow emission have shown that such events can exhibit an unusual rising flux for months which is explained only assuming that it came from a structured jet misaligned with our line of sight. `MUSE-GRB`, in its present version, considers only homogeneous (top hat) jets and on-axis GRB emission. I plan to further develop it in order to estimate the GRB afterglow radiation emitted from a structured jet assuming different scenarios to be included in my code. The dynamical evolution of a structured jet and the angular distribution of the jet physical properties will be simulated. Moreover, the effect of assuming different viewing angles from which the observer received the emitted radiation will

be introduced. This upgraded version of `MUSE-GRB` will be then a unique tool able to model the off-axis GRB afterglow emission coming from any structured jet, the current predicted scenario for short GRBs associated with GW events. As a result, from early/mid 2022, when O4 will start, my code will be ready for modeling the most interesting future events.

Appendix A

Additional Analysis Results

A.1 Fast analysis of interesting targets

Here the day by day θ^2 plots of the fast analysis on the AGN 3c279 are reported:

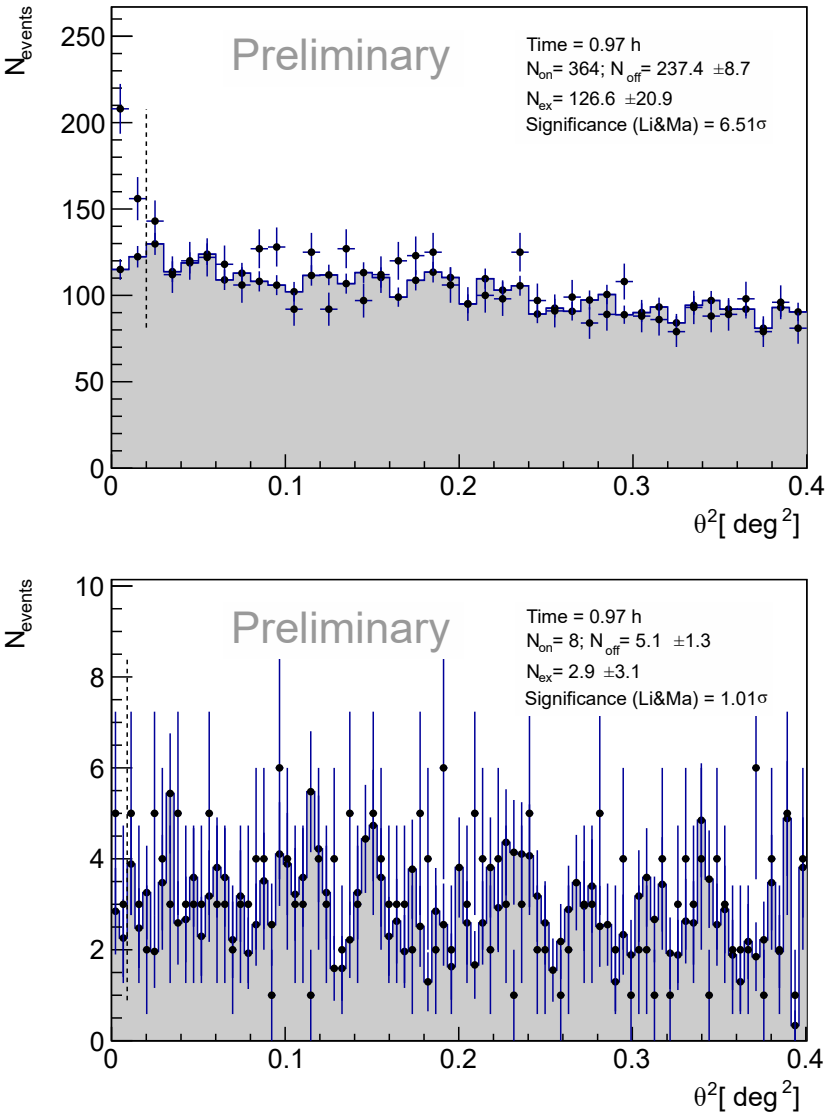

FIGURE A.1: Fast analysis of the flaring AGN 3c279, 2^{nd} June observation. **Top figure**: θ^2 plot, LE cuts. **Bottom figure**: θ^2 plot, FR cuts.

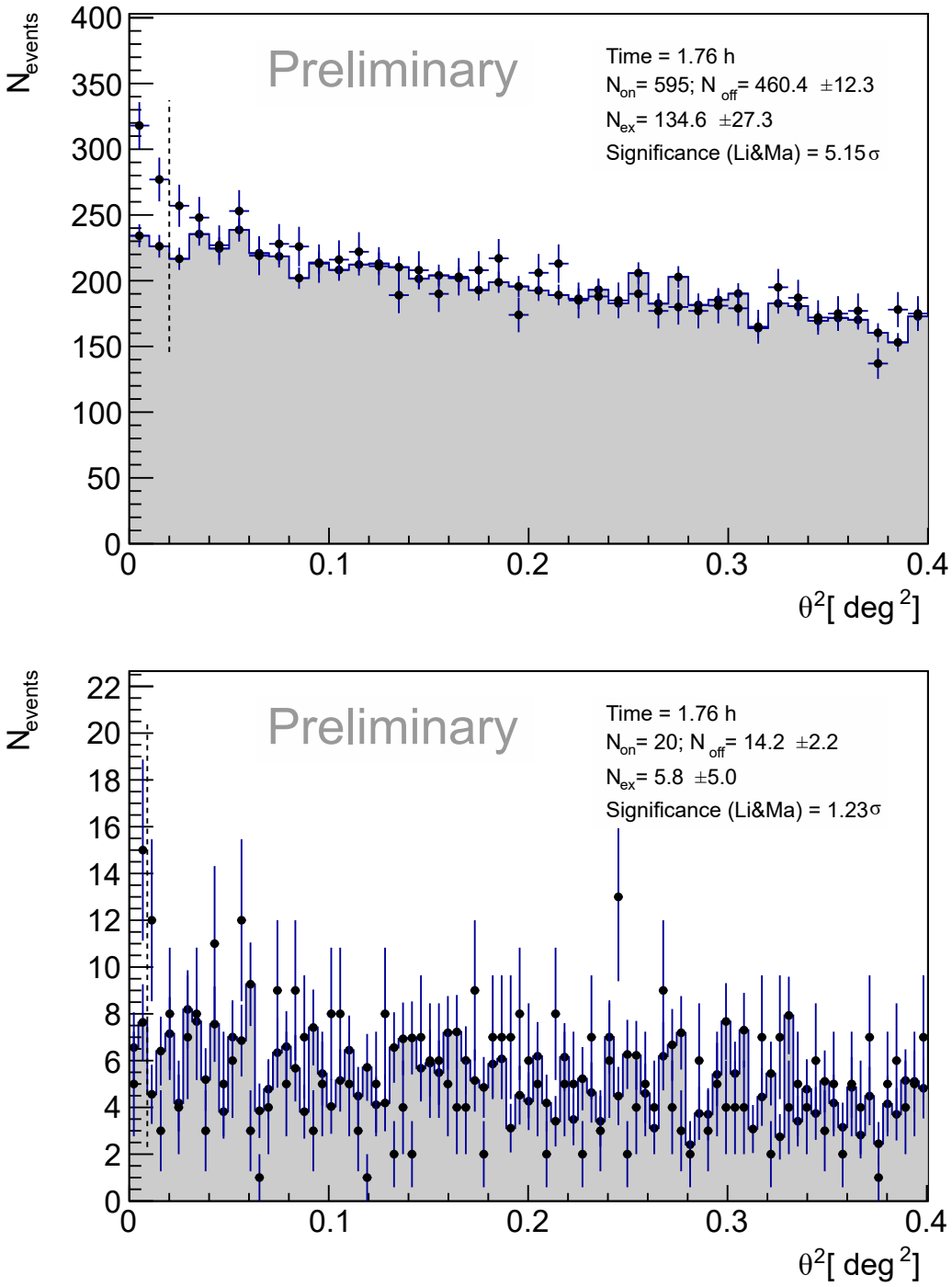

FIGURE A.2: Fast analysis of the flaring AGN 3c279, 3^{rd} June observation. **Top figure**: θ^2 plot, LE cuts. **Bottom figure**: θ^2 plot, FR cuts.

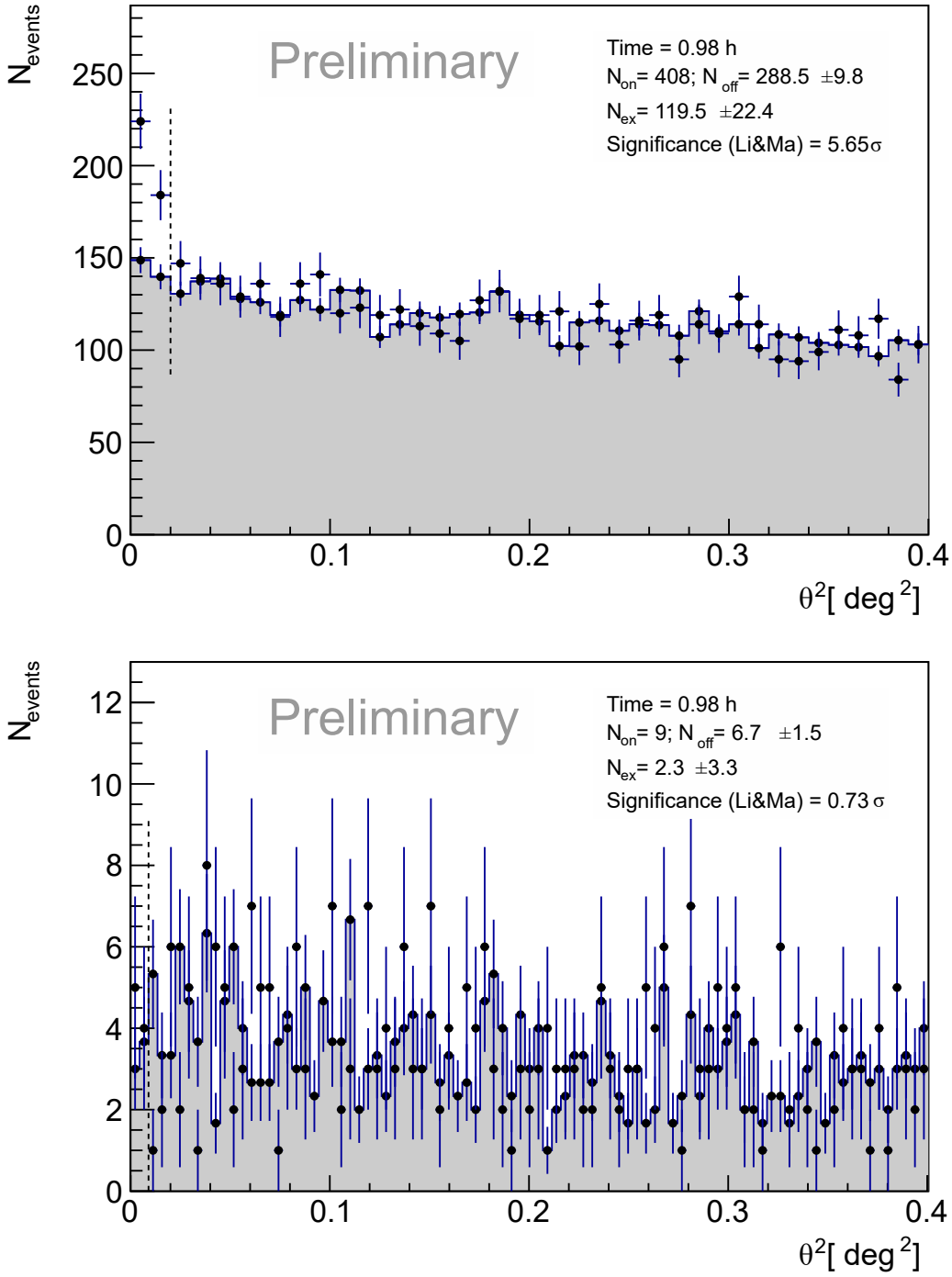

FIGURE A.3: Fast analysis of the flaring AGN 3c279, 5^{th} June observation. **Top figure**: θ^2 plot, LE cuts. **Bottom figure**: θ^2 plot, FR cuts.

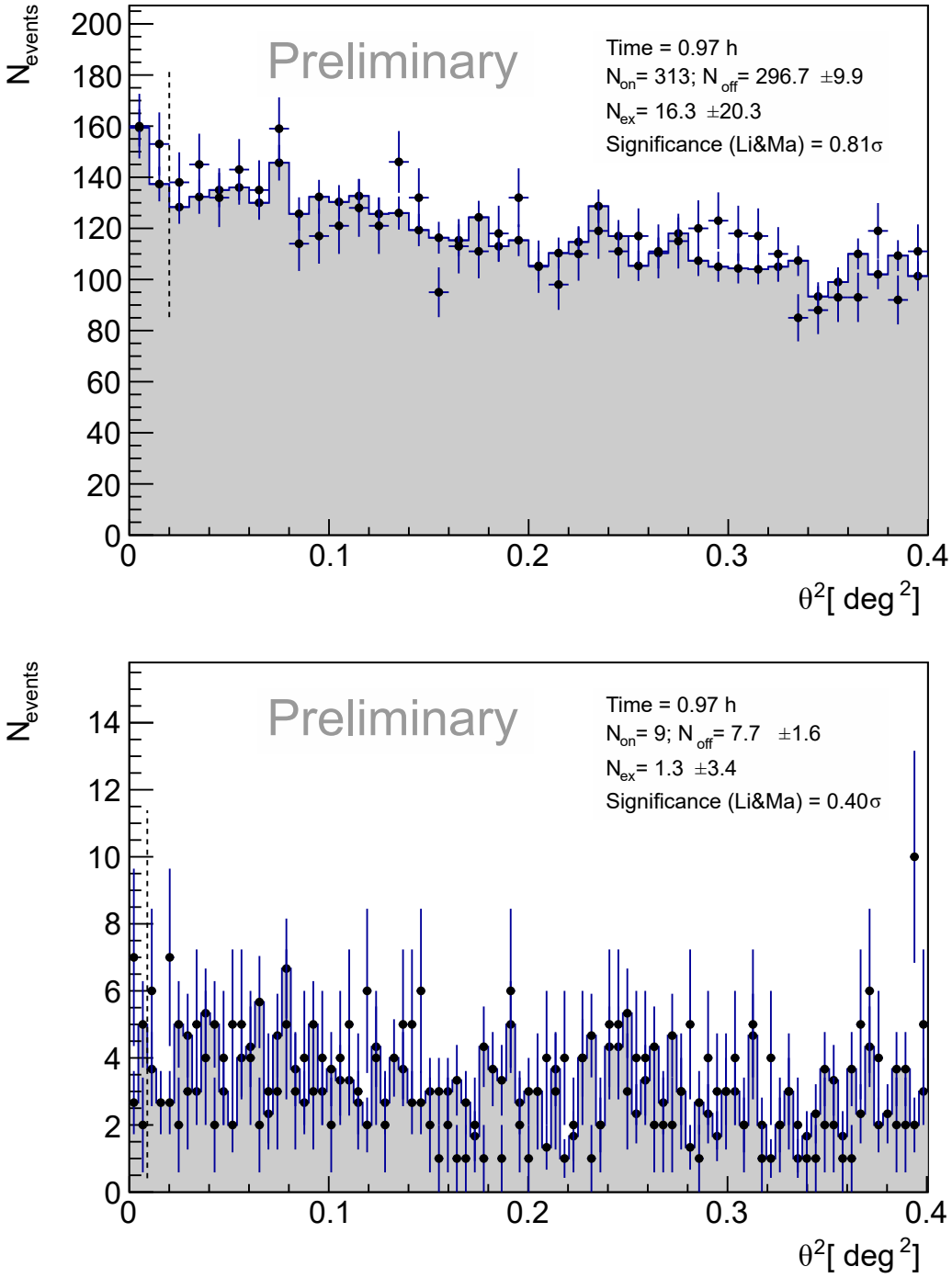

FIGURE A.4: Fast analysis of the flaring AGN 3c279, 6^{th} June observation. **Top figure**: θ^2 plot, LE cuts. **Bottom figure**: θ^2 plot, FR cuts.

A.2 GRB 190114C

The unfolded SEDs in the chosen time bins for the MWL paper analysis are here reported:

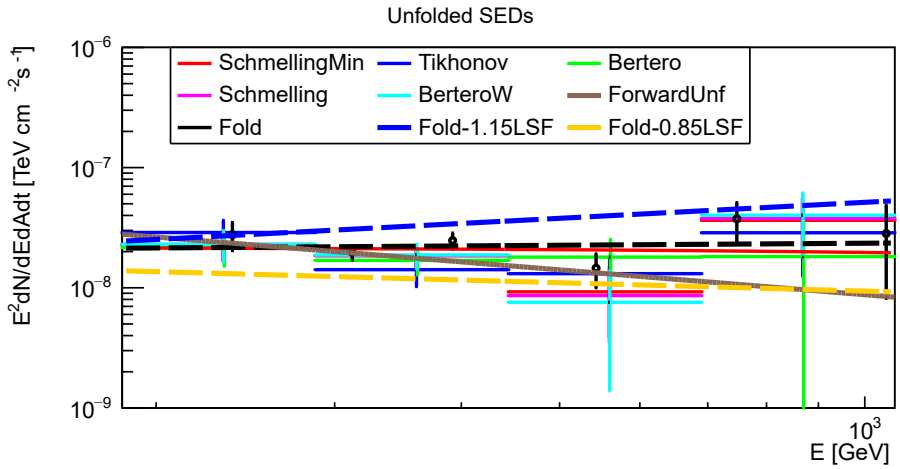

FIGURE A.5: GRB 190114C unfolded SED for time interval $T_0 + 68$ s - $T_0 + 110$ s.

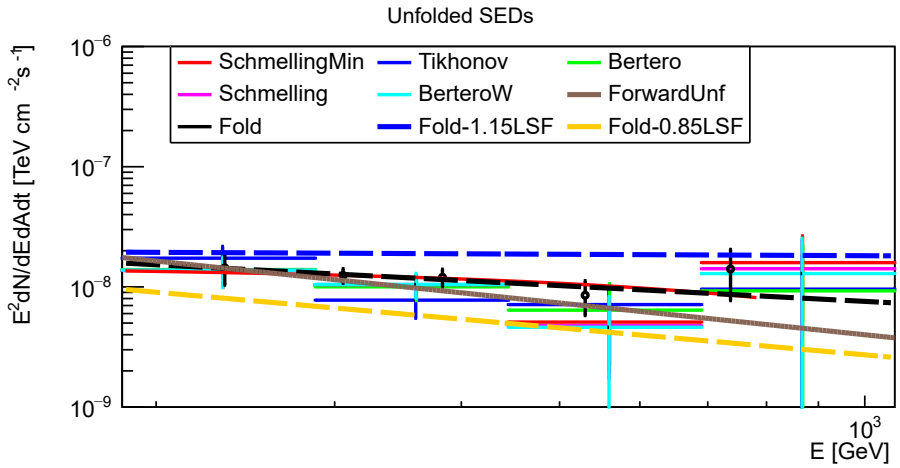

FIGURE A.6: GRB 190114C unfolded SED for time interval $T_0 + 110$ s - $T_0 + 180$ s.

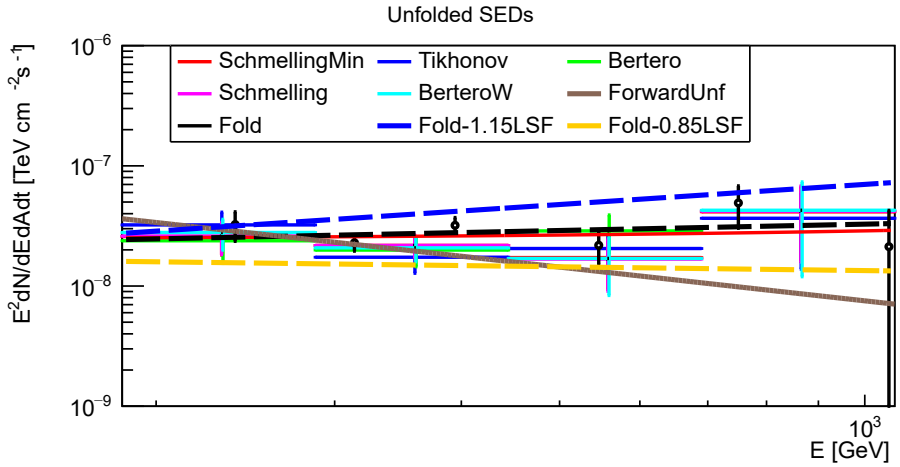

FIGURE A.7: GRB 190114C unfolded SED for time interval $T_0 + 62$ s - $T_0 + 90$ s.

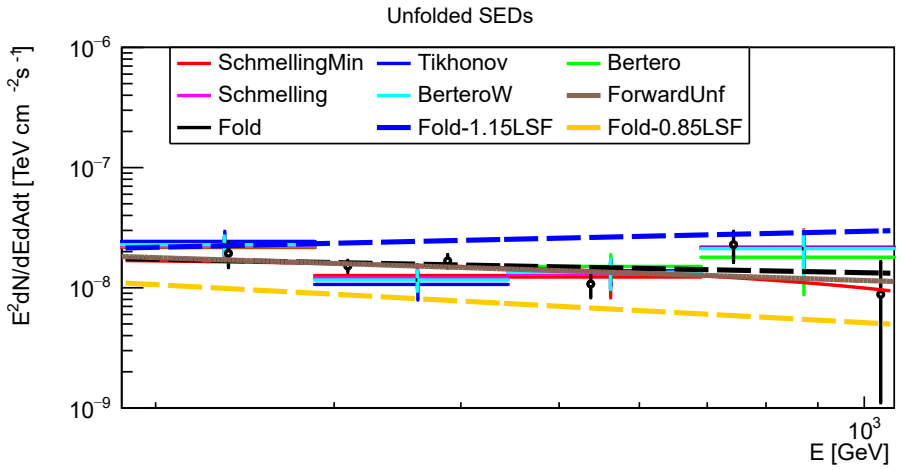

FIGURE A.8: GRB 190114C unfolded SED for time interval $T_0 + 68$ s - $T_0 + 180$ s.

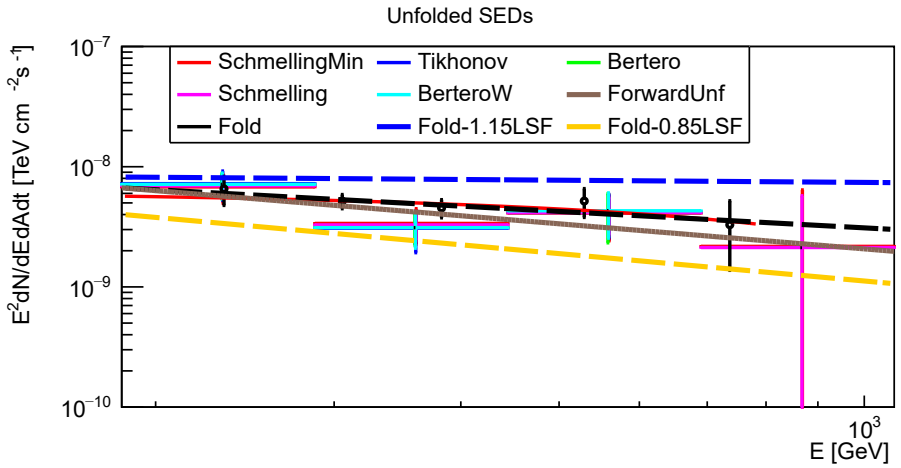

FIGURE A.9: GRB 190114C unfolded SED for time interval $T_0 + 180$ s - $T_0 + 360$ s.

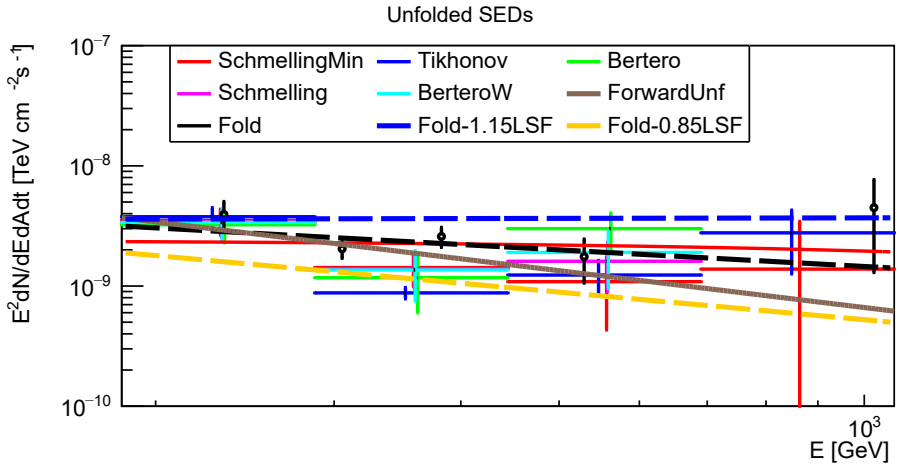

FIGURE A.10: GRB 190114C unfolded SED for time interval $T_0 + 360$ s - $T_0 + 625$ s.

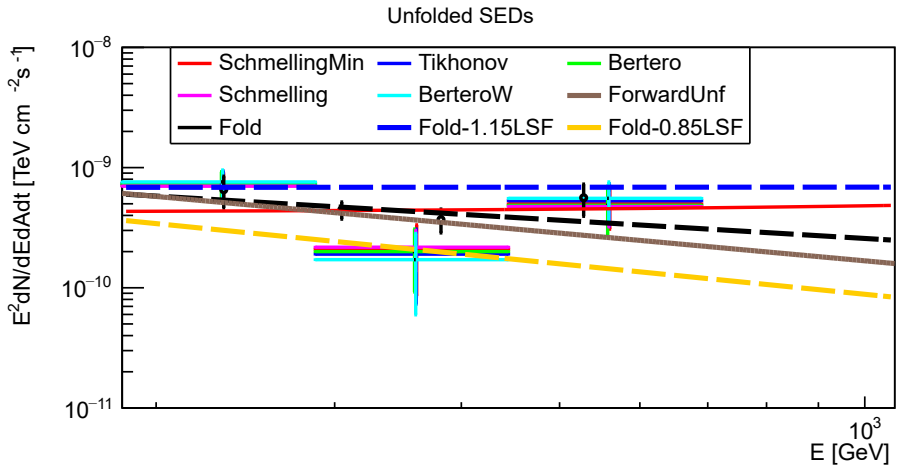

FIGURE A.11: GRB 190114C unfolded SED for time interval $T_0 + 625$ s - $T_0 + 2400$ s.

In order to compare the systematic errors and the statistical ones I ran `fold` in the time interval $T_0 + 62$ s - $T_0 + 90$ s in the nominal case and with the LSF option for the following settings:

- 12 azimuth bins and maximum relative error MC-calculated exposure in each energy bin equal to 0.4 (top panel of Figure A.12)
- 12 azimuth bins and maximum relative error MC-calculated exposure in each energy bin equal to 0.2 (middle panel of Figure A.13)
- 5 azimuth bins and maximum relative error MC-calculated exposure in each energy bin equal to 0.2 (bottom panel of Figure A.14)

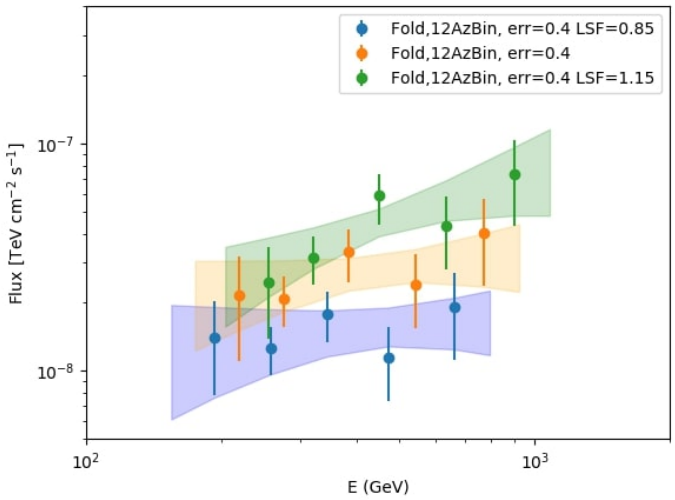

FIGURE A.12: GRB 190114C SEDs calculated with `fold` with standard options (orange) and with the LSF option assuming a light scale variations of +15% (blue) and -15% (green). The contour regions are drawn from the 1σ error of their best-fit power-law functions. The vertical bars of the data points show the 1σ errors on the flux.

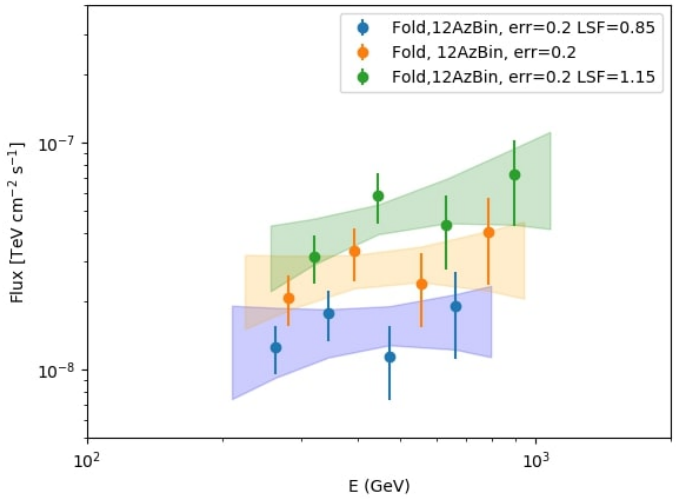

FIGURE A.13: GRB 190114C SEDs calculated with `fold` with standard options (orange) and with the LSF option assuming a light scale variations of +15% (blue) and -15% (green). The contour regions are drawn from the 1σ error of their best-fit power-law functions. The vertical bars of the data points show the 1σ errors on the flux.

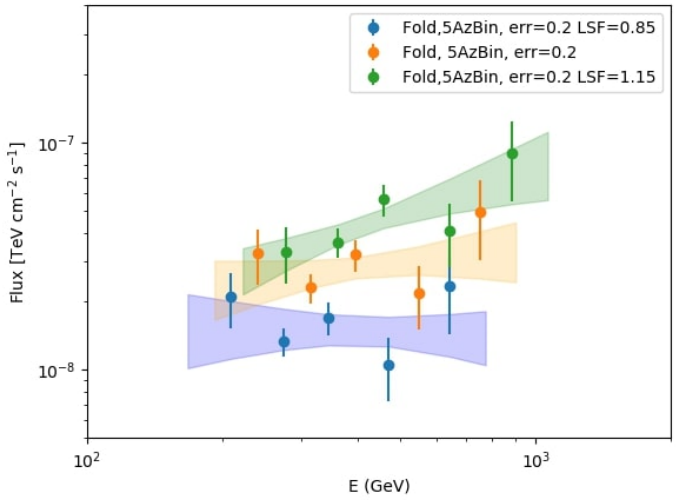

FIGURE A.14: GRB 190114C SEDs calculated with `fold` with standard options (orange) and with the LSF option assuming a light scale variations of +15% (blue) and -15% (green). The contour regions are drawn from the 1σ error of their best-fit power-law functions. The vertical bars of the data points show the 1σ errors on the flux.

A.3 MAGIC GRB UL Catalog

The results from my analysis of several GRBs are reported. In particular, I will report the ULs I have calculated assuming intrinsic spectral indices -1.6 or -2.2 and F18 or G12 EBL models.

GRB 171020A

E_1 [GeV]	E_2 [GeV]	UL TeV cm^{-2} s^{-1}
86	117	1.27×10^{-11}
117	159	3.41×10^{-12}
159	216	4.62×10^{-12}
216	294	9.84×10^{-13}
294	399	1.86×10^{-13}
399	543	3.17×10^{-14}
543	738	1.94×10^{-15}
738	1003	3.23×10^{-17}
1003	1363	3.08×10^{-18}
1363	1853	3.55×10^{-19}
1853	2519	9.62×10^{-21}
2519	3424	2.15×10^{-21}

TABLE A.1: Observed flux ULs of GRB 171020A assuming $z = 2$, intrinsic spectral index 2.2 and EBL model F18. Only energy bins above E_{thr} are shown.

E_1 [GeV]	E_2 [GeV]	UL TeV cm^{-2} s^{-1}
86	117	1.44×10^{-11}
117	159	3.92×10^{-12}
159	216	5.38×10^{-12}
216	294	1.21×10^{-12}
294	399	3.33×10^{-13}
399	543	7.36×10^{-14}
543	738	4.83×10^{-15}
738	1003	1.25×10^{-16}
1003	1363	1.19×10^{-17}
1363	1853	1.43×10^{-18}
1853	2519	4.02×10^{-20}
2519	3424	1.00×10^{-20}

TABLE A.2: Observed flux ULs of GRB 171020A assuming $z = 2$, intrinsic spectral index 1.6 and EBL model F18. Only energy bins above E_{thr} are shown.

E_1 [GeV]	E_2 [GeV]	UL TeV cm^{-2} s^{-1}
86	117	7.60×10^{-12}
117	159	1.73×10^{-12}
159	216	1.95×10^{-12}
216	294	2.72×10^{-13}
294	399	7.32×10^{-15}
399	543	4.52×10^{-16}
543	738	2.34×10^{-17}
738	1003	5.33×10^{-20}
1003	1363	4.05×10^{-21}
1363	1853	3.63×10^{-22}
1853	2519	7.89×10^{-24}
2519	3424	9.70×10^{-25}

TABLE A.3: Observed flux ULs of GRB 171020A assuming $z = 2$, intrinsic spectral index 2.2 and EBL model G12. Only energy bins above E_{thr} are shown.

E_1 [GeV]	E_2 [GeV]	UL TeV cm^{-2} s^{-1}
86	117	9.11×10^{-12}
117	159	2.11×10^{-12}
159	216	2.45×10^{-12}
216	294	3.82×10^{-13}
294	399	1.62×10^{-14}
399	543	1.23×10^{-15}
543	738	6.25×10^{-17}
738	1003	2.29×10^{-19}
1003	1363	1.77×10^{-20}
1363	1853	1.67×10^{-21}
1853	2519	3.80×10^{-23}
2519	3424	5.29×10^{-24}

TABLE A.4: Observed flux ULs of GRB 171020A assuming $z = 2$, intrinsic spectral index 1.6 and EBL model G12. Only energy bins above E_{thr} are shown.

GRB 171210A

E_1 [GeV]	E_2 [GeV]	UL TeV cm^{-2} s^{-1}
99	135	1.43×10^{-11}
135	183	5.64×10^{-12}
183	249	3.75×10^{-12}
625	849	1.64×10^{-16}
849	1154	5.79×10^{-18}
1154	1569	2.98×10^{-19}
1569	2133	4.91×10^{-20}
2133	2899	3.55×10^{-21}
2899	3941	8.50×10^{-22}
3941	5358	1.01×10^{-21}
5358	7283	2.12×10^{-22}
7283	9900	5.43×10^{-22}
13457	18294	4.22×10^{-22}

TABLE A.5: Observed flux ULs of GRB 171210A assuming $z = 2$, intrinsic spectral index 2.2 and EBL model F18. Only energy bins above E_{thr} are shown.

E_1 [GeV]	E_2 [GeV]	UL TeV cm^{-2} s^{-1}
99	135	1.68×10^{-11}
135	183	6.82×10^{-12}
625	849	4.84×10^{-16}
849	1154	2.01×10^{-17}
1154	1569	1.22×10^{-18}
1569	2133	1.97×10^{-19}
2133	2899	1.58×10^{-20}
2899	3941	3.86×10^{-21}
3941	5358	4.50×10^{-21}
5358	7283	1.04×10^{-21}
7283	9900	2.66×10^{-21}
13457	18294	1.99×10^{-21}

TABLE A.6: Observed flux ULs of GRB 171210A assuming $z = 2$, intrinsic spectral index 1.6 and EBL model F18. Only energy bins above E_{thr} are shown.

E_1 [GeV]	E_2 [GeV]	UL TeV cm^{-2} s^{-1}
99	135	7.11×10^{-12}
135	183	2.14×10^{-12}
183	249	9.49×10^{-13}
625	849	7.62×10^{-19}
849	1154	1.24×10^{-20}
1154	1569	2.90×10^{-22}
1569	2133	4.77×10^{-23}
2133	2899	2.02×10^{-24}
2899	3941	3.98×10^{-25}
3941	5358	4.98×10^{-25}
5358	7283	5.91×10^{-26}
7283	9900	1.39×10^{-25}
13457	18294	1.15×10^{-25}

TABLE A.7: Observed flux ULs of GRB 171210A assuming $z = 2$, intrinsic spectral index 2.2 and EBL model G12. Only energy bins above E_{thr} are shown.

E_1 [GeV]	E_2 [GeV]	UL TeV cm^{-2} s^{-1}
99	135	8.89×10^{-12}
135	183	2.81×10^{-12}
183	249	1.37×10^{-12}
625	849	2.62×10^{-18}
849	1154	4.90×10^{-20}
1154	1569	1.35×10^{-21}
1569	2133	2.23×10^{-22}
2133	2899	1.05×10^{-23}
2899	3941	2.16×10^{-24}
3941	5358	2.64×10^{-24}
5358	7283	3.51×10^{-25}
7283	9900	8.31×10^{-25}
13457	18294	6.73×10^{-25}

TABLE A.8: Observed flux ULs of GRB 171210A assuming $z = 2$, intrinsic spectral index 1.6 and EBL model G12. Only energy bins above E_{thr} are shown.

GRB 180512A

E_1 [GeV]	E_2 [GeV]	UL TeV cm^{-2} s^{-1}
72	98	1.18×10^{-11}
98	133	8.59×10^{-12}
133	181	2.48×10^{-12}
181	246	7.62×10^{-13}
246	334	3.13×10^{-13}
334	454	3.56×10^{-14}
454	618	7.68×10^{-15}
618	839	5.23×10^{-16}
839	1141	1.90×10^{-17}
1141	1551	2.06×10^{-19}
1551	2109	5.01×10^{-20}
2109	2866	2.75×10^{-20}

TABLE A.9: Observed flux ULs of GRB 180512A assuming $z = 2$, intrinsic spectral index 2.2 and EBL model F18. Only energy bins above E_{thr} are shown.

E_1 [GeV]	E_2 [GeV]	UL TeV cm^{-2} s^{-1}
72	98	1.33×10^{-11}
98	133	9.70×10^{-12}
133	181	2.85×10^{-12}
181	246	9.05×10^{-13}
246	334	4.12×10^{-13}
334	454	6.70×10^{-14}
454	618	2.03×10^{-14}
618	839	1.50×10^{-15}
839	1141	6.81×10^{-17}
1141	1551	9.00×10^{-19}
1551	2109	2.12×10^{-19}
2109	2866	1.10×10^{-19}

TABLE A.10: Observed flux ULs of GRB 180512A assuming $z = 2$, intrinsic spectral index 1.6 and EBL model F18. Only energy bins above E_{thr} are shown.

E_1 [GeV]	E_2 [GeV]	UL TeV cm^{-2} s^{-1}
72	98	7.84×10^{-12}
98	133	5.00×10^{-12}
133	181	1.17×10^{-12}
181	246	2.66×10^{-13}
246	334	4.46×10^{-14}
334	454	1.02×10^{-15}
454	618	5.98×10^{-17}
618	839	3.02×10^{-18}
839	1141	4.01×10^{-20}
1141	1551	1.53×10^{-22}
1551	2109	4.19×10^{-23}
2109	2866	2.69×10^{-23}

TABLE A.11: Observed flux ULs of GRB 180512A assuming $z = 2$, intrinsic spectral index 2.2 and EBL model G12. Only energy bins above E_{thr} are shown.

E_1 [GeV]	E_2 [GeV]	UL TeV cm^{-2} s^{-1}
72	98	9.20×10^{-12}
98	133	5.94×10^{-12}
133	181	1.45×10^{-12}
181	246	3.57×10^{-13}
246	334	7.72×10^{-14}
334	454	2.44×10^{-15}
454	618	1.88×10^{-16}
618	839	9.72×10^{-18}
839	1141	1.57×10^{-19}
1141	1551	7.54×10^{-22}
1551	2109	2.00×10^{-22}
2109	2866	1.24×10^{-22}

TABLE A.12: Observed flux ULs of GRB 180512A assuming $z = 2$, intrinsic spectral index 1.6 and EBL model G12. Only energy bins above E_{thr} are shown.

GRB 180715A

E_1 [GeV]	E_2 [GeV]	UL TeV cm^{-2} s^{-1}
92	125	2.48×10^{-11}
125	170	4.35×10^{-12}
170	231	4.47×10^{-12}
231	314	4.97×10^{-12}
314	427	3.30×10^{-12}
427	580	2.24×10^{-12}
580	789	2.89×10^{-12}
789	1073	4.18×10^{-13}
1073	1458	2.42×10^{-12}

TABLE A.13: Observed flux ULs of GRB 180715A assuming $z = 0.5$, intrinsic spectral index 2.2 and EBL model F18. Only energy bins above E_{thr} are shown.

E_1 [GeV]	E_2 [GeV]	UL TeV cm^{-2} s^{-1}
92	125	2.60×10^{-11}
125	170	4.54×10^{-12}
170	231	4.70×10^{-12}
231	314	5.26×10^{-12}
314	427	3.55×10^{-12}
427	580	2.56×10^{-12}
580	789	3.45×10^{-12}
789	1073	6.15×10^{-13}
1073	1458	3.50×10^{-12}

TABLE A.14: Observed flux ULs of GRB 180715A assuming $z = 0.5$, intrinsic spectral index 1.6 and EBL model F18. Only energy bins above E_{thr} are shown.

E_1 [GeV]	E_2 [GeV]	UL TeV cm^{-2} s^{-1}
92	125	2.43×10^{-11}
125	170	4.24×10^{-12}
170	231	4.38×10^{-12}
231	314	4.87×10^{-12}
314	427	3.18×10^{-12}
427	580	2.07×10^{-12}
580	789	2.54×10^{-12}
789	1073	2.97×10^{-13}
1073	1458	1.56×10^{-12}

TABLE A.15: Observed flux ULs of GRB 180715A assuming $z = 0.5$, intrinsic spectral index 2.2 and EBL model G12. Only energy bins above E_{thr} are shown.

E_1 [GeV]	E_2 [GeV]	UL TeV cm^{-2} s^{-1}
92	125	2.58×10^{-11}
125	170	4.46×10^{-12}
170	231	4.59×10^{-12}
231	314	5.15×10^{-12}
314	427	3.48×10^{-12}
427	580	2.44×10^{-12}
580	789	3.17×10^{-12}
789	1073	4.92×10^{-13}
1073	1458	2.61×10^{-12}

TABLE A.16: Observed flux ULs of GRB 180715A assuming $z = 0.5$, intrinsic spectral index 1.6 and EBL model G12. Only energy bins above E_{thr} are shown.

GRB 180720C

E_1 [GeV]	E_2 [GeV]	UL TeV cm^{-2} s^{-1}
495	673	3.46×10^{-13}
673	915	2.82×10^{-13}
915	1243	3.30×10^{-14}
1243	1690	3.07×10^{-16}
1690	2298	2.71×10^{-17}
2298	3123	1.73×10^{-17}
4246	5771	1.59×10^{-22}
5771	7845	2.22×10^{-21}

TABLE A.17: Observed flux ULs of GRB 180720C assuming $z = 2$, intrinsic spectral index 2.2 and EBL model F18. Only energy bins above E_{thr} are shown.

E_1 [GeV]	E_2 [GeV]	UL TeV cm^{-2} s^{-1}
495	673	4.95×10^{-13}
673	915	3.86×10^{-13}
915	1243	5.65×10^{-14}
1243	1690	6.98×10^{-16}
1690	2298	6.92×10^{-17}
2298	3123	4.35×10^{-17}
4246	5771	7.98×10^{-22}
5771	7845	9.60×10^{-21}

TABLE A.18: Observed flux ULs of GRB 180720C assuming $z = 2$, intrinsic spectral index 1.6 and EBL model F18. Only energy bins above E_{thr} are shown.

E_1 [GeV]	E_2 [GeV]	UL TeV cm^{-2} s^{-1}
495	673	5.18×10^{-14}
673	915	5.32×10^{-14}
915	1243	2.04×10^{-15}
1243	1690	5.04×10^{-18}
1690	2298	2.44×10^{-19}
2298	3123	1.61×10^{-19}
4246	5771	4.39×10^{-26}
5771	7845	1.17×10^{-24}

TABLE A.19: Observed flux ULs of GRB 180720C assuming $z = 2$, intrinsic spectral index 2.2 and EBL model G12. Only energy bins above E_{thr} are shown.

E_1 [GeV]	E_2 [GeV]	UL TeV cm^{-2} s^{-1}
495	673	8.00×10^{-14}
673	915	7.85×10^{-14}
915	1243	3.81×10^{-15}
1243	1690	1.25×10^{-17}
1690	2298	6.90×10^{-19}
2298	3123	4.49×10^{-19}
4246	5771	2.62×10^{-25}
5771	7845	5.98×10^{-24}

TABLE A.20: Observed flux ULs of GRB 180720C assuming $z = 2$, intrinsic spectral index 1.6 and EBL model G12. Only energy bins above E_{thr} are shown.

GRB 180904A

E_1 [GeV]	E_2 [GeV]	UL TeV cm^{-2} s^{-1}
96	130	6.27×10^{-12}
130	177	5.87×10^{-12}
177	241	1.56×10^{-12}
241	328	6.17×10^{-13}
328	446	4.44×10^{-14}
446	606	5.73×10^{-15}
606	823	4.23×10^{-16}
823	1119	2.27×10^{-18}
1119	1521	2.76×10^{-19}
1521	2068	2.37×10^{-20}
2068	2811	6.27×10^{-21}
2811	3822	1.19×10^{-21}
3822	5195	3.02×10^{-22}
5195	7062	3.74×10^{-22}
7062	9600	1.50×10^{-22}

TABLE A.21: Observed flux ULs of GRB 180904A assuming $z = 2$, intrinsic spectral index 2.2 and EBL model F18. Only energy bins above E_{thr} are shown.

E_1 [GeV]	E_2 [GeV]	UL TeV cm^{-2} s^{-1}
96	130	7.17×10^{-12}
130	177	6.89×10^{-12}
177	241	1.92×10^{-12}
241	328	8.42×10^{-13}
328	446	8.35×10^{-14}
446	606	1.39×10^{-14}
606	823	1.24×10^{-15}
823	1119	8.41×10^{-18}
1119	1521	1.13×10^{-18}
1521	2068	1.01×10^{-19}
2068	2811	2.80×10^{-20}
2811	3822	5.51×10^{-21}
3822	5195	1.44×10^{-21}
5195	7062	1.77×10^{-21}
7062	9600	7.31×10^{-22}

TABLE A.22: Observed flux ULs of GRB 180904A assuming $z = 2$, intrinsic spectral index 1.6 and EBL model F18. Only energy bins above E_{thr} are shown.

E_1 [GeV]	E_2 [GeV]	UL TeV cm^{-2} s^{-1}
96	130	3.51×10^{-12}
130	177	2.58×10^{-12}
177	241	4.53×10^{-13}
241	328	9.25×10^{-14}
328	446	1.21×10^{-15}
446	606	6.36×10^{-17}
606	823	2.18×10^{-18}
823	1119	3.74×10^{-21}
1119	1521	2.85×10^{-22}
1521	2068	1.78×10^{-23}
2068	2811	3.44×10^{-24}
2811	3822	5.03×10^{-25}
3822	5195	1.04×10^{-25}
5195	7062	1.24×10^{-25}
7062	9600	3.98×10^{-26}

TABLE A.23: Observed flux ULs of GRB 180904A assuming $z = 2$, intrinsic spectral index 2.2 and EBL model G12. Only energy bins above E_{thr} are shown.

E_1 [GeV]	E_2 [GeV]	UL TeV cm^{-2} s^{-1}
96	130	4.21×10^{-12}
130	177	3.26×10^{-12}
177	241	6.38×10^{-13}
241	328	1.53×10^{-13}
328	446	3.00×10^{-15}
446	606	1.83×10^{-16}
606	823	7.24×10^{-18}
823	1119	1.59×10^{-20}
1119	1521	1.30×10^{-21}
1521	2068	8.78×10^{-23}
2068	2811	1.81×10^{-23}
2811	3822	2.79×10^{-24}
3822	5195	5.97×10^{-25}
5195	7062	7.07×10^{-25}
7062	9600	2.37×10^{-25}

TABLE A.24: Observed flux ULs of GRB 180904A assuming $z = 2$, intrinsic spectral index 1.6 and EBL model G12. Only energy bins above E_{thr} are shown.

The effects of the chosen EBL models and spectral indices on the resulting intrinsic MAGIC ULs have also been tested. I performed a test with the following settings:

- intrinsic spectral index Γ ranging between 1.5 and 3.0;
- redshift $z = 0.5, 1, 2$;
- EBL model D11.

For the test I considered four different cases:

- **case A**: $E_{thr} = 50$ GeV and MAGIC observed UL fixed at 5×10^{-11};
- **case B**: $E_{thr} = 100$ GeV and MAGIC observed UL fixed at 5×10^{-11};
- **case C**: $E_{thr} = 200$ GeV and MAGIC observed UL fixed at 5×10^{-11};
- **case D**: settings taken from GRB 180512A analysis, $E_{thr} = 72$ GeV and MAGIC observed UL calculated from `flute`.

The intrinsic ULs calculated with these settings and in these cases are shown in Figures A.15, A.16, A.17, and A.18. Taking as reference the ULs calculated for $\Gamma = 2.2$, the variation with the other ULs is of a factor up to $\sim \pm 0.5 - 2$. Such variation holds also in case of higher redshift values or higher energy thresholds. The only effect of such settings is to increase the values of the computed intrinsic ULs up to three order of magnitudes for settings $E_{thr} = 200$ GeV and $z = 2$.

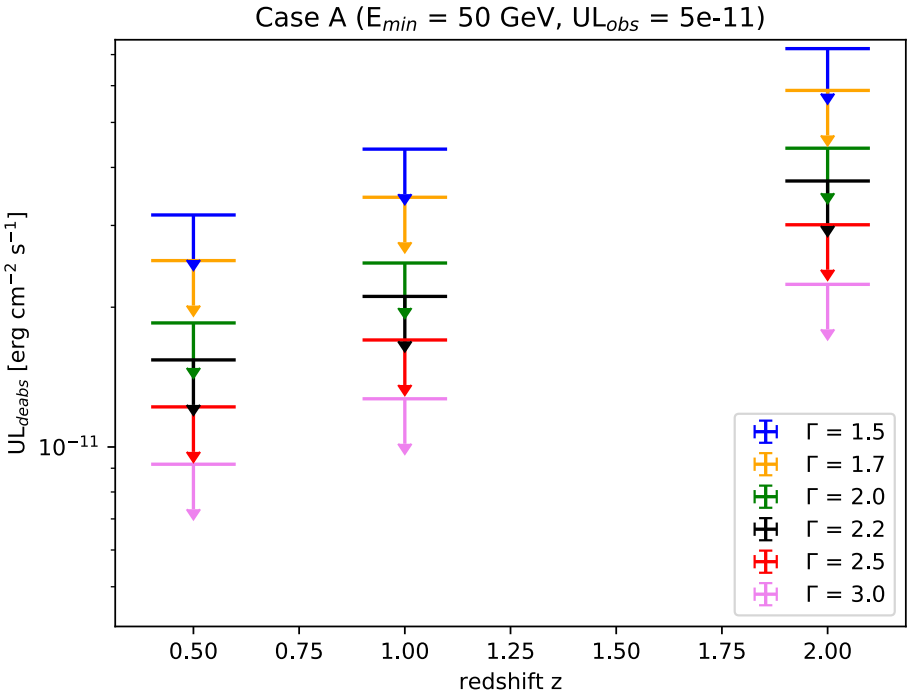

FIGURE A.15: Intrinsic ULs calculated for the settings in *case A*.

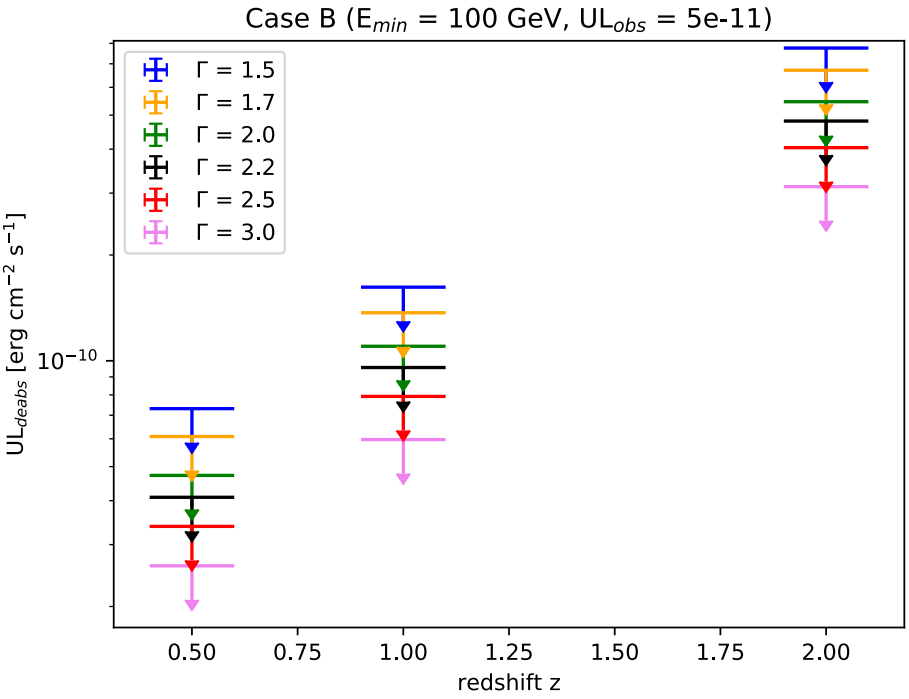

FIGURE A.16: Intrinsic ULs calculated for the settings in *case B*.

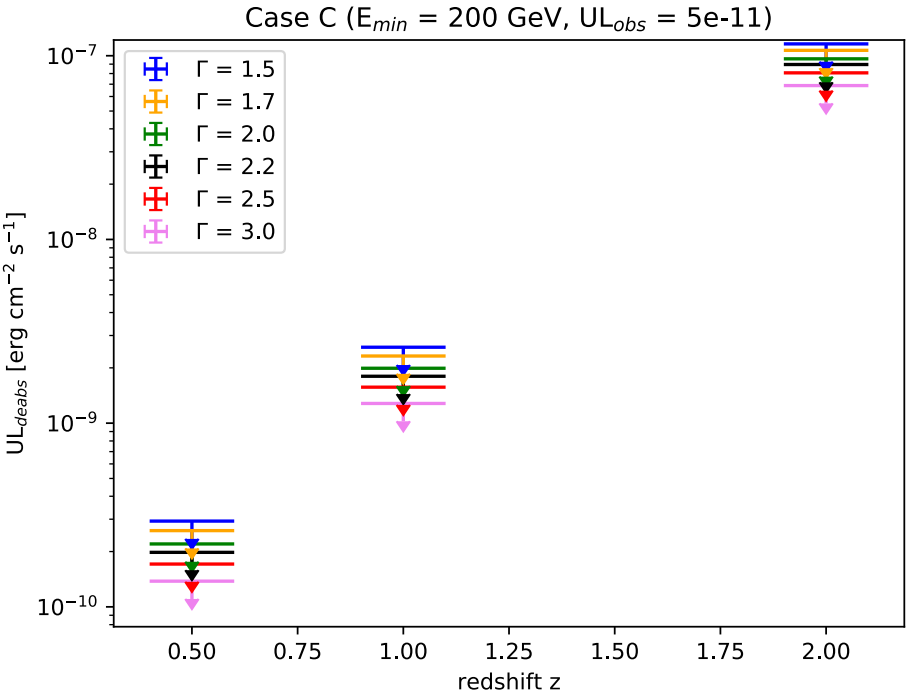

FIGURE A.17: Intrinsic ULs calculated for the settings in *case C*.

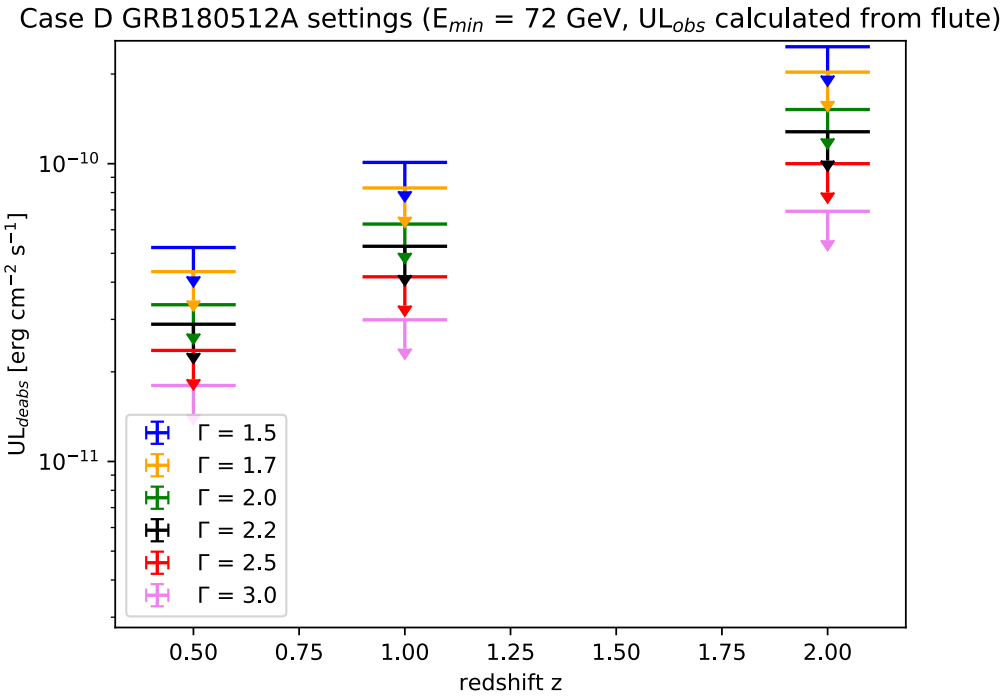

FIGURE A.18: Intrinsic ULs calculated for the settings in *case D*.

A second test was instead focused on the differences of the resulting intrinsic ULs applying different EBL models and increasing the redshift. The settings were:

- intrinsic spectral index $\Gamma = 2.2$;
- redshift $z = 0.5, 1, 2$;
- three EBL model tested: D11, G12, F18.

I considered the same four cases as in the previous test. The intrinsic ULs calculated with these settings and in these cases are shown in Figures A.19, A.20, A.21, and A.22. The results are consistent with previous tests done on the EBL models. In particular D11 and F18 give very similar results, with differences of less than 5% for $z = 0.5$ and 10% for $z = 1$. For $z = 2$ the difference is of $\sim$ 15% except for the case C where with $E_{thr} = 200$ the difference is of a factor ~ 2. The G12 model exhibits higher values of the intrinsic UL with respect to the other two models. In comparison with D11 the difference is of the order of 15% for $z = 0.5$ and of a factor up to ~ 10 for $z = 1$ and up to $\sim 15 - 30$ for $z = 2$. This test validates the choice to report at least two EBL models since the difference between each other when $z > 1$ cannot be disregarded.

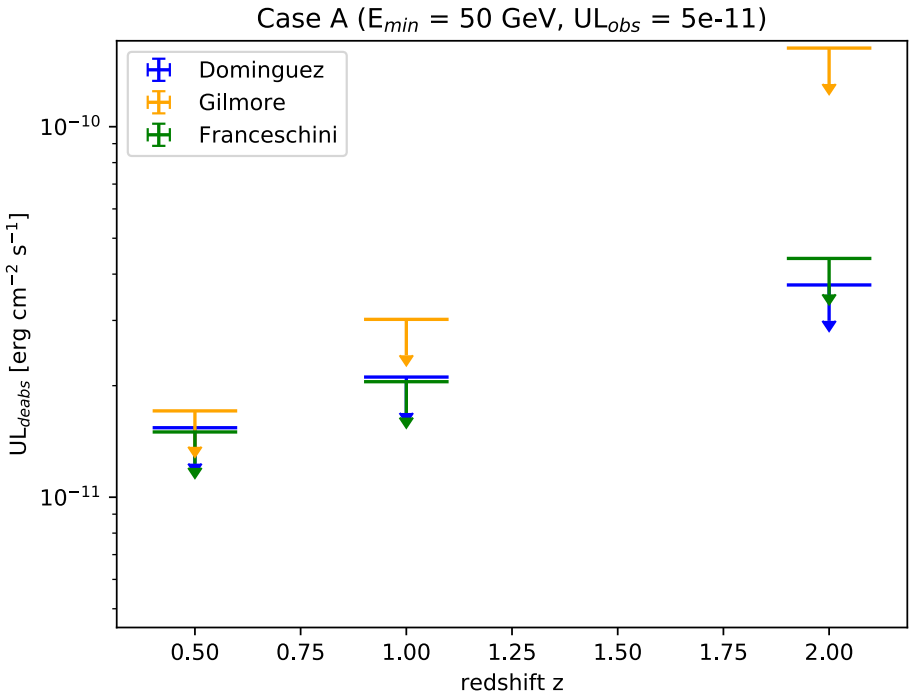

FIGURE A.19: Intrinsic ULs calculated for the settings in *case A*.

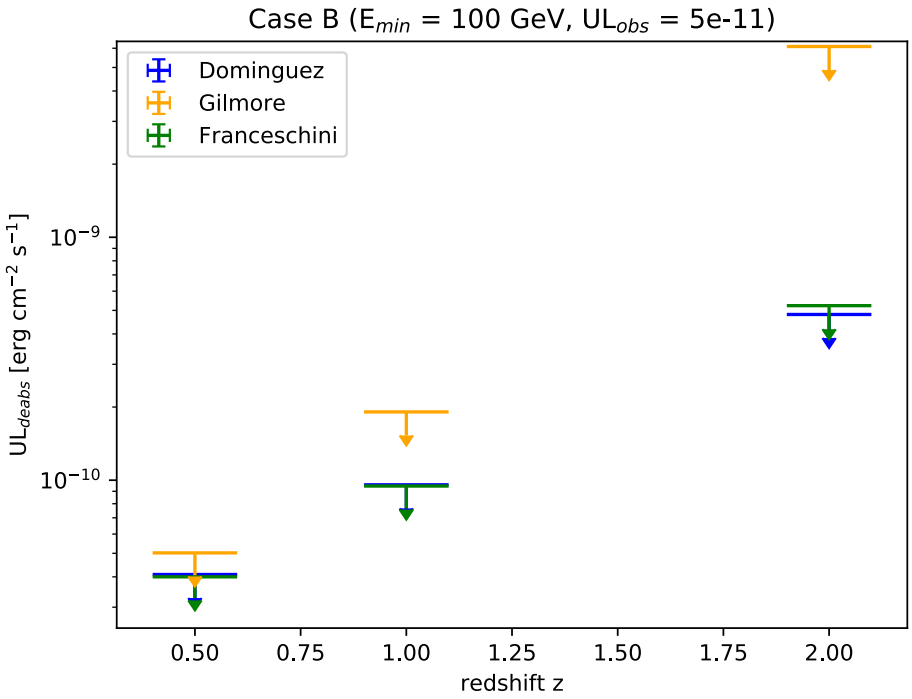

FIGURE A.20: Intrinsic ULs calculated for the settings in *case B*.

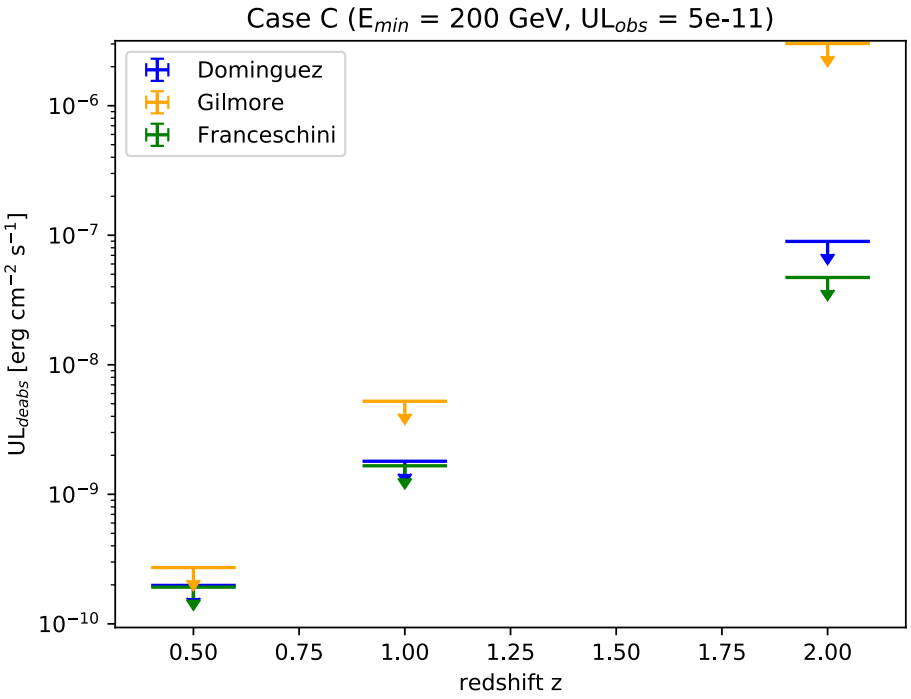

FIGURE A.21: Intrinsic ULs calculated for the settings in *case C*.

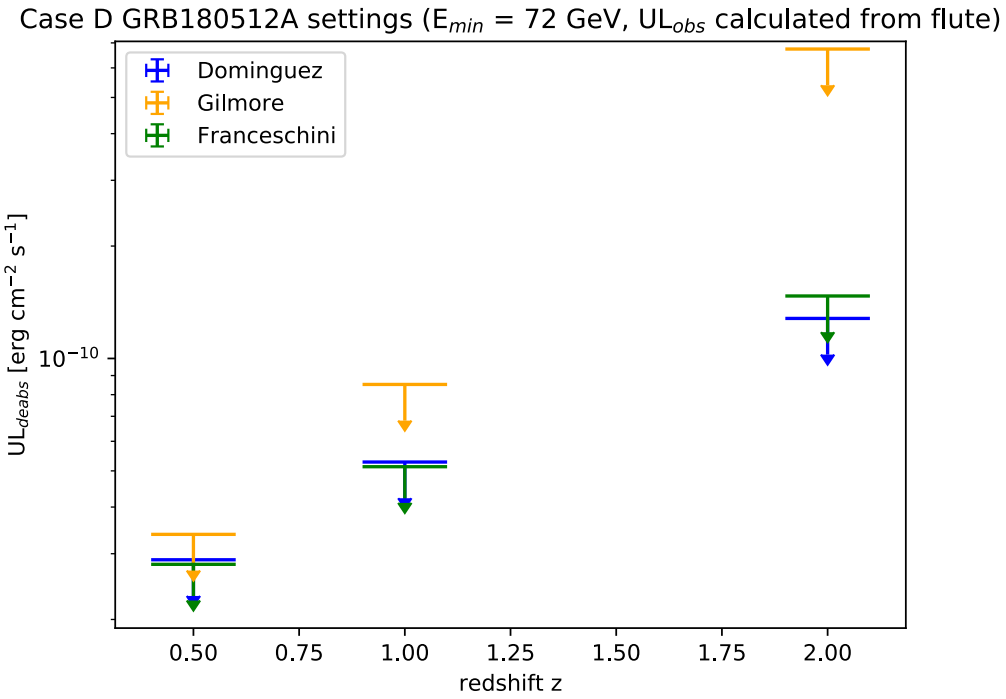

FIGURE A.22: Intrinsic ULs calculated for the settings in *case D*.

Bibliography

[1] Wulf, T. "Observations on the radiation of high penetration power on the Eiffel tower". In: *Physikalische Zeitschrift* 11 (1910), p. 811.

[2] Pacini, D. "La radiazione penetrante alla superficie ed in seno alle acque". In: *Il Nuovo Cimento* 3 (1912), pp. 93–100.

[3] Hess, V. "Über Beobachtungen der durchdringenden Strahlung bei sieben Freiballonfahrten". In: *Physikalische Zeitschrift* 13 (1912), 1084–1091.

[4] C. Evoli. *The Cosmic-Ray Energy Spectrum. Zenodo.* http://doi.org/10.5281/zenodo.2360277. Oct. 2018.

[5] Kenneth Greisen. "End to the Cosmic-Ray Spectrum?" In: Phys. Rev. Lett. 16.17 (Apr. 1966), pp. 748–750. DOI: 10.1103/PhysRevLett.16.748.

[6] G. T. Zatsepin and V. A. Kuz'min. "Upper Limit of the Spectrum of Cosmic Rays". In: *Soviet Journal of Experimental and Theoretical Physics Letters* 4 (Aug. 1966), p. 78.

[7] Pasquale Blasi. "The origin of galactic cosmic rays". In: A&A Rev. 21, 70 (Nov. 2013), p. 70. DOI: 10.1007/s00159-013-0070-7. arXiv: 1311.7346 [astro-ph.HE].

[8] A. Weinstein. "Pulsar Wind Nebulae and Cosmic Rays: A Bedtime Story". In: *Nuclear Physics B Proceedings Supplements* 256 (Nov. 2014), pp. 136–148. DOI: 10.1016/j.nuclphysbps.2014.10.017. arXiv: 1411.2532 [astro-ph.HE].

[9] Antoine Letessier-Selvon and Todor Stanev. "Ultrahigh energy cosmic rays". In: *Reviews of Modern Physics* 83.3 (July 2011), pp. 907–942. DOI: 10.1103/RevModPhys.83.907. arXiv: 1103.0031 [astro-ph.HE].

[10] A. M. Hillas. "The Origin of Ultra-High-Energy Cosmic Rays". In: ARA&A 22 (Jan. 1984), pp. 425–444. DOI: 10.1146/annurev.aa.22.090184.002233.

[11] Abbott, B.P. et al. "Observation of Gravitational Waves from a Binary Black Hole Merger". In: Phys. Rev. Lett. 116.6, 061102 (Feb. 2016), p. 061102. DOI: 10.1103/PhysRevLett.116.061102. arXiv: 1602.03837 [gr-qc].

[12] Abbott, B.P. et al. "GW170817: Observation of Gravitational Waves from a Binary Neutron Star Inspiral". In: Phys. Rev. Lett. 119.16, 161101 (Oct. 2017), p. 161101. DOI: 10.1103/PhysRevLett.119.161101. arXiv: 1710.05832 [gr-qc].

[13] Abbott, B.P. et al. "Multi-messenger Observations of a Binary Neutron Star Merger". In: ApJ 848.2, L12 (Oct. 2017), p. L12. DOI: 10.3847/2041-8213/aa91c9. arXiv: 1710.05833 [astro-ph.HE].

[14] IceCube Collaboration et al. "Multimessenger observations of a flaring blazar coincident with high-energy neutrino IceCube-170922A". In: *Science* 361.6398, eaat1378 (July 2018), eaat1378. DOI: 10.1126/science.aat1378. arXiv: 1807.08816 [astro-ph.HE].

[15] G. Breit and John A. Wheeler. "Collision of Two Light Quanta". In: *Physical Review* 46.12 (Dec. 1934), pp. 1087–1091. DOI: 10.1103/PhysRev.46.1087.

[16] Robert J. Gould and Gérard P. Schréder. "Pair Production in Photon-Photon Collisions". In: *Physical Review* 155.5 (Mar. 1967), pp. 1404–1407. DOI: 10.1103/PhysRev.155.1404.

[17] A. Domínguez et al. "Extragalactic background light inferred from AEGIS galaxy-SED-type fractions". In: MNRAS 410.4 (Feb. 2011), pp. 2556–2578. DOI: 10.1111/j.1365-2966.2010.17631.x. arXiv: 1007.1459 [astro-ph.CO].

[18] A. De Angelis and M. Mallamaci. "Gamma-ray astrophysics". In: *European Physical Journal Plus* 133.8, 324 (Aug. 2018), p. 324. DOI: 10.1140/epjp/i2018-12181-0. arXiv: 1805.05642 [astro-ph.HE].

[19] Bernard Degrange and Gérard Fontaine. "Foreword". In: *Comptes Rendus Physique* 17.6 (June 2016), pp. 581–584. DOI: 10.1016/j.crhy.2016.04.002.

[20] Mathieu de Naurois and Daniel Mazin. "Ground-based detectors in very-high-energy gamma-ray astronomy". In: *Comptes Rendus Physique* 16.6-7 (Aug. 2015), pp. 610–627. DOI: 10.1016/j.crhy.2015.08.011. arXiv: 1511.00463 [astro-ph.IM].

[21] W. Heitler. *Quantum theory of radiation*. 1954.

[22] P. A. Čerenkov. "Visible Radiation Produced by Electrons Moving in a Medium with Velocities Exceeding that of Light". In: *Physical Review* 52.4 (Aug. 1937), pp. 378–379. DOI: 10.1103/PhysRev.52.378.

[23] Alessandro De Angelis and Mário Pimenta. *Introduction to Particle and Astroparticle Physics*. 2018. DOI: 10.1007/978-3-319-78181-5.

[24] MAGIC Collaboration et al. "MAGIC very large zenith angle observations of the Crab Nebula up to 100 TeV". In: A&A 635, A158 (Mar. 2020), A158. DOI: 10.1051/0004-6361/201936899. arXiv: 2001.09566 [astro-ph.HE].

[25] Michele Peresano. "MAGIC telescopes observations at Very Large Zenith angles and the first neutrino-gamma association". PhD thesis. University of Udine, 2018.

[26] N. Park and VERITAS Collaboration. "Performance of the VERITAS experiment". In: *34th International Cosmic Ray Conference (ICRC2015)*. Vol. 34. International Cosmic Ray Conference. July 2015, p. 771. arXiv: 1508.07070 [astro-ph.IM].

[27] G. Giavitto et al. "Performance of the upgraded H.E.S.S. cameras". In: *35th International Cosmic Ray Conference (ICRC2017)*. Vol. 301. International Cosmic Ray Conference. Jan. 2017, p. 805. DOI: 10.22323/1.301.0805. arXiv: 1708.04550 [astro-ph.IM].

[28] Actis et al. "Design concepts for the Cherenkov Telescope Array CTA: an advanced facility for ground-based high-energy gamma-ray astronomy". In: *Experimental Astronomy* 32.3 (Dec. 2011), pp. 193–316. DOI: 10.1007/s10686-011-9247-0. arXiv: 1008.3703 [astro-ph.IM].

[29] https://www.cta-observatory.org/lst-prototype-records-its-first-light/.

[30] X. Bai et al. "The Large High Altitude Air Shower Observatory (LHAASO) Science White Paper". In: *arXiv e-prints*, arXiv:1905.02773 (May 2019). arXiv: 1905.02773 [astro-ph.HE].

[31] A. U. et al. Abeysekara. "The 2HWC HAWC Observatory Gamma-Ray Catalog". In: ApJ 843.1, 40 (July 2017), p. 40. DOI: 10.3847/1538-4357/aa7556. arXiv: 1702.02992 [astro-ph.HE].

[32] Aleksić, J. et al. "The major upgrade of the MAGIC telescopes, Part I: The hardware improvements and the commissioning of the system". In: *Astroparticle Physics* 72 (Jan. 2016), pp. 61–75. DOI: 10.1016/j.astropartphys.2015.04.004. arXiv: 1409.6073 [astro-ph.IM].

[33] Aleksić, J. et al. "The major upgrade of the MAGIC telescopes, Part II: A performance study using observations of the Crab Nebula". In: *Astroparticle Physics* 72 (Jan. 2016), pp. 76–94. DOI: 10.1016/j.astropartphys.2015.02.005. arXiv: 1409.5594 [astro-ph.IM].

[34] Bretz, T. et al. "The drive system of the major atmospheric gamma-ray imaging Cherenkov telescope". In: *Astroparticle Physics* 31.2 (Mar. 2009), pp. 92–101. DOI: 10.1016/j.astropartphys.2008.12.001. arXiv: 0810.4593 [astro-ph].

[35] Doro, M. et al. "The reflective surface of the MAGIC telescope". In: *Nuclear Instruments and Methods in Physics Research A* 595.1 (Sept. 2008), pp. 200–203. DOI: 10.1016/j.nima.2008.07.073.

[36] Biland, A. et al. "The Active Mirror Control of the MAGIC Telescopes". In: *International Cosmic Ray Conference*. Vol. 3. International Cosmic Ray Conference. Jan. 2008, pp. 1353–1356. arXiv: 0709.1574 [astro-ph].

[37] Borla Tridon, D. et al. "Performance of the Camera of the MAGIC II Telescope". In: *arXiv e-prints*, arXiv:0906.5448 (June 2009), arXiv:0906.5448. arXiv: 0906.5448 [astro-ph.HE].

[38] Paoletti, R. et al. "The Trigger System of the MAGIC Telescope". In: *IEEE Transactions on Nuclear Science* 54.2 (Apr. 2007), pp. 404–409. DOI: 10.1109/TNS.2007.892649.

[39] García, J.R. et al. "Status of the new Sum-Trigger system for the MAGIC telescopes". In: *arXiv e-prints*, arXiv:1404.4219 (Apr. 2014), arXiv:1404.4219. arXiv: 1404.4219 [astro-ph.IM].

[40] Francesco Dazzi. "A new stereoscopic 'Sum-Trigger-II' for the MAGIC Telescopes". PhD thesis. University of Udine, 2012.

[41] Lopez Coto, R. "Very-high-energy Gamma-ray Observations of PulsarWind Nebulae and Cataclysmic Variable Stars with MAGIC and Development of Trigger Systems for IACTs". PhD thesis. Universitat Aut'onoma de Barcelona, 2017.

[42] Aleksić, J. et al. "Observations of the Crab Pulsar between 25 and 100 GeV with the MAGIC I Telescope". In: ApJ 742.1, 43 (Nov. 2011), p. 43. DOI: 10.1088/0004-637X/742/1/43. arXiv: 1108.5391 [astro-ph.HE].

[43] Sitarek, J. et al. "Analysis techniques and performance of the Domino Ring Sampler version 4 based readout for the MAGIC telescopes". In: *Nuclear Instruments and Methods in Physics Research A* 723 (Sept. 2013), pp. 109–120. DOI: 10.1016/j.nima.2013.05.014. arXiv: 1305.1007 [astro-ph.IM].

[44] Bitossi, M., R. Paoletti, and D. Tescaro. "Ultra-Fast Sampling and Data Acquisition Using the DRS4 Waveform Digitizer". In: *IEEE Transactions on Nuclear Science* 63.4 (Aug. 2016), pp. 2309–2316. DOI: 10.1109/TNS.2016.2578963.

[45] Tescaro, D. et al. "The MAGIC Telescopes DAQ Software and the On-the-Fly Online Analysis Client". In: *International Cosmic Ray Conference*. Vol. 33. International Cosmic Ray Conference. Jan. 2013, p. 2803. arXiv: 1310.1565 [astro-ph.IM].

[46] Fruck, C. et al. "A novel LIDAR-based Atmospheric Calibration Method for Improving the Data Analysis of MAGIC". In: *arXiv e-prints*, arXiv:1403.3591 (Mar. 2014), arXiv:1403.3591. arXiv: 1403.3591 [astro-ph.IM].

[47] Galante, N. "Very High Energy observation of GRBs with the MAGIC Telescope". PhD thesis. Università degli studi di Siena., 2006.

[48] Berti, A. "Study of Astrophysical Transients with the MAGIC telescopes". PhD thesis. Università degli studi di Trieste, 2017.

[49] Fomin, V.P. et al. "New methods of atmospheric Cherenkov imaging for gamma-ray astronomy. I. The false source method". In: *Astroparticle Physics* 2.2 (May 1994), pp. 137–150. DOI: 10.1016/0927-6505(94)90036-1.

[50] Zanin, R. et al. "MARS, The MAGIC Analysis and Reconstruction Software". In: *International Cosmic Ray Conference*. Vol. 33. International Cosmic Ray Conference. Jan. 2013, p. 2937.

[51] Majumdar, P. et al. "Monte Carlo simulation for the MAGIC telescope". In: *29th International Cosmic Ray Conference (ICRC29), Volume 5*. Vol. 5. International Cosmic Ray Conference. Jan. 2005, p. 203.

[52] Heck, D. et al. *CORSIKA: a Monte Carlo code to simulate extensive air showers.* 1998.

[53] Mirzoyan, R. "On the Calibration Accuracy of Light Sensors in Atmospheric Cherenkov Fluorescence and Neutrino Experiments". In: *International Cosmic Ray Conference*. Vol. 7. International Cosmic Ray Conference. Jan. 1997, p. 265.

[54] Aliu, E. et al. "Improving the performance of the single-dish Cherenkov telescope MAGIC through the use of signal timing". In: *Astroparticle Physics* 30.6 (Jan. 2009), pp. 293–305. DOI: 10.1016/j.astropartphys.2008.10.003. arXiv: 0810.3568 [astro-ph].

[55] Garrido Terrats, D. "Limits to the Violation of Lorentz Invariance using the Emission of the Crab Pulsar at TeV Energies, Discovered with Archival Data from the MAGIC Telescopes". PhD thesis. Universitat Aut'onoma de Barcelona, 2015.

[56] Hillas, A.M. "Cerenkov Light Images of EAS Produced by Primary Gamma Rays and by Nuclei". In: *19th International Cosmic Ray Conference (ICRC19), Volume 3*. Vol. 3. International Cosmic Ray Conference. Aug. 1985, p. 445.

[57] Albert, J. et al. "Implementation of the Random Forest method for the Imaging Atmospheric Cherenkov Telescope MAGIC". In: *Nuclear Instruments and Methods in Physics Research A* 588.3 (Apr. 2008), pp. 424–432. DOI: 10.1016/j.nima.2007.11.068. arXiv: 0709.3719 [astro-ph].

[58] Gini, C et al. "Measurement of inequality of income". In: *Economic Journal* 31 (1921), pp. 22–43.

[59] Fomin, V.P. et al. "New methods of atmospheric Cherenkov imaging for gamma-ray astronomy. II. The differential position method". In: *Astroparticle Physics* 2.2 (May 1994), pp. 151–159. DOI: 10.1016/0927-6505(94)90037-X.

[60] Aleksić, J. et al. "Performance of the MAGIC stereo system obtained with Crab Nebula data". In: *Astroparticle Physics* 35.7 (Feb. 2012), pp. 435–448. DOI: 10.1016/j.astropartphys.2011.11.007. arXiv: 1108.1477 [astro-ph.IM].

[61] Li, T.P. and Y. Q. Ma. "Analysis methods for results in gamma-ray astronomy." In: ApJ 272 (Sept. 1983), pp. 317–324. DOI: 10.1086/161295.

[62] Tikhonov, A. et al. "Solutions of illposed problems". In: *Scripta series in mathematics, Winston* (1977).

[63] Schmelling, M. "The method of reduced cross-entropy A general approach to unfold probability distributions". In: *Nuclear Instruments and Methods in Physics Research A* 340.2 (Feb. 1994), pp. 400–412. DOI: 10.1016/0168-9002(94)90119-8.

[64] Bertero, M. "Linear inverse and illposed problems". In: *Academic Press, New York* 75 (1989), pp. 1–120.

[65] Rolke, W.A., Angel M. López, and Jan Conrad. "Limits and confidence intervals in the presence of nuisance parameters". In: *Nuclear Instruments and Methods in Physics Research A* 551.2-3 (Oct. 2005), pp. 493–503. DOI: 10.1016/j.nima.2005.05.068. arXiv: physics/0403059 [physics.data-an].

[66] Fruck, C. "The Galactic Center resolved with MAGIC and a new technique for Atmospheric Calibration". PhD thesis. Max-Planck-Institut fur Physik, 2015.

[67] Ahnen, M.L. et al. "Performance of the MAGIC telescopes under moonlight". In: *Astroparticle Physics* 94 (Sept. 2017), pp. 29–41. DOI: 10.1016/j.astropartphys.2017.08.001. arXiv: 1704.00906 [astro-ph.IM].

[68] D. Miceli et al. "Following up GW alerts with MAGIC: the third LIGO/Virgo observation run". In: *36th International Cosmic Ray Conference (ICRC2019)*. International Cosmic Ray Conference. July 2019, p. 743. arXiv: 1909.03971 [astro-ph.HE].

[69] Leo P. Singer et al. "Going the Distance: Mapping Host Galaxies of LIGO and Virgo Sources in Three Dimensions Using Local Cosmography and Targeted Follow-up". In: ApJ 829.1, L15 (Sept. 2016), p. L15. DOI: 10.3847/2041-8205/829/1/L15. arXiv: 1603.07333 [astro-ph.HE].

[70] B. Patricelli et al. "Searching for gamma-ray counterparts to gravitational waves from merging binary neutron stars with the Cherenkov Telescope Array". In: J. Cosmology Astropart. Phys. 2018.5, 056 (May 2018), p. 056. DOI: 10.1088/1475-7516/2018/05/056. arXiv: 1801.05167 [astro-ph.HE].

[71] P. Marziani et al. "Comparative Analysis of the High- and Low-Ionization Lines in the Broad-Line Region of Active Galactic Nuclei". In: ApJS 104 (May 1996), p. 37. DOI: 10.1086/192291.

[72] MAGIC Collaboration et al. "Very-High-Energy gamma rays from a Distant Quasar: How Transparent Is the Universe?" In: *Science* 320.5884 (June 2008), p. 1752. DOI: 10.1126/science.1157087. arXiv: 0807.2822 [astro-ph].

[73] J. et al. Aleksić. "MAGIC Observations and multiwavelength properties of the quasar 3C 279 in 2007 and 2009". In: A&A 530, A4 (June 2011), A4. DOI: 10.1051/0004-6361/201116497. arXiv: 1101.2522 [astro-ph.CO].

[74] J. et al. Aleksić. "MAGIC observations and multifrequency properties of the flat spectrum radio quasar 3C 279 in 2011". In: A&A 567, A41 (July 2014), A41. DOI: 10.1051/0004-6361/201323036. arXiv: 1311.2833 [astro-ph.HE].

[75] I. et al. Andreoni. "Follow Up of GW170817 and Its Electromagnetic Counterpart by Australian-Led Observing Programmes". In: PASA 34, e069 (Dec. 2017), e069. DOI: 10.1017/pasa.2017.65. arXiv: 1710.05846 [astro-ph.HE].

[76] N. R. Tanvir et al. "The Emergence of a Lanthanide-rich Kilonova Following the Merger of Two Neutron Stars". In: ApJ 848.2, L27 (Oct. 2017), p. L27. DOI: 10.3847/2041-8213/aa90b6. arXiv: 1710.05455 [astro-ph.HE].

[77] P. D'Avanzo et al. "The evolution of the X-ray afterglow emission of GW 170817/ GRB 170817A in XMM-Newton observations". In: A&A 613, L1 (May 2018), p. L1. DOI: 10.1051/0004-6361/201832664. arXiv: 1801.06164 [astro-ph.HE].

[78] Ray W. Klebesadel, Ian B. Strong, and Roy A. Olson. "Observations of Gamma-Ray Bursts of Cosmic Origin". In: ApJ 182 (June 1973), p. L85. DOI: 10.1086/181225.

[79] Michael S. Briggs et al. "BATSE Observations of the Large-Scale Isotropy of Gamma-Ray Bursts". In: ApJ 459 (Mar. 1996), p. 40. DOI: 10.1086/176867. arXiv: astro-ph/9509078 [astro-ph].

[80] Chryssa Kouveliotou et al. "Identification of Two Classes of Gamma-Ray Bursts". In: ApJ 413 (Aug. 1993), p. L101. DOI: 10.1086/186969.

[81] K. Hurley et al. "Detection of a γ-ray burst of very long duration and very high energy". In: Nature 372.6507 (Dec. 1994), pp. 652–654. DOI: 10.1038/372652a0.

[82] G. Boella et al. "BeppoSAX, the wide band mission for X-ray astronomy". In: A&AS 122 (Apr. 1997), pp. 299–307. DOI: 10.1051/aas:1997136.

[83] P. Meszaros and M. J. Rees. "Gamma-Ray Bursts: Multiwaveband Spectral Predictions for Blast Wave Models". In: ApJ 418 (Dec. 1993), p. L59. DOI: 10.1086/187116. arXiv: astro-ph/9309011 [astro-ph].

[84] Bing Zhang and Peter Mészáros. "Gamma-Ray Burst Beaming: A Universal Configuration with a Standard Energy Reservoir?" In: ApJ 571.2 (June 2002), pp. 876–879. DOI: 10.1086/339981. arXiv: astro-ph/0112118 [astro-ph].

[85] James E. Rhoads. "The Dynamics and Light Curves of Beamed Gamma-Ray Burst Afterglows". In: ApJ 525.2 (Nov. 1999), pp. 737–749. DOI: 10.1086/307907. arXiv: astro-ph/9903399 [astro-ph].

[86] G. R. Ricker et al. "The High Energy Transient Explorer (HETE): Mission and Science Overview". In: *Gamma-Ray Burst and Afterglow Astronomy 2001: A Workshop Celebrating the First Year of the HETE Mission*. Ed. by G. R. Ricker and R. K. Vanderspek. Vol. 662. American Institute of Physics Conference Series. Apr. 2003, pp. 3–16. DOI: 10.1063/1.1579291.

[87] https://gcn.gsfc.nasa.gov/reports.html.

[88] T. J. Galama, P. M. Vreeswijk, and van Paradijs et al. "An unusual supernova in the error box of the γ-ray burst of 25 April 1998". In: Nature 395.6703 (Oct. 1998), pp. 670–672. DOI: 10.1038/27150. arXiv: astro-ph/9806175 [astro-ph].

[89] S. R. Kulkarni et al. "Radio emission from the unusual supernova 1998bw and its association with the γ-ray burst of 25 April 1998". In: Nature 395.6703 (Oct. 1998), pp. 663–669. DOI: 10.1038/27139.

[90] K. Z. Stanek et al. "Spectroscopic Discovery of the Supernova 2003dh Associated with GRB 030329". In: ApJ 591.1 (July 2003), pp. L17–L20. DOI: 10.1086/376976. arXiv: astro-ph/0304173 [astro-ph].

[91] Jens Hjorth et al. "The optical afterglow of the short γ-ray burst GRB 050709". In: Nature 437.7060 (Oct. 2005), pp. 859–861. DOI: 10.1038/nature04174. arXiv: astro-ph/0510096 [astro-ph].

[92] T. Sakamoto et al. "Global Characteristics of X-Ray Flashes and X-Ray-Rich Gamma-Ray Bursts Observed by HETE-2". In: ApJ 629.1 (Aug. 2005), pp. 311–327. DOI: 10.1086/431235.

[93] N. Gehrels et al. "The Swift Gamma-Ray Burst Mission". In: ApJ 611.2 (Aug. 2004), pp. 1005–1020. DOI: 10.1086/422091. arXiv: astro-ph/0405233 [astro-ph].

[94] Bing Zhang et al. "Physical Processes Shaping Gamma-Ray Burst X-Ray Afterglow Light Curves: Theoretical Implications from the Swift X-Ray Telescope Observations". In: ApJ 642.1 (May 2006), pp. 354–370. DOI: 10.1086/500723. arXiv: astro-ph/0508321 [astro-ph].

[95] A. Cucchiara et al. "A Photometric Redshift of z $\sim$9.4 for GRB 090429B". In: ApJ 736.1, 7 (July 2011), p. 7. DOI: 10.1088/0004-637X/736/1/7. arXiv: 1105.4915 [astro-ph.CO].

[96] Tavani, M. and Barbiellini, G. et al. "The AGILE Mission". In: A&A 502.3 (Aug. 2009), pp. 995–1013. DOI: 10.1051/0004-6361/200810527. arXiv: 0807.4254 [astro-ph].

[97] W. B. et al. Atwood. "The Large Area Telescope on the Fermi Gamma-Ray Space Telescope Mission". In: ApJ 697.2 (June 2009), pp. 1071–1102. DOI: 10.1088/0004-637X/697/2/1071. arXiv: 0902.1089 [astro-ph.IM].

[98] Bing Zhang. "Extreme emission seen from γ-ray bursts". In: Nature 575.7783 (Nov. 2019), pp. 448–449. DOI: 10.1038/d41586-019-03503-6. arXiv: 1911.09862 [astro-ph.HE].

[99] A. von Kienlin et al. "The Fourth Fermi-GBM Gamma-Ray Burst Catalog: A Decade of Data". In: ApJ 893.1, 46 (Apr. 2020), p. 46. DOI: 10.3847/1538-4357/ab7a18. arXiv: 2002.11460 [astro-ph.HE].

[100] D. Band et al. "BATSE Observations of Gamma-Ray Burst Spectra. I. Spectral Diversity". In: ApJ 413 (Aug. 1993), p. 281. DOI: 10.1086/172995.

[101] M. S. Briggs et al. "Observations of GRB 990123 by the Compton Gamma Ray Observatory". In: ApJ 524.1 (Oct. 1999), pp. 82–91. DOI: 10.1086/307808. arXiv: astro-ph/9903247 [astro-ph].

[102] R. D. Preece et al. "The BATSE Gamma-Ray Burst Spectral Catalog. I. High Time Resolution Spectroscopy of Bright Bursts Using High Energy Resolution Data". In: ApJS 126.1 (Jan. 2000), pp. 19–36. DOI: 10.1086/313289. arXiv: astro-ph/9908119 [astro-ph].

[103] L. Nava et al. "Fermi/GBM and BATSE gamma-ray bursts: comparison of the spectral properties". In: MNRAS 415.4 (Aug. 2011), pp. 3153–3162. DOI: 10.1111/j.1365-2966.2011.18928.x. arXiv: 1012.3968 [astro-ph.HE].

[104] Z. Bosnjak et al. "The spectral catalogue of INTEGRAL gamma-ray bursts". In: *SF2A-2013: Proceedings of the Annual meeting of the French Society of Astronomy and Astrophysics*. Ed. by L. Cambresy et al. Nov. 2013, pp. 455–457.

[105] Bin-Bin Zhang et al. "A Comprehensive Analysis of Fermi Gamma-ray Burst Data. I. Spectral Components and the Possible Physical Origins of LAT/GBM GRBs". In: ApJ 730.2, 141 (Apr. 2011), p. 141. DOI: 10.1088/0004-637X/730/2/141. arXiv: 1009.3338 [astro-ph.HE].

[106] D. A. Perley et al. "The Afterglow of GRB 130427A from 1 to 10^{16} GHz". In: ApJ 781.1, 37 (Jan. 2014), p. 37. DOI: 10.1088/0004-637X/781/1/37. arXiv: 1307.4401 [astro-ph.HE].

[107] E. Costa et al. "Discovery of an X-ray afterglow associated with the γ-ray burst of 28 February 1997". In: Nature 387.6635 (June 1997), pp. 783–785. DOI: 10.1038/42885. arXiv: astro-ph/9706065 [astro-ph].

[108] S. D. Barthelmy et al. "Discovery of an Afterglow Extension of the Prompt Phase of Two Gamma-Ray Bursts Observed by Swift". In: ApJ 635.2 (Dec. 2005), pp. L133–L136. DOI: 10.1086/499432. arXiv: astro-ph/0511576 [astro-ph].

[109] R. Margutti et al. "Lag-luminosity relation in γ-ray burst X-ray flares: a direct link to the prompt emission". In: MNRAS 406.4 (Aug. 2010), pp. 2149–2167. DOI: 10.1111/j.1365-2966.2010.16824.x. arXiv: 1004.1568 [astro-ph.HE].

[110] Fang-Kun Peng et al. "Photosphere Emission in the X-Ray Flares of Swift Gamma-Ray Bursts and Implications for the Fireball Properties". In: ApJ 795.2, 155 (Nov. 2014), p. 155. DOI: 10.1088/0004-637X/795/2/155. arXiv: 1409.5261 [astro-ph.HE].

[111] M. M. González et al. "A γ-ray burst with a high-energy spectral component inconsistent with the synchrotron shock model". In: Nature 424.6950 (Aug. 2003), pp. 749–751. DOI: 10.1038/nature01869.

[112] M. et al. Ajello. "A Decade of Gamma-Ray Bursts Observed by Fermi-LAT: The Second GRB Catalog". In: ApJ 878.1, 52 (June 2019), p. 52. DOI: 10.3847/1538-4357/ab1d4e. arXiv: 1906.11403 [astro-ph.HE].

[113] Lara Nava. "High-energy emission from gamma-ray bursts". In: *International Journal of Modern Physics D* 27.13, 1842003 (Jan. 2018), p. 1842003. DOI: 10.1142/S0218271818420038. arXiv: 1804.01524 [astro-ph.HE].

[114] Qing-Wen Tang, Xiang-Yu Wang, and Ruo-Yu Liu. "Evidence of an Internal Dissipation Origin for the High-energy Prompt Emission of GRB 170214A". In: ApJ 844.1, 56 (July 2017), p. 56. DOI: 10.3847/1538-4357/aa7a58. arXiv: 1706.06092 [astro-ph.HE].

[115] G. Vianello et al. "The Bright and the Slow—GRBs 100724B and 160509A with High-energy Cutoffs at $\lesssim$100 MeV". In: ApJ 864.2, 163 (Sept. 2018), p. 163. DOI: 10.3847/1538-4357/aad6ea. arXiv: 1706.01481 [astro-ph.HE].

[116] M. et al. Ackermann. "Fermi-LAT Observations of the Gamma-Ray Burst GRB 130427A". In: *Science* 343.6166 (Jan. 2014), pp. 42–47. DOI: 10.1126/science.1242353. arXiv: 1311.5623 [astro-ph.HE].

[117] R. Atkins et al. "Evidence for TEV Emission from GRB 970417A". In: ApJ 533.2 (Apr. 2000), pp. L119–L122. DOI: 10.1086/312629.

[118] Razmik Mirzoyan. "First time detection of a GRB at sub-TeV energies; MAGIC detects the GRB 190114C". In: *The Astronomer's Telegram* 12390 (Jan. 2019), p. 1.

[119] E.L. Ruiz Velasco. *Discovery of Late-Time Very High Energy Emission from a Gamma-ray Burst Afterglow*. Presentation at the 1st CTA Science Symposium, Bologna. May 2019.

[120] M. de Naurois. "GRB190829A: Detection of VHE gamma-ray emission with H.E.S.S." In: *The Astronomer's Telegram* 13052 (Aug. 2019), p. 1.

[121] MAGIC Collaboration et al. "Observation of inverse Compton emission from a long γ-ray burst". In: Nature 575.7783 (Nov. 2019), pp. 459–463. DOI: 10.1038/s41586-019-1754-6. arXiv: 2006.07251 [astro-ph.HE].

[122] S. E. Woosley, Norbert Langer, and Thomas A. Weaver. "The Evolution of Massive Stars Including Mass Loss: Presupernova Models and Explosion". In: ApJ 411 (July 1993), p. 823. DOI: 10.1086/172886.

[123] A. I. MacFadyen and S. E. Woosley. "Collapsars: Gamma-Ray Bursts and Explosions in "Failed Supernovae"". In: ApJ 524.1 (Oct. 1999), pp. 262–289. DOI: 10.1086/307790. arXiv: astro-ph/9810274 [astro-ph].

[124] S. C. Yoon and N. Langer. "Evolution of rapidly rotating metal-poor massive stars towards gamma-ray bursts". In: A&A 443.2 (Nov. 2005), pp. 643–648. DOI: 10.1051/0004-6361:20054030. arXiv: astro-ph/0508242 [astro-ph].

[125] S. E. Woosley and J. S. Bloom. "The Supernova Gamma-Ray Burst Connection". In: ARA&A 44.1 (Sept. 2006), pp. 507–556. DOI: 10.1146/annurev.astro.43.072103.150558. arXiv: astro-ph/0609142 [astro-ph].

[126] S. C. Yoon, N. Langer, and C. Norman. "Single star progenitors of long gamma-ray bursts. I. Model grids and redshift dependent GRB rate". In: A&A 460.1 (Dec. 2006), pp. 199–208. DOI: 10.1051/0004-6361:20065912. arXiv: astro-ph/0606637 [astro-ph].

[127] Mario Vietri and Luigi Stella. "A Gamma-Ray Burst Model with Small Baryon Contamination". In: ApJ 507.1 (Nov. 1998), pp. L45–L48. DOI: 10.1086/311674. arXiv: astro-ph/9808355 [astro-ph].

[128] C. L. Fryer and S. E. Woosley. "Helium Star/Black Hole Mergers: A New Gamma-Ray Burst Model". In: ApJ 502.1 (July 1998), pp. L9–L12. DOI: 10.1086/311493. arXiv: astro-ph/9804167 [astro-ph].

[129] Chris L. Fryer. "Compact object formation and the supernova explosion engine". In: *Classical and Quantum Gravity* 30.24, 244002 (Dec. 2013), p. 244002. DOI: 10.1088/0264-9381/30/24/244002. arXiv: 1307.6141 [astro-ph.HE].

[130] V. V. Usov. "Millisecond pulsars with extremely strong magnetic fields as a cosmological source of γ-ray bursts". In: Nature 357.6378 (June 1992), pp. 472–474. DOI: 10.1038/357472a0.

[131] Edo Berger. "Short-Duration Gamma-Ray Bursts". In: ARA&A 52 (Aug. 2014), pp. 43–105. DOI: 10.1146/annurev-astro-081913-035926. arXiv: 1311.2603 [astro-ph.HE].

[132] Luciano Rezzolla et al. "The Missing Link: Merging Neutron Stars Naturally Produce Jet-like Structures and Can Power Short Gamma-ray Bursts". In: ApJ 732.1, L6 (May 2011), p. L6. DOI: 10.1088/2041-8205/732/1/L6. arXiv: 1101.4298 [astro-ph.HE].

[133] Z. G. Dai et al. "X-ray Flares from Postmerger Millisecond Pulsars". In: *Science* 311.5764 (Feb. 2006), pp. 1127–1129. DOI: 10.1126/science.1123606. arXiv: astro-ph/0602525 [astro-ph].

[134] Bing Zhang. "Early X-Ray and Optical Afterglow of Gravitational Wave Bursts from Mergers of Binary Neutron Stars". In: ApJ 763.1, L22 (Jan. 2013), p. L22. DOI: 10.1088/2041-8205/763/1/L22. arXiv: 1212.0773 [astro-ph.HE].

[135] William H. Lee and Włodzimierz Kluźniak. "Newtonian Hydrodynamics of the Coalescence of Black Holes with Neutron Stars. I. Tidally Locked Binaries with a Stiff Equation of State". In: ApJ 526.1 (Nov. 1999), pp. 178–199. DOI: 10.1086/307958. arXiv: astro-ph/9808185 [astro-ph].

[136] P. A. Evans et al. "Swift and NuSTAR observations of GW170817: Detection of a blue kilonova". In: *Science* 358.6370 (Dec. 2017), pp. 1565–1570. DOI: 10.1126/science.aap9580. arXiv: 1710.05437 [astro-ph.HE].

[137] M. Nicholl et al. "The Electromagnetic Counterpart of the Binary Neutron Star Merger LIGO/Virgo GW170817. III. Optical and UV Spectra of a Blue Kilonova from Fast Polar Ejecta". In: ApJ 848.2, L18 (Oct. 2017), p. L18. DOI: 10.3847/2041-8213/aa9029. arXiv: 1710.05456 [astro-ph.HE].

[138] B. J. Shappee et al. "Early spectra of the gravitational wave source GW170817: Evolution of a neutron star merger". In: *Science* 358.6370 (Dec. 2017), pp. 1574–1578. DOI: 10.1126/science.aaq0186. arXiv: 1710.05432 [astro-ph.HE].

[139] R. Chornock et al. "The Electromagnetic Counterpart of the Binary Neutron Star Merger LIGO/Virgo GW170817. IV. Detection of Near-infrared Signatures of r-process Nucleosynthesis with Gemini-South". In: ApJ 848.2, L19 (Oct. 2017), p. L19. DOI: 10.3847/2041-8213/aa905c. arXiv: 1710.05454 [astro-ph.HE].

[140] Daniel Kasen et al. "Origin of the heavy elements in binary neutron-star mergers from a gravitational-wave event". In: Nature 551.7678 (Nov. 2017), pp. 80–84. DOI: 10.1038/nature24453. arXiv: 1710.05463 [astro-ph.HE].

[141] Pian, E. et al. "Spectroscopic identification of r-process nucleosynthesis in a double neutron-star merger". In: Nature 551.7678 (Nov. 2017), pp. 67–70. DOI: 10.1038/nature24298. arXiv: 1710.05858 [astro-ph.HE].

[142] Yoram Lithwick and Re'em Sari. "Lower Limits on Lorentz Factors in Gamma-Ray Bursts". In: ApJ 555.1 (July 2001), pp. 540–545. DOI: 10.1086/321455. arXiv: astro-ph/0011508 [astro-ph].

[143] Frédéric Piron. "Gamma-ray bursts at high and very high energies". In: *Comptes Rendus Physique* 17.6 (June 2016), pp. 617–631. DOI: 10.1016/j.crhy.2016.04.005. arXiv: 1512.04241 [astro-ph.HE].

[144] T. Piran, A. Shemi, and R. Narayan. "Hydrodynamics of Relativistic Fireballs". In: MNRAS 263 (Aug. 1993), p. 861. DOI: 10.1093/mnras/263.4.861. arXiv: astro-ph/9301004 [astro-ph].

[145] M. J. Rees and P. Meszaros. "Unsteady Outflow Models for Cosmological Gamma-Ray Bursts". In: ApJ 430 (Aug. 1994), p. L93. DOI: 10.1086/187446. arXiv: astro-ph/9404038 [astro-ph].

[146] M. J. Rees and P. Meszaros. "Relativistic fireballs - Energy conversion and time-scales." In: MNRAS 258 (Sept. 1992), p. 41. DOI: 10.1093/mnras/258.1.41P.

[147] Shiho Kobayashi, Tsvi Piran, and Re'em Sari. "Can Internal Shocks Produce the Variability in Gamma-Ray Bursts?" In: ApJ 490 (Nov. 1997), p. 92. DOI: 10.1086/512791. arXiv: astro-ph/9705013 [astro-ph].

[148] P. Mészáros and M. J. Rees. "Poynting Jets from Black Holes and Cosmological Gamma-Ray Bursts". In: ApJ 482.1 (June 1997), pp. L29–L32. DOI: 10.1086/310692. arXiv: astro-ph/9609065 [astro-ph].

[149] M. J. Rees and P. Mészáros. "Dissipative Photosphere Models of Gamma-Ray Bursts and X-Ray Flashes". In: ApJ 628.2 (Aug. 2005), pp. 847–852. DOI: 10.1086/430818. arXiv: astro-ph/0412702 [astro-ph].

[150] P. Mészáros and M. J. Rees. "Steep Slopes and Preferred Breaks in Gamma-Ray Burst Spectra: The Role of Photospheres and Comptonization". In: ApJ 530.1 (Feb. 2000), pp. 292–298. DOI: 10.1086/308371. arXiv: astro-ph/9908126 [astro-ph].

[151] Pawan Kumar and Bing Zhang. "The physics of gamma-ray bursts & relativistic jets". In: Phys. Rep. 561 (Feb. 2015), pp. 1–109. DOI: 10.1016/j.physrep.2014.09.008. arXiv: 1410.0679 [astro-ph.HE].

[152] F. A. Harrison et al. "Optical and Radio Observations of the Afterglow from GRB 990510: Evidence for a Jet". In: ApJ 523.2 (Oct. 1999), pp. L121–L124. DOI: 10.1086/312282. arXiv: astro-ph/9905306 [astro-ph].

[153] Re'em Sari, Tsvi Piran, and J. P. Halpern. "Jets in Gamma-Ray Bursts". In: ApJ 519.1 (July 1999), pp. L17–L20. DOI: 10.1086/312109. arXiv: astro-ph/9903339 [astro-ph].

[154] Weiqun Zhang and Andrew MacFadyen. "The Dynamics and Afterglow Radiation of Gamma-Ray Bursts. I. Constant Density Medium". In: ApJ 698.2 (June 2009), pp. 1261–1272. DOI: 10.1088/0004-637X/698/2/1261. arXiv: 0902.2396 [astro-ph.HE].

[155] Gor Oganesyan et al. "Detection of Low-energy Breaks in Gamma-Ray Burst Prompt Emission Spectra". In: ApJ 846.2, 137 (Sept. 2017), p. 137. DOI: 10.3847/1538-4357/aa831e. arXiv: 1709.04689 [astro-ph.HE].

[156] Katsuaki Asano and Peter Mészáros. "Spectral-Temporal Simulations of Internal Dissipation Models of Gamma-Ray Bursts". In: ApJ 739.2, 103 (Oct. 2011), p. 103. DOI: 10.1088/0004-637X/739/2/103. arXiv: 1107.4825 [astro-ph.HE].

[157] M. et al. Ackermann. "Detection of a Spectral Break in the Extra Hard Component of GRB 090926A". In: ApJ 729.2, 114 (Mar. 2011), p. 114. DOI: 10.1088/0004-637X/729/2/114. arXiv: 1101.2082 [astro-ph.HE].

[158] Soebur Razzaque. "Modeling and Interpretation of High Energy Emission from GRBs Observed with the Fermi Gamma Ray Space Telescope". In: *APS April Meeting Abstracts*. APS Meeting Abstracts. May 2009, W8.003.

[159] Katsuaki Asano, Susumu Inoue, and Peter Mészáros. "Prompt High-Energy Emission from Proton-Dominated Gamma-Ray Bursts". In: ApJ 699.2 (July 2009), pp. 953–957. DOI: 10.1088/0004-637X/699/2/953. arXiv: 0807.0951 [astro-ph].

[160] Katsuaki Asano, Sylvain Guiriec, and Peter Mészáros. "Hadronic Models for the Extra Spectral Component in the Short GRB 090510". In: ApJ 705.2 (Nov. 2009), pp. L191–L194. DOI: 10.1088/0004-637X/705/2/L191. arXiv: 0909.0306 [astro-ph.HE].

[161] Sari, Re'em and Ann A. Esin. "On the Synchrotron Self-Compton Emission from Relativistic Shocks and Its Implications for Gamma-Ray Burst Afterglows". In: ApJ 548.2 (Feb. 2001), pp. 787–799. DOI: 10.1086/319003. arXiv: astro-ph/0005253 [astro-ph].

[162] P. Kumar and R. Barniol Duran. "On the generation of high-energy photons detected by the Fermi Satellite from gamma-ray bursts". In: MNRAS 400.1 (Nov. 2009), pp. L75–L79. DOI: 10.1111/j.1745-3933.2009.00766.x. arXiv: 0905.2417 [astro-ph.HE].

[163] Paz Beniamini et al. "Energies of GRB blast waves and prompt efficiencies as implied by modelling of X-ray and GeV afterglows". In: MNRAS 454.1 (Nov. 2015), pp. 1073–1085. DOI: 10.1093/mnras/stv2033. arXiv: 1504.04833 [astro-ph.HE].

[164] H. et al. Abdalla. "A very-high-energy component deep in the γ-ray burst afterglow". In: Nature 575.7783 (Nov. 2019), pp. 464–467. DOI: 10.1038/s41586-019-1743-9. arXiv: 1911.08961 [astro-ph.HE].

[165] MAGIC Collaboration et al. "Teraelectronvolt emission from the γ-ray burst GRB 190114C". In: Nature 575.7783 (Nov. 2019), pp. 455–458. DOI: 10.1038/s41586-019-1750-x. arXiv: 2006.07249 [astro-ph.HE].

[166] Markus Böttcher and Charles D. Dermer. "High-energy Gamma Rays from Ultra-high-energy Cosmic-Ray Protons in Gamma-Ray Bursts". In: ApJ 499.2 (June 1998), pp. L131–L134. DOI: 10.1086/311366. arXiv: astro-ph/9801027 [astro-ph].

[167] R. D. Blandford and C. F. McKee. "Fluid dynamics of relativistic blast waves". In: *Physics of Fluids* 19 (Aug. 1976), pp. 1130–1138. DOI: 10.1063/1.861619.

[168] Panaitescu, A. and P. Kumar. "Analytic Light Curves of Gamma-Ray Burst Afterglows: Homogeneous versus Wind External Media". In: ApJ 543.1 (Nov. 2000), pp. 66–76. DOI: 10.1086/317090. arXiv: astro-ph/0003246 [astro-ph].

[169] L. Nava et al. "Afterglow emission in gamma-ray bursts - I. Pair-enriched ambient medium and radiative blast waves". In: MNRAS 433.3 (Aug. 2013), pp. 2107–2121. DOI: 10.1093/mnras/stt872. arXiv: 1211.2806 [astro-ph.HE].

[170] R. J. Protheroe. "Origin and propagation of the highest energy cosmic rays". In: *arXiv e-prints*, astro-ph/9612212 (Dec. 1996), astro–ph/9612212. arXiv: astro-ph/9612212 [astro-ph].

[171] George B. Rybicki and Alan P. Lightman. *Radiative processes in astrophysics*. 1979.

[172] Malcolm S. Longair. *High Energy Astrophysics*. 2011.

[173] Gabriele Ghisellini. *Radiative Processes in High Energy Astrophysics*. Vol. 873. 2013. DOI: 10.1007/978-3-319-00612-3.

[174] Bradley W. Carroll and Dale A. Ostlie. *An Introduction to Modern Astrophysics*. 1996.

[175] P. Kumar et al. "Maximum synchrotron frequency for shock-accelerated particles". In: MNRAS 427.1 (Nov. 2012), pp. L40–L44. DOI: 10.1111/j.1745-3933.2012.01341.x. arXiv: 1210.6033 [astro-ph.HE].

[176] Sari, Re'em, Tsvi Piran, and Ramesh Narayan. "Spectra and Light Curves of Gamma-Ray Burst Afterglows". In: ApJ 497.1 (Apr. 1998), pp. L17–L20. DOI: 10.1086/311269. arXiv: astro-ph/9712005 [astro-ph].

[177] Bing Zhang and Peter Mészáros. "High-Energy Spectral Components in Gamma-Ray Burst Afterglows". In: ApJ 559.1 (Sept. 2001), pp. 110–122. DOI: 10.1086/322400. arXiv: astro-ph/0103229 [astro-ph].

[178] George R. Blumenthal and Robert J. Gould. "Bremsstrahlung, Synchrotron Radiation, and Compton Scattering of High-Energy Electrons Traversing Dilute Gases". In: *Reviews of Modern Physics* 42.2 (Jan. 1970), pp. 237–271. DOI: 10.1103/RevModPhys.42.237.

[179] Ehud Nakar, Shin'ichiro Ando, and Re'em Sari. "Klein-Nishina Effects on Optically Thin Synchrotron and Synchrotron Self-Compton Spectrum". In: ApJ 703.1 (Sept. 2009), pp. 675–691. DOI: 10.1088/0004-637X/703/1/675. arXiv: 0903.2557 [astro-ph.HE].

[180] Jonathan Granot and Re'em Sari. "The Shape of Spectral Breaks in Gamma-Ray Burst Afterglows". In: ApJ 568.2 (Apr. 2002), pp. 820–829. DOI: 10.1086/338966. arXiv: astro-ph/0108027 [astro-ph].

[181] Soebur Razzaque, Charles D. Dermer, and Justin D. Finke. "Synchrotron Radiation from Ultra-High Energy Protons and the Fermi Observations of GRB 080916C". In: *The Open Astronomy Journal* 3.1 (Aug. 2010), pp. 150–155. DOI: 10.2174/1874381101003010150. arXiv: 0908.0513 [astro-ph.HE].

[182] M. Petropoulou and A. Mastichiadis. "On the multiwavelength emission from gamma ray burst afterglows". In: A&A 507.2 (Nov. 2009), pp. 599–610. DOI: 10.1051/0004-6361/200912970. arXiv: 0909.0208 [astro-ph.HE].

[183] Pennanen, T., I. Vurm, and J. Poutanen. "Simulations of gamma-ray burst afterglows with a relativistic kinetic code". In: A&A 564, A77 (Apr. 2014), A77. DOI: 10.1051/0004-6361/201322520. arXiv: 1403.5506 [astro-ph.HE].

[184] Geoffrey Ryan et al. "Gamma-Ray Burst Afterglows in the Multimessenger Era: Numerical Models and Closure Relations". In: ApJ 896.2, 166 (June 2020), p. 166. DOI: 10.3847/1538-4357/ab93cf. arXiv: 1909.11691 [astro-ph.HE].

[185] J. S. Chang and G. Cooper. "A Practical Difference Scheme for Fokker-Planck Equations". In: *Journal of Computational Physics* 6.1 (Aug. 1970), pp. 1–16. DOI: 10.1016/0021-9991(70)90001-X.

[186] Marco Chiaberge and Gabriele Ghisellini. "Rapid variability in the synchrotron self-Compton model for blazars". In: MNRAS 306.3 (July 1999), pp. 551–560. DOI: 10.1046/j.1365-8711.1999.02538.x. arXiv: astro-ph/9810263 [astro-ph].

[187] R. Courant, K. Friedrichs, and H. Lewy. "Über die partiellen Differenzengleichungen der mathematischen Physik". In: *Mathematische Annalen* 100 (Jan. 1928), pp. 32–74. DOI: 10.1007/BF01448839.

[188] A. Crusius and R. Schlickeiser. "Synchrotron radiation in random magnetic fields". In: A&A 164.2 (Aug. 1986), pp. L16–L18.

[189] Frank C. Jones. "Calculated Spectrum of Inverse-Compton-Scattered Photons". In: *Physical Review* 167.5 (Mar. 1968), pp. 1159–1169. DOI: 10.1103/PhysRev.167.1159.

[190] P. S. Coppi and R. D. Blandford. "Reaction rates and energy distributions for elementary processes in relativistic pair plasmas". In: MNRAS 245 (Aug. 1990), pp. 453–507.

[191] J. et al. Albert. "MAGIC Upper Limits on the Very High Energy Emission from Gamma-Ray Bursts". In: ApJ 667.1 (Sept. 2007), pp. 358–366. DOI: 10.1086/520761. arXiv: astro-ph/0612548 [astro-ph].

[192] J. et al. Albert. "Flux Upper Limit on Gamma-Ray Emission by GRB 050713a from MAGIC Telescope Observations". In: ApJ 641.1 (Apr. 2006), pp. L9–L12. DOI: 10.1086/503767. arXiv: astro-ph/0602231 [astro-ph].

[193] J. et al. Aleksić. "MAGIC observation of the GRB 080430 afterglow". In: A&A 517, A5 (July 2010), A5. DOI: 10.1051/0004-6361/200913461. arXiv: 1004.3665 [astro-ph.HE].

[194] J. et al. Aleksić. "MAGIC upper limits on the GRB 090102 afterglow". In: MNRAS 437.4 (Feb. 2014), pp. 3103–3111. DOI: 10.1093/mnras/stt2041. arXiv: 1311.3637 [astro-ph.HE].

[195] S. Inoue et al. "MAGIC observations of the nearby short GRB 160821B: implications for afterglow physics and gravitational wave follow-up". In: *36th International Cosmic Ray Conference (ICRC2019)*. Vol. 36. International Cosmic Ray Conference. July 2019, p. 703.

[196] MAGIC Collaboration et al. "MAGIC observations of the nearby short gamma-ray burst GRB 160821B". In: *arXiv e-prints*, arXiv:2012.07193 (Dec. 2020), arXiv:2012.07193. arXiv: 2012.07193 [astro-ph.HE].

[197] J. D. Gropp et al. "GRB 190114C: Swift detection of a very bright burst with a bright optical counterpart." In: *GRB Coordinates Network* 23688 (Jan. 2019), p. 1.

[198] R. Hamburg et al. "GRB 190114C: Fermi GBM detection." In: *GRB Coordinates Network* 23707 (Jan. 2019), p. 1.

[199] M. et al. Ajello. "Fermi and Swift Observations of GRB 190114C: Tracing the Evolution of High-energy Emission from Prompt to Afterglow". In: ApJ 890.1, 9 (Feb. 2020), p. 9. DOI: 10.3847/1538-4357/ab5b05. arXiv: 1909.10605 [astro-ph.HE].

[200] M. E. Ravasio et al. "GRB 190114C: from prompt to afterglow?" In: A&A 626, A12 (June 2019), A12. DOI: 10.1051/0004-6361/201935214. arXiv: 1902.01861 [astro-ph.HE].

[201] J. Selsing et al. "GRB 190114C: NOT optical counterpart and redshift." In: *GRB Coordinates Network* 23695 (Jan. 2019), p. 1.

[202] A. J. Castro-Tirado et al. "GRB 190114C: refined redshift by the 10.4m GTC." In: *GRB Coordinates Network* 23708 (Jan. 2019), p. 1.

[203] A. Franceschini, G. Rodighiero, and M. Vaccari. "Extragalactic optical-infrared background radiation, its time evolution and the cosmic photon-photon opacity". In: A&A 487.3 (Sept. 2008), pp. 837–852. DOI: 10.1051/0004-6361:200809691. arXiv: 0805.1841 [astro-ph].

[204] Rudy C. Gilmore et al. "Semi-analytic modelling of the extragalactic background light and consequences for extragalactic gamma-ray spectra". In: MNRAS 422.4 (June 2012), pp. 3189–3207. DOI: 10.1111/j.1365-2966.2012.20841.x. arXiv: 1104.0671 [astro-ph.CO].

[205] Justin D. Finke, Soebur Razzaque, and Charles D. Dermer. "Modeling the Extragalactic Background Light from Stars and Dust". In: ApJ 712.1 (Mar. 2010), pp. 238–249. DOI: 10.1088/0004-637X/712/1/238. arXiv: 0905.1115 [astro-ph.HE].

[206] Mario Vietri. "GeV Photons from Ultrahigh Energy Cosmic Rays Accelerated in Gamma Ray Bursts". In: Phys. Rev. Lett. 78.23 (June 1997), pp. 4328–4331. DOI: 10.1103/PhysRevLett.78.4328. arXiv: astro-ph/9705061 [astro-ph].

[207] Alberto Franceschini and Giulia Rodighiero. "The extragalactic background light revisited and the cosmic photon-photon opacity (Corrigendum)". In: A&A 614, C1 (June 2018), p. C1. DOI: 10.1051/0004-6361/201629684e.

[208] Amy Lien et al. "The Third Swift Burst Alert Telescope Gamma-Ray Burst Catalog". In: ApJ 829.1, 7 (Sept. 2016), p. 7. DOI: 10.3847/0004-637X/829/1/7. arXiv: 1606.01956 [astro-ph.HE].

[209] S. Dichiara et al. "GRB 190829A: Swift detection of a burst consistent with a galaxy at z=0.08". In: *GRB Coordinates Network* 25552 (Aug. 2019), p. 1.

[210] Fermi GBM Team. "GRB 190829A: Fermi GBM Final Real-time Localization". In: *GRB Coordinates Network* 25551 (Aug. 2019), p. 1.

[211] Vikas Chand et al. "Peculiar Prompt Emission and Afterglow in the H.E.S.S.-detected GRB 190829A". In: ApJ 898.1, 42 (July 2020), p. 42. DOI: 10.3847/1538-4357/ab9606. arXiv: 2001.00648 [astro-ph.HE].

[212] F. Piron et al. "GRB 190829A: Fermi-LAT Upper Limits". In: *GRB Coordinates Network* 25574 (Aug. 2019), p. 1.

[213] A. F. Valeev et al. "GRB 190829A: 10.4m GTC spectroscopy". In: *GRB Coordinates Network* 25565 (Aug. 2019), p. 1.

[214] V. Lipunov et al. "GRB 190829A: MASTER confirmation of GROND SN". In: *GRB Coordinates Network* 25652 (Sept. 2019), p. 1.

[215] T. Laskar et al. "GRB 190829A: ATCA cm-band detection". In: *GRB Coordinates Network* 25676 (Sept. 2019), p. 1.

[216] I. Monageng et al. "GRB 190829A: MeerKAT radio observation". In: *GRB Coordinates Network* 25635 (Sept. 2019), p. 1.

[217] A. de Ugarte Postigo et al. "GRB 190829A: NOEMA detection of the mm afterglow". In: *GRB Coordinates Network* 25589 (Aug. 2019), p. 1.

[218] Poonam Chandra and et al. "GRB 190829A: Detection of radio afterglow with the uGMRT". In: *GRB Coordinates Network* 25627 (Sept. 2019), p. 1.

[219] L. Rhodes et al. "Radio afterglows of very high-energy gamma-ray bursts 190829A and 180720B". In: MNRAS 496.3 (June 2020), pp. 3326–3335. DOI: 10.1093/mnras/staa1715. arXiv: 2004.01538 [astro-ph.HE].

[220] T. W. Chen et al. "GRB 190829A: GROND detection of the Optical/NIR Afterglow". In: *GRB Coordinates Network* 25569 (Aug. 2019), p. 1.

[221] P. D'Avanzo et al. "GRB 190829A: TNG imaging of the NIR afterglow". In: *GRB Coordinates Network* 25591 (Aug. 2019), p. 1.

[222] Gregory S. H. Paek, Myungshin Im, and et al. "GRB 190829A: UKIRT detection of the NIR Afterglow". In: *GRB Coordinates Network* 25584 (Aug. 2019), p. 1.

[223] F. Piron et al. "GRB 190829A: Fermi-LAT Upper Limits". In: *GRB Coordinates Network* 25574 (Aug. 2019), p. 1.

[224] H. E. S. S. Collaboration et al. "Constraints on the emission region of <ASTROBJ>3C 279</ASTROBJ> during strong flares in 2014 and 2015 through VHE γ-ray observations with H.E.S.S." In: A&A 627, A159 (July 2019), A159. DOI: 10.1051/0004-6361/201935704. arXiv: 1906.04996 [astro-ph.HE].

[225] O. Blanch et al. "GRB 201216C: MAGIC detection in very high energy gamma rays". In: *GRB Coordinates Network* 29075 (Dec. 2020), p. 1.

[226] O. Blanch et al. "MAGIC observations of GRB 201015A: hint of very high energy gamma-ray signal". In: *GRB Coordinates Network* 28659 (Oct. 2020), p. 1.